Universidade de Évora - Instituto de Investigação e Formação Avançada

Programa de Doutoramento em Engenharia Mecatrónica e Energia

Área de especialização | Energia

Tese de Doutoramento

Direct Normal Irradiance and circumsolar radiation: modelling, measurement and impact on Concentrating Solar Power

Edgar Francisco Mendes Abreu

Orientador(es) | Maria João Costa

Paulo Canhoto

Évora 2023

Universidade de Évora - Instituto de Investigação e Formação Avançada

Programa de Doutoramento em Engenharia Mecatrónica e Energia

Área de especialização | Energia

Tese de Doutoramento

Direct Normal Irradiance and circumsolar radiation: modelling, measurement and impact on Concentrating Solar Power

Edgar Francisco Mendes Abreu

Orientador(es) | Maria João Costa

Paulo Canhoto

Évora 2023

A tese de doutoramento foi objeto de apreciação e discussão pública pelo seguinte júri nomeado pelo Diretor do Instituto de Investigação e Formação Avançada:

Presidente	João Manuel Figueiredo (Universidade de Évora)
Vogais	Ana Maria Silva (Universidade de Évora) Gabriel López Rodríguez (Universidad de Huelva - Dpto. Ingeniería Eléctrica y Térmica, de Diseño y Proyectos) Luís Filipe Moreira Mendes (Universidade de Lisboa) Miguel Centeno Da Costa Ferreira Brito (Universidade de Lisboa - Faculdade de Ciências) Paulo Canhoto (Universidade de Évora) (Orientador)

Évora 2023

To my parents, who teach me
To Joana, who guides me
To Francisco, who inspires me

Summary

In this work, the modelling and measurement of direct and circumsolar normal irradiance (DNI and CSNI, respectively) is studied, as well as their impact on the energy generation of concentrating solar power systems (CSP). To model DNI, two approaches are used: (i) developing a fast and simple model to estimate diffuse horizontal irradiance, and consequently, DNI; and (ii) assess the performance of three distinct state-of-the-art models with different degrees of complexity. Regarding the first approach, it was found that the developed model that considers the climate zone was able to outperform the models available in the literature. Regarding the second approach, it was found that the radiative transfer model libRadtran and the parametrization model SMARTS are the models that provide the best DNI predictions. In this way, libRadtran is used to generate a database of DNI and CSNI values. Then, a new CSNI model is developed to estimate CSNI for a half-opening angle of 2.5° that only requires solar radiation data as input. It was found that the proposed CSNI model outperforms the models available in the literature in almost all of the locations analysed. However, the half-opening angles of common CSP systems are lower than 2.5°. Therefore, an upgrade of the CSNI model is developed that enables the determination of CSNI for a specific half-opening angle. The improved model is then able to predict the CSNI that reaches the CSP receiver and estimate the variation in the system's intercept factor caused by CSNI variation. It was found that discarding CSNI could lead to up to a 7% difference between the measured DNI and the DNI that is captured by the CSP system. Furthermore, it was also found that higher rim angles are needed if the impact of CSNI variation is to be mitigated in parabolic trough concentrators.

Resumo

Irradiância Direta Normal e radiação circunsolar: modelação, medição e impacto em Sistemas de Concentração Solar

Neste trabalho, são estudadas a modelação e a medição da irradiância direta normal e circunsolar direta normal (DNI e CSNI, respetivamente), assim como o seu impacto na geração de energia em sistemas de concentração solar (CSP). São usadas duas abordagens para modelar a DNI: (i) desenvolvimento de um modelo simples e rápido para estimar a irradiância difusa horizontal e consequentemente a DNI; (ii) avaliar a performance de três modelos de última geração com diferentes graus de complexidade. Relativamente à primeira abordagem, verificou-se que o modelo desenvolvido e que considera a zona climática é capaz de superar os modelos disponíveis na literatura. Relativamente à segunda abordagem, verificou-se que os modelos de transferência radiativa libRadtran e de parametrização SMARTS são os que apresentam as melhores estimativas de DNI. Desta forma, o libRadtran é usado para gerar uma base de dados de valores de DNI e CSNI. De seguida, é desenvolvido um novo modelo para estimar a CSNI para um meio-ângulo de abertura de 2.5° que apenas necessita de dados de radiação solar. Verificou-se que o modelo desenvolvido supera os modelos disponíveis na literatura em quase todos os locais analisados. No entanto, o meio-ângulo de abertura de sistemas CSP comuns é inferior a 2.5°. Por isso, foi desenvolvida uma atualização ao modelo que permite a determinação da CSNI para um meio-ângulo de abertura específico. O modelo atualizado é capaz de prever a CSNI que chega ao recetor do sistema CSP e estimar a variação do fator de interceção do sistema causada pela variação da CSNI. Verificou-se que descartar a CSNI pode levar a uma diferença de até 7% entre a DNI medida e a DNI que é intercetada pelo sistema CSP. Verificou-se ainda que para mitigar o impacto da variação da CSNI em concentradores cilindro-parabólicos é necessário ter *rim angles* maiores.

Acknowledgments

Firstly, I would like to express my deepest gratitude to my supervisor Professor Paulo Canhoto for his patient and invaluable support, knowledge and feedback. I am also extremely thankful to my co-supervisor Professor Maria João Costa, for her encouragement, feedback and expertise.

I acknowledge the support of the Portuguese National Science Foundation – FCT (Fundação para a Ciência e a Tecnologia) – through the Grant No. SFRH/BD/136433/2018. I also acknowledge the support of the ICT - Institute of Earth Sciences through the funding provided by the European Union through the European Regional Development Fund, included in the COMPETE 2020 (Operational Program Competitiveness and Internationalization) through the ICT project (UIDB/04683/2020) with the reference POCI-01-0145-FEDER-007690. A special acknowledgement to DNI-A (ALT20-03-0145-FEDER-000011) project for the financial support at the beginning of this work.

I am also grateful to my colleagues and friends Isaías Gomes, Sara Pereira and André Albino, which helped me with feedback and moral support. Special thanks to my friends Germilly Barreto and Flávio do Couto, for all the support and shared moments.

I would also like to thank Christian A. Gueymard for his work and suggestions that enriched the content of this thesis, specifically chapter 3.

Lastly, I would be remiss in not mentioning my family, especially my parents Francisco and Irene, my spouse Joana, and my son Francisco to whom I dedicate this thesis. Their belief in me has kept my spirits and motivation high during this process. This work would not be possible without their support.

Contents

List of Papers

This thesis includes the following papers:

I. Edgar F.M. Abreu, Paulo Canhoto, and Maria J. Costa. Prediction of diffuse horizontal irradiance using a new climate zone model. *Renewable and Sustainable Energy Reviews*, 110:28-42, 2019. https://doi.org/10.1016/j.rser.2019.04.055. [Chapter 2]

II. Edgar F.M. Abreu, Christian A. Gueymard, Paulo Canhoto, and Maria J. Costa. Performance assessment of clear-sky solar irradiance predictions using state-of-the-art radiation models and input atmospheric data from reanalysis or ground measurements. *Solar Energy*, 252:309-321, 2023. https://doi.org/10.1016/j.solener.2023.01.051. [Chapter 3]

III. Edgar F.M. Abreu, Paulo Canhoto, and Maria J. Costa. Development of a clear-sky model to determine circumsolar irradiance using widely available solar radiation data. *Solar Energy*, 205:88-101, 2020. https://doi.org/10.1016/j.solener.2020.05.010. [Chapter 4]

IV. Edgar F.M. Abreu, Paulo Canhoto, and Maria J. Costa. Prediction of circumsolar irradiance and its impact on CSP systems. Under review in *Energies*. [Chapter 5]

Other papers related with the subject of the present thesis, but not included, are:

i. Elena Carra, Aitor Marzo, Jesús Ballestrín, Jesús Polo, Javier Barbero, Joaquín Alonso-Montesinos, Rafael Monterreal, Edgar F.M. Abreu, and Jesús Fernández-Reche. Atmospheric extinction levels of solar radiation using aerosol optical thickness satellite data. Validation methodology with measurement system. *Renewable Energy*, 149:1120-1132, 2020. https://doi.org/10.1016/j.renene.2019.10.106.

ii. Hugo G. Silva, Edgar F.M. Abreu, Francis M. Lopes, Afonso Cavaco, Paulo Canhoto, Jorge Neto, and Manuel Collares-Pereira. Solar Irradiation Data Processing using estimator MatriceS (SIMS) validated for Portugal (southern Europe). *Renewable Energy*, 147:515-528, 2020. https://doi.org/10.1016/j.renene.2019.09.009.

iii. Maksim Iakunin, Edgar F.M. Abreu, Paulo Canhoto, Sara Pereira, and Rui Salgado. Impact of a large artificial lake on regional climate: a Typical Meteorological Year Meso-NH simulation results. *International Journal of Climatology*, 42(2):1231– 1252, 2022.https://doi.org/10.1002/joc.7299.

iv. Sara Pereira, Edgar F.M. Abreu, Maksim Iakunin, Afonso Cavaco, Rui Salgado, and Paulo Canhoto. Method for solar resource assessment using numerical weather prediction and artificial neural network models based on typical meteorological data: Application to the south of Portugal. *Solar Energy*, 236(02):225-238, 2022. https://doi.org/10.1016/j.solener.2022.03.003.

Other publications related with the subject of the present thesis, but not included, are:

i. Rui Salgado, Francisco Lopes, Edgar F.M. Abreu, Afonso Cavaco, Masud R. Rashel, Paulo Canhoto, Maria J. Costa, Mouhaydine Tlemcani, C. Lac, and H.G. Silva. Simulation of Direct Normal Irradiation (DNI) in Alentejo with the atmospheric Meso-NH model. Several case studies. *10º Simpósio de Meteorologia e Geofísica da APMG*, 2017 (poster session). http://hdl.handle.net/10174/22989.

ii. Edgar F.M. Abreu, Paulo Canhoto, and Maria J. Costa. Direct Normal Irradiance and circumsolar radiation: modelling, measurement and impact on Concentrating Solar Power. *Jornadas do ICT*, 2017 (poster session). https://doi.org/10.13140/RG.2.2.18544.56328.

iii. Edgar F.M. Abreu, Paulo Canhoto, and Maria J. Costa. Circumsolar irradiance modelling using libRadtran and AERONET data. *SolarPACES*, 2018 (poster session). https://doi.org/10.13140/RG.2.2.23828.96648.

iv. Edgar F.M. Abreu, Paulo Canhoto, and Maria J. Costa. Circumsolar irradiance modelling using libRadtran and AERONET data. *AIP Conference Proceedings*, 2126:190001, 2019. https://doi.org/10.1063/1.5117698.

v. Edgar F.M. Abreu, Paulo Canhoto, and Maria J. Costa. Modifying a pyrheliometer to measure direct normal and circumsolar irradiance. *III Congresso Luso-Extremadurense de Ciências e Tecnologia*, 2019 (poster session). https://doi.org/10.13140/RG.2.2.17077.63203/1.

vi. Sara Pereira, Edgar F.M. Abreu, Maksim Iakunin, Paulo Canhoto, and Rui Salgado. Estimativa do potencial fotovoltaico no sul de Portugal através de simulações do modelo Meso-NH para um ano meteorológico típico. *III Congresso Luso-Extremadurense de Ciências e Tecnologia*, 2019 (poster session). https://doi.org/10.13140/RG.2.2.19961.83045.

vii. Sara Pereira, Edgar F.M. Abreu, Maksim Iakunin, Paulo Canhoto, and Rui Salgado. Prediction of Solar Resource and Photovoltaic Energy Production through the Generation of a Typical Meteorological Year and Meso-NH Simulations: Application to the South of Portugal. *2019 IEEE 2nd International Conference on Renewable Energy and Power Engineering (REPE)*, 182-186, 2019. `https://doi.org/10.1109/REPE48501.2019.9025118`.

viii. Edgar F.M. Abreu, Paulo Canhoto, and Maria J. Costa. Comparison and assessment of circumsolar ratio models for Évora, Portugal. *Jornadas do ICT*, 2020 (poster session). `http://hdl.handle.net/10174/27151`.

List of Figures

List of Tables

Chapter 1

Introduction

1.1 Preliminary remarks

One of the biggest challenges of society nowadays is to have reliable, affordable and sustainable energy for all people. To tackle this challenge, the world is slowly shifting from fossil fuels such as oil and coal, to renewable energies, such as solar energy. The efforts leading to this shift are commonly called as the energy transition.

Energy transition is a broad subject that includes energy generation, energy storage, transportation and the efficient and rational use of energy. In this thesis, we will focus on solar energy capturing and conversion. Solar energy systems can be used mainly with two goals: to generate process heat (at low and high temperatures) or to generate electricity. On one hand, process heat can be obtained using plane collectors (low temperature) and concentrating solar power (CSP) systems (medium and high temperature). On the other hand, electricity can be generated using photovoltaic (PV) cells, assembled into a plane module or using concentrating photovoltaic systems (CPV).

A CSP system uses mirrors/reflectors to concentrate solar radiation in a receiver to achieve high temperatures. The heat resulting from the concentrated solar radiation can be used directly as process heat in industrial processes, or it can be used to generate steam to drive a power cycle and generate electricity. The ability to generate electrical power and the possibility to store heat instead of electro-chemical storage (as it's more reliable and efficient) is what pushes CSP systems as an important part of the energy generation mix.

Contrary to the PV technology that can generate electricity from global irradiance on the plane of the modules, CSP systems can only use the direct component of solar radiation, i.e., direct normal irradiance (DNI). Therefore, the measurement and modelling of DNI and its circumsolar component (circumsolar normal irradiance, CSNI) is of major importance for the design and operation of CSP systems. Furthermore, the detailed angular distribution of CSNI within the DNI measurements is of great interest to accurately determine the effective DNI that is reflected by the CSP mirrors.

1.2 DNI and circumsolar irradiance modelling

According to ISO 9488:2022 [1], solar radiation refers to the emission and transfer of energy from the sun in the form of electromagnetic waves or particles. This radiation can refer to solar exposure, solar energy, solar irradiance or solar radiance [2]. In the field of solar energy research, the term solar irradiance is commonly used and refers to the radiant power incident on a surface per unit area (W/m^2).

Direct normal irradiance (DNI) is the radiant flux to the area of a plane perpendicular to the sun that is received from a small solid angle centred on the sun's disk. Despite the recommended field of view of the sensors used to measure DNI being 5 degrees, it can be measured using instruments that have a field of view up to 6 degrees [3]. However, the solar disk only has an angular diameter of approximately 0.5 degrees. This difference between the field of view of the measuring instruments and the angular diameter of the sun, leads to the circumsolar issue, and therefore requires the accurate determination of the circumsolar normal irradiance [4].

Circumsolar normal irradiance (CSNI) is the radiant flux to the area of a plane perpendicular to the sun, of the radiation scattered by the atmosphere so that it appears to originate from an area of the sky neighbouring the solar disk [1]. The study of circumsolar irradiance is important because it enables the determination of the circumsolar contribution, i.e., the contribution of a specific portion of CSNI to DNI [1].

Since the field of view of the instruments that measure DNI are larger than the field of view of the CSP systems, information on the circumsolar contribution is crucial to accurately determine the energy that effectively reaches the CSP systems, i.e. the DNI intensity and its angular distribution, as this will ultimately contribute for a better design and operation of CSP systems, and therefore, higher energy generation and efficiency..

On the same note, information on the angular distribution of CSNI can also be useful when carrying out instrument calibration. Despite the somewhat recent standardization of the aperture angle of field pyrheliometers, there are still pyrheliometers in operation with different aperture angles. In this way, information on CSNI when performing instrument calibration is useful in the cases when reference and field pyrheliometers have different aperture angles.

CSNI intensity strongly depends on atmospheric constituents such as aerosols and clouds. Aerosols are solid or liquid particles suspended in the atmosphere that can be directly produced in the atmosphere through complex chemical reactions or emitted to the atmosphere as particles. They can be originated from natural or anthropogenic processes (e.g. biomass combustion, urban pollutants, marine salt or mineral dust). In the presence of aerosols, DNI is scattered or absorbed (less

frequent), depending on the size and type of aerosols. Regarding clouds, CSP cannot operate under dense water clouds but its operation is possible in the presence of thin cirrus clouds, because DNI can still be transmitted through them, despite having its intensity and distribution altered due to scattering processes.

The scattering effect on DNI caused by aerosols and/or thin cirrus clouds results in a transfer of radiation from the solar disk to the circumsolar region, which in turn results in a larger circumsolar contribution, i.e., higher CSNI. Therefore, it is of great importance to accurately characterize the circumsolar contribution, which in turn will result in a more accurate characterization of DNI, and, consequently, in an improvement of CSP systems design, operation and energy generation.

To gather information on DNI and CSNI, two approaches are commonly used: to use instruments to directly or indirectly measure these quantities, and/or to use mathematical models with several degrees of complexity to estimate these quantities. In the next sections, DNI and CSNI modelling and measurement approaches are briefly addressed and reviewed.

1.2.1 Radiative transfer models

Radiative transfer models (RTMs) are detailed models that are used to estimate the radiation field within different atmospheric characteristics as well as surface conditions [5, 6]. These models can be used to determine the solar irradiance reaching a given surface, hence their application in solar energy, but they can also be used in numerous other research areas such as atmospheric chemistry, weather prediction or remote sensing [7].

RTMs are able to accurately describe the conditions of the atmosphere at a given instant and location, addressing details such as trace gas profiles, aerosol profiles, water vapour, and water and ice clouds to name a few [7]. Through this detailed characterization, RTMs are able to evaluate the broadband or spectral, downwelling or upwelling, irradiances, radiances or reflectances, in different spectral regions and pressure levels in the atmosphere [8]. This high level of detail in both input and output of RTMs is what allows to use them as reference (the most accurate) in solar radiation modelling studies (e.g. [8, 9]).

One of such radiative transfer models is libRadtran [7]. LibRadtran comprises a library of radiative transfer routines and programs that allows the user to setup and modify the atmospheric constituents, such as molecules, aerosol particles, water and ice clouds, and define a surface as lower boundary. It is also possible to choose from several solvers to the radiative transfer equation such as the discrete ordinate radiative transfer solver (DISORT) [10] or a Monte Carlo solver (MYSTIC) [11, 12, 13, 14, 15]. LibRadtran has been used in many studies available in the literature, both in the atmospheric sciences and in the solar energy engineering fields (e.g. [16, 17, 18]).

Another example of a radiative transfer model is the MODerate resolution atmospheric TRANsmission (MODTRAN) [19]. MODTRAN computes line-of-sight atmospheric spectral transmittances and radiances across the entire solar radiation spectrum (from infrared to ultraviolet). The atmosphere is modelled using vertical profiles of its constituents which can be defined through built-in routines or by user-specified radiosonde or climatological data. Similarly to libRadtran, MODTRAN is also found in several studies available in the solar energy literature (e.g. [9, 20, 21]).

The main advantages of RTMs are related to the detail of inputs and outputs. Regarding the inputs, RTMs are able to use information on almost all of the possible atmosphere's constituents, which gives them the capacity to accurately describe the atmospheric conditions at a given instant and location. This translates into more precise predictions of solar irradiance on any user-defined surface. Thus, regarding the outputs, RTMs are not only able to provide both spectral and integrated data, but can also predict the two components of solar irradiance that reach the Earth's surface, namely direct and diffuse irradiances (DirHI and DHI, respectively, when considering the horizontal plane). RTM models are also able to compute the sky radiance, which after integration over both zenith and azimuth angles can provide information on the circumsolar irradiance.

However, this high level of detail also has its drawbacks that prevent RTMs to be widely used in solar energy engineering, the most important being the difficulty on accessing all of the required inputs to accurately characterize the atmosphere and being arduous to run for a large set of data due to the management of all inputs, complexity of the model and required computation time and power.

1.2.2 Parametrization models

When simulating solar irradiance, it is common to firstly simulate the clear-sky irradiance and then to superimpose the impact of clouds [22]. Because of this, the use of radiative transfer models (RTMs) as the reference model is of major importance in solar energy. However, such models require a set of atmospheric inputs that are not always readily available, are more difficult to operate and run, and are thus take more time to provide results. For these reasons, parametrization models were developed.

A parametrized model is a model that provides solar irradiance predictions based on a number of simplifications of RTMs. These simplifications can be either of the physical phenomena that occur in the atmosphere or based on empirical approximations. In this way, parametrization models are able to offer better predictions than entirely empirical models, but also usually require more computation time and power and higher input data quality and/or quantity.

One example of a parametrization model is the Simple Model of the Atmospheric

Radiative Transfer of Sunshine (SMARTS) [23, 24]. SMARTS is a simple transmittance parametrization that is able to predict direct, diffuse, global and circumsolar irradiance on horizontal or tilted surfaces. It allows the user to choose from ten reference atmospheres that consist of different vertical profiles of temperature, pressure and concentration of the most common gases. The DNI is determined using the extra-terrestrial irradiance (taking into account the variation of the sun-earth distance) and several transmittances for different extinction phenomena, namely Rayleigh scattering, absorption by nitrogen dioxide, ozone, uniformly mixed gases, water vapour and aerosol extinction. Regarding CSNI, a correction factor is used to predict the irradiance measured by radiometers with a field of view larger than the solar disk. This has to due with the aforementioned scattering of the sun rays near the vicinity of the sun caused by aerosols and cirrus clouds. In this way, SMARTS is able to estimate all components of the solar radiation that reach a given surface and are of importance for solar energy, namely GHI, DNI, DHI and CSNI. Some examples of the use of the SMARTS model in solar energy engineering can be found in [8], [25] and [26].

Another example of a parametrization model is McClear [27]. McClear is a clear-sky model (a model that is only intended to predict solar irradiance in cloudless skies) that was created to use the data from the Monitoring Atmosphere Composition and Climate (MACC) project. This model uses an abacus (more known as a lookup table) to estimate the clearness index (ratio between the global horizontal irradiance at the Earth's surface and at the top of the atmosphere) and direct clearness index (ratio between the direct normal irradiance at the Earth's surface and at the top of the atmosphere) according to solar zenith angle, ground albedo, elevation and other parameters that describe the optical state of the atmosphere. The main purpose of this model is to estimate DNI and GHI at the surface under clear-sky conditions. The McClear model has been used in several studies available in the literature, such as in [8], [28] and [29], to name a few.

Regarding circumsolar irradiance, the availability of parametrization models is very low. A remarkable example is the work by Sun et al. [30]. In this study, the authors developed a phase function scaling method to determine DNI and CSNI. This method was incorporated in two other models to estimate DNI, resulting on improved DNI estimates because of the inclusion of CSNI.

The major issue of parametrization models is to accurately model extreme conditions such as high aerosol loads, high site elevations and low solar altitudes [8]. This issue poses a quite inconvenient problem, since high potential sites for installing solar energy systems usually have one or more of the atmospheric conditions mentioned above. However, parametrization models still remain one of the most effective ways to generate solar radiation data, getting the best trade-off between model accuracy,

input data quality/quantity and modelling speed.

1.2.3 Empirical models

Empirical models are simple mathematical relationships between different parameters. These mathematical equations can use several input parameters (e.g. atmospheric parameters like the ambient temperature or solar ratios such as clearness index) and have different degrees of complexity (e.g. linear, cubic, exponential, etc.). An example of such empirical models is the model from the American Society of Heating Refrigeration and Air Conditioning Engineers (ASHRAE) [31], which uses the day of year to estimate the clear-sky DNI. Many other models in this category can be found in the literature, and the reader is advised to look into more detailed reviews on this subject like the one by Ruiz-Arias and Gueymard [28] for more in this topic.

A more specific and widely used type of empirical models are the so-called *separation models*. Separation models are simple and empirical models that are used to separate the diffuse and direct components of GHI. These models use the clearness index (ratio between the GHI and the extra-terrestrial horizontal irradiance) and other parameters, to estimate de diffuse fraction (ratio between the DHI and GHI). The majority of separation models available in the literature only require GHI as input (e.g. [32, 33, 34]), but there are some that use more than one predictor in an attempt to increase model performance (e.g. [35, 36, 37]). Despite the number of predictors, separation models are able to predict DHI and DNI (through the use of the so-called *closure equation*: $\text{GHI} = \text{DHI} + \text{DNI} \cdot \cos(\theta)$, where θ is the solar zenith angle) in a very fast and simple way.

However, since separation models are empirical and simple, their performance is not the most accurate; there is a trade-off between fastness and simplicity and accuracy. An extensive review of such models was presented in [38]. In this work, the authors analysed the capability of 140 separation models with different predictors to determine DNI. It was found that model performance was related to specific conditions in the locations under study (e.g. atmospheric turbidity) as well as to the number of predictors of each model (e.g. solar zenith angle, air mass, air temperature, etc.). Moreover, higher number of predictors did not guaranteed higher performance. In the same study, the authors also highlighted the necessity for separation models to take into account cloud enhancement effects, which are important to the design and operation of solar energy systems.

Whilst some years ago the standard procedure was to use hourly averaged values of solar irradiance, nowadays the standard is to use one-minute average values because it allows representing the small time scale changes and processes. However, this also results in more complexity in separation models due to cloud-enhancement effects which occurs when the radiation scattered off cloud's edges leads to a significant

increase in global irradiance at the Earth's surface [39]. While cloud-enhancement effects are not observed in hourly mean values, their occurrence in one-minute data becomes evident and the importance of the models to account for these effects cannot be overlooked [39].

Another concern with separation models is climate-specific fitting. It is possible to find very distinct atmospheric and climate conditions across the globe. This results in over-fitting of the separation models to the climate where they were developed, which in turn lowers their accuracy under different climate conditions. To address this, researchers can use only site-specific models (which is not optimal), use an ensemble of different models [40], or can use new *worldwide* models [41].

Accounting for both advantages (simple and fast) and disadvantages (relatively low accuracy), separation models can be used in solar energy engineering to: a) estimate the irradiance on tilted surfaces, and with that, predict the output of photovoltaic systems; b) estimate DNI, and do a first analysis on the suitability of a location to install CSP systems.

Contrary to the high number of empirical/separation models available in the literature that can be used to model DNI, empirical models that can be used to model CSNI are quite rare. Possible reasons to explain this are: a) low availability of CSNI datasets that can be used to develop these models; and b) the magnitude of CSNI is related to several and not so readily available data of atmospheric variables such as aerosol optical depth and precipitable water vapour.

Nonetheless, a remarkable example of an empirical model to estimate CSNI is the one presented by Eissa et al. [42]. This model uses different site-specific coefficients to estimate the circumsolar ratio (CSR), using as input the sky clearness (an empirical index that is defined using DNI, DHI and θ). The modelled CSNI values showed a relative root mean square error of $\sim 20\%$, relative bias of -2.7% and a correlation coefficient of 0.871. These statistical indicators were determined using reference CSNI values modelled with libRadtran (using atmospheric observations as input).

When deriving empirical models, it is common practice to not use the same data to both train and validate the newly proposed model, because it can result in over-fitting of the model. In this work, this common practice was respected and all of the datasets used were divided into two different groups: training; and validation datasets.

1.2.4 Input data

Both radiative transfer models as well as parametrization models (and also a minority of empirical models) need accurate atmospheric data to generate accurate solar radiation estimates. Examples of these atmospheric data are: surface pressure, surface albedo, total column ozone amount, precipitable water vapour, and Angstrom's

turbidity and exponent [28]. Because of the high level of detail of RTMs and of some parametrization models, it can be stated that the quality of the model's outputs is closely related to the quality of the inputs.

In solar radiation modelling, there are usually two types of atmospheric datasets that are used: measured and synthetic. The atmospheric measured data commonly used in solar radiation estimates is obtained from AERONET (AErosol RObotic NETwork). AERONET is a ground-based remote sensing aerosol network established by NASA and PHOTONS (PHOtométrie pour le Traitement Opérationnel de Normalisation Satellitaire) [43, 44]. The network comprises more than 500 sites scattered around the world and provides measurements of parameters that greatly affect DNI such as aerosol optical depth and precipitable water vapour. AERONET also has an inversion algorithm that provides quantities such as aerosol phase function and size distribution, which are relevant aerosol characteristics.

In solar energy engineering, AERONET is commonly used as input to RTMs and parametrization models to estimate solar radiation (e.g. [42]). It is also used to study the impact of atmospheric constituents in solar energy applications (e.g. [45, 46]). Additionally, since AERONET is one of the most reliable sources of atmospheric data, it is also used as benchmark in assessment studies of other data sources, such as reanalyses [47, 48].

AERONET has its own quality filters and produces three datasets with three different quality control tiers: AERONET data level 1.0, 1.5 and 2.0. AERONET data level 1.0 are unscreened, do not have calibration applied and therefore are rarely used in the literature. AERONET data level 1.5 are screened for anomalies and some examples of its use can be found in the literature (e.g. [45, 49, 50]). AERONET data level 2.0 are screened for anomalies, are calibrated and are quality assured, being the data level used in the majority of studies (e.g. [42, 51, 52]). Despite the filtering provided by AERONET, some researchers developed their own filters in order to achieve an even more *clean* data set. For example, Gueymard and Yang [47] added two more filters to AERONET data level 2.0 to account for sensor malfunctioning, uncertainty in the readings with low aerosol optical depth, soiling and missing readings at specific wavelengths that can affect the determination of output variables.

Although AERONET has a high number of stations and extensive worldwide coverage, there are still many regions that have potential for installing solar energy applications and systems that cannot rely on AERONET data. Thus, one way for researchers to deal with this issue is to use reanalysis datasets such as CAMS or MERRA-2. Reanalysis datasets (sometimes referred as "maps without gaps") are datasets consistent in time that cover the entire globe and represent historical data of weather and climate. These datasets are a blend of observations alongside weather forecasts that were rerun with state-of-the-art Numerical Weather Prediction (NWP)

models.

Reanalysis datasets are mainly used to study climate change and extreme weather phenomena. However, solar energy researchers are increasingly adopting these datasets into solar radiation modelling because of their time consistency and worldwide availability [46, 48]. However, the quality of reanalysis datasets is not yet as good as the measured AERONET data, as showed in a recent study [47]. This is the major drawback of using these datasets in solar radiation modelling, since the quality of solar radiation models' outputs is closely related to the quality of their inputs.

The quality of reanalysis data has been increasing due to advances in modelling and the increasing use of high-quality observations, however, some bias still exists due to modelling inconsistencies or errors on the assimilation of experimental data [47]. Therefore, a simple filter that removes impossible physically values should be employed to account for extreme events that might trigger modelling outliers such as extreme smoke or pollution events in densely urban populated areas, as found by Gueymard and Yang [47].

In addition to the above data sources, solar radiation indexes derived directly from more readily available ground-based measurements (e.g. clearness index) are mainly used in empirical models. Almost all of the separation models described in the literature use the clearness index as input. However, other models also use other solar radiation data such as the model presented by Engerer [37]. In this work, the author used both the clearness index and the clear-sky index (which is obtained using the GHI from a clear-sky model) in the development of the proposed empirical (separation) model to estimate the diffuse fraction at Australia. The use of solar radiation indexes in the modelling of solar irradiance requires that both modelled and measured data are obtained using an accurate method, in order to guarantee the quality of the model outputs and the proper model's assessment.

1.3 DNI and circumsolar irradiance measurement

In this section, the ways of measuring DNI and CSNI are described, from the most accurate and expensive - complete radiometric stations - to some more affordable but less accurate alternative sources using fewer instruments. In addition to that, instrument calibration as well as quality control and data filtering procedures are addressed since they are crucial to ensure the quality of the measured data.

1.3.1 Radiometric stations

A radiometric station is a set of instruments that aim to measure the solar radiation incident on one or more surfaces at a specific location. Since there are several ways of installing and operating a radiometric station, a standard approach in how to

measure solar radiation using radiometric stations is needed, to ensure both the quality of the measurements as well as a fair comparison between the measurements available at different locations. To address this issue, the World Meteorological Organization (WMO) published the *Guide to Meteorological Instruments and Methods of Observation* [3]. In this guide, good practices for measuring solar radiation and other atmospheric parameters, as well as other sources of additional advice, are presented.

One of such sources is the Baseline Surface Radiation Network (BSRN) guidelines. BSRN is a global network of radiometric stations created by the World Climate Research Programme (WCRP) that is now incorporated in the WCRP Global Energy and Water Cycle Experiment (GEWEX). According to BSRN guidelines, a radiometric station must at least measure the following radiation fluxes in a high temporal resolution: DNI, DHI, GHI, and long-wave downward radiation [53]. The measurements must be taken preferably at 1 Hz sampling rate and one-minute average, minimum, maximum and standard deviation values must be recorded. The standard output should include these one-minute values for DNI, DHI, GHI, and long-wave radiation [54].

To measure these quantities, several instruments are used. DNI is measured using a pyrheliometer. GHI and DHI are measured using pyranometers. However, whilst the pyranometer is unshaded in the measurement of GHI, it needs to have a separate device (shadowing sphere or disk or shadow-band) to block the direct sun rays in the measurement of DHI. The long-wave downward radiation is measured using a shaded pyrgeometer.

There are two types of pyrheliometers: the more common field pyrheliometer (usually a thermopile sensor) and the active cavity radiometer. A field pyrheliometer is a thermopile sensor that and it is the standard and most reliable way to measure the radiation that comes directly from the sun within a given solid angle. The pyrheliometer has the shape of a tube and resembles a telescope. In one end of the tube, there is a quartz window through which the direct solar radiation enters into the tube and, in the other end, there is a thermopile sensor that generates an electric signal according to the temperature difference between the sensor body and the sensing element which, in turn, depends on the irradiance intensity that is to be measured. In this way, the higher the solar irradiance, the higher the temperature of the thermopile is, and therefore, the higher it is the electric signal that is generated. A calibration factor characteristic of each instrument is then used to convert the electric signal in solar irradiance units (usually W/m^2).

The active cavity radiometer (ACR) is a pyrheliometer that defines the absolute radiation scale. It has high-precision temperature sensors and heaters that make the ACR operate at an equilibrium temperature. The electrical power given/taken

to/from the heater to achieve the equilibrium temperature is equivalent to the change in incident solar irradiance. However, contrary to what happens with field pyrheliometers, active cavity radiometers are not used to perform solar resource assessment because they are expensive, its operation is complex, and it is more difficult to obtain continuous DNI measurements due to its working principles. Nonetheless, active cavity radiometers are very important since they provide the most accurate DNI measurements and, because of this, are used to calibrate field pyrheliometers.

Since pyrheliometers are used to measure the DNI that comes within a given solid angle centred with the sun, it needs to be installed in a sun tracking system. A sun tracking system (also known as sun tracker) is a device that rotates around two axes (elevation and azimuth) and uses a solar position algorithm to align with the apparent position of the sun in the sky. In addition to the algorithm, a sun tracker can also use a dedicated sun sensor for fine alignment, thus increasing the sun tracking accuracy. Despite the higher cost of measuring DNI with a pyrheliometer and a sun tracker, this is, currently, the most accurate way to measure DNI.

Because pyrheliometers have an aperture angle greater than the sun disk diameter, CSNI is included in the DNI measurements. This led some researchers to use pyrheliometers in order to gather more information on CSNI by changing the aperture angles of the instruments. This can be achieved through three ways: (i) increasing the length of the pyrheliometer's body; (ii) reducing the aperture diameter; or (iii) a combination of the previous two. An example of this is the device known as BPI CSR460 [55] used to gather information on CSNI which consists of two pyrheliometers with different aperture angles.

A pyranometer is a device that, similarly to a pyrheliometer, uses a thermopile to measure solar irradiance. However, instead of measuring DNI, a pyranometer is used to measure hemispherical solar radiation due to its 2π sr view angle. In this way, if the direct sun rays are not blocked, a pyranometer levelled with the horizontal measures GHI. But if the direct sun rays are blocked (eith using a disk, a sphere or a shadow band), then the same levelled pyranometer measures DHI.

Lastly, the pyrgeometer is an instrument also based on a thermopile that measures the net radiative exchange in the infra-red range between the sensor and the atmosphere. This can be used to determine the downward infra-red radiation from the atmosphere knowing the sensor temperature but, in this case, it is used to correct the zero-offset of pyranometers through a simple correlation. In fact, the pyranometers are affected by a zero-offset error due to: (i) fast variation of the temperature of the pyranometer body; and (ii) net thermal radiation exchange with the atmosphere, despite pyranometers being equipped with special glass domes. A correlation between the net infra-red exchange measurements from the pyrgeometer and this small zero-offset (night values) is used to improve the accuracy of measurements from

pyranometers.

In addition to the measuring instruments and the aforementioned sun tracker, a data logger is necessary to effectively run a radiometric station. A data logger is an electronic device that is used to convert analogue signals to digital and to record the readings from the sensors. It is able to measure the small voltage generated by the sensor's thermopiles and record it to after be converted into radiation units, using a specific sensor calibration factor.

Contrarily to DNI, there is no standard way of measuring CSNI. Until now, it was measured using several techniques, such as a specially designed telescope [56], high-resolution cameras [57, 58, 59], pyrheliometers with different aperture angles [55, 60, 61, 62] and rotative shadowband irradiometers (RSI) [63]. This lack of standardization on the measurement of CSNI translates in lack of consistency in the way it is measured in the radiometric stations, which highlights the need of alternative ways of gathering information on CSNI, namely through modelling.

1.3.2 Alternative sources

In this subsection, alternative sources to gather information on DNI and CSNI are described. As stated in the previous section, the most accurate and recommended way of measuring DNI is using a pyrheliometer mounted on a sun tracking system. However, to have a full radiometric station in operation is costly due to equipment cost and maintenance. Therefore, other ways of indirectly measuring DNI were found as described next.

An easier alternative of estimating DNI is to use two pyranometers to measure GHI and DHI. Then, using the closure equation, DNI data can be obtained. This option is cheaper than having a full radiometric station because the pyranometers don't require the sun tracking system to operate efficiently. However, it is important to note that it is less accurate due to the higher uncertainty associated with the measurement of pyranometers with respect to the pyrheliometer's measurements [54], and the fact that DHI measurements are obtained here using an adjustable shadow-band, thus blocking an higher fraction of diffuse irradiance from the sky (although there are empirical models that can be used to correct this).

Another way of indirectly estimating DNI that also makes use of the closure equation is based on the measurements of a rotative shadowband irradiometer (RSI) [64]. A RSI is a device constituted by two horizontal silicon photodiodes that detect radiation. Directly above the sensors, there is a spherically curved rotative shadow-band which can block the direct beam from the sun disk. This configuration allows the RSI to measure both GHI and DHI, which in turn can be converted into DNI using the closure equation. While the shadow-band is in the rest position, the RSI measures GHI because the shadow-band is positioned below (or in the side, depending on the

instrument model) the sensor. When the shadow-band is activated, it is momentarily placed in position relative to the sensor, in order to block the direct radiation and enabling the RSI to measure DHI.

1.3.3 Instrument calibration

Measuring DNI with a pyrheliometer is the most accurate way to gather information on DNI, as mentioned in Section 1.3.1. However, this is true only if the instrument is properly maintained and calibrated. And the same is also true for alternative methods to gather DNI such as using pyranometers or any other radiometers.

Generally speaking, a field radiometer is calibrated comparing its measurements against a previously calibrated radiometer, also known as reference radiometer. The calibration procedure consists of exposing the two radiometers to the same atmospheric conditions (radiation, wind speed and ambient temperature) as well as sky conditions (presence of clouds), and comparing their outputs. A calibration constant or responsivity of the field radiometer is then obtained in order to adjust its output to match the reference radiometer output.

The calibration process of pyranometers and pyrheliometers is well described in specific international organization for standardization (ISO) standards. The calibration of field pyranometers can be performed by comparison against a reference pyranometer (ISO 9847 [65]) or against a reference pyrheliometer (ISO 9846 [66]), while the calibration of field pyrheliometers can only be carried out against a reference pyrheliometer (ISO 9059 [67]). Despite not describing a specific calibration procedure, ISO 9060 [68] is worth to mention here because it defines several concepts used in the aforementioned calibration standards.

To perform a pyrheliometer calibration, the procedure described in ISO 9059 [67] must be followed. Regarding equipment, this calibration procedure needs a reference pyrheliometer, a sun tracker, a data acquisition system (data logger) and, obviously, the field pyrheliometer. The reference and field pyrheliometers must be installed and aligned on the sun-tracking system, and connected to the data acquisition system. Then, measurements must be taken during 10 to 20 minutes until a minimum of 10, or preferably 20, data series are collected with a minimum of 10 instantaneous readings. After this is achieved, a mathematical procedure of the data is required in order to eliminate data series that do not meet the quality requirements. Data that have been subject to operational problems or series in which the correspondent responsivity deviates more than 2% of the mean responsivity of all series must be rejected. Only then the final calibration factor should be determined.

To determine the uncertainty of the calibration procedure, the uncertainty of the reference pyrheliometer must be taken into account as well as the uncertainty of the data acquisition system. It is important to note that the uncertainty of the calibration

procedure strongly depends on the atmospheric conditions, namely on circumsolar irradiance and the aperture angles of the field and reference pyrheliometers. If the pyrheliometers have the same aperture angle (not only in the current calibration procedure, but also in the calibration procedure of the reference pyrheliometer) and the circumsolar radiation is small and strongly forward, then the uncertainty of the calibration is lower. However, if the reference and field pyrheliometers have different aperture angles, then a circumsolar correction must be applied in the mathematical procedure. To account for this effect, CSNI correction values are given in ISO 9059 [67] for several atmospheric conditions (aerosol type, spectral optical thickness, spectral Linke turbidity factors and solar elevation angles) and aperture angles.

To complete and record the calibration procedure, a calibration certificate where information such as location, time, the calibration method, the characteristics of the pyrheliometers used, the atmospheric conditions during which the calibration took place, the number of data points and the newly determined calibration factor must be stated. An example of a calibration report is presented in Appendix A. It is also recommended to store the calibration procedure raw data during the lifetime of the instrument.

According to ISO 9059 [67], all pyrheliometers shall be referred to the World Radiometric Reference (WRR), a high-quality measurement standard adopted by the World Meteorological Organization that is realized by a group of at least four pyrheliometers of different design, which are installed and maintained at the World Radiation Centre (Davos, Switzerland). This traceability to WRR, alongside the detailed calibration procedure follow-up, ensures that all pyrheliometers have a similar reference and allow for a fair comparison between measurements taken by different instruments at different locations. Similarly, the calibration of a field pyranometer can be performed using a reference pyranometer according to ISO 9847 [65], or, preferably, using a reference pyrheliometer according to ISO 9846 [66].

1.3.4 Quality control and data filtering

In solar energy engineering, it is important to use data filters in order to ensure that final results are not strongly affected by the quality of the input data. This is valid for both input data to solar radiation models as well as measured solar irradiance to assess model performance or study the viability, design and operation of solar energy systems.

The most common solar radiation data filters are those developed for the BSRN stations and account for physically possible limits, extremely rare limits and comparison tests [69], as shown in Table 1.1. These filters were established taking into account the data from the several BSRN stations around the globe and are meant to provide the user with a *clean* data set.

Table 1.1: BSRN physically possible limits, extremely rare minimum limits and comparison tests. Legend: S_a - solar constant adjusted for Earth-Sun distance; θ - solar zenith angle; and μ_0 - $\cos(\theta)$.

Variable	Min. value	Max. value	Condition
Physically possible limits			
DNI	$-4W/m^2$	S_a	-
DHI	$-4W/m^2$	$S_a \times 0.95 \times \mu_0^{1.2} + 50W/m^2$	-
GHI	$-4W/m^2$	$S_a \times 1.5 \times \mu_0^{1.2} + 100W/m^2$	-
Extremely rare limits			
DNI	$-2W/m^2$	$S_a \times 0.95 \times \mu_0^{0.2} + 10W/m^2$	-
DHI	$-2W/m^2$	$S_a \times 0.75 \times \mu_0^{1.2} + 30W/m^2$	-
GHI	$-2W/m^2$	$S_a \times 1.2 \times \mu_0^{1.2} + 50W/m^2$	-
Comparison tests			
$\frac{\text{GHI}}{\text{DNI} \times \mu_0 + \text{DHI}}$	$1.0 - 8\%$	$1.0 + 8\%$	$\theta < 75°$ and (DNI$\times\mu_0$+DHI)$> 50W/m^2$
$\frac{\text{GHI}}{\text{DNI} \times \mu_0 + \text{DHI}}$	$1.0 - 15\%$	$1.0 + 15\%$	$93° > \theta > 75°$ and (DNI$\times\mu_0$+DHI)$> 50W/m^2$
$\frac{\text{DHI}}{\text{GHI}}$	-	1.05	$\theta < 75°$ and GHI$> 50W/m^2$
$\frac{\text{DHI}}{\text{GHI}}$	-	1.10	$93° > \theta > 75°$ and GHI$> 50W/m^2$

In addition to the BSRN filters, some researchers developed their own filters based on their expertise and in the specific characteristics of the radiometric stations that are used in their studies. For example, Gueymard and Ruiz-Arias [39] used a portion of the BSRN quality filters and added some of their own, namely a filter that rejected data for high solar zenith angles, as this situations are of low irradiance and have marginal importance on solar energy systems (and correspond to situations when the solar radiation instruments and models are more prone to error), and some ratios to ensure that the uncertainty in the measurements did not affect the overall solar irradiance data set.

When the study requires or is intended for clear-sky conditions only, it is crucial to guarantee that the experimental data is not affected by scattered clouds in the sky, having a truly clear sky instead of having only a clear path between the sensor and the sun. To ensure that these conditions are met, it is common to use clear-sky detection models (e.g. [70, 71]). These models require as input mostly solar radiation data to identify the presence of clouds in the sky. They can also use atmospheric parameters (such as those provided by AERONET) in order to identify if if clouds are present (or not) in the sky, but the basis working principle is always to compare the solar radiation at a specific instant against its theoretical clear-sky intensity.

1.4 Impact of DNI and circumsolar radiation on CSP systems

1.4.1 Summary on the gathering of DNI and CSNI data

DNI is the most important solar radiation component regarding CSP systems design and operation. However, the angular distribution of CSNI can strongly affect the capability of CSP systems to capture the available solar energy. Whilst the importance of DNI from the sun disk is largely accepted and its measurement and modelling is widely studied, the same cannot be stated about CSNI. In Figure 1.1, a summary of the common approaches to obtain DNI and CSNI data are shown.

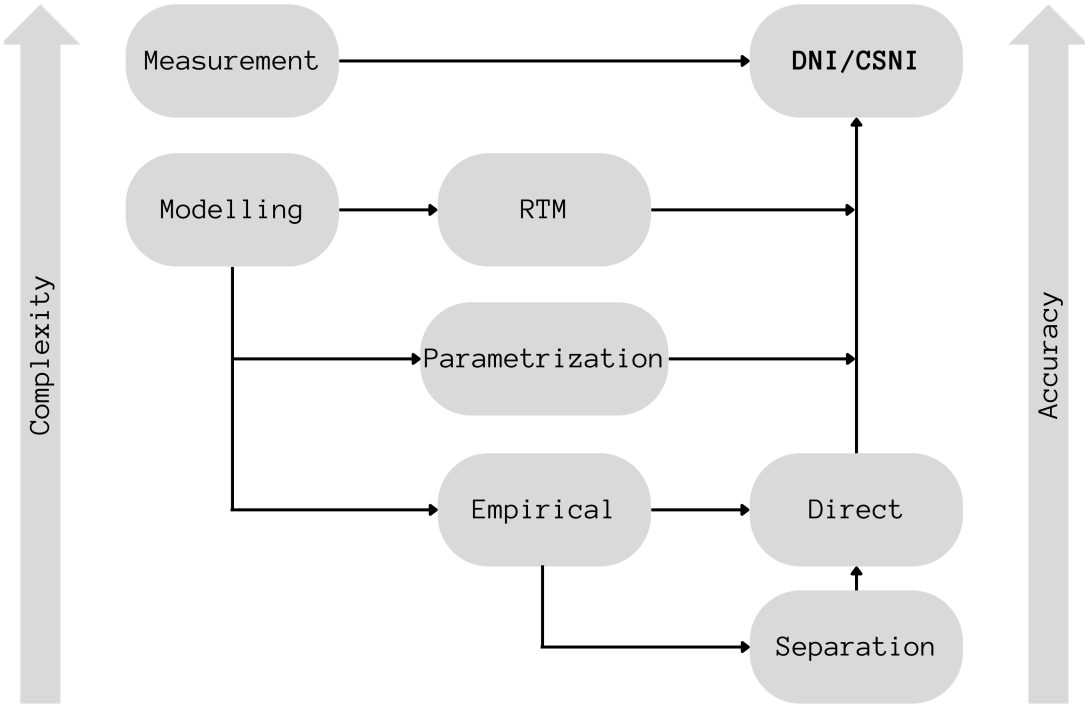

Fig. 1.1: Common approaches to obtain DNI and CSNI data.

The best approach to gather information on solar radiation is to use a well maintained and calibrated sensor to measure it. Whilst for DNI there is a standard process to perform measurements, the same is not true for CSNI because of the sharp decrease of intensity between the centre of the solar disk and the outer limit of the field of view of the measuring instruments [4]. Despite the attempts to measure CSNI mentioned in Section 1.3.1, the next best alternative to obtain CSNI data is to resort to modelling.

The most accurate way of modelling CSNI is through a radiative transfer model (RTM). However, its major drawbacks are the required inputs, as they are many and difficult to gather, and the more complicated set up and run of these models, because they need high computation time and power and they usually are less user friendly. This leads to the next best option that is to use parametrization models

such as SMARTS [23, 24], for instance. Although these models are easier to use than RTMs, the need for sophisticated atmospheric data input is similar and can be an obstacle to being widely adopted by the solar energy engineering community.

The simplest way to obtain CSNI data is then to use an empirical model such as the one presented by Eissa et al. [42]. These empirical models *only* require as inputs the more readily available solar radiation data, namely DNI, DHI and GHI. One can even say that these models only require GHI if a separation model is used to derive DHI, and then, DNI (see Section 1.2.3) Therefore, they can be easily used in engineering applications in the field, despite having a lower accuracy when compared to the more sophisticated options mentioned above.

1.4.2 Assessing the impact of DNI and CSNI on CSP systems

The issue with DNI, CSNI and CSP systems is that CSP systems usually have a lower acceptance angle than that of the pyrheliometers used to measure DNI. This can lead to significant discrepancies between the measured DNI and the DNI that reaches the CSP system, especially under turbid atmospheres [4]. The higher the concentration of aerosols and/or the presence of cirrus clouds in the atmosphere, the higher the amount of CSNI, and the higher are the errors of directly using DNI measurements to design and operate CSP systems.

The impact of CSNI on the performance of CSP systems is best defined analysing how the optical efficiency of the CSP reflectors (or heliostats, depending on the CSP technology) varies according to CSNI or CSR. The intercept factor is defined as the ratio of the energy intercepted by the receiver to the energy reflected by the focusing device [72], and can be determined using different techniques such as ray-tracing or analytical models, incidence angle modifiers or look-up tables [2].

1.4.2.1 Ray tracing tools

By using ray tracing tools, one can study the path that a single ray travels from the sun disk until it is absorbed. The principle of ray-tracing techniques, also known as Monte Carlo or statistical techniques, is to randomly choose a very large set of rays coming from the solar disk and circumsolar region, and then determine which of them arrive to the receiver or absorber of the CSP system [73]. Each ray is randomly generated according to a given sun disk and circumsolar radiance distribution and, in each interaction of the ray with the reflector surfaces and receiver, it is decided if the ray is reflected or absorbed according to the properties of the materials, using also random numbers. If reflected, a new direction is determined according to the law of reflection and taking into account the imperfections and misalignment of the reflectors. This process is then repeated until the ray is either absorbed or escapes.

Since the number of rays that leave the source and that reach the receiver/absorber are known, it is possible to determine the intercept factor. In this way, it is possible to use several CSR profiles and assess the impact of CSNI distribution on intercept factor.

Examples of ray-tracing software based on this algorithm are Tonatiuh [74], MIRVAL [75], STRAL [76] and SolTrace [77]. It is worth mentioning that the computation time increases with the number of rays used in the simulations. Examples of works from the literature that used ray-tracing methods to study CSP systems are: Schubnell [57] studied a solar furnace, Chapman and Arias [78] studied a parabolic trough system, Wilbert [2] studied a solar tower and parabolic trough system, and Fossa et al. [79] studied linear Fresnel.

1.4.2.2 Analytical models

In addition to ray-tracing, analytical optical performance models can also be used to study the impact of CSNI in CSP systems. These models use analytical equations that, when solved, are able to describe the path of the rays through the optical system. One of the most used analytical models in the literature is the model from Bendt/Rabl [80, 81]. This model can be used for two CSP technologies: parabolic trough and solar dish. The application of this model can be found in several studies in the literature such as the works from Malali et al. [82], Ho et al. [83] and Riveros-Rosas et al. [84]. Another example of an analytical model is the HFLCAL software [85] that can also be used to calculate and optimize the layout of the heliostats on the field.

In comparison to ray-tracing, analytical models are easier and faster to use. However, effects such as shading and blocking of the sun rays can only be included using corrective factors, and not directly as is the case of most ray tracing algorithms.

1.4.2.3 Incidence angle modifiers and look-up tables

The simplest technique to calculate the optical performance of a CSP system is to use incidence angle modifiers or look-up tables. This technique only uses constants and functions that are capable of describing the change in optical performance of a CSP system according to the solar angles [2]. One such function is called the incident angle modifier (IAM) which is defined as the ratio of the optical efficiency as a function of the incidence angle and the optical efficiency for zero incidence angle, and can be derived from experiments or from calculations performed by the other more complex techniques mentioned above.

Regarding look-up tables, an example of its use on the determination of optimal efficiency of CSP systems, namely solar tower systems, is *greenius*, a software for

technical and economic analysis of renewable energy systems [86, 87]. This software has look-up tables for the following solar tower system components: heliostat field, power block and receiver.

The various techniques described above allow to determine the optical efficiency of different CSP systems with several degrees of complexity, accuracy and speed, giving researchers the option to choose between them according to their requirements.

1.5 Objectives of the thesis

The purpose of this work is to study the modelling of direct normal and circumsolar irradiance (DNI and CSNI, respectively), as well as their impact on the energy generation of concentrating solar power (CSP) systems. For this purpose, DNI and CSNI were modelled using the following approaches: (i) empirical models; (ii) parametrization models; and (iii) radiative transfer models. To assess the impact of DNI and CSNI on the energy generation of CSP system, a parametrization model was used.

Thus, as a final objective, this work intends to develop simple and fast models capable to accurately predict DNI and CSNI using widely available solar radiation data. To achieve this, high-quality solar radiation measurements were used for model's development and validation, and climate zone was taken into consideration.

These efforts contribute to: (i) facilitate the modelling of DNI and CSNI; (ii) improve the accuracy of DNI and CSNI models available in the literature; and (iii) highlight the importance of considering CSNI and quantify the impact of its variation when designing and operating CSP systems.

1.6 Outline of the thesis

This thesis comprises six chapters. Chapter 1 presents an introduction to the work, including the review of the tools available to researchers and engineers to model and measure direct normal and circumsolar irradiance (DNI and CSNI, respectively), as well as how to assess the impact of DNI and CSNI variation on the energy generation of concentrating solar power (CSP) systems. Chapter 2 presents a literature review on the *separation models* used to estimate DHI from GHI (and, consequently, DNI) as well as the propose of a new separation model that uses minutely data and takes into account the climate zone. Chapter 3 presents a performance assessment of different models and data sources that can be used to predict DNI (and, in some extent, CSNI). Chapter 4 presents the modelling of DNI and CSNI using a radiative transfer model and the development of a simple and fast model to estimate CSNI. Chapter 5 presents an upgrade of the CSNI model developed in Chapter 4, enabling it to predict CSNI for different half-opening angles, thus allowing to study the impact of

CSNI and its variation on CSP systems, namely in parabolic trough concentrators. In resume, in Chapter 2, the most simple way to estimate DNI is addressed while in Chapter 3 more sophisticated (and accurate) possibilities are explored, and in Chapter 4, one of such sophisticated options (a radiative transfer model) is used to create a database of DNI and CSNI values, which is then used as the basis for the development of the CSNI model, as well as the study on the impact of DNI and CSNI on the energy generation of CSP systems, presented in Chapter 5. These chapters of the thesis are organized by and correspond to scientific papers, in which Chapters 2 through 4 are published papers in international peer-reviewed journals, and Chapter 5 is under review in one of such journals. In Chapter 6, the general conclusions of this thesis are drawn.

References

[1] ISO 9488:2022. Solar energy — Vocabulary. Standard, International Organization for Standardization, Geneva, CH, Mar. 2022.

[2] S. Wilbert. *Determination of Circumsolar Radiation and its Effect on Concentrating Solar Power*. PhD thesis, RWTH Aachen University, 2014.

[3] W. M. O. (WMO). Guide to Instruments and Methods of Observation. Volume I - Measurement of Meteorological Variables. Technical Report WMO-No. 8, Geneva, 2021.

[4] P. Blanc, B. Espinar, N. Geuder, C. Gueymard, R. Meyer, R. Pitz-Paal, B. Reinhardt, D. Renné, M. Sengupta, L. Wald, and S. Wilbert. Direct normal irradiance related definitions and applications: The circumsolar issue. *Solar Energy*, 110: 561–577, Dec. 2014.

[5] B. Mayer and A. Kylling. Technical note: The libRadtran software package for radiative transfer calculations – description and examples of use. *Atmos. Chem. Phys.*, 23, 2005.

[6] B. Mayer, A. Kylling, C. Emde, U. Hamann, R. Buras, J. Gasteiger, and B. Richter. libRadtran User's Guide. 153, 2020.

[7] C. Emde, R. Buras-Schnell, A. Kylling, B. Mayer, J. Gasteiger, U. Hamann, J. Kylling, B. Richter, C. Pause, T. Dowling, and L. Bugliaro. The libRadtran software package for radiative transfer calculations (version 2.0.1). *Geoscientific Model Development*, 9(5):1647–1672, May 2016.

[8] J. A. Ruiz-Arias and C. A. Gueymard. A multi-model benchmarking of direct

and global clear-sky solar irradiance predictions at arid sites using a reference physical radiative transfer model. *Solar Energy*, 171:447–465, Sept. 2018.

[9] C. A. Gueymard. Prediction and validation of cloudless shortwave solar spectra incident on horizontal, tilted, or tracking surfaces. *Solar Energy*, 82(3):260–271, Mar. 2008.

[10] K. Stamnes, S.-C. Tsay, W. Wiscombe, and K. Jayaweera. Numerically stable algorithm for discrete-ordinate-method radiative transfer in multiple scattering and emitting layered media. *Appl. Opt.*, 27(12):2502–2509, Jun 1988.

[11] Mayer, B. Radiative transfer in the cloudy atmosphere. *EPJ Web of Conferences*, 1:75–99, 2009.

[12] C. Emde and B. Mayer. Simulation of solar radiation during a total eclipse: a challenge for radiative transfer. *Atmospheric Chemistry and Physics*, 7(9): 2259–2270, 2007.

[13] C. Emde, R. Buras, B. Mayer, and M. Blumthaler. The impact of aerosols on polarized sky radiance: model development, validation, and applications. *Atmospheric Chemistry and Physics*, 10(2):383–396, 2010.

[14] R. Buras and B. Mayer. Efficient unbiased variance reduction techniques for monte carlo simulations of radiative transfer in cloudy atmospheres: The solution. *Journal of Quantitative Spectroscopy and Radiative Transfer*, 112(3):434–447, 2011.

[15] C. Emde, R. Buras, and B. Mayer. Alis: An efficient method to compute high spectral resolution polarized solar radiances using the monte carlo approach. *Journal of Quantitative Spectroscopy and Radiative Transfer*, 112(10):1622–1631, jul 2011.

[16] A. Razagui, K. Abdeladim, K. Bouchouicha, N. Bachari, S. Semaoui, and A. Hadj Arab. A new approach to forecast solar irradiances using WRF and libRadtran models, validated with MERRA-2 reanalysis data and pyranometer measures. *Solar Energy*, 221:148–161, June 2021.

[17] F. Plag, I. Kröger, S. Riechelmann, and S. Winter. Multidimensional model to correct PV device performance measurements taken under diffuse irradiation to reference conditions. *Solar Energy*, 174:431–444, Nov. 2018.

[18] J. Polo, J. Ballestrín, and E. Carra. Sensitivity study for modelling atmospheric attenuation of solar radiation with radiative transfer models and the impact in solar tower plant production. *Solar Energy*, 134:219–227, Sept. 2016.

[19] A. Berk, P. Conforti, R. Kennett, T. Perkins, F. Hawes, and J. van den Bosch. MODTRAN6: a major upgrade of the MODTRAN radiative transfer code. 90880H, Baltimore, Maryland, USA, June 2014.

[20] G. López, C. A. Gueymard, J. L. Bosch, I. Rapp-Arrarás, J. Alonso-Montesinos, I. Pulido-Calvo, J. Ballestrín, J. Polo, and J. Barbero. Modeling water vapor impacts on the solar irradiance reaching the receiver of a solar tower plant by means of artificial neural networks. *Solar Energy*, 169:34–39, July 2018.

[21] J. Ballestrín and A. Marzo. Solar radiation attenuation in solar tower plants. *Solar Energy*, 86(1):388–392, Jan. 2012.

[22] A. Oumbe, Z. Qu, P. Blanc, M. Lefèvre, L. Wald, and S. Cros. Decoupling the effects of clear atmosphere and clouds to simplify calculations of the broadband solar irradiance at ground level. *Geoscientific Model Development*, 7(4):1661–1669, 2014.

[23] C. A. Gueymard. Parameterized transmittance model for direct beam and circumsolar spectral irradiance. *Solar Energy*, 71(5):325–346, 2001.

[24] C. A. Gueymard. The SMARTS spectral irradiance model after 25 years: New developments and validation of reference spectra. *Solar Energy*, 187:233–253, July 2019.

[25] C. A. Gueymard and M. Kocifaj. Clear-sky spectral radiance modeling under variable aerosol conditions. *Renewable and Sustainable Energy Reviews*, 168: 112901, Oct. 2022.

[26] M. Vogt, C. R. Tobon, A. Alcañiz, P. Procel, Y. Blom, A. N. El Din, T. Stark, Z. Wang, E. G. Goma, J. Etxebarria, H. Ziar, M. Zeman, R. Santbergen, and O. Isabella. Introducing a comprehensive physics-based modelling framework for tandem and other PV systems. *Solar Energy Materials and Solar Cells*, 247: 111944, Oct. 2022.

[27] M. Lefèvre, A. Oumbe, P. Blanc, B. Espinar, B. Gschwind, Z. Qu, L. Wald, M. Schroedter-Homscheidt, C. Hoyer-Klick, A. Arola, A. Benedetti, J. W. Kaiser, and J.-J. Morcrette. McClear: a new model estimating downwelling solar radiation at ground level in clear-sky conditions. *Atmospheric Measurement Techniques*, 6(9):2403–2418, Sept. 2013.

[28] J. A. Ruiz-Arias and C. A. Gueymard. Worldwide inter-comparison of clear-sky solar radiation models: Consensus-based review of direct and global irradiance components simulated at the earth surface. *Solar Energy*, 168:10–29, July 2018.

[29] P. Ineichen. Validation of models that estimate the clear sky global and beam solar irradiance. *Solar Energy*, 132:332–344, July 2016.

[30] Z. Sun, J. Li, G. Shi, J. Manners, and J. Li. Fast scheme for determination of direct normal irradiance. Part II: Parameterization of circumsolar radiation. *Solar Energy*, 199:256–267, Mar. 2020.

[31] R. American Society of Heating and A. Air-Conditioning Engineers Inc. *ASHRAE Handbook 1985 Fundamentals*. ASHRAE, 1985.

[32] G. Abal, D. Aicardi, R. Alonso Suárez, and A. Laguarda. Performance of empirical models for diffuse fraction in Uruguay. *Solar Energy*, 141:166–181, Jan. 2017.

[33] E. P. Marques Filho, A. P. Oliveira, W. A. Vita, F. L. Mesquita, G. Codato, J. F. Escobedo, M. Cassol, and J. R. A. França. Global, diffuse and direct solar radiation at the surface in the city of Rio de Janeiro: Observational characterization and empirical modeling. *Renewable Energy*, 91:64–74, June 2016.

[34] E. Paulescu and R. Blaga. Regression models for hourly diffuse solar radiation. *Solar Energy*, 125:111–124, Feb. 2016.

[35] N. Helbig, H. Löwe, B. Mayer, and M. Lehning. Explicit validation of a surface shortwave radiation balance model over snow-covered complex terrain. *Journal of Geophysical Research*, 115(D18):D18113, Sept. 2010.

[36] J. Boland, J. Huang, and B. Ridley. Decomposing global solar radiation into its direct and diffuse components. *Renewable and Sustainable Energy Reviews*, 28: 749–756, Dec. 2013.

[37] N. Engerer. Minute resolution estimates of the diffuse fraction of global irradiance for southeastern Australia. *Solar Energy*, 116:215–237, June 2015.

[38] C. A. Gueymard and J. A. Ruiz-Arias. Validation of direct normal irradiance predictions under arid conditions: A review of radiative models and their turbidity-dependent performance. *Renewable and Sustainable Energy Reviews*, 45:379–396, May 2015.

[39] C. A. Gueymard and J. A. Ruiz-Arias. Extensive worldwide validation and climate sensitivity analysis of direct irradiance predictions from 1-min global irradiance. *Solar Energy*, 128:1–30, Apr. 2016.

[40] D. Yang and C. A. Gueymard. Ensemble model output statistics for the separation of direct and diffuse components from 1-min global irradiance. *Solar Energy*, 208:591–603, Sept. 2020.

[41] D. Yang. Estimating 1-min beam and diffuse irradiance from the global irradiance: A review and an extensive worldwide comparison of latest separation models at 126 stations. *Renewable and Sustainable Energy Reviews*, 159:112195, May 2022.

[42] Y. Eissa, P. Blanc, H. Ghedira, A. Oumbe, and L. Wald. A fast and simple model to estimate the contribution of the circumsolar irradiance to measured broadband beam irradiance under cloud-free conditions in desert environment. *Solar Energy*, 163:497–509, Mar. 2018.

[43] B. Holben, T. Eck, I. Slutsker, D. Tanré, J. Buis, A. Setzer, E. Vermote, J. Reagan, Y. Kaufman, T. Nakajima, F. Lavenu, I. Jankowiak, and A. Smirnov. Aeronet—a federated instrument network and data archive for aerosol characterization. *Remote Sensing of Environment*, 66(1):1–16, 1998.

[44] D. M. Giles, A. Sinyuk, M. G. Sorokin, J. S. Schafer, A. Smirnov, I. Slutsker, T. F. Eck, B. N. Holben, J. R. Lewis, J. R. Campbell, E. J. Welton, S. V. Korkin, and A. I. Lyapustin. Advancements in the Aerosol Robotic Network (AERONET) Version 3 database – automated near-real-time quality control algorithm with improved cloud screening for Sun photometer aerosol optical depth (AOD) measurements. *Atmospheric Measurement Techniques*, 12(1): 169–209, Jan. 2019.

[45] A. Masoom, P. Kosmopoulos, A. Bansal, A. Gkikas, E. Proestakis, S. Kazadzis, and V. Amiridis. Forecasting dust impact on solar energy using remote sensing and modeling techniques. *Solar Energy*, 228:317–332, 2021.

[46] E. Carra, A. Marzo, J. Ballestrín, J. Polo, J. Barbero, J. Alonso-Montesinos, R. Monterreal, E. F. Abreu, and J. Fernández-Reche. Atmospheric extinction levels of solar radiation using aerosol optical thickness satellite data. Validation methodology with measurement system. *Renewable Energy*, 149:1120–1132, Apr. 2020.

[47] C. A. Gueymard and D. Yang. Worldwide validation of CAMS and MERRA-2 reanalysis aerosol optical depth products using 15 years of AERONET observations. *Atmospheric Environment*, 225:117216, Mar. 2020.

[48] V. Salamalikis, I. Vamvakas, P. Blanc, and A. Kazantzidis. Ground-based validation of aerosol optical depth from CAMS reanalysis project: An uncertainty input on direct normal irradiance under cloud-free conditions. *Renewable Energy*, 170:847–857, June 2021.

[49] H. Breitkreuz, M. Schroedter-Homscheidt, and T. Holzer-Popp. A case study to prepare for the utilization of aerosol forecasts in solar energy industries. *Solar Energy*, 81(11):1377–1385, 2007.

[50] C.-A. Lin, Y. Zhang, G. Heath, D. K. Henze, M. Sengupta, and C.-H. Lu. Improvement of aerosol optical depth data for localized solar resource assessment. *Solar Energy*, 249:457–466, 2023.

[51] X. Sun, D. Yang, C. A. Gueymard, J. M. Bright, and P. Wang. Effects of spatial scale of atmospheric reanalysis data on clear-sky surface radiation modeling in tropical climates: A case study for singapore. *Solar Energy*, 241:525–537, 2022.

[52] T. Elias, D. Ramon, L. Dubus, M. Am-Shallem, and G. Kroyzer. Dni and slant path transmittance for the solar resource of tower thermal solar plants: The validation of the asora method and impact in exploiting a global data set. *Solar Energy*, 217:78–92, 2021.

[53] A. Driemel, J. Augustine, K. Behrens, S. Colle, C. Cox, E. Cuevas-Agulló, F. M. Denn, T. Duprat, M. Fukuda, H. Grobe, M. Haeffelin, N. Hyett, O. Ijima, A. Kallis, W. Knap, V. Kustov, C. N. Long, D. Longenecker, A. Lupi, M. Maturilli, M. Mimouni, L. Ntsangwane, H. Ogihara, X. Olano, M. Olefs, M. Omori, L. Passamani, E. B. Pereira, H. Schmithüsen, S. Schumacher, R. Sieger, J. Tamlyn, R. Vogt, L. Vuilleumier, X. Xia, A. Ohmura, and G. König-Langlo. Baseline Surface Radiation Network (BSRN): structure and datadescription (1992–2017). preprint, Atmosphere – Meteorology, Feb. 2018.

[54] M. Sengupta, A. Habte, S. Wilbert, C. Gueymard, and J. Remund. Best practices handbook for the collection and use of solar resource data for solar energy applications: Third edition. 4 2021.

[55] S. Wilbert, R. Pitz-Paal, and J. Jaus. Comparison of measurement techniques for the determination of circumsolar irradiance. 162–167, Miyazaki, Japan, 2013.

[56] J. E. Noring, D. F. Grether, and A. J. Hunt. Circumsolar radiation data: The Lawrence Berkeley Laboratory reduced data base. *NASA STI/Recon Technical Report N*, 92:19628, Dec. 1991.

[57] M. Schubnell. Sunshape and Its Influence on the Flux Distribution in Imaging Solar Concentrators. *Journal of Solar Energy Engineering*, 114(4):260–266, Nov. 1992.

[58] A. Neumann, A. Witzke, S. A. Jones, and G. Schmitt. Representative Terrestrial Solar Brightness Profiles . *Journal of Solar Energy Engineering*, 124(2):198–204, 04 2002.

[59] A. Gambardella and R. Galleano. Characterization of a ccd-camera-based system for measurement of the solar radial energy distribution. *Measurement Science and Technology*, 22(10):105902, 2011.

[60] T. H. Jeys and L. L. Vant-Hull. The contribution of the solar aureole to the measurements of pyrheliometers. *Solar Energy*, 18(4):343–348, 1976.

[61] J. Hickey and A. Karoli. A variable field of view pyrheliometer. In *Proceedings of the 1977 Annual Meeting of the American Society of the International So1ar Energy Society*, 6–10, 1977.

[62] G. Major. A method for determining the circumsolar sky function. *Tellus*, 32 (4):340–347, 1980.

[63] S. Wilbert, M. Röger, J. Csambor, M. Breitbach, F. Klinger, B. Nouri, N. Hanrieder, F. Wolfertstetter, D. Schüler, S. Shaswattam, N. Goswami, S. Kumar, A. Ghennioui, R. Affolter, N. Geuder, and B. Kraas. Sunshape measurements with conventional rotating shadowband irradiometers. *AIP Conference Proceedings*, 2033(1):190016, 2018.

[64] L. Harrison, J. Michalsky, and J. Berndt. Automated multifilter rotating shadowband radiometer: an instrument for optical depth and radiation measurements. *Appl. Opt.*, 33(22):5118–5125, Aug 1994.

[65] ISO 9847:2023. Solar energy — Calibration of pyranometers by comparison to a reference pyranometer. Standard, International Organization for Standardization, Geneva, CH, Jan. 2023.

[66] ISO 9846:1993. Solar energy — Calibration of a pyranometer using a pyrheliometer. Standard, International Organization for Standardization, Geneva, CH, Dec. 1993.

[67] ISO 9059:1990. Solar energy — Calibration of field pyrheliometers by comparison to a reference pyrheliometer. Standard, International Organization for Standardization, Geneva, CH, Nov. 1990.

[68] ISO 9060:2018. Solar energy — Specification and classification of instruments for measuring hemispherical solar and direct solar radiation. Standard, International Organization for Standardization, Geneva, CH, Nov. 2018.

[69] C. Long and E. G. Dutton. Bsrn global network recommended qc tests, v2.x. 2010.

[70] J. M. Bright, X. Sun, C. A. Gueymard, B. Acord, P. Wang, and N. A. Engerer. Bright-Sun: A globally applicable 1-min irradiance clear-sky detection model. *Renewable and Sustainable Energy Reviews*, 121:109706, Apr. 2020.

[71] M. Larrañeta, M. Reno, I. Lillo-Bravo, and M. Silva-Pérez. Identifying periods of clear sky direct normal irradiance. *Renewable Energy*, 113:756–763, Dec. 2017.

[72] S. A. Kalogirou. Chapter three - Solar Energy Collectors. In S. A. Kalogirou, editor, *Solar Energy Engineering*, 121–217. Academic Press, Boston, Jan. 2009. ISBN 978-0-12-374501-9.

[73] P. Garcia, A. Ferriere, and J.-J. Bezian. Codes for solar flux calculation dedicated to central receiver system applications: A comparative review. *Solar Energy*, 82 (3):189–197, Mar. 2008.

[74] M. J. Blanco, J. M. Amieva, and A. Mancillas. The tonatiuh software development project: an open source approach to the simulation of solar concentrating systems. 157–164, 2005.

[75] P. L. Leary and J. D. Hankins. User's guide for MIRVAL: a computer code for comparing designs of heliostat-receiver optics for central receiver solar power plants. Technical Report SAND-77-8280, Sandia National Lab. (SNL-CA), Livermore, CA (United States), Feb. 1979.

[76] B. Belhomme, R. Pitz-Paal, P. Schwarzbözl, and S. Ulmer. A New Fast Ray Tracing Tool for High-Precision Simulation of Heliostat Fields. *Journal of Solar Energy Engineering*, 131(3), June 2009.

[77] *SolTRACE: A New Optical Modeling Tool for Concentrating Solar Optics*, volume Solar Energy of *International Solar Energy Conference*, 03 2003.

[78] D. J. Chapman and D. A. Arias. Effect of Solar Brightness Profiles on the Performance of Parabolic Concentrating Collectors. 581–587. American Society of Mechanical Engineers Digital Collection, Sept. 2010.

[79] M. Fossa, A. Boccalatte, and S. Memme. Solar Fresnel modelling, geometry enhancement and 3D ray tracing analysis devoted to different energy efficiency definitions and applied to a real facility. *Solar Energy*, 216:75–89, Mar. 2021.

[80] P. Bendt, A. Rabl, H. W. Gaul, and K. A. Reed. Optical analysis and optimization of line focus solar collectors. Technical Report SERI/TR-34-092, Solar Energy Research Inst., Golden, CO (USA), Sept. 1979.

[81] A. Rabl and P. Bendt. Effect of Circumsolar Radiation on Performance of Focusing Collectors. *Journal of Solar Energy Engineering*, 104:237–250, 1982.

[82] P. D. Malali, S. K. Chaturvedi, and R. Agarwala. Effects of circumsolar radiation on the optimal performance of a Stirling heat engine coupled with a parabolic dish solar collector. *Applied Thermal Engineering*, 159:113961, Aug. 2019.

[83] C. K. Ho, C. M. Ghanbari, and R. B. Diver. Methodology to Assess Potential Glint and Glare Hazards From Concentrating Solar Power Plants: Analytical Models and Experimental Validation. *Journal of Solar Energy Engineering*, 133 (3), Aug. 2011.

[84] D. Riveros-Rosas, J. Herrera-Vázquez, C. A. Pérez-Rábago, C. A. Arancibia-Bulnes, S. Vázquez-Montiel, M. Sánchez-González, F. Granados-Agustín, O. A. Jaramillo, and C. A. Estrada. Optical design of a high radiative flux solar furnace for Mexico. *Solar Energy*, 84(5):792–800, May 2010.

[85] P. Schwarzbözl, R. Pitz-Paal, and M. Schmitz. Visual HFLCAL - A Software Tool for Layout and Optimisation of Heliostat Fields. In T. Mancini and R. Pitz-Paal, editors, *Proceedings*, Berlin, Sept. 2009. ISBN 978-3-00-028755-8.

[86] V. Quaschning, W. Ortmanns, R. Kistner, and M. Geyer. Greenius: a new simulation environment for technical and economical analysis of renewable independent power projects. In *International Solar Energy Conference*, volume 16702, 413–417. American Society of Mechanical Engineers, 2001.

[87] J. Dersch, P. Schwarzbözl, and T. Richert. Annual Yield Analysis of Solar Tower Power Plants With GREENIUS. *Journal of Solar Energy Engineering*, 133(3), July 2011.

Nomenclature

DHI	Diffuse Horizontal Irradiance
DNI	Direct Normal Irradiance
GHI	Global Horizontal Irradiance
S_a	solar constant adjusted for Earth-Sun distance (W/m^2)

Greek symbols

θ	solar zenith angle (°)
μ_0	$\cos\theta$

Acronyms

ACR	Active Cavity Radiometer
BSRN	Baseline Surface Radiation Network
CPV	Concentrating Photovoltaics
CSNI	Circumsolar Normal Irradiance
CSP	Concentrating Solar Power
CSR	Circumsolar Ratio
DHI	Diffuse Horizontal Irradiance
DirHI	Direct Horizontal Irradiance
IAM	Incidence Angle Modifier
ISO	International Organization for Standardization
NWP	Numerical Weather Prediction
PV	Photovoltaics
RSI	Rotating Shadowband Irradiometer
RTM	Radiative Transfer Model
WMO	World Meteorological Organization
WRR	World Radiometric Reference

Chapter 2

Prediction of diffuse horizontal irradiance using a new climate zone model[†]

Abstract

Knowledge on the diffuse horizontal irradiance (DHI), and direct normal irradiance (DNI) is crucial for the estimation of the irradiance on tilted surfaces, which in turn is critical for photovoltaic (PV) applications and for designing and simulating concentrated solar power (CSP) plants. Since global horizontal irradiance (GHI) is the most commonly measured solar radiation variable, it is advantageous for establishing a suitable method that uses it to compute DHI and DNI. In this way, a new model for predicting the diffuse fraction (K_d) based on the climate zone is proposed, using only the clearness index (K_t) as the predictor and one-minute resolution GHI data. A review of the literature on models that use hourly and sub-hourly K_t values to compute K_d was also carried out, and an extensive performance assessment of both the proposed model and the models from the literature was conducted using ten statistical indicators and a global performance index (GPI). A set of model parameters was determined for each climate zone considered in this study (arid, high albedo, temperate and tropical) using 48 worldwide radiometric stations. It was found that the best overall performing model was the model proposed in this work.

Keywords: Diffuse horizontal irradiance; Global horizontal irradiance; Direct Normal Irradiance; Clearness index; Diffuse fraction; Separation method.

[†]Edgar F.M. Abreu[(1)], Paulo Canhoto[(1,2)], and Maria J. Costa[(1,2)]. Prediction of diffuse horizontal irradiance using a new climate zone model. *Renewable and Sustainable Energy Reviews*, 110:28-42, 2019.

[(1)] Institute of Earth Sciences, University of Évora.

[(2)] Physics Department, School of Sciences and Technology, University of Évora.

2.1 Introduction

Global horizontal irradiance (GHI) is the most commonly measured solar radiation variable in the ground-based meteorological stations around the world, both in historical datasets and in geographical distribution. Therefore, it is the best dataset available to quantify solar energy resource and assess undergoing or future solar energy projects. On the other hand, information on both diffuse horizontal irradiance (DHI) and direct normal irradiance (DNI) is also crucial to properly design and optimise solar energy systems. In this way, it is advantageous to find a suitable and accurate method based on the GHI measurements to estimate both DHI and DNI, thus enabling the reconstitution of temporal series of these two components in locations where only GHI measurements are available, mainly due to budget limitations and higher requirements for maintenance and calibration procedures. In fact, whereas pyranometer installations are relatively cheap (USD 5-10 K with a data logger), full stations equipped with a sun tracker, pyranometers and a pyrheliometer are quite expensive (arround USD 30 K) [1]. DHI and DNI data are essential to accurately determine the global solar irradiance on tilted surfaces, for example in sizing and operation of photovoltaic (PV) systems [2]. The models for the diffuse fraction allow to estimate those components based on the GHI and then determine the irradiance on a tilted surface, by opposition to the one-step methods of converting GHI, as for example the isotropic sky model [3], the Klucher model [4], the Hay-Davies model [5] and the Reindl model [6]. Concentrated Solar Power (CSP) systems mainly use DNI in its energy capturing and conversion processes due to its directional nature and field of view (aperture angle) that depends on the concentration factor [7]. Therefore, the accurate computation of DHI is of vital importance to design, assess the performance and operate such systems [8].

The response of the scientific community for the need of obtaining DHI and DNI data at low cost was given by developing separation models in which the work of Liu and Jordan [9] was the pioneer. That work reported the relation between the clearness index (the ratio between GHI that reaches the surface of the earth and the extraterrestrial irradiance on a horizontal surface, K_t) and the diffuse fraction (the ratio of DHI to GHI, K_d) using measurements from 98 stations in Canada and United States. The good results obtained by Liu and Jordan lead to the development of several other separation models for different locations. Page [10] developed a model based on monthly mean values for latitudes between 40°N and 40°S. Tuller [11] analysed daily and monthly data to establish models for four locations in Canada. Klein [12] used experimental measurements to assess and validate the model proposed by Liu and Jordan [9] and extended it to allow calculation of monthly average solar irradiation on surfaces with multiple orientations. Although several other daily and

monthly basis models were presented and are available in the literature, they are not the focus of this work. The work of Khorasanizadeh and Mohammadi [13] reports a comprehensive review of such models. Separation models for high-frequency GHI data are needed until high-resolution DNI measurements are available in a global scale, since required temporal resolution of nowadays reported solar radiation data increased, due to the requirements of high-frequency measurements in the simulation of CSP projects [14]. Therefore, because sub-hourly models are relatively rare in the literature, this work focuses on the available hourly and sub-hourly separation models whose solo predictor is the K_t and on their ability in representing high-frequency data in a global scale and for different climates. The main reason for using only K_t as the predictor is due to the greater availability of GHI data worldwide, thus allowing a straightforward evaluation of the model for the higher number of locations as possible. Regarding this type of models that use only K_t as the predictor, Orgill and Hollands [15] presented a separation model using hourly measurements covering the period from September 1967 to August 1971 for Toronto Airport, Canada. This was the first model found in the literature that met the features mentioned above. In Section 2.2 are presented all the other models reviewed in this work.

The assessment of new separation models is usually carried out through the comparison of that new model against ground measurements and other models [1] using statistical indicators. Beside some researchers have already presented performance analysis using only models available in the literature [14, 16, 17], the majority of the validation studies were reported when new models were derived, as is the case of this work. The first hourly models presented [15, 18] were compared against the Liu and Jordan monthly model [9]. As time went by, more hourly models became available for test, and therefore models such as the Orgill and Hollands [15] and the Erbs et al. [19] were used in numerous validation studies (e.g. [20, 21, 6]). Liu and Jordan's model is still occasionally used with the purpose of presenting a historical comparison of the separation models evolution [22]. Regarding the validation using ground-based measurements, the most used statistical indicators to assess the performance of separation models are the mean bias error (MBE), the root mean square error (RMSE) and the correlation coefficient (R).

One-minute data resolution models are very scarce in the literature. One of the few examples is the work of Engerer [1], which presents a diffuse fraction model based on one-minute clearness index data together with other predictors for southeastern Australia. Gueymard and Ruiz-Arias [14] reported the incapability of hourly models to account for cloud enhancement effects, aiming at the need for reliability in hourly models until more specific minutely models appear in the literature. Therefore, the purpose of this study is to develop a new diffuse fraction model based on one-minute measurements from stations around the globe. Since the model presented by Engerer

[1] requires more than one input parameter, the performance assessment of the model developed in this work will be conducted against hourly and sub-hourly models whose only predictor is K_t. To that end, ten statistical indicators were used, namely the mean bias error (MBE), mean absolute error (MAE), root mean square error (RMSE), mean percentage error (MPE), uncertainty at 95% (U95), relative root mean square error (RRMSE), maximum absolute error (erMAX), correlation coefficient (R) and mean absolute relative error (MARE). These statistical indicators were also combined into a global performance index (GPI). The GPI was used in previous studies in this field by Jamil and Akhtar [23]. Other option to combine different statistical indicators is the combined performance index (CPI), as described by Gueymard [24]. A Taylor diagram and a skill score [25] were also used to provide an additional statistical analysis. In this view, a comprehensive performance assessment of the proposed model as well as of other models in the literature is presented aiming at the identification of the best performing model for the estimation of DHI in a minute resolution all over the world. The organization of this paper is as follows: Section 2.2 presents a review of the hourly and sub-hourly models for estimating the diffuse fraction, Section 4.7 presents the data used in this study and the model development, Section 2.4 presents the results and discussion , and, finally, conclusions are drawn in Section 4.9.

2.2 Review of the available models

The models available in the literature were developed using several functional forms, number of predictors and for different time resolutions. The first form to obtain the diffuse fraction was a second degree polynomial as a function of the clearness index, as first proposed by Liu and Jordan [9] in 1960. Later, other models were presented using higher polynomial degrees as well as other functions such as the logistic [26] and the double exponential [27] forms. Several models included other predictors than K_t, such as sunshine duration, zenith angle, air mass, etc. Regarding time resolution, the available models were proposed to estimate the monthly, daily, hourly and sub-hourly diffuse fraction. In this work, a review of the models that use only K_t as the predictor with hourly or sub-hourly time resolutions is presented. The authors were able to find 121 different models that met the requirements specified above, although more models may be available in other publications or internal reports and communications that are not readily acessible. In many cases, authors present the same model but for different locations. These models are treated here as unique models when assessing their performance in Section 2.4. Table 2.1 presents the models studied in this work. The various locations from which authors used data to develop their models are classified according to the climate region as follows [14]: temperate (TM), arid (AR), tropical (TR) and high albedo (HA).

Table 2.1: Review of hourly and sub-hourly K_d models whose only predictor is K_t.

Model	Reference	Location	Climate	Data period	Constrains	K_d
1	Orgill and Hollands [15]	Toronto, Canada	TM	1967-1971	$K_t \leq 0.35$	$1.0 - 0.249K_t$
					$0.35 \leq K_t \leq 0.75$	$1.557 - 1.840K_t$
					$K_t > 0.75$	0.177
2	Bruno [18]	Hamburg, Germany	TM	1973-1974	-	$0.310K_t + 0.139\sin(4.620K_t)$
3	Erbs et al. [19]	Four cities in the United States	Various climates	1974-1976 (Various data periods)	$K_t \leq 0.22$	$1.0 - 0.0900K_t$
					$0.22 < K_t \leq 0.80$	$0.9511 - 0.1604K_t + 4.3880K_t^2 - 16.6380K_t^3 + 12.3360K_t^4$
					$K_t > 0.80$	0.165
4	Spencer [28]	Albany, Australia	AR	1973-1977	$K_t < 0.35$	0.890
					$0.35 \leq K_t \leq 0.75$	$1.414 - 1.736K_t$
					$K_t > 0.75$	0.110
5	Spencer [28]	Alice Springs, Australia	AR	1974-1977	$K_t < 0.35$	0.750
					$0.35 \leq K_t \leq 0.75$	$1.183 - 1.444K_t$
					$K_t > 0.75$	0.110
6	Spencer [28]	Geraldton, Australia	AR	1972-1977	$K_t < 0.35$	0.850
					$0.35 \leq K_t \leq 0.75$	$1.345 - 1.644K_t$
					$K_t > 0.75$	0.110
7	Spencer [28]	Guildford, Australia	AR	1975-1977	$K_t < 0.35$	0.780
					$0.35 \leq K_t \leq 0.75$	$1.254 - 1.595K_t$
					$K_t > 0.75$	0.060
8	Spencer [28]	Hobart, Australia	TM	1971-1977	$K_t < 0.35$	0.860
					$0.35 \leq K_t \leq 0.75$	$1.360 - 1.678K_t$
					$K_t > 0.75$	0.100
9	Spencer [28]	Laverton, Australia	AR	1976-1977	$K_t < 0.35$	0.860
					$0.35 \leq K_t \leq 0.75$	$1.360 - 1.678K_t$
					$K_t > 0.75$	0.150
10	Spencer [28]	Melbourne, Australia	AR	1970-1977	$K_t < 0.35$	0.850
					$0.35 \leq K_t \leq 0.75$	$1.352 - 1.668K_t$
					$K_t > 0.75$	0.100
11	Spencer [28]	Mildura, Australia	AR	1972-1977	$K_t < 0.35$	0.870
					$0.35 \leq K_t \leq 0.75$	$1.366 - 1.666K_t$

(continued on next page)

(continued)

Model	Reference	Location	Climate	Data period	Constrains	K_d
					$K_t > 0.75$	0.120
12	Spencer [28]	Mt Gambier, Australia	AR	1974-1977	$K_t < 0.35$	0.930
					$0.35 \leq K_t \leq 0.75$	$1.450 - 1.744K_t$
					$K_t > 0.75$	0.140
13	Spencer [28]	Port Hedland, Australia	AR	1974-1977	$K_t < 0.35$	0.710
					$0.35 \leq K_t \leq 0.75$	$1.142 - 1.431K_t$
					$K_t > 0.75$	0.070
14	Spencer [28]	Rockhampton, Australia	AR	1974-1977	$K_t < 0.35$	0.790
					$0.35 \leq K_t \leq 0.75$	$1.245 - 1.527K_t$
					$K_t > 0.75$	0.100
15	Spencer [28]	Waga Waga, Australia	AR	1974-1977	$K_t < 0.35$	0.800
					$0.35 \leq K_t \leq 0.75$	$1.280 - 1.605K_t$
					$K_t > 0.75$	0.080
16	Spencer [28]	Australia (average)	Various climates	1970-1977 (Various data periods)	$K_t < 0.35$	0.830
					$0.35 \leq K_t \leq 0.75$	$1.321 - 1.624K_t$
					$K_t > 0.75$	0.100
17	Hawlader [20]	Singapore	TM	1962	$K_t < 0.225$	0.9150
					$0.225 \leq K_t \leq 0.775$	$1.1389 - 0.9422K_t - 0.3878K_t^2$
					$K_t > 0.775$	0.2150
18	Ineichen et al. [29]	Geneva, Switzerland	TM	1978-1984	$K_t < 0.15$	0.98
					$K_t \geq 0.15$	$0.80 + 2.25K_t - 7.93K_t^2 + 5.26K_t^3$
19	Ineichen et al. [29]	Geneva, Switzerland	TM	1978-1984	$K_t < 0.25$	1.0
					$0.25 \leq K_t \leq 0.80$	$1.38 - 1.52K_t$
					$K_t > 0.80$	0.16
20	Ineichen et al. [29]	Geneva, Switzerland	TM	1978-1984	$K_t < 0.25$	1.0
					$K_t \geq 0.25$	$1.28K_t - 1.40K_t^2$
21	Muneer et al. [21]	New Delhi, India	TR	1971, 1974	$K_t < 0.175$	0.9500
					$0.175 \leq K_t \leq 0.775$	$0.9698 + 0.4353K_t - 3.4499K_t^2 + 2.1888K_t^3$
					$K_t > 0.775$	0.2600

(continued on next page)

(continued)

Model	Reference	Location	Climate	Data period	Constrains	K_d
22	Bakhsh et al. [30]	Dharan, Saudi Arabia	AR	1983-1984	$K_t < 0.23$	$1.0 - 0.220K_t$
					$0.23 \leq K_t \leq 0.80$	$1.235 - 1.260K_t$
					$K_t > 0.80$	0.225
23	Hollands [31]	Toronto, Canada	TM	1967-1971	-	$[1 - b - \sqrt{(1-b)^2 - 4ab^2K_t(1-aK_t)}]/(2abK_t)$
						$a = 1.115$; $b = 0.491$
24	Reindl et al. [6]	Five locations in North America and Europe	Various climates	1979-1982 (Various data periods)	$K_t \leq 0.30$	$1.020 - 0.248K_t$
					$0.30 < K_t < 0.78$	$1.450 - 1.670K_t$
					$K_t \geq 0.78$	0.147
25	Al-Rihai [32]	Fudhaliyah, Iraq	AR	1984-1987	$K_t < 0.25$	0.932
					$0.25 \leq K_t \leq 0.70$	$1.293 - 1.631K_t$
					$K_t > 0.70$	0.151
26	Bourges [33]	37 stations across Europe	TM	At least four years of measurements	$K_t \leq 0.20$	1.0
					$0.20 < K_t \leq 0.35$	$1.116 - 0.580K_t$
					$0.35 < K_t \leq 0.75$	$1.557 - 1.840K_t$
					$K_t > 0.75$	0.177
27	Chandrasekaran and Kumar [34]	Madras, India	TR	1983-1987	$K_t \leq 0.24$	$1.0086 - 0.1780K_t$
					$0.24 < K_t \leq 0.80$	$0.9686 + 0.1325K_t + 1.4183K_t^2 - 10.1860K_t^3 + 8.3733K_t^4$
					$K_t > 0.80$	0.1970
28	Chendo and Maduekwe [35]	Lagos, Nigeria	TM	Two years of measurements	$K_t \leq 0.30$	$1.022 - 0.156K_t$
					$0.30 < K_t < 0.80$	$1.385 - 1.396K_t$
					$K_t \geq 0.80$	0.264
29	Maduekwe and Chendo [36]	Lagos, Nigeria	TM	1990-1991	$K_t \leq 0.30$	$1.021 - 0.151K_t$
					$0.30 < K_t < 0.80$	$1.385 - 1.396K_t$
					$K_t \geq 0.80$	0.295
30	Lam and Li [37]	Hong Kong, China	TM	1991-1994	$K_t \leq 0.15$	0.977
					$0.15 < K_t \leq 0.70$	$1.237 - 1.361K_t$
					$K_t > 0.70$	0.273

(continued on next page)

(continued)

Model	Reference	Location	Climate	Data period	Constrains	K_d
31	Hijazin [38]	Amman, Jordan	AR	1985	$K_t < 0.10$	0.744
					$0.10 \leq K_t \leq 0.80$	$0.842 - 0.977K_t$
					$K_t > 0.80$	0.060
32	Hijazin [38]	Amman, Jordan	AR	1985	-	$0.847 - 0.985K_t$
33	González and Calbó [39]	Two locations in Iberian Peninsula	TM	1994-1996 (Various data periods)	$0.25 < K_t < 0.75$	$1.421 - 1.670K_t$
					$K_t \geq 0.75$	$-0.043 + 0.290K_t$
34	Boland et al. [26]	Geelong, Australia	TM	67 days	-	$1.0/[1.0 + \exp\{8.645(K_t - 0.613)\}]$
35	Boland et al. [26]	Geelong, Australia	TM	67 days	-	$1.0/[1.0 + \exp\{7.997(K_t - 0.586)\}]$
36	De Miguel et al. [40]	North Mediterranean belt area (11 stations)	TM	1974-1996 (Various data periods)	$K_t \leq 0.21$	$0.995 - 0.081K_t$
					$0.21 < K_t \leq 0.76$	$0.724 + 2.738K_t - 8.320K_t^2 + 4.967K_t^3$
					$K_t > 0.76$	0.180
37	Li and Lam [41]	Hong Kong, China	TM	1991-1998	$K_t \leq 0.15$	0.976
					$0.15 < K_t \leq 0.70$	$0.996 + 0.036K_t - 1.589K_t^2$
					$K_t > 0.70$	0.230
38	Oliveira et al. [42]	São Paulo, Brazil	TM	1994-1999	$0.17 < K_t < 0.75$	$0.97 + 0.80K_t - 3.00K_t^2 - 3.1K_t^3 + 5.2K_t^4$
39	Ulgen and Hepbasli [43]	Izmir, Turkey	TM	1994-1998	$K_t \leq 0.32$	0.6800
					$0.32 < K_t \leq 0.62$	$1.0609 - 1.2138K_t$
					$K_t > 0.62$	0.3000
40	Ulgen and Hepbasli [43]	Izmir, Turkey	TM	1994-1998	$K_t \leq 0.32$	0.6800
					$0.32 < K_t \leq 0.62$	$0.0743 - 19.3430K_t + 206.9100K_t^2 - 719.7200K_t^3 + 1053.4000K_t^4 - 562.69K_t^5$
					$K_t > 0.62$	0.3000
41	Karatasou et al. [44]	Athens, Greece	TM	1996-1998	$K_t \leq 0.78$	$0.9995 - 0.0500K_t - 2.4156K_t^2 + 1.4926K_t^3$
					$K_t > 0.78$	0.2000
42	Tsubo and Walker [45]	Southern Africa	AR	2000	-	$0.613 - 0.334K_t + 0.121K_t^2$
43	Tsubo and Walker [45]	Southern Africa	AR	2000	$K_t < 0.140$	0.907
					$0.140 \leq K_t \leq 0.794$	
					$K_t > 0.794$	0.138
44	Tsubo and Walker [45]	Southern Africa	AR	2000	$K_t < 0.140$	0.907
					$0.140 \leq K_t \leq 0.794$	$1.063 - 1.114K_t$

(continued on next page)

(continued)

Model	Reference	Location	Climate	Data period	Constrains	K_d
					$K_t > 0.793$	0.180
45	Soares et al. [46]	São Paulo, Brazil	TM	1998-2001	-	$0.90 + 1.10K_t - 4.50K_t^2 + 0.01K_t^3 + 3.14K_t^4$
46	Mondol et al. [47]	Ballymena, Northern Ireland	TM	21 months of data	$K_t \leq 0.20$	0.9800
					$K_t > 0.20$	$0.5836 + 3.6259K_t - 10.1710K_t^2 + 6.3380K_t^3$
47	Jacovides et al. [48]	Athalassa, Cyprus	AR	1998-2002	$K_t \leq 0.10$	0.987
					$0.10 < K_t \leq 0.80$	$0.940 + 0.937K_t - 5.010K_t^2 + 3.320K_t^3$
					$K_t > 0.80$	0.177
48	Elminir et al. [49]	Aswan, Egypt	AR	1999-2001	$K_t \leq 0.22$	$0.653 - 1.728K_t$
					$0.22 < K_t \leq 0.80$	$0.724 - 1.821K_t + 8.221K_t^2 - 16.370K_t^3 + 9.845K_t^4$
					$K_t > 0.80$	0.217
49	Elminir et al. [49]	Cairo, Egypt	AR	2003	$K_t \leq 0.22$	$0.793 - 2.198K_t$
					$0.22 < K_t \leq 0.80$	$1.341 - 9.566K_t + 32.200K_t^2 - 47.909K_t^3 + 25.419K_t^4$
					$K_t > 0.80$	0.131
50	Elminir et al. [49]	South-Valley, Egypt	AR	2003	$K_t \leq 0.22$	$0.8526 - 1.7780K_t$
					$0.22 < K_t \leq 0.80$	$0.8140 - 1.1060K_t + 0.3660K_t^2 - 0.9970K_t^3 + 1.2210K_t^4$
					$K_t > 0.80$	0.213
51	Boland et al. [50]	Adelaide, Australia	AR	-	-	$1.0/[1.0 + \exp(-5.83 + 9.87K_t)]$
52	Boland et al. [50]	Bracknell, England	TM	-	-	$1.0/[1.0 + \exp(-4.38 + 6.62K_t)]$
53	Boland et al. [50]	Darwin, Australia	TM	-	-	$1.0/[1.0 + \exp(-4.53 + 8.05K_t)]$
54	Boland et al. [50]	Lisbon, Portugal	TM	-	-	$1.0/[1.0 + \exp(-4.80 + 7.98K_t)]$
55	Boland et al. [50]	Macau, China	TM	-	-	$1.0/[1.0 + \exp(-4.87 + 8.12K_t)]$
56	Boland et al. [50]	Maputo, Mozambique	AR	-	-	$1.0/[1.0 + \exp(-5.18 + 8.80K_t)]$
57	Boland et al. [50]	Uccle, Belgium	TM	-	-	$1.0/[1.0 + \exp(-4.94 + 8.66K_t)]$
58	Boland et al. [50]	Multi-location average	Various climates	-	-	$1.0/[1.0 + \exp(-4.94 + 8.30K_t)]$
59	Boland and Ridley [51]	Multi-locations world-wide	Various climates	-	-	$1.0/[1.0 + \exp(-5.00 + 8.60K_t)]$
60	Furlan and Oliveira [52]	São Paulo, Brazil	TM	2002	$K_t \leq 0.228$	0.961
					$K_t > 0.228$	$1.337 - 1.650K_t$
61	Mondol et al. [53]	Aldergrove, Northern Irland	TM	1989-1998	$K_t \leq 0.20$	0.9800
					$0.20 < K_t \leq 0.70$	$0.6109 + 3.6259K_t - 10.1710K_t^2 + 6.3380K_t^3$

(continued on next page)

(continued)

Model	Reference	Location	Climate	Data period	Constrains	K_d
					$K_t > 0.70$	$0.6720 - 0.4740K_t$
62	Moreno et al. [54]	Seville, Spain	TM	2000-2008	$K_t \leq 0.27$	0.9930
					$0.27 < K_t \leq 0.82$	$1.4946 - 1.7899K_t$
					$K_t > 0.82$	0.0450
63	Pagola et al. [55]	3 locations in Spain	TM	2005-2008	$K_t \leq 0.35$	$0.9818 - 0.5870K_t$
					$0.35 < K_t \leq 0.75$	$1.2056 - 1.3240K_t$
					$K_t > 0.75$	0.2552
64	Pagola et al. [55]	3 locations in Spain	TM	2005-2008	$K_t \leq 0.22$	$0.9522 - 0.3119K_t$
					$0.22 < K_t \leq 0.80$	$0.6059+2.9877K_t-10.5675K_t^2+10.1833K_t^3-3.0475K_t^4$
					$K_t > 0.80$	0.3209
65	Posadillo and Lopez Luque [56]	Córdoba, Spain	TM	1993-2002	-	$K_t(1.17 - 1.381K_t)$
66	Posadillo and Lopez Luque [56]	Córdoba, Spain	TM	1993-2002	-	$-0.00829 + 1.16300K_t + 0.43300K_t^2 - 5.83900K_t^3 + 4.64880K_t^4$
67	Janjai et al. [57]	Chiang Mai, Thailand	TR	1995-2006	-	$0.9429 - 0.3707K_t + 6.4927K_t^2 - 30.3560K_t^3 + 39.1626K_t^4 - 15.4850K_t^5$
68	Janjai et al. [57]	Nakhon Pathom, Thailand	TR	1995-2006	-	$0.7699 + 2.3552K_t - 8.1480K_t^2 + 5.3811K_t^3$
69	Janjai et al. [57]	Songkhla, Thailand	TR	1995-2006	-	$0.869 + 1.559K_t - 11.176K_t^2 + 26.143K_t^3 - 38.302K_t^4 + 31.799K_t^5 - 10.602K_t^6$
70	Janjai et al. [57]	Ubon Ratchathani, Thailand	TR	1995-2006	-	$0.846 + 1.841K_t - 13.425K_t^2 + 42.888K_t^3 - 85.804K_t^4 + 84.476K_t^5 - 30.637K_t^6$
71	Ruiz-Arias et al. [27]	Albacete, Spain	TM	2002-2006	-	$0.086 + 0.880e^{-\exp(-3.877+6.138K_t)}$
72	Ruiz-Arias et al. [27]	Boulder, USA	TM	1961-1990	-	$0.967 - 1.024e^{-\exp(2.473-5.324K_t)}$
73	Ruiz-Arias et al. [27]	Dresden, Germany	TM	1981-1990	-	$0.140 + 0.962e^{-\exp(-1.976+4.067K_t)}$
74	Ruiz-Arias et al. [27]	Pittsburgh, USA	TM	1961-1990	-	$1.001 - 1.000e^{-\exp(2.450-5.048K_t)}$
75	Ruiz-Arias et al. [27]	Savannah, USA	TM	1961-1990	-	$0.988 - 1.000e^{-\exp(2.456-5.172K_t)}$
76	Ruiz-Arias et al. [27]	Talkeetna, USA	HA	1961-1990	-	$0.985 - 0.962e^{-\exp(2.655-6.003K_t)}$
77	Ruiz-Arias et al. [27]	Tucson, USA	AR	1961-1990	-	$0.988 - 1.073e^{-\exp(2.298-4.909K_t)}$
78	Ruiz-Arias et al. [27]	7 locations in Europe and USA	Various climates	1961-2006 (Various data periods)	-	$0.952 - 1.041e^{-\exp(2.3-4.702K_t)}$
79	Torres et al. [58]	Pamplona, Spain	TM	2006-2008	$K_t \leq 0.24$	$1.0058 - 0.2195K_t$

(continued on next page)

(continued)

Model	Reference	Location	Climate	Data period	Constrains	K_d
					$0.24 < K_t < 0.75$	$1.3264 - 1.5120K_t$
					$K_t \geq 0.75$	0.1923
80	Torres et al. [58]	Pamplona, Spain	TM	2006-2008	$K_t \leq 0.22$	$0.9920 - 0.0980K_t$
					$0.22 < K_t < 0.75$	$1.2158 - 1.0467K_t - 0.4480K_t^2$
					$K_t \geq 0.75$	0.1787
81	Torres et al. [58]	Pamplona, Spain	TM	2006-2008	$K_t \leq 0.22$	$0.9923 - 0.0980K_t$
					$0.24 < K_t \leq 0.755$	$1.1459 - 0.5612K_t - 1.4952K_t^2 + 0.7103K_t^3$
					$K_t > 0.755$	0.1755
82	Torres et al. [58]	Pamplona, Spain	TM	2006-2008	$K_t \leq 0.225$	$0.9943 - 0.1165K_t$
					$0.225 < K_t \leq 0.755$	$1.4101 - 2.9918K_t + 6.4599K_t^2 - 10.3290K_t^3 + 5.5140K_t^4$
					$K_t > 0.755$	0.1800
83	Chikh et al. [59]	Alger, Algeria	AR	1992	$K_t \leq 0.175$	$1.0 - 0.232K_t$
					$0.175 < K_t \leq 0.87$	$1.170 - 1.230K_t$
					$K_t > 0.87$	0.203
84	Chikh et al. [59]	Bechar, Algeria	AR	1990-1992	$K_t \leq 0.175$	$1.0 - 0.3000K_t$
					$0.175 < K_t \leq 0.87$	$1.1370 - 1.0770K_t$
					$K_t > 0.87$	0.2043
85	Chikh et al. [59]	Tamanrasset, Algeria	AR	1990-1992	$K_t \leq 0.175$	$1.0 - 0.640K_t$
					$0.175 < K_t \leq 0.87$	$1.052 - 0.935K_t$
					$K_t > 0.87$	0.240
86	Sanchez et al. [60]	Badajoz, Spain	TM	2009-2010	$K_t < 0.30$	0.78
					$0.30 \leq K_t \leq 0.75$	$1.23 - 1.43K_t$
					$K_t > 0.75$	0.13
87	Lee et al. [61]	South Korea	TM	1986-2005	$K_t \leq 0.20$	0.9200
					$K_t > 0.20$	$0.6910 + 2.4306K_t - 7.3371K_t^2 + 4.7002K_t^3$
88	Yao et al. [62]	Shanghai, China	TM	2012	$K_t \leq 0.30$	$0.9381 - 0.1481K_t$
					$0.30 < K_t \leq 0.80$	$1.5197 - 1.5340K_t$
					$K_t > 0.80$	0.2700
89	Yao et al. [62]	Shanghai, China	TM	2012	-	$0.8142 + 2.0792K_t - 6.1439K_t^2 + 3.4707K_t^3$
90	Yao et al. [62]	Shanghai, China	TM	2012	$K_t \leq 0.20$	$0.8755 + 1.3991K_t - 4.9285K_t^2$
					$0.20 < K_t \leq 0.80$	$1.1209 - 2.1699K_t + 11.0600K_t^2 - 22.3550K_t^3 + 12.8630K_t^4$

(continued on next page)

(continued)

Model	Reference	Location	Climate	Data period	Constrains	K_d
					$K_t > 0.80$	0.2700
91	Yao et al. [62]	Shanghai, China	TM	2012	-	$0.2421 + 0.7202/[1 + \exp\{(K_t - 0.6203)/0.0749\}]$
92	Tapakis et al. [63]	Athalassa, Cyprus	AR	2001-2010	$K_t < 0.10$	$0.9100 + 2.4993K_t - 18.8580K_t^2$
					$0.10 \leq K_t \leq 0.78$	$0.9605 + 0.4482K_t - 2.0011K_t^2 - 1.5581K_t^3 + 2.0080K_t^4$
					$K_t > 0.78$	$-2.4518 + 3.3014K_t$
93	Abreu et al. [64]	Évora, Portugal	TM	2015-2016	-	$[1.0 + (1.502 - 1.820K_t)^{-48.589}]^{-1.0/48.589}$
94	Marques Filho et al. [65]	Rio de Janeiro, Brazil	TM	2011-2014	-	$1.0/[1.0 + \exp(-4.90 + 8.78K_t)]$
95	Marques Filho et al. [65]	Rio de Janeiro, Brazil	TM	2011-2014	-	$0.13 + 0.86/[1.0 + \exp(-6.29 + 12.26K_t)]$
96	Paulescu and Blaga [66]	Timisoara, Romania	TM	2009-2010	$K_t < 0.247$	$0.936 + 0.194K_t$
					$K_t \geq 0.247$	$1.436 - 1.824K_t$
97	Abal et al. [67]	Montevideo, Uruguay	TM	2011-2013	$K_t < 0.20$	1.0
					$0.20 \leq K_t \leq 0.85$	$0.50 + 5.92K_t - 22.22K_t^2 + 29.51K_t^3 - 19.54K_t^4 + 6.09K_t^5$
					$K_t > 0.85$	0.10
98	Abal et al. [67]	Salto, Uruguay	TM	1998-2003	$K_t < 0.20$	1.0
					$0.20 \leq K_t \leq 0.85$	$0.72 + 2.80K_t - 6.62K_t^2 - 4.66K_t^3 + 14.13K_t^4 - 6.20K_t^5$
					$K_t > 0.85$	0.09
99	Abal et al. [67]	Luján, Uruguay	TM	2011-2012	$K_t < 0.20$	1.0
					$0.20 \leq K_t \leq 0.85$	$0.80 + 1.97K_t - 3.93K_t^2 - 5.97K_t^3 + 10.96K_t^4 - 3.56K_t^5$
					$K_t > 0.85$	0.11
100	Abal et al. [67]	Artigas, Uruguay	TM	2014-2015	$K_t < 0.20$	1.0
					$0.20 \leq K_t \leq 0.85$	$0.86 + 0.87K_t + 3.53K_t^2 - 28.43K_t^3 + 39.51K_t^4 - 16.21K_t^5$
					$K_t > 0.85$	0.11
101	Abal et al. [67]	Treinta y Tres, Uruguay	TM	2014-2015	$K_t < 0.20$	1.0
					$0.20 \leq K_t \leq 0.85$	$1.04 - 1.45K_t + 13.21K_t^2 - 43.80K_t^3 + 48.79K_t^4 - 17.60K_t^5$
					$K_t > 0.85$	0.12
102	Abal et al. [67]	Uruguay	TM	1998-2015 (Various data periods)	$K_t < 0.20$	1.0
					$0.20 \leq K_t \leq 0.85$	$0.77 + 2.16K_t - 3.91K_t^2 - 9.02K_t^3 + 17.00K_t^4 - 6.79K_t^5$
					$K_t > 0.85$	0.10
103	Abal et al. [67]	Montevideo, Uruguay	TM	2011-2013	$K_t < 0.35$	$1.0 - 0.40K_t$
					$0.35 \leq K_t \leq 0.75$	$1.51 - 1.86K_t$

(continued on next page)

(continued)

Model	Reference	Location	Climate	Data period	Constrains	K_d
					$K_t > 0.75$	0.12
104	Abal et al. [67]	Salto, Uruguay	TM	1998-2003	$K_t < 0.35$	$1.0 - 0.29K_t$
					$0.35 \leq K_t \leq 0.75$	$1.60 - 2.00K_t$
					$K_t > 0.75$	0.10
105	Abal et al. [67]	Luján, Uruguay	TM	2011-2012	$K_t < 0.35$	$1.0 - 0.24K_t$
					$0.35 \leq K_t \leq 0.75$	$1.60 - 1.95K_t$
					$K_t > 0.75$	0.14
106	Abal et al. [67]	Artigas, Uruguay	TM	2014-2015	$K_t < 0.35$	$1.0 - 0.33K_t$
					$0.35 \leq K_t \leq 0.75$	$1.56 - 1.93K_t$
					$K_t > 0.75$	0.11
107	Abal et al. [67]	Treinta y Tres, Uruguay	TM	2014-2015	$K_t < 0.35$	$1.0 - 0.19K_t$
					$0.35 \leq K_t \leq 0.75$	$1.63 - 1.99K_t$
					$K_t > 0.75$	0.14
108	Abal et al. [67]	Uruguay	TM	1998-2015 (Various data periods)	$K_t < 0.35$	$1.0 - 0.28K_t$
					$0.35 \leq K_t \leq 0.75$	$1.59 - 1.96K_t$
					$K_t > 0.75$	0.12
109	Abal et al. [67]	Montevideo, Uruguay	TM	2011-2013	$K_t < 0.22$	$1.0 - 0.24K_t$
					$0.22 \leq K_t \leq 0.80$	$0.70 + 2.63K_t - 7.38K_t^2 + 1.86K_t^3 + 2.67K_t^4$
					$K_t > 0.80$	0.13
110	Abal et al. [67]	Salto, Uruguay	TM	1998-2003	$K_t < 0.22$	1.0
					$0.22 \leq K_t \leq 0.80$	$0.38 + 6.54K_t - 21.25K_t^2 + 21.37K_t^3 - 6.99K_t^4$
					$K_t > 0.80$	0.09
111	Abal et al. [67]	Luján, Uruguay	TM	2011-2012	$K_t < 0.22$	$1.0 - 0.06K_t$
					$0.22 \leq K_t \leq 0.80$	$0.62 + 3.70K_t - 10.83K_t^2 + 7.00K_t^3 - 0.30K_t^4$
					$K_t > 0.80$	0.12
112	Abal et al. [67]	Artigas, Uruguay	TM	2014-2015	$K_t < 0.22$	$1.0 - 0.15K_t$
					$0.22 \leq K_t \leq 0.80$	$0.68 + 2.91K_t - 7.75K_t^2 + 1.47K_t^3 + 3.24K_t^4$
					$K_t > 0.80$	0.13
113	Abal et al. [67]	Treinta y Tres, Uruguay	TM	2014-2015	$K_t < 0.22$	$1.0 - 0.10K_t$

(continued on next page)

(continued)

Model	Reference	Location	Climate	Data period	Constrains	K_d
					$0.22 \leq K_t \leq 0.80$	$0.85 + 0.98K_t - 0.06K_t^2 - 9.75K_t^3 + 8.62K_t^4$
					$K_t > 0.80$	0.13
114	Abal et al. [67]	Uruguay	TM	1998-2015 (Various data periods)	$K_t < 0.22$	$1.0 - 0.09K_t$
					$0.22 \leq K_t \leq 0.80$	$0.60 + 3.97K_t - 11.74K_t^2 + 7.76K_t^3 - 0.28K_t^4$
					$K_t > 0.80$	0.11
115	Abal et al. [67]	Montevideo, Uruguay	TM	2011-2013	-	$0.95 - 0.97\mathrm{e}^{-\exp(2.96-6.07K_t)}$
116	Abal et al. [67]	Salto, Uruguay	TM	1998-2003	-	$1.00 - 1.07\mathrm{e}^{-\exp(2.82-5.82K_t)}$
117	Abal et al. [67]	Luján, Uruguay	TM	2011-2012	-	$0.98 - 1.05\mathrm{e}^{-\exp(2.96-5.75K_t)}$
118	Abal et al. [67]	Artigas, Uruguay	TM	2014-2015	-	$0.95 - 0.92\mathrm{e}^{-\exp(3.57-7.32K_t)}$
119	Abal et al. [67]	Treinta y Tres, Uruguay	TM	2014-2015	-	$0.96 - 0.97\mathrm{e}^{-\exp(3.46-6.68K_t)}$
120	Abal et al. [67]	Uruguay	TM	1998-2015 (Various data periods)	-	$0.97 - 1.01\mathrm{e}^{-\exp(3.07-6.17K_t)}$
121	Al-Najar and Al-Khazzar [68]	Baghdad, Iraq	AR	2015	-	$1.5973 - 4.6603K_t + 5.7190K_t^2 - 2.5719K_t^3$

Based on the information of Table 2.1, it is notorious that the majority of the models were derived using a polynomial form, followed by the double exponential and logistic functions. This information is also useful to see the distribution of the data used to derive the models according to the climate zone and to identify the length of the datasets, as this is a crucial factor on the determination of the coefficients of the models. Figure 2.1 presents the distribution of models as a function of the number of years of the datasets and climate zone. Only the models that presented an explicit dataset length in their respective publications were used to produce Figure 2.1. Models based on data from several locations, different climatic zones or models derived from distinct dataset lengths were not considered, hence the 100 models examined in Figure 2.1. The higher number of models was developed for the temperate (TM) zone, followed by the arid (AR), tropical (TR) and finally the high albedo (HA) zones. This representativeness of the climate zones is also useful to perceive the distribution of solar radiation measuring stations around the globe and how this may affect the model's development. One can conclude that the high albedo and the tropical climate zones are not well represented. However, nowadays there are more meteorological stations in these climate zones (see, e.g. [69]). The most typical length of the training datasets is two years, followed by one, three and four years. It worths to note that some authors used twenty and even thirty years of data to derive their models (e.g. [27, 61]).

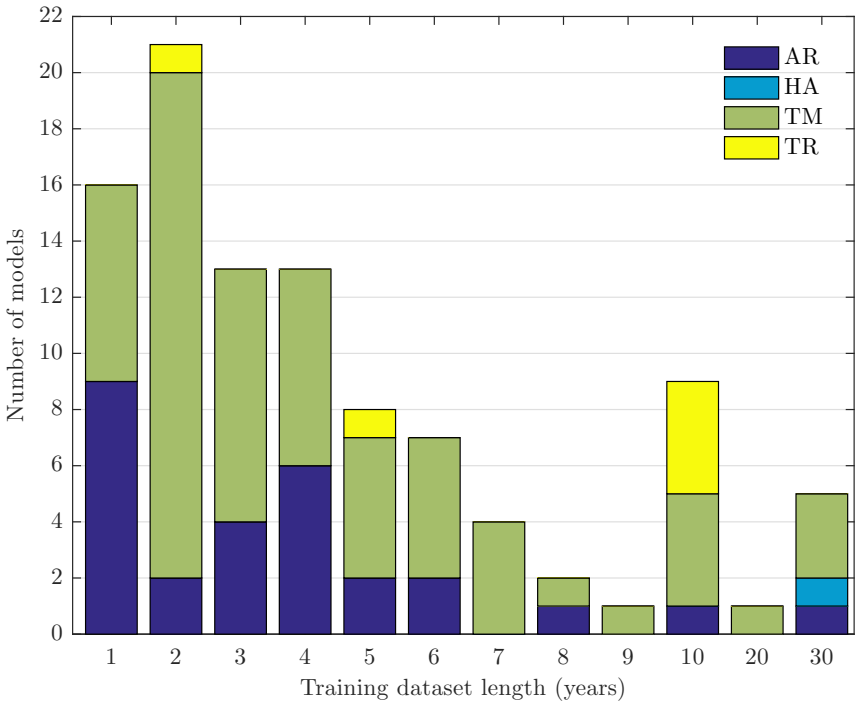

Fig. 2.1: Distribution of the models according to the length of the training datasets and climate zone: temperate (TM), arid (AR), tropical (TR) and high albedo (HA).

2.3 Model development and test data

2.3.1 Model formulation

The model proposed in this study is based on the correlation of two limiting functions for large and small values of K_t through the expression disclosed by Churchill and Usagi [70] for the correlation of transfer phenomena, described as follows:

$$Y = (1 + Z^n)^{\frac{1}{n}} \tag{2.1}$$

where the arbitrary exponent n needs to be selected in order to correlate those functions accurately [70]. This expression can be used to any phenomenon varying uniformly, for example in heat transfer modelling [71] and fluid flow and heat transfer optimisation when combined with the concept of the intersection of asymptotes [72, 73]. In the case of modelling the diffuse fraction as a function of the clearness index, the functions used here are the physically possible limit of $K_d = 1$ and a function Z that is the best fit for the clear sky periods. The occurrence of cloud enhancement effects in one-minute resolution data is quite frequent [1, 14], then function Z was defined as the best fit to the clear sky data using a second degree polynomial in the form:

$$Z = A(K_t - 0.5)^2 + B(K_t - 0.5) + 1 \tag{2.2}$$

Since K_d is a concave function of K_t, the exponents used in Eq. 1 must be $-n$ and $-1/n$, and thus, the final form of the model is given by:

$$K_d = \left\{1 + [A(K_t - 0.5)^2 + B(K_t - 0.5) + 1]^{-n}\right\}^{-\frac{1}{n}} \tag{2.3}$$

Figure 2.2 shows the fitting of the model to the data of Fort Peck station (FPE), USA, as an example of the procedures implemented in this work for all the analysed stations. Red lines represent the limiting functions $K_d = 1$ and Z (fitted to the FPE dataset), and the blue line represents the fitted model. The three parameters of the adjusted model for FPE station are also presented, as well as the period of data used.

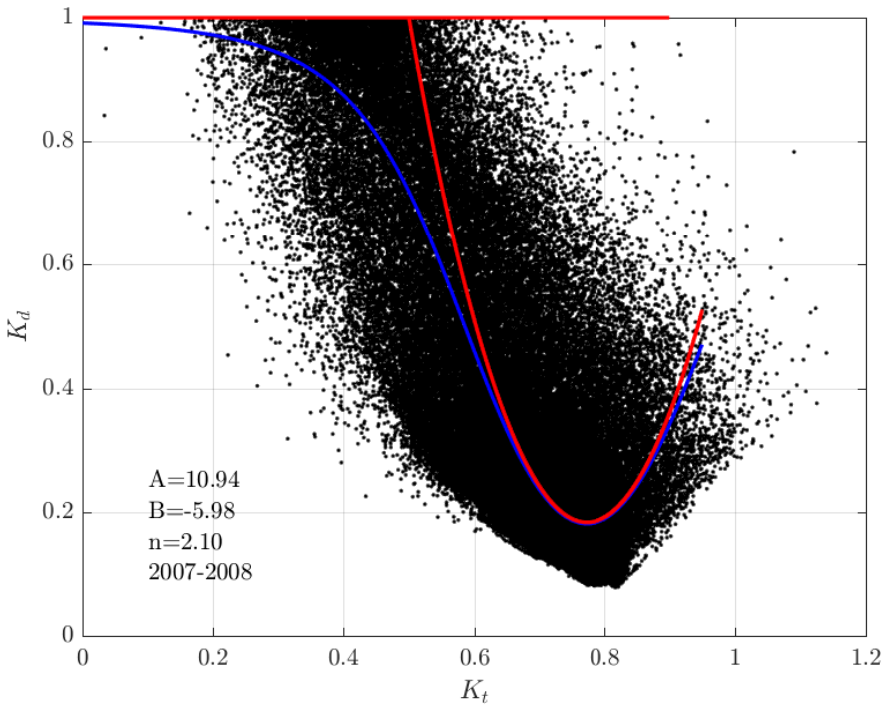

Fig. 2.2: Data for the FPE station (Fort Peck, USA) and representation of the limiting functions (red) and model correlation (blue).

2.3.2 Test stations and data quality control

The data used in this study is from the Baseline Surface Radiation Network (BSRN) [69, 74] and the Institute of Earth Sciences (IES) at the University of Évora, Portugal. The BSRN is a project of the Global Energy and Water Cycle Experiment (GEWEX) under the umbrella of the World Climate Research Programme (WCRP). The primary objective of this network is to detect changes in the radiation field at the Earth's surface which may be related to climate changes. Measurements of solar radiation in the IES station are taken likewise as in the BSRN stations: the diffuse horizontal irradiation (DHI) is measured by a Kipp&Zonnen CM6B pyranometer and shading ball attached to the sun tracker and the global horizontal irradiance is also measured by a Kipp&Zonnen CM6B pyranometer. The sensors are installed on a Kipp&Zonnen Solys2 sun tracker and are properly maintained and calibrated according to the BSRN and WMO guidelines and recommendations [69, 75]. Table 4.1 shows detailed information on the stations used in this study : location, climate zone, data period, number of valid data points and mean GHI of all valid measurements.

Table 2.2: Information on the data of BSRN and IES stations. Acronyms: AR (Arid), HA (High albedo), TM (Temperate), and TR (Tropical).

Station	Code	Lat. (°N)	Long. (°E)	Elev. (m)	Climate	Data period	Samples	Mean GHI (W/m^2)
Alert	ALE	82.490	−62.420	127	HA	2009-2011	631284	223.84
Alice Springs	ASP	−23.798	133.888	547	AR	2007-2009	704784	561.96
Bermuda	BER	32.267	−64.667	8	TM	2006-2008	458837	497.33
Billings	BIL	36.605	−97.516	317	TM	2005-2007	631822	451.65
Bondville	BON	40.067	−88.367	213	TM	2007-2009	220046	507.54
Boulder	BOU	40.050	−105.007	1577	TM	2002-2004	481571	519.33
Brasilia	BRB	−15.601	−47.713	1023	TR	2009-2011	598116	472.22
Carpentras	CAR	44.083	5.059	100	TM	2003-2005	619585	419.19
Chesapeake Light	CLH	36.905	−75.713	37	TM	2011-2013	681269	408.60
Cener	CNR	42.816	−1.601	471	TM	2010-2012	666202	374.60
Cocos Island	COC	−12.193	96.835	6	TR	2006-2008	556163	505.99
De Aar	DAA	−30.667	23.993	1287	AR	2002-2004	592787	518.07
Darwin	DAR	−12.425	130.891	30	TR	2009-2011	699416	489.94
Concordia station	DOM	−75.100	123.383	3233	HA	2005-2007	255370	377.86
Desert Rock	DRA	36.626	−116.018	1007	AR	2007-2009	324644	596.47
Évora	EVR	38.568	−7.912	293	TM	2016-2017	199169	504.11
Eureka	EUR	79.989	−85.940	85	HA	2009-2011	654421	230.99
Fort Peck	FPE	48.317	−105.100	634	TM	2007-2009	227621	481.02
Fukuoka	FUA	33.582	130.376	3	TM	2011-2013	715368	337.10
Goodwin Creek	GCR	34.250	−89.870	98	TM	2007-2009	244471	529.24
Gobabeb	GOB	−23.561	15.042	407	AR	2012-2014	627165	596.64
Georg von Neumayer	GVN	−70.650	−8.250	42	HA	2011-2013	509631	316.63
Ilorin	ILO	8.533	4.567	350	TR	1995,1999,2000	160661	307.77
Ishigakijima	ISH	24.337	124.163	6	TM	2011-2013	710421	374.30
Izana	IZA	28.309	−16.499	2373	AR	2011-2013	680660	612.14
Kwajalein	KWA	8.720	167.731	10	TR	1998-2000	517467	544.96
Lauder	LAU	−45.045	169.689	350	TM	2005-2007	583349	399.17
Lerwick	LER	60.139	−1.185	80	TM	2004-2006	586958	213.18
Lindenberg	LIN	52.210	14.122	125	TM	2001-2003	665675	285.77
Momote	MAN	−2.058	147.425	6	TR	2008-2010	689159	470.82
Minamitorishima	MNM	24.288	153.983	7	TM	2011-2013	727974	470.67
Nauru Island	NAU	−0.521	166.917	7	TR	2005-2007	649304	513.96
Ny-Alesund	NYA	78.925	11.930	11	HA	2007-2009	619576	187.06
Palaiseau	PAL	48.713	2.208	156	TM	2009-2011	701389	302.24
Payerne	PAY	46.815	6.944	491	TM	2008-2010	573646	349.50
Rock Springs	PSU	40.720	−77.933	376	TM	2007-2009	203868	471.41
Petrolina	PTR	−9.068	−40.319	387	TR	2007-2009	149097	566.04
Regina	REG	50.205	−104.713	578	TM	2009-2011	620001	365.50
Sapporo	SAP	43.060	141.328	17	AR	2011-2013	722699	305.91
Sede Boqer	SBO	30.860	34.779	480	TM	2009-2011	662564	542.45
Sonnblick	SON	47.054	12.958	3109	HA	2013-2015	462080	371.23
Solar Village	SOV	24.907	46.397	768	AR	2000-2002	717011	564.91
Sioux Falls	SXF	43.730	−96.620	473	TM	2007-2009	228600	475.41
Tamanrasset	TAM	22.790	5.529	1385	AR	2006-2008	644908	596.17
Tateno	TAT	36.050	140.133	25	TM	2008-2010	683402	334.39
Tiksi	TIK	71.586	128.919	48	HA	2011-2013	617716	211.72
Toravere	TOR	58.254	26.462	70	TM	2010-2012	649189	245.32
Xianghe	XIA	39.754	116.962	32	TM	2008-2010	561393	381.54

Data quality control was performed by applying the quality filters defined by Long and Shi [76] for the global horizontal irradiance (GHI). Furthermore, K_d values higher than 1 and lower than 0 were removed for the fitting of the model parameters A and B, since measurements of diffuse irradiance higher than global irradiance are very dubious. However, instrumental errors can occur, and therefore, the K_d maximum value was set to 1.2 when determining the parameter n. Finally, measurements taken when the zenith angle was higher than 85° were also removed due to disturbances caused mainly by the horizon line and also due to instrumental and modelling accuracy issues in that case [14]. Since one-minute data was used in this work, the extraterrestrial irradiance on a horizontal surface, E_{oh}, that is needed to determine the K_t was simply calculated based on the solar constant ($G_s = 1361.1 W m^{-2}$ [77]) and the solar zenith angle, this last being calculated through the very accurate solar position algorithm developed by Reda and Andreas [78]. The data was divided into two sets: the training set with two years of data used to determine the fitting parameters of the proposed model; and the validation set with one year of data, used to validate the developed model as well as the models available in the literature (Section 2.2). These datasets are composed of years with high number of valid measurements, i.e., records that successfully passed the quality control procedures [76], as shown in Table 4.1.

2.3.3 Statistical indicators for model assessment

The developed model, as well as the models reviewed in Section 2.2, were evaluated using the statistical indicators described below taking the measured values as reference. Lower values indicate better model accuracy except for the mean bias error and mean percentage error, in which values closer to zero indicate a better model accuracy, and for the correlation coefficient, in which a value closer to 1 represents better model accuracy. In the following, H and N stand for minutely diffuse horizontal irradiance (DHI) and number of observations, respectively, and the subscripts m, e and avg stand for measured, estimated and average, respectively.

2.3.3.1 Mean bias error (MBE)

$$\mathrm{MBE} = \frac{1}{N}\sum_{i=1}^{N}(H_{e,i} - H_{m,i}) \tag{2.4}$$

2.3.3.2 Mean absolute error (MAE)

$$\mathrm{MAE} = \frac{1}{N}\sum_{i=1}^{N}|H_{e,i} - H_{m,i}| \tag{2.5}$$

2.3.3.3 Root mean square error (RMSE)

$$\mathrm{RMSE} = \left[\frac{1}{N}\sum_{i=1}^{N}(H_{e,i} - H_{m,i})^2\right]^{\frac{1}{2}} \tag{2.6}$$

2.3.3.4 Mean percentage error (MPE)

$$\mathrm{MPE} = \frac{1}{N}\sum_{i=1}^{N}\left(\frac{H_{e,i} - H_{m,i}}{H_{m,i}}\right) \times 100 \tag{2.7}$$

2.3.3.5 Uncertainty at 95% (U95)

$$\mathrm{U95} = 1.96(SD^2 + RMSE^2)^{\frac{1}{2}} \tag{2.8}$$

where SD represents the standard deviation of the difference between H_e and H_m.

2.3.3.6 Relative root mean square error (RRMSE)

$$\mathrm{RRMSE} = \frac{RMSE}{H_{m,avg}} \tag{2.9}$$

2.3.3.7 t-statistics (TSTAT)

$$\mathrm{TSTAT} = \left[\frac{(N-1)MBE^2}{RMSE^2 - MBE^2}\right]^{\frac{1}{2}} \tag{2.10}$$

2.3.3.8 Maximum absolute relative error (erMAX)

$$\mathrm{erMAX} = \max\left\{\left|\frac{H_{e,i} - H_{m,i}}{H_{m,i}}\right|, i = 1, ..., N\right\} \tag{2.11}$$

2.3.3.9 Correlation coefficient (R)

$$\mathrm{R} = \frac{\sum_{i=1}^{N}(H_{e,i} - H_{e,avg})(H_{m,i} - H_{m,avg})}{\sqrt{\sum_{i=1}^{N}(H_{e,i} - H_{e,avg})^2 \sum_{i=1}^{N}(H_{m,i} - H_{m,avg})^2}} \tag{2.12}$$

2.3.3.10 Mean absolute relative error (MARE)

$$\mathrm{MARE} = \frac{1}{N}\sum_{i=1}^{N}\left|\frac{H_{e,i} - H_{m,i}}{H_{m,i}}\right| \tag{2.13}$$

2.3.3.11 Global Performance Index (GPI)

The global performance index, firstly proposed by Behar et al. [79], then modified by Despotovic et al. [80] and used by Jamil and Akthar [23, 81], is also used here to combine all the statistical indicators presented in Subsections 2.3.3.1 to 2.3.3.10. The need for using this index is due to the incapacity of those statistical indicators to, consistently, identify the best model (see Table 2.4). The values of the statistical indicators need to be scaled between 0 (worst performing model) and 1 (best performing model) to determine the GPI values, which otherwise would make difficult to compare the models. This normalisation also allows using the same statistical weight for all of the indicators when determining the GPI, as follows:

$$\mathrm{GPI} = \sum_{j=1}^{10} \alpha_j (\bar{y}_j - y_{ij}) \tag{2.14}$$

where $\bar{y}_j$ is the median of the scaled values of the indicator j, y_{ij} is the scaled value of the statistical indicator j for the model i, and α_j equals to 1 for all statistical indicators except R, in which α_j equals to -1. The GPI also allows to combine several indicators regardless if the value of a single indicator is 0 or not, which is not possible if a simple product of the indicators is computed, and therefore a higher GPI stands for better accuracy of a given model.

2.4 Results and discussion

2.4.1 Determination of model parameters and climate analysis

Figure 2.3 shows the distribution of the K_t values for the climate zones considered, which is useful to identify the range of the clearness index and the clear sky occurrences (frequency). The AR climate zone presents the highest relative frequency for high values of K_t, reaching a relative frequency of 0.038 for $K_t \simeq 0.77$, followed by the TM and TR climate zones with maximum relative frequency around 0.030 for approximately the same K_t value. The HA climate zone presents the lower values of K_t relative frequency for clear sky. The training of the model was performed using the stations from the BSRN network, while the IES station (EVR) was used only in the validation of the model. The parameters A and B for each station were found by fitting Eq. 2.2 to the data in the range of $K_t \geq 0.5$, using the non-linear least squares method. Then, the parameter n was obtained through an optimisation process in order to achieve the maximum GPI value for the entire range of the data. One also investigated the existence of a possible relationship between these parameters and the elevation of the stations according to the climate zone, as shown in Figure 2.4. However no conclusions can be drawn on the existence of any clear dependence, and therefore, no traditional fitting equations using the parameters of the model

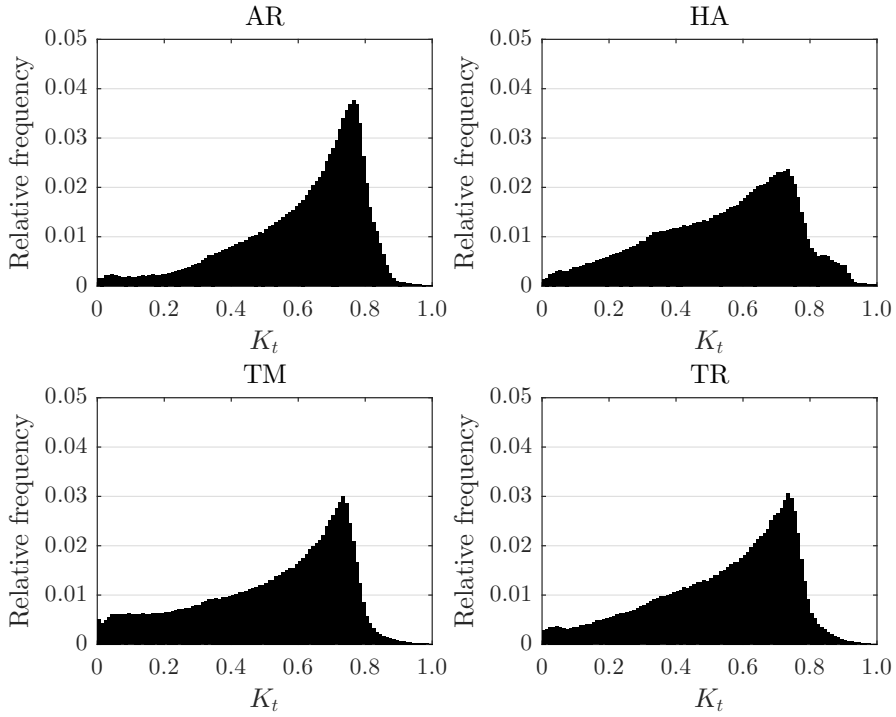

Fig. 2.3: Relative frequency of K_t in BSRN stations according to the climate zone.

and the elevation of the stations were able to present an acceptable coefficient of determination. To develop a model based only on the K_t as predictor for each climate

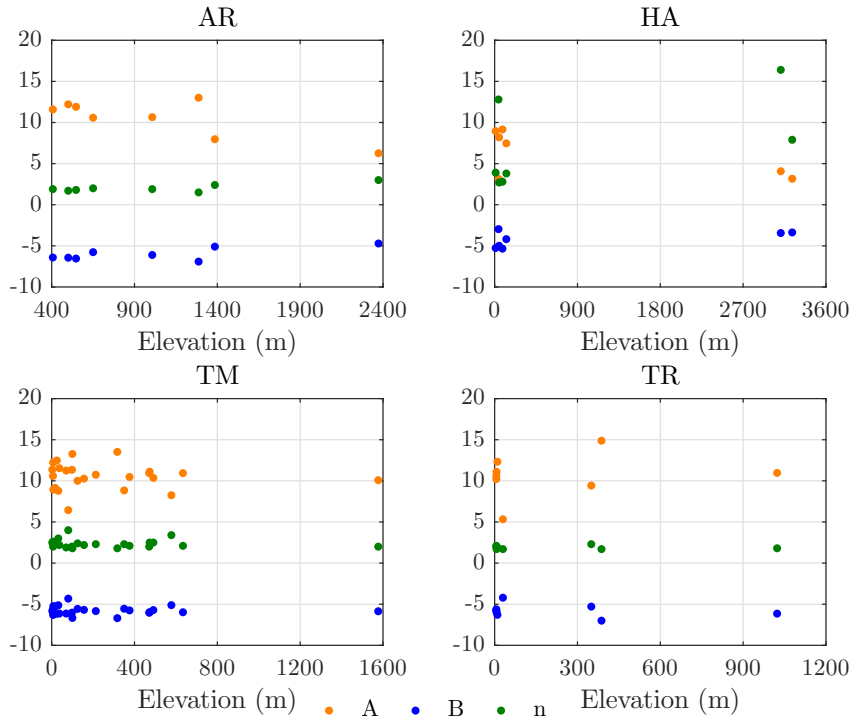

Fig. 2.4: Variation of the parameters A, B and n according to the elevation of the stations and climate zone: Arid (AR), High Albedo (HA), Temperate (TM) and Tropical (TR).

region, the mean value and standard deviation of these parameters were calculated for the four zones considered, and the stations in which at least one of the three parameters were out of the confidence interval defined by the mean ± standard deviation were excluded from this calculation. After this procedure, the values inside this imposed range are averaged in order to obtain the mean values of A, B and n for each climate zone, as shown in Table 2.3. These parameters were used for the model performance assessment as presented in the following section.

Table 2.3: Parameters of the developed model according to the climate zone: Arid (AR), High Albedo (HA), Temperate (TM) and Tropical (TR).

Parameters	Climate Zone			
	AR	HA	TM	TR
A	11.39	7.83	10.79	11.59
B	−6.25	−4.59	−5.87	−6.14
n	1.86	3.25	2.24	1.87

2.4.2 Performance assessment

The statistical tools presented in Section 2.3.3 were used to assess the performance of the models from the literature as well as of the model developed in this work using measurements from the EVR station and the datasets from the BSRN, as presented in Table 2.2. The performance assessment was carried out using the corresponding set of parameters according to the climate zone of the 48 radiometric stations analysed in this study. The performance assessment is presented in detail for the EVR station as an example of both the methodology used in this study and as a completely independent assessment since data from this station was not included in the determination of the model parameters. Table 2.4 presents the results of the statistical analysis of the selected models using the indicators shown in Section 2.3.3 for the EVR station. The bold font indicates the optimal values of the statistical indicators, i.e., it indicates the best model according to each statistical indicator.

Table 2.4: Statistical analysis of the selected models for the EVR station.

Model	MBE ($W\ m^{-2}$)	RMSE ($W\ m^{-2}$)	TSTAT	MPE (%)	U95 ($W\ m^{-2}$)	erMAX	RRMSE	MAE ($W\ m^{-2}$)	R	MARE	GPI
1	−40.31	111.13	36.42	−6.42	297.74	2.00	0.86	75.41	0.19	0.55	0.22
2	−29.87	102.79	28.42	3.82	278.84	2.11	0.79	71.26	0.30	0.54	0.64
3	−46.36	112.67	42.25	−12.76	298.80	1.79	0.87	75.05	0.19	0.53	0.13
4	−74.08	124.44	69.34	−41.84	312.87	**0.89**	0.96	79.87	0.19	0.50	−0.46
5	−79.12	127.30	74.25	−47.13	316.96	0.90	0.98	82.42	0.19	0.52	−0.63

(continued on next page)

(continued)

Model	MBE ($W\ m^{-2}$)	RMSE ($W\ m^{-2}$)	TSTAT	MPE (%)	U95 ($W\ m^{-2}$)	erMAX	RRMSE	MAE ($W\ m^{-2}$)	R	MARE	GPI
6	−74.08	124.44	69.34	−41.84	312.87	**0.89**	0.96	79.87	0.19	0.50	−0.46
7	−99.29	140.53	93.43	−68.28	337.45	0.94	1.08	99.29	0.19	0.68	−1.46
8	−79.12	127.30	74.25	−47.13	316.96	0.90	0.98	82.42	0.19	0.52	−0.63
9	−53.92	115.14	49.60	−20.69	301.16	1.54	0.89	75.16	0.19	0.51	0.00
10	−79.12	127.30	74.25	−47.13	316.96	0.90	0.98	82.42	0.19	0.52	−0.63
11	−69.04	121.78	64.41	−36.56	309.23	1.03	0.94	77.95	0.19	0.49	−0.32
12	−58.96	117.11	54.53	−25.98	303.36	1.37	0.90	75.67	0.19	0.50	−0.10
13	−94.25	136.99	88.73	−62.99	331.75	0.93	1.06	94.31	0.19	0.63	−1.24
14	−79.12	127.30	74.25	−47.13	316.96	0.90	0.98	82.42	0.19	0.52	−0.63
15	−89.21	133.59	83.95	−57.70	326.42	0.92	1.03	89.69	0.19	0.58	−1.02
16	−79.12	127.30	74.25	−47.13	316.96	0.90	0.98	82.42	0.19	0.52	−0.63
17	−21.15	109.03	18.51	13.67	299.35	2.64	0.84	78.71	0.19	0.64	0.24
18	28.34	79.71	35.61	56.30	213.84	2.98	0.62	63.06	0.68	0.69	0.91
19	−48.88	113.43	44.69	−15.41	299.45	1.71	0.88	75.01	0.19	0.52	0.09
20	−38.25	107.47	35.65	−3.12	288.30	2.10	0.83	69.93	0.24	0.49	0.45
21	1.53	112.10	1.28	37.46	310.72	3.40	0.87	85.97	0.19	0.78	−0.01
22	−16.11	109.19	13.96	18.96	301.01	2.81	0.84	80.05	0.19	0.67	0.20
23	**0.42**	82.32	**0.48**	28.96	228.18	2.45	0.64	54.46	0.59	0.51	1.66
24	−55.43	115.71	51.08	−22.28	301.76	1.49	0.89	75.28	0.19	0.50	−0.03
25	−53.41	114.96	49.11	−20.17	300.96	1.56	0.89	75.13	0.19	0.51	0.01
26	−40.31	111.13	36.42	−6.42	297.74	2.00	0.86	75.41	0.19	0.55	0.22
27	−30.22	109.49	26.88	4.15	297.65	2.34	0.85	76.76	0.19	0.59	0.29
28	3.55	112.66	2.95	39.58	312.20	3.47	0.87	86.76	0.19	0.80	−0.09
29	19.18	118.40	15.36	55.97	326.03	3.99	0.91	93.67	0.19	0.91	−0.69
30	8.09	114.07	6.65	44.34	315.79	3.62	0.88	88.64	0.19	0.83	−0.26
31	−99.29	140.53	93.43	−68.28	337.45	0.94	1.08	99.29	0.19	0.68	−1.46
32	−56.45	105.00	59.68	−26.47	269.19	1.77	0.81	60.44	0.49	0.33	0.64
33	−47.02	121.55	39.26	−12.54	324.08	2.03	0.94	82.07	0.08	0.60	−0.29
34	−129.12	164.09	119.34	−99.48	377.92	1.00	1.27	129.12	0.18	0.99	−2.82
35	14.18	77.91	17.32	42.93	214.17	2.63	0.60	58.39	0.65	0.60	1.37
36	−38.79	110.81	34.98	−4.83	297.59	2.05	0.86	75.56	0.19	0.56	0.24
37	−13.59	109.39	11.72	21.60	302.03	2.89	0.84	80.77	0.19	0.69	0.18
38	21.99	87.63	24.26	45.07	239.04	5.94	0.68	60.85	0.61	0.60	0.49
39	21.70	119.55	17.27	58.61	328.63	4.08	0.92	94.89	0.19	0.93	−0.79
40	21.70	119.55	17.27	58.61	328.63	4.08	0.92	94.89	0.19	0.93	−0.79
41	−28.71	109.34	25.47	5.74	297.82	2.39	0.84	77.04	0.19	0.60	0.28
42	91.34	162.12	63.82	130.84	412.18	6.25	1.25	131.34	0.23	1.48	−3.61
43	−59.97	117.54	55.52	−27.04	303.86	1.34	0.91	75.82	0.19	0.50	−0.12
44	−38.79	110.81	34.98	−4.83	297.59	2.05	0.86	75.56	0.19	0.56	0.24
45	4.17	75.61	5.17	28.26	209.41	4.19	0.58	52.45	0.67	0.47	1.56
46	35.49	81.81	45.07	63.51	215.83	3.10	0.63	65.77	0.69	0.74	0.64
47	−40.31	111.13	36.42	−6.42	297.74	2.00	0.86	75.41	0.19	0.55	0.22
48	−20.14	109.03	17.59	14.73	299.64	2.67	0.84	78.97	0.19	0.65	0.23
49	−63.50	119.10	58.98	−30.74	305.76	1.22	0.92	76.47	0.19	0.49	−0.20
50	−22.16	109.03	19.43	12.61	299.08	2.61	0.84	78.47	0.19	0.64	0.25
51	0.97	74.95	1.21	27.30	207.75	2.63	0.58	50.05	0.67	0.47	1.92
52	80.04	123.80	79.32	114.80	305.19	4.66	0.96	101.68	0.51	1.22	−1.94
53	−1.70	75.32	2.12	25.91	208.75	2.26	0.58	51.50	0.67	0.47	1.96
54	25.21	82.06	30.22	54.78	222.02	2.88	0.63	64.16	0.64	0.69	0.89
55	22.66	80.81	27.34	51.93	219.55	2.85	0.62	62.57	0.64	0.67	1.01
56	8.51	75.99	10.54	36.20	209.99	2.64	0.59	54.50	0.67	0.54	1.62

(continued on next page)

(continued)

Model	MBE ($W\ m^{-2}$)	RMSE ($W\ m^{-2}$)	TSTAT	MPE (%)	U95 ($W\ m^{-2}$)	erMAX	RRMSE	MAE ($W\ m^{-2}$)	R	MARE	GPI
57	−2.72	74.91	3.40	24.30	207.57	2.33	0.58	50.11	0.67	0.46	1.97
58	17.72	78.78	21.61	46.49	215.59	2.77	0.61	59.71	0.65	0.62	1.23
59	5.25	75.53	6.53	32.87	209.11	2.52	0.58	53.32	0.67	0.52	1.75
60	−48.27	108.42	46.53	−19.98	285.25	2.48	0.84	57.67	0.42	0.36	0.56
61	38.92	113.31	34.23	75.18	304.68	4.23	0.87	92.15	0.31	0.97	−0.91
62	−106.85	146.12	100.33	−76.21	346.67	0.96	1.13	106.85	0.19	0.76	−1.80
63	−0.89	111.49	0.74	34.92	309.04	3.32	0.86	85.04	0.19	0.77	0.06
64	32.23	124.95	24.99	69.66	340.53	4.43	0.96	100.26	0.19	1.01	−1.23
65	−72.77	123.26	68.46	−39.64	310.46	2.34	0.95	74.37	0.23	0.42	−0.50
66	−57.44	104.79	61.34	−28.93	267.76	2.56	0.81	65.17	0.51	0.39	0.43
67	17.89	77.44	22.22	44.70	211.78	2.80	0.60	58.85	0.67	0.60	1.30
68	17.38	74.36	22.50	44.68	203.28	2.59	0.57	57.34	0.70	0.60	1.44
69	54.08	108.58	53.76	86.97	281.68	4.31	0.84	87.56	0.47	0.99	−0.92
70	10.66	75.44	13.35	38.81	208.07	6.90	0.58	56.61	0.68	0.56	0.86
71	8.27	74.35	10.48	36.44	205.45	2.64	0.57	55.35	0.69	0.55	1.66
72	−24.73	80.84	30.08	2.11	218.76	1.88	0.62	47.74	0.66	0.33	1.87
73	−7.55	78.20	9.08	21.51	216.24	2.09	0.60	55.36	0.66	0.47	1.84
74	18.79	80.38	22.50	48.26	219.75	2.67	0.62	61.71	0.64	0.64	1.15
75	3.70	76.96	4.50	32.28	213.19	2.17	0.59	55.20	0.65	0.52	1.78
76	−16.42	77.36	20.33	10.66	211.99	1.89	0.60	49.07	0.68	0.38	1.97
77	−20.39	80.17	24.61	6.91	218.59	1.91	0.62	48.59	0.65	0.36	1.87
78	−9.96	78.53	11.97	18.35	216.80	1.92	0.61	51.70	0.64	0.43	1.88
79	−32.59	109.77	29.10	1.67	297.48	2.26	0.85	76.37	0.19	0.58	0.29
80	−39.45	110.95	35.60	−5.52	297.65	2.03	0.86	75.49	0.19	0.55	0.23
81	−41.06	111.30	37.15	−7.21	297.83	1.97	0.86	75.35	0.19	0.55	0.21
82	−38.79	110.81	34.98	−4.83	297.59	2.05	0.86	75.56	0.19	0.56	0.24
83	−27.20	109.23	24.06	7.33	298.03	2.44	0.84	77.34	0.19	0.61	0.27
84	−26.54	109.18	23.46	8.01	298.14	2.46	0.84	77.48	0.19	0.61	0.27
85	−8.55	110.00	7.29	26.89	304.45	3.06	0.85	82.35	0.19	0.72	0.14
86	−64.00	119.33	59.47	−31.27	306.06	1.20	0.92	76.58	0.19	0.49	−0.21
87	84.34	128.86	81.01	116.82	316.63	5.10	0.99	103.80	0.50	1.24	−2.17
88	6.58	113.58	5.43	42.75	314.55	3.57	0.88	88.00	0.19	0.82	−0.20
89	92.63	132.94	90.92	126.87	320.66	5.13	1.03	108.04	0.51	1.32	−2.49
90	88.67	123.26	96.91	119.65	294.17	4.67	0.95	100.93	0.61	1.24	−2.00
91	87.44	121.89	96.37	119.29	291.17	4.63	0.94	100.66	0.61	1.24	−1.97
92	−179.35	287.33	74.77	−141.81	714.66	5.68	2.22	202.48	−0.30	1.59	−6.35
93	−18.41	72.93	24.41	5.27	198.91	2.15	0.56	**44.95**	0.72	0.36	2.08
94	−11.85	75.52	14.87	14.47	208.03	2.23	0.58	47.25	0.68	0.39	1.98
95	−5.82	71.58	7.64	19.72	198.07	2.30	0.55	47.76	0.72	0.41	**2.12**
96	−60.98	121.20	54.48	−33.86	313.97	2.74	0.94	67.90	0.38	0.46	−0.10
97	−79.12	127.30	74.25	−47.13	316.96	0.90	0.98	82.42	0.19	0.52	−0.63
98	−84.16	130.36	79.13	−52.42	321.48	0.91	1.01	85.68	0.19	0.55	−0.82
99	−74.08	124.44	69.34	−41.84	312.87	**0.89**	0.96	79.87	0.19	0.50	−0.46
100	−74.08	124.44	69.34	−41.84	312.87	**0.89**	0.96	79.87	0.19	0.50	−0.46
101	−69.04	121.78	64.41	−36.56	309.23	1.03	0.94	77.95	0.19	0.49	−0.32
102	−79.12	127.30	74.25	−47.13	316.96	0.90	0.98	82.42	0.19	0.52	−0.63
103	−69.04	121.78	64.41	−36.56	309.23	1.03	0.94	77.95	0.19	0.49	−0.32
104	−79.12	127.30	74.25	−47.13	316.96	0.90	0.98	82.42	0.19	0.52	−0.63
105	−58.96	117.11	54.53	−25.98	303.36	1.37	0.90	75.67	0.19	0.50	−0.10
106	−74.08	124.44	69.34	−41.84	312.87	**0.89**	0.96	79.87	0.19	0.50	−0.46
107	−58.96	117.11	54.53	−25.98	303.36	1.37	0.90	75.67	0.19	0.50	−0.10

(continued on next page)

(continued)

Model	MBE ($W\ m^{-2}$)	RMSE ($W\ m^{-2}$)	TSTAT	MPE (%)	U95 ($W\ m^{-2}$)	erMAX	RRMSE	MAE ($W\ m^{-2}$)	R	MARE	GPI
108	−69.04	121.78	64.41	−36.56	309.23	1.03	0.94	77.95	0.19	0.49	−0.32
109	−64.00	119.33	59.47	−31.27	306.06	1.20	0.92	76.58	0.19	0.49	−0.21
110	−84.16	130.36	79.13	−52.42	321.48	0.91	1.01	85.68	0.19	0.55	−0.82
111	−69.04	121.78	64.41	−36.56	309.23	1.03	0.94	77.95	0.19	0.49	−0.32
112	−64.00	119.33	59.47	−31.27	306.06	1.20	0.92	76.58	0.19	0.49	−0.21
113	−64.00	119.33	59.47	−31.27	306.06	1.20	0.92	76.58	0.19	0.49	−0.21
114	−74.08	124.44	69.34	−41.84	312.87	**0.89**	0.96	79.87	0.19	0.50	−0.46
115	−15.14	76.83	18.81	11.50	210.89	2.11	0.59	47.82	0.67	0.38	1.95
116	−24.37	80.74	29.63	**1.31**	218.65	2.19	0.62	45.81	0.65	**0.32**	1.84
117	−6.69	76.75	8.19	20.13	212.34	2.34	0.59	49.23	0.66	0.43	1.91
118	−14.95	75.02	19.03	10.74	205.86	2.27	0.58	46.33	0.69	0.36	2.01
119	−2.52	74.47	3.16	23.97	206.36	2.44	0.57	49.39	0.68	0.45	1.98
120	−16.08	77.31	19.90	10.01	211.97	2.25	0.60	46.70	0.67	0.36	1.93
121	1.42	92.87	1.44	34.45	257.41	2.85	0.72	69.35	0.42	0.62	0.95
This work	25.84	**70.80**	36.68	47.87	**189.61**	2.59	**0.55**	53.70	**0.76**	0.58	1.43

The statistical evaluation regarding the accuracy of the models presented in Table 2.4 for EVR does not give a unanimous decision on which of the models is considered the most accurate. The model developed in this work is the best performing model if we consider the RMSE (70.80 $W\ m^{-2}$), U95 (189.61 $W\ m^{-2}$), RRMSE (0.55) and R (0.76) statistical indicators. On the other hand, the model 23 presented by Hollands [31], is the most accurate model regarding the MBE (0.42 $W\ m^{-2}$) and TSTAT (0.48) indicators. Considering the values of MPE (1.31%) and MARE (0.32) of the model 116 derived by Abal et al. [67], it would be selected as the best performing model for this station. Regarding the erMAX, it does not allow identifying the single most accurate model, due to presenting the same value for several models. The analysis of these results shows the advantage of using the GPI in order to present a more concise performance evaluation, allowing the combination of several statistical indicators and providing, through a simple procedure, a result easy to understand. Therefore, the model with higher GPI for the station being analysed (EVR) is the model 95 presented by Marques Filho et al. [65] with a GPI value of 2.12, although it was not considered the best performing model according to any of the statistical indicators separately. This result is due to the scaling down of the values of the statistical indicators mentioned above in the GPI determination procedure, which allows for a fair comparison of the models under study.

This analysis was also carried out for all of the BSRN stations in order to identify the best performing model for various locations in different climate zones. Figure 2.5 presents the result of this comprehensive performance assessment, where the absolute frequency of selection as the best performing model (based on the maximum GPI) is shown, also according to the climate zone of the stations. The best overall performing model is the one presented in this work (Eq. 2.3 and Table 2.3), followed by model

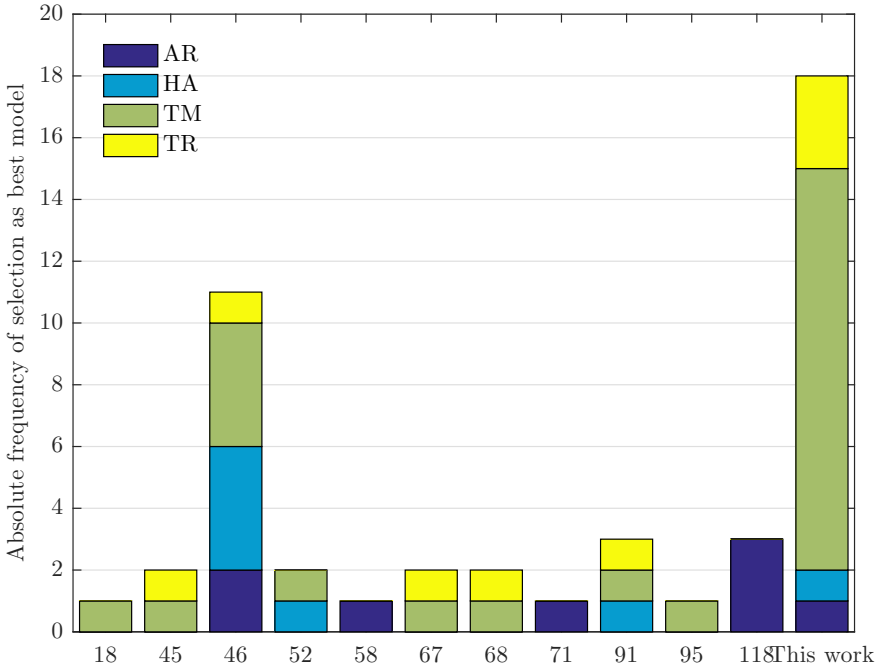

Fig. 2.5: Best performing models according to the climate zone: arid (AR), high albedo (HA), temperate (TM) and tropical (TR).

46 by Mondol et al. [47]. The best performing model for the AR climate zone is the model 118 proposed by Abal et al. [67] while the best performing model for the HA climate zone is the model 46 derived by Mondol et al. [47]. The best performing model for the TM and TR climate zones is the model presented in this work (Eq. 2.3 and Table 2.3). The results presented in Figure 2.5 show the advantage in deriving specific model parameters for each climate zone as suggested by Gueymard and Ruiz-Arias [14], despite the good performance of the model proposed by Mondol [47]. Only the model proposed here, and the model proposed by Mondol [47] were selected as best performing models for the four climate zones considered, showing excellent versatility regarding climate zone selection. On the other hand, the higher number of stations in the temperate (TM) zone allows for a better characterisation of the model parameters in comparison against other climate zones, where less data is available.

To further test the closeness of the two best performing models from Figure 2.5 to the measured data, i.e., model 46 and the one proposed in this work, a Taylor diagram [25] is presented in Figure 2.6 for all stations. This diagram helps to identify the closeness between the modelled and observed data in terms of their correlation coefficient (azimuthal position, R) and standard deviation of model output normalised by the standard deviation of the corresponding observations (radial distance, nSD). In this diagram, a better accuracy is achieved when the model is located close to the normalised standard deviation unit line [14], while the open circle in the coordinates (nSD=1, R=1) represents the point of perfect match between

model and observations. It is worth to mention that the distance between the model representation and this point is the so-called centred pattern Root Mean Square Difference, which accounts for the mean values of both data series, and is also a measure of the model closeness to the observed data (not shown). Instead, a more elaborated skill score proposed by Taylor [25] was determined as a function of the correlation coefficient (R) and the normalized standard deviation (nSD) in the form $S = 4(1+R)/[(nSD+1/nSD)^2(1+R_0)]$ with $R_0 = \max(R)$, which is represented in Figure 2.6 by the S isolines. This definition allows guaranteeing that the skilfulness of the model increases when $nSD \to 1$, which is not assured by the centred pattern RMSE for lower values of R. Best model accuracy is achieved when skill score values tend to unity. In this way, the best performing model according to Figure 2.6 is the model proposed in this work, with a skill score higher than 0.80 for the majority of the stations and with nSD values in general higher than those of model 46. This conclusion is in agreement with the results presented in Figure 2.5, showing that the proposed model has best accuracy, using two distinct statistical analysis.

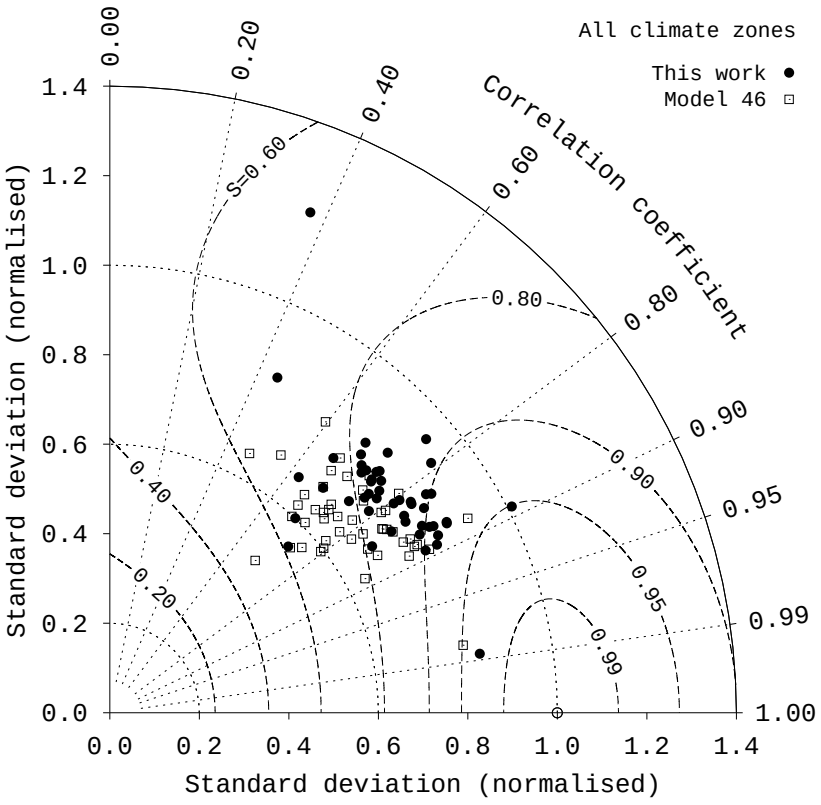

Fig. 2.6: Taylor diagram for the results of model 46 and the model developed in this work for all climate zones.

2.5 Conclusions

In this work is presented a newly developed model based on minute resolution data and climate zone classification. A review of the literature on models that use hourly and sub-hourly K_t values to compute K_d was carried out. An extensive statistical analysis of the proposed as well as of other 121 models found in the literature was performed, using one-minute resolution data. In this analysis, the elevation of the stations was not an essential factor when determining the parameters of the new model. The performance assessment was done using several statistical indicators and a Global Performance Index (GPI), which is a composite indicator that simplifies the analysis. The best performing model for the arid (AR) climate zone was found to be the model proposed by Abal et al. [67], while the best model for the high albedo (HA) climate zone is the model proposed by Mondol et al. [47]. The best model for the temperate (TM) and tropical (TR) climate zones is the model proposed in this work. It was also found that the best overall performing model (highest GPI in the more significant number of stations and highest skill score) was the model proposed in this work followed by the model by Mondol et al. [47]. This work helps to identify the best model that uses only the K_t according to the climate zone, thus allowing to easily estimate the diffuse horizontal irradiance (DHI) and consequently the direct normal irradiance (DNI), based only on global horizontal irradiance (GHI) measurements. The proposed model is also a tool for long-term data series quality control and gap-filling.

References

[1] N. A. Engerer. Minute resolution estimates of the diffuse fraction of global irradiance for southeastern Australia. *Solar Energy*, 116:215–237, 2015.

[2] T. O. Kaddoura, M. A. M. Ramli, and Y. A. Al-Turki. On the estimation of the optimum tilt angle of PV panel in Saudi Arabia. *Renewable and Sustainable Energy Reviews*, 65:626–634, 2016.

[3] H. Hottel and A. Whillier. Evaluation of flat-plate solar collector performance. *Trans. Conf. Use of Solar Energy*, 3 (Thermal Processes) Part 2, 1955.

[4] T. M. Klucher. Evaluation of models to predict insolation on tilted surfaces. *Solar Energy*, 23:111–114, 1979.

[5] J. E. Hay and J. A. Davies. Calculations of the solar radiation incident on an inclined surface. *Proceedings of First Canadian Solar Radiation Data Workshop*, 59–72, 1980.

[6] D. T. Reindl, W. A. Beckman, and J. A. Duffie. Diffuse fraction correlations. *Solar Energy*, 45(1):1–7, 1990.

[7] J. Polo, C. Fernández-Peruchena, and M. Gastón. Analysis on the long-term relationship between DNI and CSP yield production for different technologies. *Solar Energy*, 155:1121–1129, 2017.

[8] N. Bailek, K. Bouchouicha, Z. Al-Mostafa, M. El-Shimy, N. Aoun, A. Slimani, and S. Al-Shehri. A new empirical model for forecasting the diffuse solar radiation over Sahara in the Algerian Big South. *Renewable Energy*, 117:530–537, 2018.

[9] B. Y. Liu and R. C. Jordan. The interrelationship and characteristic distribution of direct, diffuse and total solar radiation. *Solar Energy*, 4(3):1–19, 1960.

[10] J. K. Page. The estimation of monthly mean values of daily total short wave radiation on vertical and inclined surfaces from sunshine records for latitudes 40N-40S. In *Proc. UN Conf. New Sources Energy*, volume 4, 378–387, 1964.

[11] S. E. Tuller. The relationship between diffuse, total and extra terrestrial solar radiation. *Solar Energy*, 18:259–263, 1976.

[12] S. A. Klein. Calculation of monthly average insolation on tilted surfaces. *Solar Energy*, 19:64–74, 1977.

[13] H. Khorasanizadeh, K. Mohammadi, and N. Goudarzi. Prediction of horizontal diffuse solar radiation using clearness index based empirical models; A case study. *International Journal of Hydrogen Energy*, 41(47):21888–21898, 2016.

[14] C. A. Gueymard and J. A. Ruiz-Arias. Extensive worldwide validation and climate sensitivity analysis of direct irradiance predictions from 1-min global irradiance. *Solar Energy*, 128:1–30, 2016.

[15] J. F. Orgill and K. G. T. Hollands. Correlation equation for hourly diffuse radiation on a horizontal surface. *Solar Energy*, 19(4):357–359, 1977.

[16] T. Muneer and S. Munawwar. Improved Accuracy Models For Hourly Diffuse Solar Radiation. *Journal of Solar Energy Engineering*, 128(1):104–117, 2006.

[17] F. Lanini. Division of global radiation into direct radiation and diffuse radiation. Master's thesis, Faculty of Science, University of Bern, Switzerland, 2010.

[18] R. Bruno. A correction procedure for separating direct and diffuse insolation on a horizontal surface. *Solar Energy*, 20(1):97–100, 1978.

[19] D. G. Erbs, S. A. Klein, and J. A. Duffie. Estimation of the diffuse radiation fraction for hourly, daily and monthly-average global radiation. *Solar Energy*, 28(4):293–302, 1982.

[20] M. N. Hawlader. Diffuse, global and extra-terrestrial solar radiation for Singapore. *International Journal of Ambient Energy*, 5(1):31–38, 1984.

[21] T. Muneer, M. M. Hawas, and K. Sahili. Correlation between hourly diffuse and global radiation for New Delhi. *Energy Conversion and Management*, 24 (4):265–267, 1984.

[22] C. Gueymard. Progress in Direct Irradiance modeling and validation. In *Solar 2010 Conf.*, Phoenix, 2010.

[23] B. Jamil and N. Akhtar. Comparative analysis of diffuse solar radiation models based on sky-clearness index and sunshine period for humid-subtropical climatic region of India: A case study. *Renewable and Sustainable Energy Reviews*, 78 (April):329–355, 2017.

[24] C. A. Gueymard. A review of validation methodologies and statistical performance indicators for modeled solar radiation data: Towards a better bankability of solar projects. *Renewable and Sustainable Energy Reviews*, 39:1024–1034, 2014.

[25] K. E. Taylor. Summarizing multiple aspects of model performance in a single diagram. *Journal of Geophysical Research*, 106(D7):7183–7192, 2001.

[26] J. Boland, L. Scott, and M. Luther. Modelling the diffuse fraction of global solar radiation on a horizontal surface. *Environmetrics*, 12:1003–116, 2001.

[27] J. A. Ruiz-Arias, H. Alsamamra, J. Tovar-Pescador, and D. Pozo-Vázquez. Proposal of a regressive model for the hourly diffuse solar radiation under all sky conditions. *Energy Conversion and Management*, 51(5):881–893, 2010.

[28] J. W. Spencer. A comparison of methods for estimating hourly diffuse solar radiation from global solar radiation. *Solar Energy*, 29(1):19–32, 1982.

[29] P. Ineichen, O. Guisan, and A. Razafindraibe. *Indice de clarté, Mesures d' ensoleillement à Genève*, volume 9. University of Geneva, Switzerland, 1984.

[30] H. Bakhsh, R. Srinivasan, and V. Bahel. Correlation between hourly diffuse and global radiation for Dhahran, Saudi Arabia. *Solar & Wind Technology*, 2:59–61, 1985.

[31] K. G. T. Hollands. A derivation of the diffuse fraction's dependence on the clearness index. *Solar Energy*, 35(2):131–136, 1985.

[32] M. Al-Riahi, N. Al-Hamdani, and K. Tahir. An empirical method for estimation of hourly diffuse fraction of global radiation. *Renewable Energy*, 2(4-5):451–456, 1992.

[33] B. Bourges. *Climatic data handbook for Europe*. Kluwer, Dordrecht, 1992.

[34] J. Chandrasekaran and S. Kumar. Hourly diffuse fraction correlation at a tropical location. *Solar Energy*, 53(6):505–510, 1994.

[35] M. A. Chendo and A. A. L. Maduekwe. Hourly global and diffuse radiation of Lagos, Nigeria - Correlation with some atmospheric parameters. 52(3):247–251, 1994.

[36] A. A. Maduekwe and M. A. Chendo. Atmospheric turbidity and the diffuse irradiance in Lagos, Nigeria. *Solar Energy*, 61(4):241–249, 1998.

[37] J. C. Lam and D. H. Li. Correlation between global solar radiation and its direct and diffuse components. *Building and Environment*, 31(6):527–535, 1996.

[38] M. I. Hijazin. The diffuse fraction of hourly solar radiation for Amman/Jordan. *Renewable Energy*, 13(2):249–253, 1998.

[39] J. A. González and J. Calbó. Influence of the global radiation variability on the hourly diffuse fraction correlations. *Solar Energy*, 65(2):119–131, 1999.

[40] A. De Miguel, J. Bilbao, R. Aguiar, H. Kambezidis, and E. Negro. Diffuse solar irradiation model evaluation in the North Mediterranean Belt area. *Solar energy*, 70(2):143–153, 2001.

[41] D. H. Li and J. C. Lam. Analysis of solar heat gain factors using sky clearness index and energy implications. *Energy Conversion and Management*, 42(5): 555–571, 2001.

[42] A. P. Oliveira, J. F. Escobedo, A. J. Machado, and J. Soares. Correlation models of diffuse solar-radiation applied to the city of São Paulo, Brazil. *Applied Energy*, 71(1):59–73, 2002.

[43] K. Ulgen and A. Hepbasli. Prediction of Solar Radiation Parameters Through Clearness Index for Izmir, Turkey. 24(8):773–785, 2002.

[44] S. Karatasou, M. Santamouri, and V. Geros. Analysis of experimental data on diffuse solar radiation in Athens, Greece, for building applications. *International Journal of Sustainable Energy*, 23(1-2):1–11, 2003.

[45] M. Tsubo and S. Walker. Relationships between photosynthetically active radiation and clearness index at Bloemfontein, South Africa. *Theoretical and Applied Climatology*, 80(1):17–25, 2005.

[46] J. Soares, A. P. Oliveira, M. Z. Božnar, P. Mlakar, J. F. Escobedo, and A. J. Machado. Modeling hourly diffuse solar-radiation in the city of São Paulo using a neural-network technique. *Applied Energy*, 79(2):201–214, 2004.

[47] J. D. Mondol, Y. G. Yohanis, M. Smyth, and B. Norton. Long-term validated simulation of a building integrated photovoltaic system. *Solar Energy*, 78(2): 163–176, 2005.

[48] C. P. Jacovides, F. S. Tymvios, V. D. Assimakopoulos, and N. A. Kaltsounides. Comparative study of various correlations in estimating hourly diffuse fraction of global solar radiation. *Renewable Energy*, 31(15):2492–2504, 2006.

[49] H. K. Elminir, Y. A. Azzam, and F. I. Younes. Prediction of hourly and daily diffuse fraction using neural network, as compared to linear regression models. *Energy*, 32(8):1513–1523, 2007.

[50] J. Boland, B. Ridley, and B. Brown. Models of diffuse solar fraction. *Renewable Energy*, 33:575–584, 2008.

[51] J. Boland and B. Ridley. Models of diffuse solar fraction. In *Modeling Solar Radiation at the Earth's Surface: Recent Advances*, 193–219. Springer, Berlin, 2008.

[52] C. Furlan and A. P. Oliveira. Hourly diffuse solar radiation in the presence of clouds and other environmental parameters: the city of São Paulo. *University of Padua, Italy*, 2008.

[53] J. D. Mondol, Y. G. Yohanis, and B. Norton. Solar radiation modelling for the simulation of photovoltaic systems. *Renewable Energy*, 33(5):1109–1120, 2008.

[54] S. Moreno and M. Silva. Comparison of methodologies to estimate direct normal irradiation from daily values of global horizontal irradiation. *SolarPaces Conference*, 2009.

[55] Í. Pagola, M. Gastón, C. M. Fernández-Peruchena, J. L. Torres, M. Silva, and L. Ramírez. Comparison and fitting of several Global-to-beam irradiance models in Spain. In *15th SolarPACES Conference*, 11724, Berlin, 2009.

[56] R. Posadillo and R. López Luque. Hourly distributions of the diffuse fraction of global solar irradiation in Córdoba (Spain). *Energy Conversion and Management*, 50(2):223–231, 2009.

[57] S. Janjai, P. Phaprom, R. Wattan, and I. Masiri. Statistical models for estimating hourly diffuse solar radiation in different regions of Thailand. *Proceedings of the International Conference on Energy and Sustainable Development: Issues and Strategies (ESD 2010)*, (Esd):1–6, 2010.

[58] J. L. Torres, M. De Blas, A. García, and A. de Francisco. Comparative study of various models in estimating hourly diffuse solar irradiance. *Renewable Energy*, 35(6):1325–1332, 2010.

[59] M. Chikh, A. Mahrane, and M. Haddadi. Modeling the diffuse part of the global solar radiation in Algeria. *Energy Procedia*, 18:1068–1075, 2012.

[60] G. Sánchez, M. L. Cancillo, and A. Serrano. Adapting the Spencer model for diffuse solar radiation in Badajoz. *Optica Pura y Aplicada*, 45(1):5–9, 2012.

[61] K. Lee, H. Yoo, and G. J. Levermore. Quality control and estimation hourly solar irradiation on inclined surfaces in South Korea. *Renewable Energy*, 57: 190–199, 2013.

[62] W. Yao, Z. Li, Y. Lu, F. Jiang, and C. Li. New models for separating hourly diffuse and direct components of global solar radiation. *Lecture Notes in Electrical Engineering*, 261(VOL. 1):653–663, 2014.

[63] R. Tapakis, S. Michaelides, and A. G. Charalambides. Computations of diffuse fraction of global irradiance: Part 2 – Neural Networks. *Solar Energy*, 139: 723–732, 2016.

[64] E. F. M. Abreu, P. Canhoto, and M. J. Costa. Contribution to the diffuse radiation modeling in Évora, Portugal. In *Workshop on Earth Sciences*, Évora, 2016.

[65] E. P. Marques Filho, A. P. Oliveira, W. A. Vita, F. L. Mesquita, G. Codato, J. F. Escobedo, M. Cassol, and J. R. A. França. Global, diffuse and direct solar radiation at the surface in the city of Rio de Janeiro: Observational characterization and empirical modeling. *Renewable Energy*, 91:64–74, 2016.

[66] E. Paulescu and R. Blaga. Regression models for hourly diffuse solar radiation. *Solar Energy*, 125:111–124, 2016.

[67] G. Abal, D. Aicardi, R. Alonso Suárez, and A. Laguarda. Performance of empirical models for diffuse fraction in Uruguay. *Solar Energy*, 141:166–181, 2017.

[68] H. M. T. Al-Najjar and A. A. A. Al-Khazzar. Experimental Prediction of Hourly Diffuse Solar Radiation with Clearness Index in Baghdad (Iraq). *International Journal of Computer Applications*, 158(7):20–28, 2017.

[69] A. Ohmura, E. G. Dutton, B. Forgan, C. Fröhlich, H. Gilgen, H. Hegner, A. Heimo, G. König-Langlo, B. McArthur, G. Müller, R. Philipona, R. Pinker, C. H. Whitlock, K. Dehne, and M. Wild. Baseline Surface Radiation Network (BSRN/WCRP): New Precision Radiometry for Climate Research. *Bulletin of the American Meteorological Society*, 79(10):2115–2136, 1998.

[70] S. W. Churchill and R. Usagi. A general expression for the correlation of rates of transfer and other phenomena. *AIChE Journal*, 18(6):1121–1128, 1972.

[71] P. Canhoto and A. H. Reis. *Heat transfer in the thermal entry region of singly-connected tubes with uniform wall temperature*, 231–240. Jornadas de Física por ocasião da Jubilação do Professor Rui Namorado Rosa, 2010.

[72] P. Canhoto and A. H. Reis. Optimization of forced convection heat sinks with pumping power requirements. *International Journal of Heat and Mass Transfer*, 54:1441–1447, 2011.

[73] P. Canhoto and A. H. Reis. Optimization of fluid flow and internal geometric structure of volumes cooled by forced convection in an array of parallel tubes. *International Journal of Heat and Mass Transfer*, 54:1441–1447, 2011.

[74] A. Driemel, J. Augustine, K. Behrens, S. Colle, C. Cox, E. Cuevas-Agulló, F. M. Denn, T. Duprat, M. Fukuda, H. Grobe, M. Haeffelin, G. Hodges, N. Hyett, O. Ijima, A. Kallis, W. Knap, V. Kustov, C. N. Long, D. Longenecker, A. Lupi, M. Maturilli, M. Mimouni, L. Ntsangwane, H. Ogihara, X. Olano, M. Olefs, M. Omori, L. Passamani, E. B. Pereira, H. Schmithüsen, S. Schumacher, R. Sieger, J. Tamlyn, R. Vogt, L. Vuilleumier, X. Xia, A. Ohmura, and G. König-Langlo. Baseline surface radiation network (bsrn): structure and data description (1992–2017). *Earth System Science Data*, 10:1491–1501, 2018.

[75] *Guide to Meteorological Instruments and Methods of Observation*, volume WMO - No. 8. World Meteorological Organization (WMO), 2017.

[76] C. Long and Y. Shi. The QCRad Value Added Product: Surface Radiation Measurement Quality Control Testing, Including Climatology Configurable Limits. 2006.

[77] C. A. Gueymard. Revised composite extraterrestrial spectrum based on recent solar irradiance observations. *Solar Energy*, 169:434–440, 2018.

[78] I. Reda and A. Andreas. Solar position algorithm for solar radiation applications. *Solar Energy*, 76(5):577–589, 2004.

[79] O. Behar, A. Khellaf, and K. Mohammedi. Comparison of solar radiation modelsand their validation under algerian climate - the case of direct irradiance. *Energy Conversion and Management*, 98:236–251, 2012.

[80] M. Despotovic, V. Nedic, D. Despotovic, and S. Cvetanovic. Review and statistical analysis of different global solar radiation sunshine models. *Renewable and Sustainable Energy Reviews*, 52:1869–1880, 2015.

[81] B. Jamil and N. Akhtar. Comparison of empirical models to estimate monthly mean diffuse solar radiation from measured data: Case study for humid-subtropical climatic region of India. *Renewable and Sustainable Energy Reviews*, 77(December 2016):1326–1342, 2017.

Nomenclature

A	model parameter
B	model parameter
E_{oh}	extraterrestrial irradiance on a horizontal surface (W/m^2)
erMAX	maximum absolute relative error
GPI	Global Performance Index
G_s	Solar constant (W/m^2)
H	minutely diffuse horizontal irradiance
K_d	diffuse fraction
K_t	clearness index
MAE	mean absolute error
MARE	mean absolute relative error
MBE	mean bias error
MPE	mean percentage error
n	model parameter
N	number of observations

nSD	normalized standard deviation
R	correlation coefficient
RMSE	root mean square error
RRMSE	relative root mean square error
S	skill score
TSTAT	*t-statistics*
U95	uncertainty at 95%
y	scaled value of a statistical indicator
$\bar{y}$	median of scaled values of a statistical indicator

Greek symbols

α	part of GPI equation (= 1 or -1)

Subscripts

avg	average
e	estimated
i	measurement / model
j	statistical indicator
m	measured

Acronyms

AR	arid climate zone
BSRN	Baseline Surface Radiation Network
CSP	Concentrating Solar Power
DHI	Diffuse Horizontal Irradiance
DNI	Direct Normal Irradiance
GHI	Global Horizontal Irradiance
HA	high albedo climate zone
IES	Institute of Earth Sciences
MAE	mean absolute error
MARE	mean absolute relative error

MBE	mean bias error
MPE	mean percentage error
nSD	normalized standard deviation
PV	photovoltaics
R	correlation coefficient
RMSE	root mean square error
RRMSE	relative root mean square error
TM	temperate climate zone
TR	tropical climate zone
TSTAT	*t-statistics*
U95	uncertainty at 95%

Chapter 3

Performance assessment of clear-sky solar irradiance predictions using state-of-the-art radiation models and input atmospheric data from reanalysis or ground measurements[†]

Abstract

In this work, the performance of clear-sky direct normal irradiance (DNI) and global horizontal irradiance (GHI) predictions generated with three state-of-the-art solar radiation models with different degrees of complexity is assessed by comparison with high-quality measured irradiance data at Évora, Portugal. The libRadtran, SMARTS, and REST2 radiation models are alternatively operated using input data from three different data sources: co-located AERONET ground-based measurements, and CAMS and MERRA-2 gridded reanalysis data. For these nine combinations (three models and three data sources), the results are assessed using five statistical indicators, namely mean bias error (MBE), root mean square error (RMSE), fractional bias (FB), fractional gross error (FGE), and coefficient of determination (R^2). Overall, it is found that AERONET is the data source that provides the best DNI estimates. In general, libRadtran and SMARTS produced closer estimates to the ground-based DNI observations. For GHI, however, no firm conclusion can be drawn regarding the best data source. MERRA-2 produces better estimates in combination with libRadtran and SMARTS according to all statistical indicators except R^2, whereas AERONET is to be preferred according to FB, FGE, and R^2 when using REST2.

[†]Edgar F.M. Abreu[(1)], Christian A. Gueymard[(2)], Paulo Canhoto[(1,3)], and Maria J. Costa[(1,4,5)]. Performance assessment of clear-sky solar irradiance predictions using state-of-the-art radiation models and input atmospheric data from reanalysis or ground measurements. *Solar Energy*, 252:309-321, 2023.

[(1)] Institute of Earth Sciences, University of Évora.

[(2)] Solar Consulting Services, Colebrook, NH 03576, USA

[(3)] Mechatronic Engineering Department, School of Sciences and Technology, University of Évora.

[(4)] Physics Department, School of Sciences and Technology, University of Évora.

[(5)] Earth Remote Sensing Laboratory – EaRSLab, University of Évora.

Curiously, the latter generates better GHI estimates despite being the simplest model. Overall, it is concluded that the best combinations of model/data source to estimate DNI are either libRadtran/MERRA-2 (according to MBE and FB) and SMARTS/AERONET (according to RMSE, FGE, and R^2). In the case of GHI, the best combinations are REST2/AERONET (according to FB, FGE, and R^2) and REST2/MERRA-2 (according to MBE and RMSE).

Keywords: Solar Energy; Solar radiation; DNI; Ground-based measurements; Reanalysis data; Solar radiation models.

3.1 Introduction

The successful development of solar energy projects is strongly related to the reliability of their solar resource assessment since it has a direct impact on the design, simulation, financing, and performance evaluation of such systems [1]. The most reliable solar radiation data source are still ground-based radiometric measurements [2], with the caveat that the installation and maintenance of radiometric stations are highly demanding [3] and high-quality ground-based measurements are thus not available at most potential locations of interest. In general, therefore, resource assessment analyses must be primarily conducted using modelled (as opposed to measured) data. Recent studies indeed suggest that ground-based measurements can be complemented or replaced by gridded products from satellite data or reanalysis of Numerical Weather Prediction (NWP) model outputs [4, 5]. Reanalyses have the advantage of being available globally, even at high latitudes, and for longer periods than satellite-derived irradiance estimates. Several studies exist on the accuracy of such irradiance databases relatively to reference ground-based measurements [5, 6, 7, 8, 9]. Nevertheless, Yang and Bright Yang and Bright [5] concluded that, regarding surface solar irradiance estimates, satellite-derived products are better than reanalysis products under squared loss. This adds to the generally accepted conclusion that the former's performance is still superior to the latter's; e.g., [2, 10, 11]. This situation is apparently related to the fact that reanalysis models are focused on the global atmospheric circulation, but have difficulty with the proper modeling of cloud-radiation interactions at high spatio-temporal resolution. Moreover, reanalyses are focused on the assimilation of vast quantities of meteorological observations to initialize the NWP algorithms [12], rather than on solar energy applications. To provide an alternative and reliable approach for solar resource assessments, a potentially interesting avenue would consist in combining reanalysis datasets with state-of-the-art solar radiation modelling, using advanced site adaptation procedures [13].

Reanalysis data sets such as ERA5 [13], the Modern-Era Retrospective analysis for Research and Applications, Version 2 (MERRA-2) [14, 15, 16], or the Copernicus

Atmosphere Monitoring Service (CAMS) [17, 18, 19, 20] offer important atmospheric variables for solar applications, such as temperature, atmospheric pressure, and relative humidity at the surface, or columnar estimates of atmospheric constituents such as aerosols, water vapour, or ozone. Such atmospheric information is central to the present investigation. Some of these reanalyses also provide surface solar irradiance predictions.

Under clear-sky conditions, the main atmospheric variables that affect the surface irradiance are the aerosol optical depth (AOD) and precipitable water vapour (PWV) [21, 22, 23]. In solar applications, two irradiance components are of paramount importance: Global Horizontal Irradiance (GHI) and Direct Normal Irradiance (DNI). GHI is essential to evaluate the maximum solar potential as well as the limits of energy generation from photovoltaic or solar thermal systems [23]. In parallel, DNI (which is normally the main part of GHI, at least under cloudless or partly cloudy conditions) constitutes the solar resource for concentrating technologies, and is also necessary to evaluate the total irradiance incident on tilted surfaces. DNI is primarily affected by the total scattering effect, hence ultimately AOD [21, 24, 25]. Therefore, to obtain accurate predictions of DNI (and, consequently, GHI) based on reanalysis-derived atmospheric inputs, it is critical to assess the accuracy of such gridded AOD information against ground-based reference measurements. The latter are typically provided by AERONET, a remote-sensing aerosol network created by NASA and PHOTONS [26]. The AERONET sunphotometers provide aerosol and water vapor data at hundreds of sites worldwide and at relatively high temporal resolution. This extensive database is often used in studies covering many fields, such as solar energy, atmospheric physics, meteorology, climate, or water resource assessment [19, 27, 28, 29, 30, 31, 32, 33]. In particular, Gueymard and Yang [28] evaluated the CAMS and MERRA-2 AOD data against the "ground truth" from 793 AERONET stations scattered worldwide. They found that, in general, CAMS and MERRA-2 perform relatively similarly, and that these data sets offer significant advantages over satellite observations because of the absence of gaps over space or time, their global coverage, and their data availability extending over longer periods.

Considering these advantages, reanalysis-based aerosol data products have been used in various studies related to solar energy. For example, Ruiz-Arias et al. [34] analysed the impact of the accuracy of aerosol datasets, namely from MERRA-2 and MACC (the precursor of CAMS), on the modelling of DNI under clear-sky conditions at four arid locations. Two experiments were carried out: one using AERONET aerosol data and the other using MERRA-2 or MACC data as input to the SMARTS radiation model. They found that the bias and random errors in the modelled DNI increase by a maximum factor of six when MERRA-2 or MACC AOD values are used in lieu of AERONET reference data. The need for an efficient cloud-screening

procedure was also highlighted in their study. Similar results were demonstrated in other studies at Tamanrasset, Algeria [35], and Shagaya, Kuwait [36]. Psiloglou et al. [37] studied the performance of the Meteorological Radiation Model [38], when using either satellite-based or PVGIS-ERA5 reanalysis atmospheric data. They found good agreement under clear-sky conditions between the modelled data and ground-based irradiance measurements at Athens, Greece. Carra et al. [27] studied the atmospheric extinction coefficient that characterizes the atmospheric extinction in DNI between the heliostats and central receiver of concentrating solar power plants with a tower design. Their results showed good agreement on average when using either AERONET or MERRA-2 aerosol data, considering the uncertainty of the measuring system, even though the MERRA-2 AOD showed variance compared to AERONET's.

When modelling DNI under clear-sky conditions, the literature reviewed above demonstrates that a major source of uncertainty is related to the composition of the atmosphere [34]. Stated differently, some propagation of errors exists between the atmospheric inputs and the modelled irradiances. That is why, normally, the validation of clear-sky radiation models is preferably done using observed atmospheric data from, e.g., AERONET [25, 39, 40], even though that can only be done at stations having radiometers collocated with a sunphotometer — a relatively rare situation. Hence, validation studies dealing with a large number of world stations need to use reanalysis atmospheric data, which introduces uncertainty [41, 42, 43]. In general, it is therefore difficult to separate the errors caused by the radiation model itself from those caused by the input errors. This difficulty is the reason why the uncertainty in modeled irradiance data — as opposed to that of measured data — cannot be established precisely, as discussed further in Chapter 7 of [2].

To clarify this situation, it appears important to evaluate the performance of different atmospheric data sets when used to provide key inputs to high-performance radiation models, and to evaluate how such models behave vis-à-vis the error propagation issue. This provides the justification for the present investigation, where both DNI and GHI are modelled using reanalysis data from MERRA-2 and CAMS for comparative purposes. Additionally, the AERONET ground truth is also used to validate the reanalysis-based modelled solar irradiance estimates.

To investigate the relative impacts of error propagation, three state-of-the-art and high-performance models with different approaches and complexities (both in model formulation and execution) are used: the libRadtran radiative transfer model [44, 45], the Simple Model of the Atmospheric Radiative Transfer of Sunshine (SMARTS) [46, 47], and the Reference Evaluation of Solar Transmittance, 2 bands (REST2) model [48], in decreasing order of sophistication. To predict the surface irradiance, libRadtran uses rigorous methods to solve the equation of radiative transfer spectrally

and at multiple atmospheric levels. This approach is extremely time consuming, hence the model might require a supercomputer if a large number of situations is to be simulated. This explains why that model is normally more appropriate in the field of atmospheric sciences than in solar engineering. In the present context, however, it is very useful because it represents the ultimate reference in terms of modelling accuracy. In contrast, SMARTS also provides spectral irradiance outputs, but its solver is highly parametrized, which makes it fast enough for many solar applications requiring spectral information. Finally, REST2 is a two-band model that has been derived from parametrizations of SMARTS results. It is very fast and widely used in solar applications that require consistently good broadband irradiance estimates with no spectral detail. The three models have apparently never been inter-compared directly, which adds novelty here.

To guarantee a fair comparison, the assessment of clear-sky models is usually done considering only a single source of input data for all models. However, the validation results (e.g., model ranking) are somewhat dependent on the accuracy of this data source at each site, which makes these results specific to the input data source. Hence, selecting a different source of input data would likely lead to a different model ranking. For that reason, there are two different views on selecting the ideal input data source. For some studies (e.g.: [40, 25]), the important criterion is to use the input data with the least uncertainty (typically AERONET) as a way to make sure that the prediction error is almost entirely attributable to the model itself — inasmuch as the irradiance measurements are consistently unbiased, which is typically assumed but might not always be the case in practice. The downside of that approach is that it is possible at only a few stations in the world where a radiometric station is collocated with a sunphotometric station, which limits the geographical representativeness of the results. The other option is to use reanalysis data whenever the goal is to (i) evaluate models at a large number of sites, such as in Sun et al. [43, 49], (ii) intercompare models globally without explicit ranking [50], or (iii) analyse the irradiance's small-scale spatial variability [51]. This other option does increase spatial representativeness, but at the expense of prediction accuracy. That occurs because the irradiance predictions are then not only affected by the intrinsic model performance but also by error propagation from the uncertain inputs. A novelty in the present study is that this contradiction is addressed by using both approaches. This is possible because the measurements from the research-class radiometric station of Évora, Portugal [24, 52] are used in combination with the quality-controlled observations from the collocated AERONET station, thus providing reference performance results against which the reanalysis-based results can be assessed.

The three radiative models under scrutiny are alternatively operated with the

three sources of atmospheric data described above, thus resulting in a total of nine modelled datasets of both DNI and GHI, whose performance is evaluated here using various statistical metrics. These datasets and their performance assessment are then used to address the main goals of this study, which are: (i) to assess whether reanalysis-based atmospheric data are conducive to accurate solar irradiance predictions under clear skies; and (ii) to assess the impact of atmospheric data uncertainty on solar irradiance predictions under clear skies, using several solar radiation models with different levels of complexity and spectral detail. Additionally, this study also aims to (i) provide a comparison between ground-observed and reanalysis-modelled atmospheric information, such as aerosol optical depth and precipitable water vapour; (ii) assess the performance of several solar radiation models with different degrees of complexity when using various sources of input data; and (iii) determine which combination of data source and model provides the most accurate DNI and GHI estimates under clear skies.

This paper is organized as follows: Section 5.2 describes the data used and the quality control procedure. Section 5.3 presents algorithmic details on how the three models evaluate both DNI and GHI. Section 5.4 discusses the results and puts them in context. Conclusions are finally drawn in Section 5.5.

3.2 Data sources and quality control

3.2.1 AERONET data

The AErosol RObotic NETwork (AERONET) project consists of a ground-based network of stations that provide continuous and free-access to data of aerosol optical, microphysical, and radiative properties. It was set up by the National Aeronautics and Space Administration (NASA) and the PHOtométrie pour le Traitement Opérationnel de Normalisation Satellitaire (PHOTONS). In this work, the following retrievals are used at Level 2.0 from Version 3.0 of the retrieval algorithm [53]: AOD at multiple wavelengths, and PWV. The ozone total column concentration data are interpolated from a climatology obtained by NASA's Total Ozone Mapping Spectrometer (TOMS). The AERONET AOD's four main wavelengths (440, 500, 675 and 870 nm) are used here to determine the Ångström's exponent, α, through a linear fit after linearisation of Ångström's law [54]:

$$\tau_\lambda = \tau_{\lambda_0} \left(\frac{\lambda}{\lambda_0} \right)^{-\alpha}, \tag{3.1a}$$

hence

$$\ln(\tau_\lambda) = \ln(\tau_{\lambda_0}) - \alpha \ln \left(\frac{\lambda}{\lambda_0} \right), \tag{3.1b}$$

where τ_λ is AOD at wavelength λ (in nm) and τ_{λ_0} is the AOD at the reference wavelength λ_0 (λ_0=1000 nm). Since the Ångström turbidity coefficient (τ_{λ_0}, often

represented as β) is not known, both α and τ_{λ_0} can be determined through the fitting of Eq. 3.1 to the data. This linear fitting process is how AERONET's retrieval algorithm derives α. In the current literature, however, the Ångström turbidity coefficient has been relegated as a legacy measure of atmospheric turbidity and is just ignored in practice, whereas the AOD at 550 nm, τ_{550}, has now become the reference turbidity quantity in most databases, such as MERRA-2. This quantity, which is not directly observed by AERONET, is obtained here by fitting the spectral data to a modified version of Eq. 3.1b:

$$\ln(\tau_\lambda) = \ln(\tau_{550}) - \alpha \ln\left(\frac{\lambda}{550}\right). \tag{3.1c}$$

It is emphasized that τ_{550} is required to allow a fair comparison between data sources and radiation models since it can be obtained from all the data sources considered here (AERONET, CAMS, and MERRA-2), and is also a key input to libRadtran, SMARTS, and REST2.

Although high-quality AERONET data are used here, it is known that Level-2.0 data can still contain anomalous values [36]. Furthermore, soiling of the sunphotometer optics or other issues can affect the AOD retrieval and increase the AOD uncertainty. For these reasons, only those values that comply with the following criteria are kept in the present study: $0 < \tau_{550} < 5$ and, $-0.25 \leq \alpha \leq 2.5$. In addition, it is known that the evaluation of α through Eq. 3.1b is sensitive to the number of available wavelengths, and that its uncertainty increases when that number decreases [36]. Hence, records that had one or more AOD missing in the 440–870 nm range are filtered out.

3.2.2 CAMS data

The CAMS reanalysis data covers the period 2003-2018 with a three-hourly temporal resolution and a spatial resolution of $0.5\times0.5°$. This dataset of atmospheric composition is generated by the Copernicus Atmosphere Monitoring Service (CAMS) and can be retrieved through the ECMWF Web API. Although surface level data are used here, atmospheric data are available for several pressure and potential temperature levels as well as at one potential vorticity level. CAMS assimilate data from the Moderate Resolution Imaging Spectroradiometer (MODIS) and the Advanced Along-Track Scanning Radiometer (AATSR). The CAMS variables used in this work are: AOD, ozone total column concentration, precipitable water vapour, surface pressure, and surface albedo for both the visible and near infrared. These variables are interpolated to 1-minute resolution using a piecewise cubic Hermite interpolating polynomial. Similar to the procedure performed to AERONET data, the α and τ_{λ_0} values are obtained through a linear fit (Eq. 3.1) to the AOD values provided natively by CAMS at 469, 550, 670, and 865 nm.

3.2.3 MERRA-2 data

The MERRA-2 reanalysis provides a large volume of atmospheric information that spans many decades, starting in 1980. Data can be retrieved using NASA's Goddard Earth Sciences Data and Information Services Center (GES DISC) with an hourly temporal resolution and a spatial resolution of 0.5×0.625°. MERRA-2 assimilates data from MODIS, the Multi-angle Imaging SpectroRadiometer (MISR), the Advanced Very High-Resolution Radiometer (AVHRR), and AERONET. The variables used in this work are: AOD (for both total extinction and its scattering part), Ångström exponent, ozone total column, precipitable water vapour, surface pressure, and surface albedo for both the visible and near infrared spectral ranges. The same interpolation process used in the case of CAMS data is also applied to MERRA-2 data to generate a dataset with a 1-minute resolution. The aerosol single-scattering albedo (an input variable required by all radiation models under scrutiny here) is simply obtained as the ratio between the pure-scattering AOD and the total-extinction AOD.

3.2.4 Solar radiation data

The ground-based DNI, diffuse irradiance (DIF), and GHI data used in this work are measured at the radiometric station of the Institute of Earth Sciences (IES), University of Évora, Portugal (Lat. 38.568°, Lon. -7.912°, Elev. 293 m). The solar irradiance observations used here are from the period 2015-2018 and follow the detailed Baseline Surface Radiation Network (BSRN) protocol [24, 52]. DNI is measured with a Kipp & Zonen CHP1 pyrheliometer, whereas both GHI and DIF are measured with CM6B pyranometers. All sensors are installed on a Solys2 sun tracker from Kipp & Zonen, which also supports the tracking shade for the diffuse measurements. Additionally, the net infrared radiation is measured with a shaded Eppley PIR pyrgeometer, installed also on the sun tracker just beside the pyranometers. The sensors are properly maintained and calibrated, and their outputs are sampled every second. The mean, maximum, minimum, and standard deviation values are recorded every minute.

Regarding sensor calibration, four calibration procedures have been carried out during the period 2010-2021 in the case of the diffuse pyranometer and five calibration procedures in the period 2014-2022 in the case of the pyrheliometer. The transition between responsivity values is obtained here through a linear interpolation instead of the standard approach of just replacing the old responsivity value by the new value after each calibration procedure (see Appendix 5.6).

The BSRN quality check filters [55] are used in the data quality control procedure. These filters account for physically possible and extremely rare limits, and also for the ratios between the different solar radiation components. Additionally, measurements

that do not meet the following requirements are filtered out [56]:

$$Z < 85^{\circ}$$

$$\mathrm{DNI} < 1100 + 0.03\mathrm{Elev}$$

$$Abs(\mathrm{Closr}) < 5\%$$

where Elev is the elevation of the station in meters, Z is the solar zenith angle, and Closr is the closure equation error in percent ($\mathrm{Closr} = 100[(\mathrm{DNI}\cos(Z) + \mathrm{DIF} - \mathrm{GHI})/\mathrm{GHI}]$). The solar zenith angle filter is meant to eliminate measurements with low solar irradiance and avoid the perturbations of the horizon line, which are more prone to both experimental and modelling errors [56]. Additionally, consecutive 1-minute DNI measurements with a difference higher than 5 W/m^2 are removed to account for random errors in the clear-sky detection procedure (see Section 3.2.5).

Finally, the expanded uncertainty in both DNI and DIF measurements is determined using the International Guidelines of Uncertainty in Measurement (GUM), following [57]. This procedure relies on the measurement equation of the solar radiation component being measured, and also accounts for the standard uncertainties in instrument responsivity and in the data acquisition system. The procedure additionally accounts for the longwave radiation transfer between the pyranometers and the sky and its resulting effect on the zero offset of the instruments, as described in [57]; see Appendix 5.6. Any DNI or DIF observation with an expanded uncertainty higher than 2.5% and 5%, respectively, is filtered out. Finally, the GHI data used in the following sections is actually calculated from the filtered DNI and DIF measurements to decrease its uncertainty, per the best practices [2, 58], i.e., $\mathrm{GHI} = \mathrm{DNI}\cos(Z) + \mathrm{DIF}$.

3.2.5 Clear-sky detection and data synchronization

Although AERONET data Level 2.0 are cloud screened, some situations can occur where a clear line of sight to the sun might not exist, namely during the passage of thin and homogeneous cirrus clouds. Such situations are infrequent but cannot be easily detected by the AERONET cloud-screening process [53]. Similarly, the pyrheliometer might be obscured by a cloud just before or after the AERONET measurement [34], all the more that the aperture half-angle (2.5°) of the pyrheliometer is much larger than that of the sunphotometer (0.63°). Additionally, a clear line of sight to the sun is not sufficient here because truly cloudless situations are needed to validate the model predictions of clear-sky GHI. To account for these requirements, the state-of-the-art Bright-Sun clear-sky detection method [59] is used, based on the Matlab (MathWorks, Natick, MA) code provided by the method's authors [60]. This detection method addresses the issues pointed by Gueymard et al. [61] and others, who concluded that the performance of radiation models was not the same

for distinct atmospheric conditions. The Bright-Sun model adopts and efficiently adapts the best features from several methods available in the literature, and can thus be considered the current state of the art. In the present implementation, the theoretical clear-sky GHI and DIF data needed as input to the Bright-Sun model are determined with the MAC2 model [43, 62], available from Bright [60].

The necessary synchronization between the AERONET atmospheric data and the ground-based solar radiation data is obtained by considering that each AERONET data point is representative of the atmospheric conditions during the solar radiation measurements within a period of ±1 minute centred on the AERONET timestamp. In this way, two consecutive 1-minute solar radiation measurements are normally associated to a single AERONET timestamp. After this, the CAMS and MERRA-2 data are synchronized with the solar radiation data, using the temporal interpolation procedure described in Sections 3.2.2 and 3.2.3, respectively. Although AERONET and reanalysis data are available before 2015, there are no adequate solar radiation measurements at the location of interest before that date.

3.2.6 Comparison between ground-based and reanalysis atmospheric data

In this section, the τ_{550}, α, and PWV values from CAMS and MERRA-2 are compared with the corresponding AERONET data. Fig. 3.1 shows such a comparison for τ_{550}. Taking AERONET as the reference, the performance of the reanalysis data is assessed using the mean bias error, MBE, the root-mean square error, RMSE, and the determination coefficient, R^2.

$$\mathrm{MBE} = \frac{1}{n}\sum_{i=1}^{n}(pi - oi), \tag{3.2}$$

$$\mathrm{RMSE} = \sqrt{\left[\frac{1}{n}\sum_{i=1}^{n}(pi - o_i)^2\right.} \tag{3.3}$$

$$R^2 = 1 - \frac{\sum_{i=1}^{n}(o_i - p_i)^2}{\sum_{i=1}^{n}(o_i - \overline{o})^2} \tag{3.4}$$

where p_i are the model predictions, o_i are the corresponding observations, $\overline{o}$ is the mean value of the observations, and $i = 1, \ldots, n$, where n is the total number of data points.

Both CAMS and MERRA-2 agree moderately well with AERONET's τ_{550}, with R^2 values of 0.7085 and 0.7469, respectively. In particular, the MERRA-2 estimates appear more appropriate than those of CAMS under very clear conditions (AOD < 0.1), which are the most frequent at Évora, and correspond to the highest possible DNI situations.

In the case of α, conversely, Fig. 3.2 indicates that the two reanalysis databases agree much less with AERONET. In particular, a somewhat better performance is

obtained by CAMS (R^2=0.3520) in comparison with MERRA-2 (R^2=0.1982). These suboptimal results tend to corroborate those from earlier validation studies (e.g.: Gueymard and Yang [28]).

Regarding PWV, Fig. 3.3 clearly indicates that both reanalysis datasets are slightly positively biased relatively to AERONET. MERRA-2 (MBE = 12.98%) has a lower bias than CAMS (MBE = 16.86%). By comparison with Figs. 3.1 and 3.2, however, it is obvious that, for both reanalyses, PWV is much better correlated than AOD with the ground measurements. A positive bias is also observed when comparing AERONET data to local Global Navigation Satellite System (GNSS) PWV measurements (MBE = 5.61%). This positive bias is in accordance with other studies found in the literature (e.g.: Pérez-Ramírez et al. [63]). Hence, PWV from both MERRA-2 and CAMS is too high (18.6-22.5%) compared to the reference GNSS observations.

Since both τ_{550} and PWV - and less critically α — do affect DNI much more strongly than GHI [21], it can be expected that the errors observed in the reanalysis-derived input variables ultimately impact the modelled DNI relatively to its reference determination using "ground truth" AERONET data. This expectation stems, in particular, from the results in Gueymard [36], although those were obtained for a station in a widely different climate.

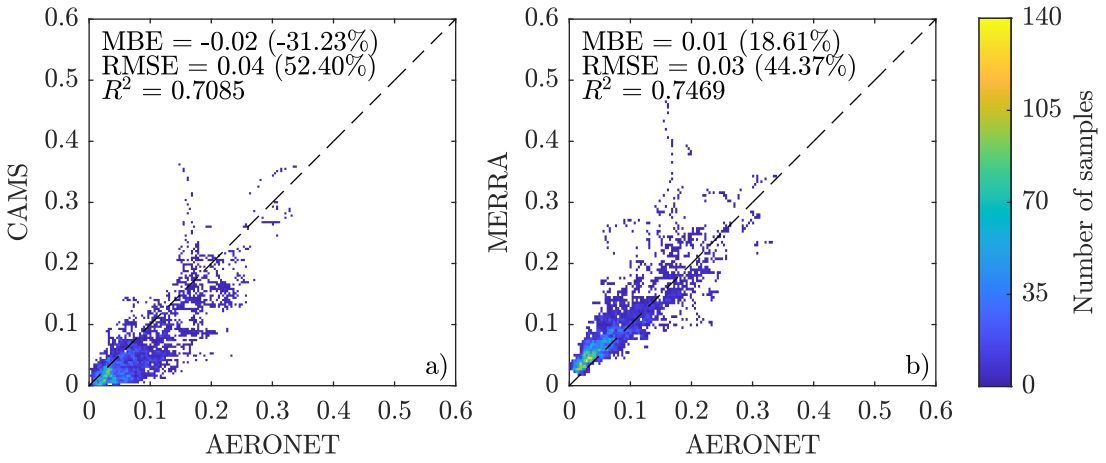

Fig. 3.1: Comparison of τ_{550} values between reanalysis datasets and AERONET: a) CAMS and b) MERRA-2.

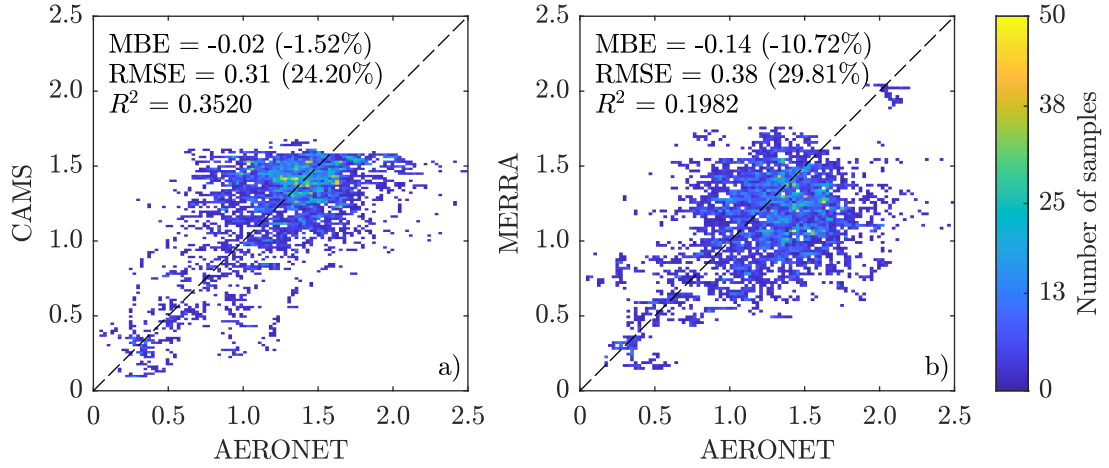

Fig. 3.2: Comparison of α values between reanalysis datasets and AERONET: a) CAMS and b) MERRA-2.

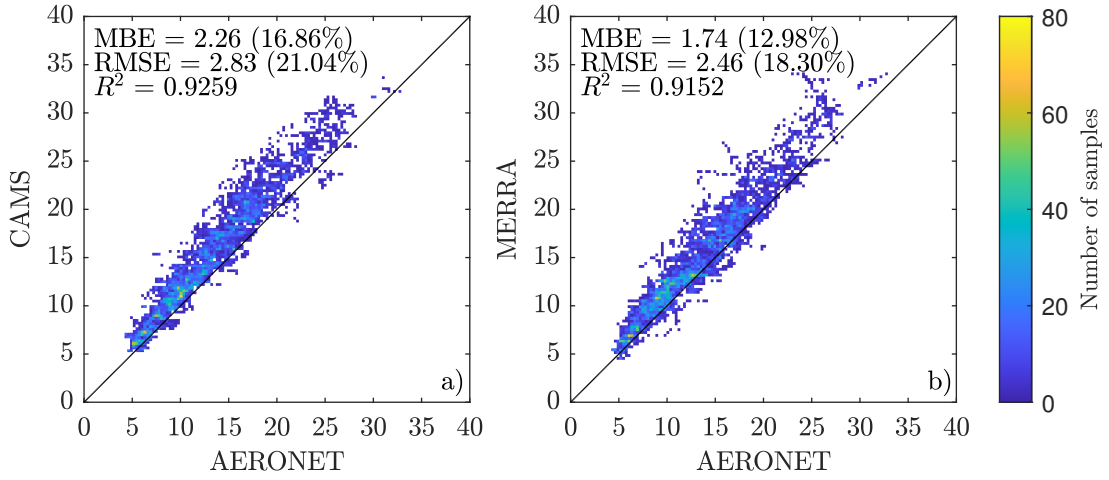

Fig. 3.3: Comparison of PWV values between reanalysis datasets and AERONET: a) CAMS and b) MERRA-2.

3.3 DNI and GHI modelling

As mentioned earlier, three state-of-the-art radiation models are used here to evaluate DNI and GHI: libRadtran [44, 45], SMARTS [46, 47], and REST2 [48]. These three models encompass a large range of sophistication, from a spectral code developed for detailed atmospheric applications (libRadtran), to a parametrized spectral code mainly intended for solar applications (SMARTS), and finally to a two-band simplified engineering-type model (REST2).

LibRadtran is a rigorous code that consists of several routines and functions that allow the user to construct and modify a representation of the atmosphere's structure and composition considering various components such as clouds, aerosols, and gases. LibRadtran also provides the user with several options to solve the radiative transfer

equation, the most popular ones being DISORT [64] and MYSTIC [65]. In this work, libRadtran version 1.7 is used for consistency with previous work [24]. Despite version 2.0.1 being now available, both versions are known to produce the same outputs in the present context of evaluating the shortwave irradiance incident at the surface [66]. The radiative transfer solver used here is DISORT [64], using 16 streams. This approach is considered to provide "exact" irradiance predictions [44]. Because libRadtran uses first principle to solve the radiative transfer equation, its execution is extremely slow, which is why it is typically not used in the practice of solar energy applications. For the present study, libRadtran was operated on the Institute of Earth Sciences' (University of Évora) supercomputer.

SMARTS is a parametrized spectral model that estimates the clear-sky solar irradiance at the surface using spectral transmittance functions to describe various atmospheric extinction processes [46, 47]. It was designed to offer an optimal compromise between the more detailed but also time- and resource-demanding radiative transfer models (e.g., libRadtran) and the simpler and less satisfactory approaches that attempt to replace detailed modelling with empirical parametrizations. The latest version (2.9.9) is used here. It includes the possibility to determine the direct irradiance emanating from both the sun's disk only and from a larger sky area, i.e., the sun's disk and a circumsolar zone up to 10° from sun center, hence making it possible to simulate what is sensed by a pyrheliometer. Further discussion about the definition and simulation of circumsolar radiation is available in [24, 66, 67].

REST2 is a two-band model to predict the broadband irradiance, illuminance, and photosynthetically active radiation from atmospheric data, under clear-sky conditions [48]. It is based on a parametrization of a large number of SMARTS simulations, and it is easier and much faster to use than SMARTS or, even more so, libRadtran. It simulates what is sensed by a pyrheliometer with a 2.5° aperture angle. Its latest version (v9.9) is used here.

From the description just above, it becomes apparent that one of the objectives of the present study is to evaluate the impact of model sophistication on the accuracy of DNI and GHI estimates, particularly when the atmospheric inputs are not measured on site and are rather modelled, thus having significant uncertainty.

In this work, ground-based measurements of aerosol and water vapour properties from AERONET are taken as the reference data source to evaluate DNI and GHI at the location of interest, using the three solar radiation models mentioned above. Then, the same models are used with alternate atmospheric data from CAMS and MERRA-2, aiming at assessing the impact of any error propagation from these data sources to the prediction of DNI and GHI. The inputs required by each model with respect to the specificity of each data source are described in Table 3.1, in which τ_{550} is the aerosol optical depth at 550 nm, α is the Ångström exponent, SSA is the

aerosol single-scattering albedo, PWV is the precipitable water vapour, O_3 is the total column ozone concentration, SP is the surface pressure, and ALB_{vis} and ALB_{nir} are the surface albedo in the visible and near-infrared spectral regions, respectively.

Table 3.1: Inputs required by each radiation model, as obtained from the AERONET, CAMS and MERRA-2 data sources. Key: X - as provided in the dataset; C - calculated from other available variables; D - defaulted to a fixed value (between brackets).

Data source	τ_{550}	α	SSA	PWV	O_3	SP	ALB_{vis}	ALB_{nir}
AERONET	C[a]	X	D (0.932)	X	X	X	D (0.070)	D (0.252)
CAMS	X	C[b]	D (0.932)	X	X	X	X	X
MERRA-2	X	X	C[c]	X	X	X	X	X

[a]Calculated using Ångström's law, Eq. 3.1

[b]Calculated using linear interpolation between 469 and 865 nm in log-log scale

[c]Calculated as the ratio between the scattering and total aerosol optical depths.

3.4 Results and discussion

The accuracy of each pair of data source/model for the prediction of both DNI and GHI is assessed using a variety of statistical indicators. The three conventional statistics (MBE, RMSE, and R^2) - whose usefulness was reviewed in Gueymard [68] - are defined in Eqs. 3.2, 3.3 and 3.4. Two lesser-known statistical indicators of recent uptake (e.g.: Gueymard and Yang [28]) are also added for increased scrutiny: fractional bias (FB) and fractional gross error (FGE), defined as follows:

$$\mathrm{FB} = \frac{2}{n}\sum_{i=1}^{n}\frac{pi - o_i}{pi + o_i}, \tag{3.5}$$

$$\mathrm{FGE} = \frac{2}{n}\sum_{i=1}^{n}\frac{|pi - o_i|}{|pi + o_i|}, \tag{3.6}$$

A comparison between ground-based measurements and model predictions is shown in Figs. 3.4 and 3.5 for DNI and GHI, respectively. Furthermore, to facilitate the comparison between the different models and data sources, the performance results of the model/data source combinations for DNI and GHI are shown in Tables 3.2 and 3.3, respectively. In Table 3.2, the SMARTS statistics include results for the simulations for both the sun-only DNI, DNI_S, and for the sun + circumsolar, DNI_{S+CS}. As explained above, the results for libRadtran are for DNI_S only, whereas those for REST2 are for DNI_{S+CS} only.

When comparing data sources, the statistical results in Table 3.2 show that AERONET is the data source that provides the best DNI estimates when using either REST2 or SMARTS (for both sun-only and sun + circumsolar DNI). Surprisingly,

the bias in the libRadtran/AERONET combo is non-negligible (3%) and is virtually the same here as in the GHI case. One possible explanation is that the measured DNI is underestimated by ≈3% since - considering that the measured DNI constitutes the major part of GHI - this would also explain the observed bias of the same magnitude in the GHI modelled results. Nevertheless, the overestimation of DNI obtained here using this combo was unexpected because it disagrees with the virtually unbiased results obtained in a previous study [24]. Although the same version 1.7 of libRadtran was used then, both its AERONET-based inputs and the reference DNI data were processed slightly differently. It is possible, for instance, that the use of AOD at 550 nm only (which is determined from a fit to the original AERONET values at other wavelengths) in the present libRadtran simulations, might not represent the local conditions accurately enough. More generally, that sophisticated model depends on a number of specialized assumptions regarding its inputs. These need to be made by the user a priori, but might not be the best at each possible instant or location. That makes it the most susceptible model to such misrepresentations. In the present work, and in contrast with the previous study [24], the libRadtran inputs were systematically simplified to match the same inputs as those of the other two models under scrutiny, and to also accept those variables that are common between AERONET and the reanalysis datasets (Table 3.1). Conversely, the two other models evaluated here (particularly REST2) only consider bulk aerosol properties, which makes them presumably less susceptible to this kind of error propagation. Even though this ambiguous situation is not critical, while actually providing some useful context about the current limitations of validation studies of this kind, additional scrutiny and a follow-up study would be desirable to evaluate the dependence of the performance of libRadtran and/or similar models on the specific selection and degree of detail of their input data.

When considering the dispersion metrics, i.e., RMSE and R^2, AERONET is the data source that performs better regardless of the model used, as could be expected (see Fig. 3.4 a), d), g), and j)). On the reanalysis side, MERRA-2 induces better performance according to MBE, FB, and FGE when used with libRadtran, whereas CAMS does not perform best in any circumstance.

Regarding model performance, libRadtran is the best performing model when using the MERRA-2 data source according to all statistical indicators. In contrast, SMARTS and REST2 deliver the best results when using AERONET according to all metrics. Moreover, the SMARTS DNI_{S+CS} predictions perform best according to R^2, whereas their DNI_S counterpart performs best according to all other statistics.

The overall combination of model and data source that delivers the best DNI performance is libRadtran/MERRA-2 when MBE and FB are considered, and alternatively SMARTS/AERONET when rather using RMSE, FGE, and R^2. AERONET

is the data source that provides results with the lowest dispersion (lower RMSE and higher R^2 values); this is contrary to what occurs with GHI, as discussed below. This may be related to the more accurate ground measurements of AOD in comparison with the model estimates in the reanalyses datasets, interacting with the much larger sensitivity of DNI to AOD than GHI [21].

Regarding the best possible combinations of data source and model (marked with * in Table 3.2), it is found that the more sophisticated models - libRadtran and SMARTS - perform better than REST2. A tentative explanation is that the two spectral models have a better capability to take the precise impacts of AOD and PWV on DNI into account, possibly thanks to their much greater spectral resolution.

Compared to the predictions obtained with AERONET, the results in Table 3.2 indicate that the use of CAMS inputs results in an additional bias of 1.80%, 1.97%, 1.90%, and 1.85% for libRadtran (DNI_S), SMARTS (DNI_S), SMARTS (DNI_{S+CS}), and REST2 (DNI_{S+CS}), respectively. Similarly, the alternate use of MERRA-2 inputs results in a change in bias of -3.30%, -3.48%, -3.43%, and -3.45% for the same models, respectively. The consistency of the inter-model agreement in these differences is remarkable, which suggests that, for DNI, all these models respond similarly to minute changes in atmospheric conditions - which would not usually be the case with simpler empirical models, for instance. Moreover, the sign of the change in bias (positive for CAMS and negative for MERRA-2) is consistent with the (opposite) sign of their overall AOD bias relative to AERONET, as displayed in Fig. 3.1.

Regarding GHI, the statistical results presented in Table 3.3 show that MERRA-2 is the data source that produces closer estimates to the ground-based GHI measurements, according to MBE and RMSE. For all models, the bias is positive (Fig. 3.5) and larger with AERONET than with the reanalysis data, which can be viewed as counter-intuitive, considering the discrepancies of the latter data in Figs. 3.1, 3.2 and 3.3. Tentative explanations include: (i) an imperfect clear-sky classification, resulting in some data points having a lower actual GHI than its ideal clear-sky value; and (ii) the calibration factor of at least one (most likely the pyrheliometer) of the two radiometers involved in the calculated GHI being too low. The input-dependent bias range (between the highest and lowest MBEs) is 1.3–1.6% depending on model, whereas the model-dependent bias range is 1.7–2.1% depending on input. These results suggest that, for the state-of-the-art models analysed here, the inter-model differences are similar to - albeit a bit higher than - those created by using alternate high-quality input sources in a specific model. Additionally, it can be concluded that, in terms of bias, the error propagation from inadequacies in the input to the resulting accuracy of the output is somewhat model specific: some input errors might be either compensated or amplified depending on model architecture. Since this is contrary to what was observed above in the case of DNI, it is likely that each model's diffuse

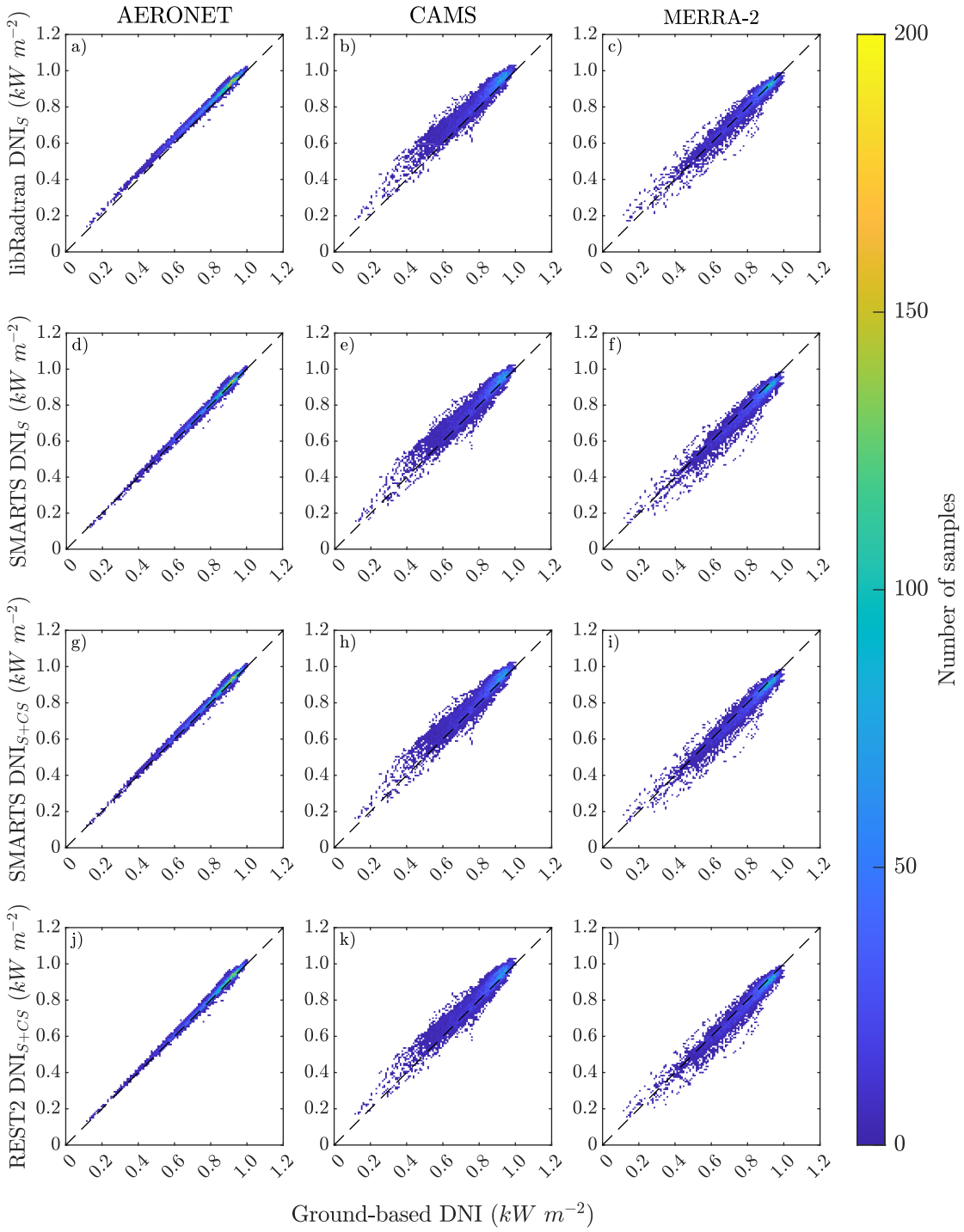

Fig. 3.4: Comparison between measured and predicted DNI using AERONET and reanalysis (CAMS, MERRA-2) data for different models: a) - c) libRadtran (DNI$_S$); d) – f) SMARTS (DNI$_S$); g) - i) SMARTS (DNI$_{S+CS}$); j) – l) REST2 (DNI$_{S+CS}$).

algorithm responds more or less specifically to a change in atmospheric conditions. It thus appears desirable to analyse the multi-dimensional response of a model to changes in its main atmospheric inputs. A complete analysis of such impacts is well beyond the objectives of this study. Nevertheless, for the case of REST2, a limited

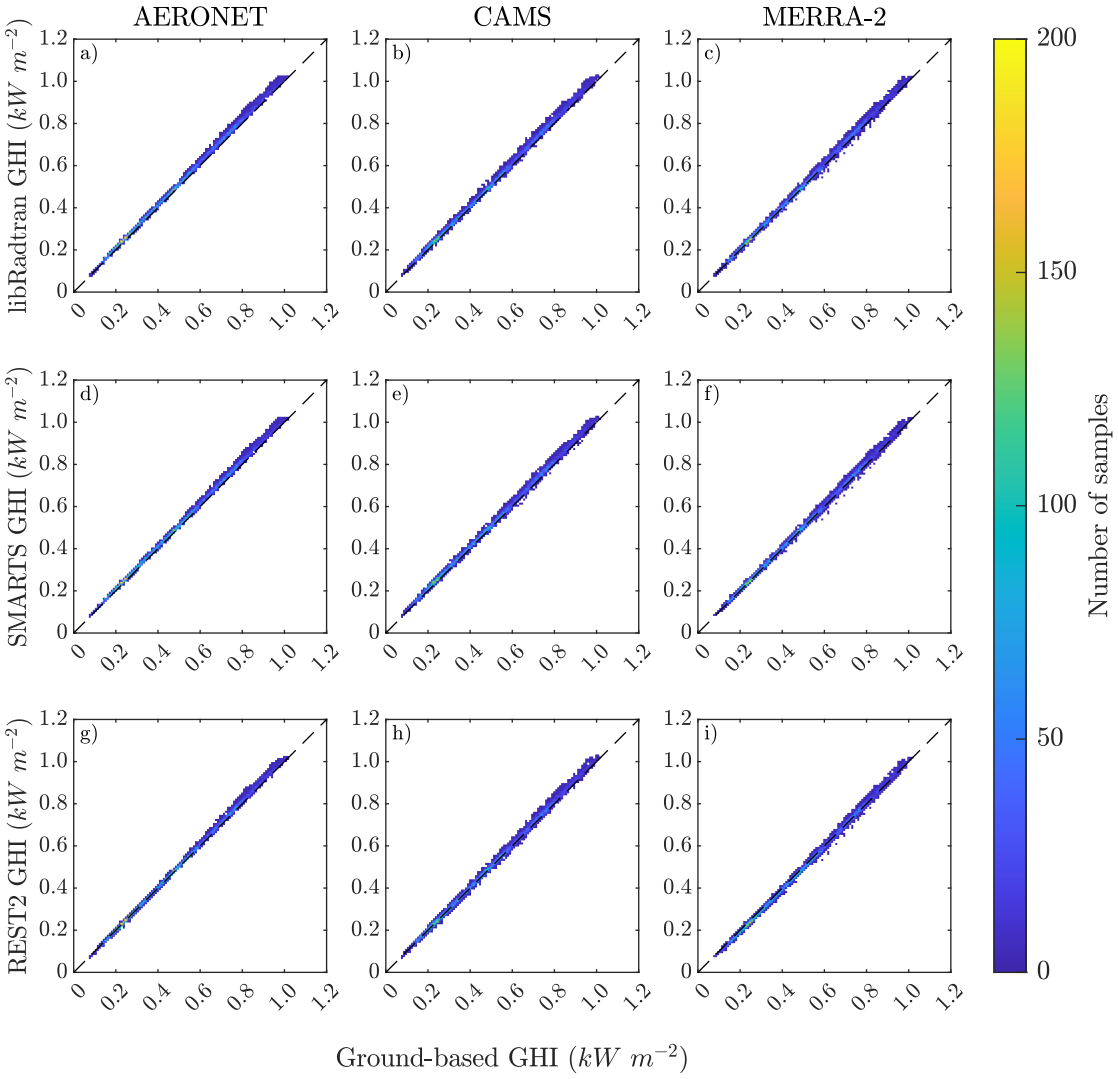

Fig. 3.5: Comparison between measured and predicted GHI using AERONET and reanalysis (CAMS, MERRA-2) data for different models: a) – c) libRadtran; d) – f) SMARTS; g) – i) REST2.

case study is presented in Fig. 3.6 for further reference. It shows the differences ("deltas") between AERONET and reanalysis AOD, α, and PWV, and the resulting percent differences in predictions when using reanalysis data vs. AERONET.

In Table 3.3, the FB and FGE metrics provide mutually-consistent results, where MERRA-2 is outperformed only by AERONET in combination with REST2. Regarding R^2, all values are similarly high (>0.998), contrarily to the DNI case discussed above, in which the R^2 statistics differed significantly according to both model and input data source. Although MERRA-2 is not the best-performing data source for any of the three models, its R^2 values are only within 0.0002 of those of AERONET, which can be considered insignificant. Overall, AERONET is the data source that generates higher R^2 values, regardless of the model used.

Table 3.2: Statistical analysis of data sources/models combinations for DNI prediction. The best performing data source is represented in boldface for each model, the best performing model is underlined for each data source, and the best combination of data source and model is marked with *. Total number of data points N = 11,611; mean measured DNI = 798.7 W/m^2.

Statistical Indicator	Data source	libRadtran DNI_S	SMARTS DNI_S	SMARTS DNI_{S+CS}	REST2 DNI_{S+CS}
MBE (%)	AERONET	3.00	**0.87**	**1.17**	**1.23**
	CAMS	4.84	2.84	3.07	3.08
	MERRA-2	**-0.30***	-2.61	-2.26	-2.22
RMSE (%)	AERONET	**3.38**	**1.73***	**1.88**	**1.96**
	CAMS	6.58	5.35	5.43	5.43
	MERRA-2	3.93	4.80	4.58	4.57
FB	AERONET	0.0320	**0.0086**	**0.0121**	**0.0124**
	CAMS	0.0518	0.0305	0.0331	0.0330
	MERRA-2	**-0.0016***	-0.0279	-0.0236	-0.0234
FGE	AERONET	0.0325	**0.0132***	**0.0150**	**0.0151**
	CAMS	0.0568	0.0445	0.0452	0.0453
	MERRA-2	**0.0323**	0.0396	0.0377	0.0381
R^2	AERONET	**0.9930**	**0.9931**	**0.9932***	**0.9929**
	CAMS	0.9383	0.9355	0.9367	0.9371
	MERRA-2	0.9517	0.9504	0.9510	0.9512

Looking at Table 3.3 from another perspective, it is found that REST2 is the model that performs best based on all statistical indicators, regardless of the data source used (except for FGE when MERRA-2 is used). Curiously, this is the opposite to what was found above for DNI, in which case the more complex models performed better (Table 3.2).

A possible explanation for these counter-intuitive results is that, since REST2 is a less sophisticated model derived from parametrizations for only two wide bands, it is less affected by the input uncertainty. Its simplified nature, compared to the two other models, might also introduce (by chance) favourable compensations of errors. As a result, the model then produces better GHI estimates - at least in appearance (i.e., if there is no bias in the irradiance measurements). A similar phenomenon, where simpler models appear to perform better than more sophisticated ones because of the input data bias, was emphasized in a recent study [51].

In contrast, both SMARTS and libRadtran obtain their best GHI results when coupled with MERRA-2 (except for R^2). If AERONET data were not available on site and only reanalysis data could be used, the REST2/MERRA-2 combination

Table 3.3: Statistical analysis of data sources/models combinations for GHI prediction. The best performing data source is represented in boldface for each model, the best performing model is underlined for each data source, and the best combination of data source and model is marked with *. Total number of data points N = 11,611; Mean measured GHI = 483.9 W/m^2.

Statistical Indicator	Data source	libRadtran	SMARTS	REST2
MBE (%)	AERONET	2.96	2.45	1.14
	CAMS	2.82	2.20	1.14
	MERRA-2	**1.58**	**1.12**	**-0.50***
RMSE (%)	AERONET	3.52	3.00	2.18
	CAMS	3.58	3.04	2.51
	MERRA-2	**2.64**	**2.26**	**2.08***
FB	AERONET	0.0308	0.0263	**0.0076***
	CAMS	0.0306	0.0246	0.0088
	MERRA-2	**0.0152**	**0.0117**	-0.0116
FGE	AERONET	0.0310	0.0264	**0.0135***
	CAMS	0.0314	0.0261	0.0189
	MERRA-2	**0.0195**	**0.0173**	0.0198
R^2	AERONET	**0.9990**	**0.9990**	**0.9991***
	CAMS	0.9983	0.9983	0.9983
	MERRA-2	0.9984	0.9984	0.9985

would be the solution of choice (according to MBE, RMSE and R^2). Additionally, if AERONET data are to be used, REST2 still provides better results.

It is undeniably surprising that the best GHI results are not always obtained with the AERONET input data, since these are always considered "ground truth" and of much better accuracy than any reanalysis. Furthermore, it is also surprising that the best results are obtained by the simplest model (REST2) and not by libRadtran, even though the latter's calculations are considered "exact" from a pure radiative transfer perspective. Conversely, if it is postulated that the libRadtran/AERONET combo results are actually "exact", it would mean the experimental conditions must be suboptimal, for the reasons indicated above (imperfect cloud screening and/or radiometer calibration). For instance, increasing the experimental GHI by 2.96% would zero out the libRadtran/AERONET bias, and would simultaneously introduce an underestimation of 1.82% in REST2. All the other metrics would obviously be affected too, now essentially in favour of libRadtran. This exercise confirms that, when it comes to state-of-the-art irradiance models, it might be difficult to determine their relative performance under clear conditions since it is then comparable to

the irradiance measurement accuracy [40]. This has obvious consequences when conducting large-scale performance assessments of clear-sky irradiance models, in particular (e.g.: [49]).

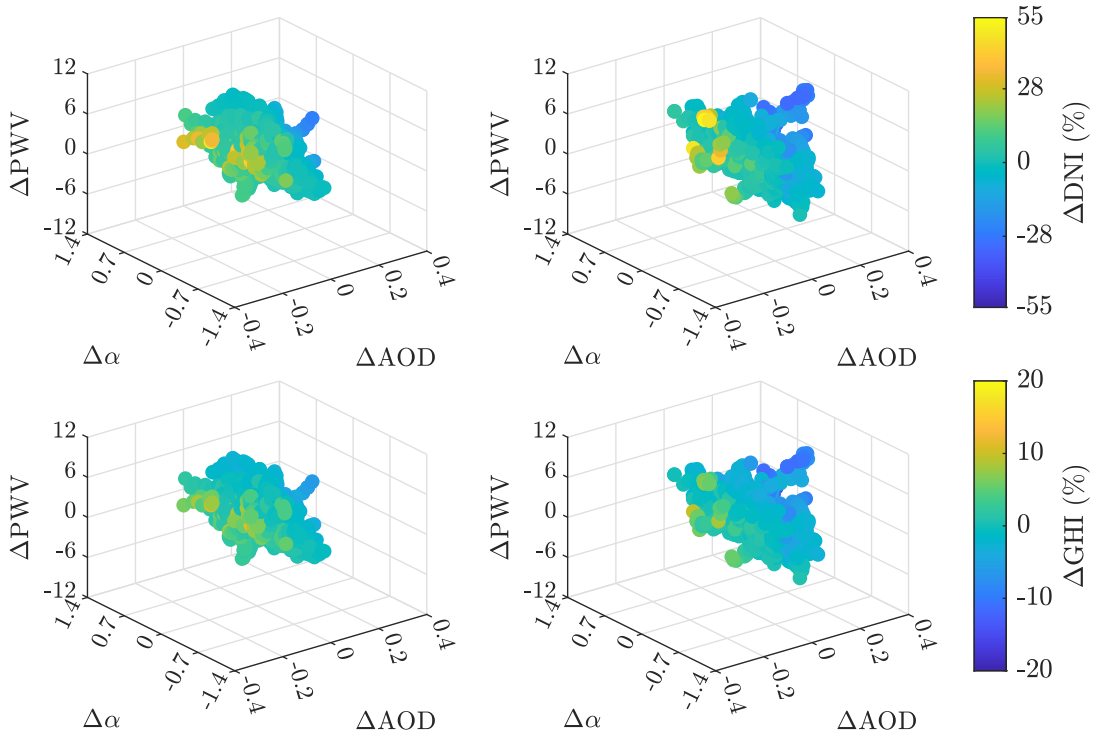

Fig. 3.6: Impact of the differences between reanalysis (first column: CAMS; second column: MERRA-2) and AERONET atmospheric data of AOD, α, and PWV on the percent differences between the respective predicted values of DNI (first row) and GHI (second row) for the REST2 model. All differences, indicated by the symbol Δ, are relative to AERONET inputs or irradiance predictions obtained with them.

To put the present results in perspective, it is worth emphasizing again that the results obtained in this work are affected by errors in both experimental radiation data and atmospheric input data. Regarding the solar radiation measurements, the maximum expanded uncertainty is 2.5% and 5% for DNI and GHI, respectively (see Appendix 5.6). In parallel, the AERONET AOD uncertainty of ≈0.010–0.021 [49], as well as the perceptible PWV bias in all data sources (Fig. 3.3), contribute to an inevitable error propagation of the inputs into the irradiance estimates (Fig. 3.6), with more impact on DNI because of its much larger sensitivity to AOD than GHI [21]. This error propagation appears to be the main reason why the assumed "reference" combination of model/data source i.e., libRadtran/AERONET, does not produce the best estimates for either DNI or GHI. However, further analysis of this critical issue is beyond the goal of this study and should be addressed in future work.

3.5 Conclusions

In this contribution, three different atmospheric data sources (AERONET, CAMS, and MERRA-2) and three distinct solar radiation models (libRadtran, SMARTS, and REST2) have been used to assess the performance of DNI and GHI irradiance predictions using the nine possible combinations of model/data sources, taking as reference the high-quality DNI and GHI ground-based measurements obtained at Évora, Portugal. Both the atmospheric inputs to the models and the reference irradiance data were filtered for optimal quality, and then processed using clear-sky detection techniques as well as a data synchronization procedure. A total of 11,611 valid data points were obtained over the period 2015-2018.

A comparison between AERONET (commonly referred to as "ground reference" in the literature) and reanalysis data (CAMS and MERRA-2) was performed for the most important variables. The reanalysis AOD at 550 nm, τ_{550}, was found to compare moderately well to its AERONET counterpart, with R^2 values higher than 0.70. Conversely, the reanalysis Ångström's exponent, α, displays significant scatter, with a R^2 lower than 0.36. Regarding the precipitable water vapour, PWV, a positive bias higher than 12% was found for both CAMS and MERRA-2 against AERONET, albeit with low dispersion.

Using AERONET data as inputs, the prediction of DNI was found better when the SMARTS model is used. It was also found that the overall combination of model/data source that delivers the best DNI performance is libRadtran/MERRA-2 when mean bias error, MBE, and fractional bias, FB, are considered, and alternatively SMARTS/AERONET when rather using the root mean square error, RMSE, the fractional gross error, FGE, or the coefficient of determination, R^2.

Regarding GHI, the best performing data sources are AERONET and MERRA-2. The latter produces closer estimates according to MBE and RMSE. In contrast, AERONET performs better when considering FB, FGE, and R^2. Similarly, for DNI, AERONET performs better according to R^2, regardless of the model used. From a modeling perspective, REST2 performs best according to MBE and RMSE, regardless of the input data set used (except for FGE when MERRA-2 is used). To estimate GHI, in particular, REST2/AERONET was found to be the best overall combination of model/data source.

Overall, the present findings suggest that, for Évora at least, the clear-sky direct and global irradiances can be simulated with relatively similar accuracy using any of the tested models, combined with either one of three input datasets. This suggests that is not necessary to rely on a highly sophisticated model, such as libRadtran, to obtain high-quality clear-sky irradiance predictions. It also confirms previous studies to the effect that high-performance radiative models can provide excellent predictions

with an uncertainty similar to that of actual measurements. In turn, this implies that any accidental bias in these irradiance measurements is likely to lead to the wrong conclusions when comparing the performance of such models.

Some of the results here were unexpected or counter-intuitive. Most importantly, considering that libRadtran was the more complex model here, whose rigorous radiative transfer solver is assumed to provide "exact" irradiance predictions, and that AERONET is commonly considered in the literature as the ultimate reference (or "ground truth") for the instantaneous determination of the essential atmospheric inputs, it was expected that the combination of libRadtran with AERONET would produce the best irradiance estimates. That logical assumption was not verified in the present analysis, however. The proposed possible explanations included (i) imperfect clear-sky classification, (ii) measurement uncertainty in AOD, α, and/or PWV and subsequent error propagation to the irradiance estimates, and (iii) impact of experimental errors (such as bias) associated to the measured DNI and GHI values (despite the high level of station's maintenance and data quality control achieved here). Possible reasons to explain the slight discrepancy between the present results and those of a previous study that focused on DNI, in which no prediction bias was found when using libRadtran, have been provided.

In any case, further work is required to address and quantify the impact of various modelling issues on solar radiation estimates at multiple high-quality stations, and to better understand the propagation of errors from the atmospheric inputs to the modelled irradiance, depending on radiation model architecture and local conditions.

3.6 Appendix A – Additional information on the processing of the reference solar radiation data

In this work, the variation of the responsivity of the sensors along time was modelled using linear interpolation instead of just using constant responsivity values between calibration events. This procedure is shown in Fig. 3.7 for both the pyranometer measuring DIF and the pyrheliometer measuring DNI.

Four calibration events were used in the pyranometer's fitting procedure, whilst five calibration events were used for the pyrheliometer. The first responsivity value corresponds to the factory calibration, whereas the remaining responsivities were obtained according to the calibration procedures described in ISO 9847:1992 and ISO 9059:1990 standards, for the pyranometer and pyrheliometer, respectively.

Additionally, the expanded uncertainty of the measured solar radiation data used as reference in this work was determined. According to the International Guidelines of Uncertainty in Measurement ("GUM"), the expanded uncertainty is determined using the measurement equation of the variable being studied. Whereas the measurement

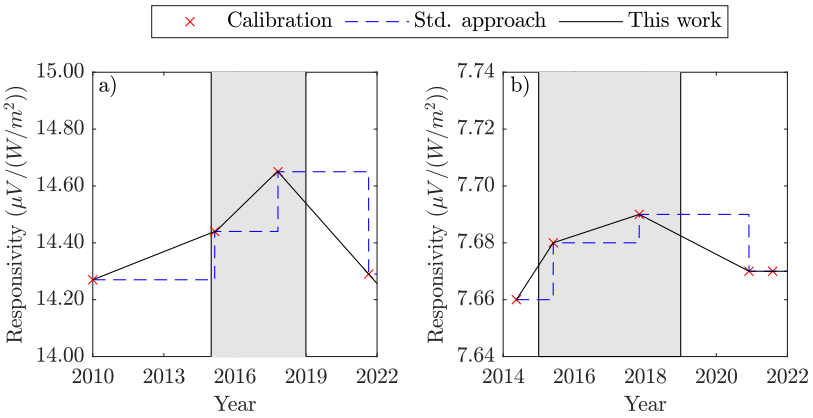

Fig. 3.7: Interpolation procedure between the different responsivity values through time (the first data point is the original factory calibration; the experimental data period considered here is shaded in grey): a) pyranometer, b) pyrheliometer.

equation of DNI has only two variables (the responsivity and the output voltage of the pyrheliometer), the measurement equation of DIF has four variables (responsivity, output voltage, net longwave responsivity of the pyranometer, and net longwave irradiance measured by a pyrgeometer). After determining the standard uncertainties induced by each variable, the combined uncertainty is obtained. Using a coverage factor of 1.96 (which results in a 95% confidence interval), the expanded uncertainty (U95) of the DIF and DNI measurements are found.

Fig. 3.8 shows the variation of U95 according to zenith angle, Z. For DIF, U95 increases with Z and exhibits some dispersion. In contrast, DNI's U95 remains nearly constant for $Z < 60°$, but increases sharply for $Z > 75°$. Aiming at a reference solar radiation dataset as accurate as possible, any DIF or DNI data point with an expanded uncertainty higher than 5% and 2.5%, respectively, was filtered out [57, 69].

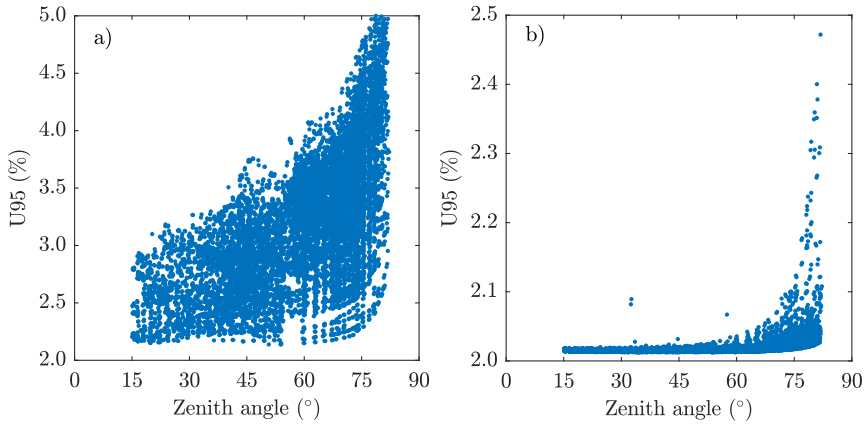

Fig. 3.8: Expanded Uncertainty with a 95% confidence interval (U95) variation according to the zenith angle for (a) DIF and (b) DNI.

References

[1] D. Yang and C. A. Gueymard. Producing high-quality solar resource maps by integrating high- and low-accuracy measurements using gaussian processes. *Renewable and Sustainable Energy Reviews*, 113:109260, 10 2019.

[2] M. Sengupta, A. Habte, S. Wilbert, C. Gueymard, and J. Remund. *Best Practices Handbook for the Collection and Use of Solar Resource Data for Solar Energy Applications: Third Edition*. Golden, CO: National Renewable Energy Laboratory, 4 2021.

[3] N. Engerer. Minute resolution estimates of the diffuse fraction of global irradiance for southeastern australia. *Solar Energy*, 116:215–237, 6 2015.

[4] S. Pereira, E. F. M. Abreu, M. Iakunin, A. Cavaco, R. Salgado, and P. Canhoto. Method for solar resource assessment using numerical weather prediction and artificial neural network models based on typical meteorological data: Application to the south of portugal. *Solar Energy*, 236:225–238, 4 2022.

[5] D. Yang and J. M. Bright. Worldwide validation of 8 satellite-derived and reanalysis solar radiation products: A preliminary evaluation and overall metrics for hourly data over 27 years. *Solar Energy*, S0038092X20303893, 4 2020.

[6] A. Boilley and L. Wald. Comparison between meteorological re-analyses from era-interim and merra and measurements of daily solar irradiation at surface. *Renewable Energy*, 75:135–143, 3 2015.

[7] C. W. Frank, S. Wahl, J. D. Keller, B. Pospichal, A. Hense, and S. Crewell. Bias correction of a novel european reanalysis data set for solar energy applications. *Solar Energy*, 164:12–24, 4 2018.

[8] P. Juruš, K. Eben, J. Resler, P. Krč, I. Kasanický, E. Pelikán, M. Brabec, and J. Hošek. Estimating climatological variability of solar energy production. *Solar Energy*, 98:255–264, 12 2013.

[9] G. Salazar, C. Gueymard, J. B. Galdino, O. de Castro Vilela, and N. Fraidenraich. Solar irradiance time series derived from high-quality measurements, satellite-based models, and reanalyses at a near-equatorial site in brazil. *Renewable and Sustainable Energy Reviews*, 117:109478, 1 2020.

[10] C. A. Gueymard. Solar radiation resource: Measurement, modeling, and methods. In *Reference Module in Earth Systems and Environmental Sciences*. Elsevier, 1 2021.

[11] R. Urraca, T. Huld, A. Gracia-Amillo, F. J. Martinez-de Pison, F. Kaspar, and A. Sanz-Garcia. Evaluation of global horizontal irradiance estimates from era5 and cosmo-rea6 reanalyses using ground and satellite-based data. *Solar Energy*, 164:339–354, 4 2018.

[12] D. P. Dee, S. M. Uppala, A. J. Simmons, P. Berrisford, P. Poli, S. Kobayashi, U. Andrae, M. A. Balmaseda, G. Balsamo, P. Bauer, P. Bechtold, A. C. M. Beljaars, L. van de Berg, J. Bidlot, N. Bormann, C. Delsol, R. Dragani, M. Fuentes, A. J. Geer, L. Haimberger, S. B. Healy, H. Hersbach, E. V. Hólm, L. Isaksen, P. Kållberg, M. Köhler, M. Matricardi, A. P. McNally, B. M. Monge-Sanz, J.-J. Morcrette, B.-K. Park, C. Peubey, P. de Rosnay, C. Tavolato, J.-N. Thépaut, and F. Vitart. The era-interim reanalysis: configuration and performance of the data assimilation system. *Quarterly Journal of the Royal Meteorological Society*, 137(656):553–597, 4 2011.

[13] D. Yang and C. A. Gueymard. Probabilistic post-processing of gridded atmospheric variables and its application to site adaptation of shortwave solar radiation. *Solar Energy*, 225:427–443, 9 2021.

[14] V. Buchard, C. A. Randles, A. M. da Silva, A. Darmenov, P. R. Colarco, R. Govindaraju, R. Ferrare, J. Hair, A. J. Beyersdorf, L. D. Ziemba, and H. Yu. The merra-2 aerosol reanalysis, 1980 onward. part ii: Evaluation and case studies. *Journal of Climate*, 30(17):6851–6872, 9 2017.

[15] R. Gelaro, W. McCarty, M. J. Suárez, R. Todling, A. Molod, L. Takacs, C. A. Randles, A. Darmenov, M. G. Bosilovich, R. Reichle, K. Wargan, L. Coy, R. Cullather, C. Draper, S. Akella, V. Buchard, A. Conaty, A. M. da Silva, W. Gu, G.-K. Kim, R. Koster, R. Lucchesi, D. Merkova, J. E. Nielsen, G. Partyka, S. Pawson, W. Putman, M. Rienecker, S. D. Schubert, M. Sienkiewicz, and B. Zhao. The modern-era retrospective analysis for research and applications, version 2 (merra-2). *Journal of Climate*, 30(14):5419–5454, 7 2017.

[16] A. Molod, L. Takacs, M. Suarez, and J. Bacmeister. Development of the geos-5 atmospheric general circulation model: evolution from merra to merra2. *Geoscientific Model Development*, 8(5):1339–1356, 5 2015.

[17] A. Benedetti, J.-J. Morcrette, O. Boucher, A. Dethof, R. J. Engelen, M. Fisher, H. Flentje, N. Huneeus, L. Jones, J. W. Kaiser, S. Kinne, A. Mangold, M. Razinger, A. J. Simmons, and M. Suttie. Aerosol analysis and forecast in the european centre for medium-range weather forecasts integrated forecast system: 2. data assimilation. *Journal of Geophysical Research*, 114(D13):D13205, 7 2009.

[18] J. Flemming, V. Huijnen, J. Arteta, P. Bechtold, A. Beljaars, A.-M. Blechschmidt, M. Diamantakis, R. J. Engelen, A. Gaudel, A. Inness, L. Jones, B. Josse, E. Katragkou, V. Marecal, V.-H. Peuch, A. Richter, M. G. Schultz, O. Stein, and A. Tsikerdekis. Tropospheric chemistry in the integrated forecasting system of ecmwf. *Geoscientific Model Development*, 8(4):975–1003, 4 2015.

[19] A. Inness, M. Ades, A. Agustí-Panareda, J. Barré, A. Benedictow, A.-M. Blechschmidt, J. J. Dominguez, R. Engelen, H. Eskes, J. Flemming, V. Huijnen, L. Jones, Z. Kipling, S. Massart, M. Parrington, V.-H. Peuch, M. Razinger, S. Remy, M. Schulz, and M. Suttie. The cams reanalysis of atmospheric composition. *Atmospheric Chemistry and Physics*, 19(6):3515–3556, 3 2019.

[20] J.-J. Morcrette, O. Boucher, L. Jones, D. Salmond, P. Bechtold, A. Beljaars, A. Benedetti, A. Bonet, J. W. Kaiser, M. Razinger, M. Schulz, S. Serrar, A. J. Simmons, M. Sofiev, M. Suttie, A. M. Tompkins, and A. Untch. Aerosol analysis and forecast in the european centre for medium-range weather forecasts integrated forecast system: Forward modeling. *Journal of Geophysical Research*, 114(D6):D06206, 2009.

[21] C. A. Gueymard. Temporal variability in direct and global irradiance at various time scales as affected by aerosols. *Solar Energy*, 86(12):3544–3553, 2012.

[22] C. A. Gueymard. Direct solar transmittance and irradiance predictions with broadband models. part i: detailed theoretical performance assessment. *Solar Energy*, 74(5):355–379, 2003.

[23] I. Vamvakas, V. Salamalikis, D. Benitez, A. Al-Salaymeh, S. Bouaichaoui, N. Yassaa, A. Guizani, and A. Kazantzidis. Estimation of global horizontal irradiance using satellite-derived data across middle east-north africa: The role of aerosol optical properties and site-adaptation methodologies. *Renewable Energy*, 157:312–331, 2020.

[24] E. F. M. Abreu, P. Canhoto, and M. J. Costa. Development of a clear-sky model to determine circumsolar irradiance using widely available solar radiation data. *Solar Energy*, 205:88–101, 7 2020.

[25] C. A. Gueymard and J. A. Ruiz-Arias. Validation of direct normal irradiance predictions under arid conditions: A review of radiative models and their turbidity-dependent performance. *Renewable and Sustainable Energy Reviews*, 45:379–396, 5 2015.

[26] B. Holben, T. Eck, I. Slutsker, D. Tanré, J. Buis, A. Setzer, E. Vermote, J. Reagan, Y. Kaufman, T. Nakajima, F. Lavenu, I. Jankowiak, and A. Smirnov. Aeronet—a

federated instrument network and data archive for aerosol characterization. *Remote Sensing of Environment*, 66(1):1–16, 10 1998.

[27] E. Carra, A. Marzo, J. Ballestrín, J. Polo, J. Barbero, J. Alonso-Montesinos, R. Monterreal, E. F. M. Abreu, and J. Fernández-Reche. Atmospheric extinction levels of solar radiation using aerosol optical thickness satellite data. validation methodology with measurement system. *Renewable Energy*, 149:1120–1132, 4 2020.

[28] C. A. Gueymard and D. Yang. Worldwide validation of cams and merra-2 reanalysis aerosol optical depth products using 15 years of aeronet observations. *Atmospheric Environment*, 225:117216, 3 2020.

[29] M. A. Obregón, G. Rodrigues, M. J. Costa, M. Potes, and A. M. Silva. Validation of esa sentinel-2 l2a aerosol optical thickness and columnar water vapour during 2017–2018. *Remote Sensing*, 11(14):1649, 1 2019.

[30] G. Rodrigues, M. Potes, A. M. Penha, M. J. Costa, and M. M. Morais. The use of sentinel-3/olci for monitoring the water quality and optical water types in the largest portuguese reservoir. *Remote Sensing*, 14(9):2172, 1 2022.

[31] V. Salgueiro, M. J. Costa, J. L. Guerrero-Rascado, F. T. Couto, and D. Bortoli. Characterization of forest fire and saharan desert dust aerosols over south-western europe using a multi-wavelength raman lidar and sun-photometer. *Atmospheric Environment*, 252:118346, 5 2021.

[32] E. Sun, X. Xu, H. Che, Z. Tang, K. Gui, L. An, C. Lu, and G. Shi. Variation in merra-2 aerosol optical depth and absorption aerosol optical depth over china from 1980 to 2017. *Journal of Atmospheric and Solar-Terrestrial Physics*, 186: 8–19, 5 2019.

[33] T. Zhang, L. Zang, F. Mao, Y. Wan, and Y. Zhu. Evaluation of himawari-8/ahi, merra-2, and cams aerosol products over china. *Remote Sensing*, 12(10):1684, 5 2020.

[34] J. A. Ruiz-Arias, C. A. Gueymard, and T. Cebecauer. Direct normal irradiance modeling: Evaluating the impact on accuracy of worldwide gridded aerosol databases. 190013, Casablanca, Morocco, 2019. SOLARPACES 2018: International Conference on Concentrating Solar Power and Chemical Energy Systems.

[35] C. Gueymard, M. Al-Rasheedi, A. Ismail, and T. Hussain. Long-term variability of aerosol optical depth, dust episodes, and direct normal irradiance over kuwait for csp applications. 1–10, Abu Dhabi, 2017. International Solar Energy Society.

[36] C. A. Gueymard. Clear-sky radiation models and aerosol effects. In J. Polo, L. Martín-Pomares, and A. Sanfilippo, editors, *Solar Resources Mapping*, 137–182. Springer International Publishing, Cham, 2019.

[37] B. Psiloglou, H. Kambezidis, D. Kaskaoutis, D. Karagiannis, and J. Polo. Comparison between mrm simulations, cams and pvgis databases with measured solar radiation components at the methoni station, greece. *Renewable Energy*, 146:1372–1391, 2 2020.

[38] H. D. Kambezidis, B. E. Psiloglou, D. Karagiannis, U. C. Dumka, and D. G. Kaskaoutis. Meteorological radiation model (mrm v6.1): Improvements in diffuse radiation estimates and a new approach for implementation of cloud products. *Renewable and Sustainable Energy Reviews*, 74:616–637, 7 2017.

[39] F. Antonanzas-Torres, R. Urraca, J. Polo, O. Perpiñán-Lamigueiro, and R. Escobar. Clear sky solar irradiance models: A review of seventy models. *Renewable and Sustainable Energy Reviews*, 107:374–387, 6 2019.

[40] C. A. Gueymard. Clear-sky irradiance predictions for solar resource mapping and large-scale applications: Improved validation methodology and detailed performance analysis of 18 broadband radiative models. *Solar Energy*, 86(8): 2145–2169, 8 2012.

[41] F. Antonanzas-Torres, J. Antonanzas, R. Urraca, M. Alia-Martinez, and F. J. Martinez-de Pison. Impact of atmospheric components on solar clear-sky models at different elevation: Case study canary islands. *Energy Conversion and Management*, 109:122–129, 2 2016.

[42] P. Ineichen. Validation of models that estimate the clear sky global and beam solar irradiance. *Solar Energy*, 132:332–344, 7 2016.

[43] X. Sun, J. M. Bright, C. A. Gueymard, X. Bai, B. Acord, and P. Wang. Worldwide performance assessment of 95 direct and diffuse clear-sky irradiance models using principal component analysis. *Renewable and Sustainable Energy Reviews*, 135:110087, 1 2021.

[44] C. Emde, R. Buras-Schnell, A. Kylling, B. Mayer, J. Gasteiger, U. Hamann, J. Kylling, B. Richter, C. Pause, T. Dowling, and L. Bugliaro. The libradtran software package for radiative transfer calculations (version 2.0.1). *Geoscientific Model Development*, 9(5):1647–1672, 5 2016.

[45] B. Mayer and A. Kylling. Technical note: The libradtran software package for radiative transfer calculations – description and examples of use. *Atmos. Chem. Phys.*, 23, 2005.

[46] C. A. Gueymard. The smarts spectral irradiance model after 25 years: New developments and validation of reference spectra. *Solar Energy*, 187:233–253, 7 2019.

[47] C. A. Gueymard. Parameterized transmittance model for direct beam and circumsolar spectral irradiance. *Solar Energy*, 71(5):325–346, 11 2001.

[48] C. A. Gueymard. Rest2: High-performance solar radiation model for cloudless-sky irradiance, illuminance, and photosynthetically active radiation – validation with a benchmark dataset. *Solar Energy*, 82(3):272–285, 3 2008.

[49] X. Sun, J. M. Bright, C. A. Gueymard, B. Acord, P. Wang, and N. A. Engerer. Worldwide performance assessment of 75 global clear-sky irradiance models using principal component analysis. *Renewable and Sustainable Energy Reviews*, 111:550–570, 9 2019.

[50] J. A. Ruiz-Arias and C. A. Gueymard. Worldwide inter-comparison of clear-sky solar radiation models: Consensus-based review of direct and global irradiance components simulated at the earth surface. *Solar Energy*, 168:10–29, 7 2018.

[51] X. Sun, D. Yang, C. A. Gueymard, J. M. Bright, and P. Wang. Effects of spatial scale of atmospheric reanalysis data on clear-sky surface radiation modeling in tropical climates: A case study for singapore. *Solar Energy*, 241:525–537, 7 2022.

[52] E. F. Abreu, P. Canhoto, and M. J. Costa. Prediction of diffuse horizontal irradiance using a new climate zone model. *Renewable and Sustainable Energy Reviews*, 110:28–42, 8 2019.

[53] D. M. Giles, A. Sinyuk, M. G. Sorokin, J. S. Schafer, A. Smirnov, I. Slutsker, T. F. Eck, B. N. Holben, J. R. Lewis, J. R. Campbell, E. J. Welton, S. V. Korkin, and A. I. Lyapustin. Advancements in the aerosol robotic network (aeronet) version 3 database – automated near-real-time quality control algorithm with improved cloud screening for sun photometer aerosol optical depth (aod) measurements. *Atmospheric Measurement Techniques*, 12(1):169–209, 1 2019.

[54] A. Ångström. On the atmospheric transmission of sun radiation and on dust in the air. *Geografiska Annaler*, 11(2):156–166, 8 1929.

[55] C. N. Long and Y. Shi. An automated quality assessment and control algorithm for surface radiation measurements. *The Open Atmospheric Science Journal*, 2 (1):23–37, 4 2008.

[56] C. A. Gueymard and J. A. Ruiz-Arias. Extensive worldwide validation and climate sensitivity analysis of direct irradiance predictions from 1-min global irradiance. *Solar Energy*, 128:1–30, 4 2016.

[57] I. Reda. Method to calculate uncertainty estimate of measuring shortwave solar irradiance using thermopile and semiconductor solar radiometers. Technical report, 7 2011.

[58] C. A. Gueymard and D. R. Myers. Evaluation of conventional and high-performance routine solar radiation measurements for improved solar resource, climatological trends, and radiative modeling. *Solar Energy*, 83(2):171–185, 2 2009.

[59] J. M. Bright, X. Sun, C. A. Gueymard, B. Acord, P. Wang, and N. A. Engerer. Bright-sun: A globally applicable 1-min irradiance clear-sky detection model. *Renewable and Sustainable Energy Reviews*, 121:109706, 4 2020.

[60] D. J. M. Bright. Clear-sky detection methodology library, 11 2021. URL `https://github.com/JamieMBright/csd-library`. original-date: 2018-11-01T04:48:47Z.

[61] C. A. Gueymard, J. M. Bright, D. Lingfors, A. Habte, and M. Sengupta. A posteriori clear-sky identification methods in solar irradiance time series: Review and preliminary validation using sky imagers. *Renewable and Sustainable Energy Reviews*, 109:412–427, 7 2019.

[62] J. A. Davies and D. C. McKay. Estimating solar irradiance and components. *Solar Energy*, 29(1):55–64, 1982.

[63] D. Pérez-Ramírez, D. N. Whiteman, A. Smirnov, H. Lyamani, B. N. Holben, R. Pinker, M. Andrade, and L. Alados-Arboledas. Evaluation of aeronet precipitable water vapor versus microwave radiometry, gps, and radiosondes at arm sites. *Journal of Geophysical Research: Atmospheres*, 119(15):9596–9613, 2014.

[64] K. Stamnes, S.-C. Tsay, W. Wiscombe, and K. Jayaweera. Numerically stable algorithm for discrete-ordinate-method radiative transfer in multiple scattering and emitting layered media. *Applied optics*, 27(12):2502–2509, 1988.

[65] B. Mayer. Radiative transfer in the cloudy atmosphere. *The European Physical Journal Conferences*, 1:75–99, 2009.

[66] Y. Eissa, P. Blanc, H. Ghedira, A. Oumbe, and L. Wald. A fast and simple model to estimate the contribution of the circumsolar irradiance to measured broadband beam irradiance under cloud-free conditions in desert environment. *Solar Energy*, 163:497–509, 3 2018.

[67] P. Blanc, B. Espinar, N. Geuder, C. Gueymard, R. Meyer, R. Pitz-Paal, B. Reinhardt, D. Renné, M. Sengupta, L. Wald, and S. Wilbert. Direct normal irradiance

related definitions and applications: The circumsolar issue. *Solar Energy*, 110: 561–577, 12 2014.

[68] C. A. Gueymard. A review of validation methodologies and statistical performance indicators for modeled solar radiation data: Towards a better bankability of solar projects. *Renewable and Sustainable Energy Reviews*, 39:1024–1034, 11 2014.

[69] A. Habte and M. Sengupta. Best practices to uncertainty estimation for the national solar radiation database (nsrdb 1998–2015). 2470 – 2474. 33rd European Photovoltaic Solar Energy Conference and Exhibition, 2017.

Nomenclature

Closr	closure equation
DNI	direct normal irradiance
Elev	elevation
FB	fractional bias
FGE	fractional gross error
GHI	global horizontal irradiance
MBE	mean bias error
n	total number of data points
o	observation
$\overline{o}$	observation's average
O_3	total column ozone concentration
p	prediction
R^2	coefficient of determination
RMSE	root mean square error
Z	solar zenith angle

Greek symbols

α	Ångström's exponent
β	Ångström's exponent
Δ	difference between AERONET and reanalyses
λ	wavelength
τ	aerosol optical depth

Subscripts

0	reference wavelength (1000 nm)
i	data point
S	sun
$S + CS$	sun + circumsolar

Acronyms

AERONET	Aerosol Robotic Network
ALB_{nir}	surface albedo in the near-infrared spectral region
ALB_{vis}	surface albedo in the visible spectral region
AOD	aerosol optical depth
BSRN	Baseline Surface Radiation Network
CAMS	Copernicus Atmosphere Monitoring Service
Closr	closure equation
DIF	diffuse horizontal irradiance
DNI	direct normal irradiance
Elev	elevation
FB	fractional bias
FGE	fractional gross error
GHI	global horizontal irradiance
IES	Institute of Earth Sciences
MERRA-2	Modern-Era Retrospective analysis for Research and Applications, Version 2
NWP	numerical weather prediction
PWV	precipitable water vapour

R^2	coefficient of determination
REST2	Reference Evaluation of Solar Transmittance, 2 bands
RMSE	root mean square error
SMARTS	Simple Model of the Atmospheric Radiative Transfer of Sunshine
SP	surface pressure
SSA	single scattering albedo
U95	expendend uncertainty at 95%

Chapter 4

Development of a clear-sky model to determine circumsolar irradiance using widely available solar radiation data[†]

Abstract

Accurate assessment of the solar irradiance reaching the absorber of concentrating solar power (CSP) systems is crucial for accurate energy generation estimates as well as for power plants design and operation. Due to a larger aperture angle, direct normal irradiance (DNI) measurements taken by pyrheliometers include circumsolar normal irradiance (CSNI), i.e., the diffuse radiance from the vicinity of the sun disk, which in some cases is not totally captured by the CSP systems because of their lower aperture angles. This work reports the modelling of DNI and CSNI using a radiative transfer model and atmospheric measurements and aims to develop a fast and simple model to estimate the CSNI based on more common solar irradiance measurements such as the DNI, global horizontal irradiance (GHI) and diffuse horizontal irradiance (DHI). The proposed model performs better than other models available in the literature for the six locations analysed (scattered around the globe), thus contributing to a more accurate solar resource assessment and CSP systems design and operation.

Keywords: Circumsolar irradiance; Direct Normal Irradiance; DNI; Solar resource assessment; Concentrating Solar Power; CSP.

4.1 Introduction

Concentrating solar power (CSP) systems are seen by the solar energy community as a reliable technology for energy production (thermal and thermo-electric) [1]. The high potential of these systems stimulated the development of several studies

[†]Edgar F.M. Abreu[(1)], Paulo Canhoto[(1,2)], and Maria J. Costa[(1,2)]. Development of a clear-sky model to determine circumsolar irradiance using widely available solar radiation data. *Solar Energy*, 205:88-101, 2020.

[(1)] Institute of Earth Sciences, University of Évora.

[(2)] Physics Department, School of Sciences and Technology, University of Évora.

covering a variety of research fields, from the solar radiation modelling and forecast to the concentrator optics and solar thermal receivers design and optimisation. Solar resource assessment is a crucial step in any CSP system installation since it is important to estimate energy production and, therefore, economic viability of the project [2]. It is also needed to design, operate and maintain the CSP power plants. High concentration ratio CSP systems use only the direct irradiance component on a plane normal to the sun rays, i.e., direct normal irradiance (DNI) [3], to generate heat, which is then used to generate electricity.

High-quality solar radiation data are needed to produce a useful solar resource assessment study [4]. Usually, these data are obtained from meteorological stations with state-of-the-art instruments and periodic calibrations and maintenance procedures. DNI is measured using a pyrheliometer aligned with the sun, in which sunlight reaches a thermopile placed at the bottom of a tube through a window at the other end of the tube, with the thermopile converting temperature increase to an electrical signal [5]. The issue when recording DNI data is that the aperture angle of the pyrheliometer, which depends on the window and thermopile diameters and tube length, is larger than the sun disk, resulting in the measurement of not only direct beam irradiance from the sun, but also of the diffuse irradiance in the vicinity of the sun disk, known as circumsolar irradiance (CSNI) [3]. However, high concentration ratio CSP systems have low aperture angles, usually lower than the pyrheliometers, which leads to an overestimation of the energy reaching the solar thermal receivers if pyrheliometer measurements are directly used as input in the analysis of these systems, depending on the intensity and angular distribution of CSNI. In this way, information on CSNI is crucial to assure a proper solar resource assessment, design, operation and modelling of CSP systems [6].

CSNI is caused by the scattering of the sun rays by molecules, aerosols and cirrus clouds. These atmospheric constituents scatter the solar rays from the direct beam to a broader cone-shaped circumsolar region [7]. Whereas DNI from the sun disk only is strongly related to the atmospheric transmittance and total scattering effect, CSNI is also strongly related to the scattering angle, i.e., the angular distance from the center of the sun disk [8]. Measuring CSNI is difficult because of this sharp decrease of intensity between the centre of the sun disk and the outer limit of the measuring instrument field of view [3]. Some attempts of measuring CSNI are available in the literature and are presented and reviewed in the following.

CSNI was measured for the first time at the Lawrence Berkeley Laboratory (LBL) at 11 locations in the United States from 1976 to 1981 [9]. In that work, the measurement of the sunshape, i.e, azimuthal average radiance profile normalized with the radiance at the center of the sun [3], was done using a special telescope. This instrument measured the radiance inside the sun disk and in its vicinity up to a

scattering angle of $\approx 3°$, with an aperture of 0.025° within 0.5° on either side of the sun disk, and an aperture of 0.075° in the circumsolar region. The database created in this way by Noring et al. [9] is the basis of the widely known Buie model [10], which allows a determination of the sunshape using the circumsolar ratio (CSR), i.e., the ratio between CSNI and DNI.

Later, Schubnell [11] used a standard high-resolution CCD-camera mounted on a tracker to record the sunshape at Paul Scherrer Institute, Switzerland. His goal was to study the influence of the sunshape on the overall optical efficiency of solar concentrators. Neumann et al. [12] used a camera developed at the German Aerospace Center (DLR) to measure the sunshape in various locations in France, Germany and Spain. Their measurements were found to be slightly different from the LBL measurements, which can be explained by the averaging of LBL data caused by the telescope aperture field of view and the higher number of points in the LBL database [6, 12]. The CCD-camera method was also used by Gambardella and Galleano [13] with the system uncertainty being determined using indoor test procedures.

Wilbert et al. [14] developed a sunshape measurement system that consists of a sun and aureole measurement instrument (SAM), an AERONET (AErosol RObotic NETwork) sun photometer [15] and post-processing software. The SAM device consists of two cameras: one used to observe the sun disk and one to observe the aureole. Both cameras have changeable filters that provide spectral measurements at 440 nm, 670 nm and 870 nm. To obtain the sunshape in a broadband spectral range, the AERONET sun photometer is used alongside post-processing software based on the simple model of the atmospheric radiative transfer of sunshine (SMARTS) [16]. According to Wilbert et al. [14], this method results in lower uncertainty than that of the camera used by DLR. In the study of Wilbert et al. [17], a comparison between different techniques to measure CSNI is presented. The reference system was the aforementioned SAM device and measurements were compared against data from the BPI-CSR460 system. The BPI-CSR460 system was developed by Black Photons Instruments and consists of two pyrheliometers with different aperture angles. Different types of collimators can be attached to the sensor enclosures to obtain different aperture angles. Wilbert et al. [17] found that the BPI-CSR460 provides accurate measurements of circumsolar radiation in the angular interval of the selected collimators (corresponding to opening angles of 0.704° and 2.638°). Although CSR values can be obtained through this method, deviations from the reference system (SAM) were found due to the application of the Buie model, since the same CSR value can be representative of distinct atmospheric conditions [17]. The use of two pyrheliometers to obtain information on the angular distribution of circumsolar radiation was previously used by Jeys and Vant-Hull [18], Hickey and Karoli [19] and Major [20].

Al-Ansary et al. [21] measured CSR using a photographic camera. Their method consists in taking high-resolution photographs of the sun and identifying the sun disk through a computer code that uses pixel intensity to obtain the intensity distribution across the sun's disk and in the circumsolar region. However, their study was exploratory and preliminary, and no validation of the measured data was presented.

Wilbert et al. [22] used a conventional rotating shadowband irradiometer (RSI) without any hardware modification to measure the sunshape. Their method consists in analysing the RSI signal to determine the circumsolar distribution, and, consequently, CSR. Results were validated with four RSIs in Spain, India and Morocco and their method is presented as requiring lower maintenance, producing less data gaps and lower cost when compared to other devices and methods.

CSNI modelling is usually done using radiative transfer models (RTM). Thomalla et al. [23] calculated CSNI for various atmospheric conditions. In their work, the variation of CSNI was demonstrated taking into account the absorption and scattering of solar radiation by molecules, aerosols and cirrus clouds. The absorption by gases and the effect of different solar elevation angles were also studied. Eissa et al. [24] compared the CSR obtained from the Perez and Michalsky [25] model against the CSR calculated by the RTM called library for radiative transfer (libRadtran) [26], over cloudless turbid atmospheres. They found that the former is lower than the latter. However, high correlation between the CSRs obtained from the two methods was found, suggesting that corrections to the Perez and Michalsky [25] model can be made to improve the modelling of CSR.

Reinhardt et al. [27] developed a method that uses satellite-retrieved cirrus cloud properties to determine CSNI. After retrieving the optical thickness and the effective radius of the cirrus cloud, CSNI is determined through a look-up table generated from a modified version of the MYSTIC RTM [28]. They also found that manual screening of sub-scale cumulus clouds improves the agreement between satellite and ground-based measurements. In the work of Eissa et al. [29], the monochromatic CSNI was modelled using AERONET data as input to libRadtran [26] and SMARTS [16] models. Results were compared against the SAM measurements, and both models produced accurate estimates of the sun-disk DNI. They also found that libRadtran exhibited the most accurate results when the AERONET aerosol phase function was represented as a two-term Henyey-Greenstein phase function. Abreu et al. [8] reported the modelling of monochromatic CSNI using libRadtran and AERONET data at Évora, Portugal. The simulated data indicate an improvement in the modelling of DNI when CSNI is included, taking DNI ground-based measurements from a field pyrheliometer as reference.

Cole and Gottschalg [30] proposed a modification to the Buie et al. [10] model

based on an improved parametrisation of CSNI. Their model reduces the DNI overestimation of the Buie et al. [10] model through a more accurate representation of CSR. A model extension including the differences between the spectral distributions in the sun disk and circumsolar regions is also presented, which is useful for the analysis of concentrator photovoltaics (CPV) systems. Sun et al. [31] studied the inclusion of CSNI in the DNI determination using numerical weather prediction (NWP) models. They found that using the delta-Eddington scaling method in the DNI modelling results in higher errors than if it is not used. Therefore, they presented a simple parametrisation of dust aerosols effect that can be used to account for the scattering contribution of this specific type of aerosols. Haapanala et al. [32] reported the influence of ice clouds in the disk and circumsolar radiances using a Monte Carlo RTM and compared their results against SAM measurements. They found that ice crystal roughness is the most sensitive parameter regarding angular dependence of the sun disk and circumsolar radiances. They also report that better agreement with the SAM measurements is found if ice crystals are assumed as rough and the ground-based measurements of DNI are corrected to take into account the higher values and broader distribution of circumsolar radiance in the presence of ice clouds. Eissa et al. [7] reported the modelling of CSNI using libRadtran and AERONET data in a desert environment. A good agreement between ground-based DNI measurements and the modelled DNI data when adding the CSNI component was found. They also reported a model to estimate CSR using the sky clearness [33, 25], defined through the solar zenith angle (θ), Global Horizontal Irradiance (GHI), DNI and Diffuse Horizontal Irradiance (DHI). Sun et al. [34] presented a method that modifies the radiative transfer equation for DNI calculation, including the CSNI within a cone of the pyrheliometer field-of-view and considering the contributions from all aerosol species and clouds. This is achieved by using a new phase function scaling method instead of the delta-Eddington method. They found a good agreement with the results of other models in the literature as well as ground-based measurements. Regarding CSNI, the results found were poor when compared with the model from Eissa et al. [7] and other models. A possible explanation for this is the low magnitude of CSNI, which can be strongly affected by the uncertainties in the input data.

The circumsolar ratio (CSR) provides information on the amount of energy in the circumsolar region. This information can be used to assess locations regarding CSP systems design and deployment as well as to improve the operation of such systems, aiming at a more accurate determination of the irradiance that is effectively reaching the solar absorber, since the optical efficiency strongly depends on CSR, as shown by Zou et al. [35]. It can also be used to select the technology to be installed at a specific location. On one hand, CSP systems with larger aperture angles should be installed in locations with higher probability of occurrence of high CSR values,

thus slightly decreasing the concentration factor while maintaining the level of solar energy harvesting. On the other hand, CSP systems with lower aperture angles can be installed in locations with higher probability of occurrence of low CSR values, since the irradiance in the circumsolar region is lower.

Since CSNI modelling through RTM is not an easy task to perform, and due to the necessity of high-quality measurements of aerosol properties and other relevant meteorological parameters, such as precipitable water vapour, that may not be readily available at locations of interest for CSP systems installation, simple models to compute CSR using more commonly available measurements such as DNI or GHI (or parameters derived from these measurements) are referred in the literature. In addition to the model from Eissa et al. [7], Neumann et al. [36] used the ratio between GHI and DNI as well as the solar altitude angle as predictors to develop their model at the Plataforma Solar de Almeria, Spain. Ivanova [37] developed a model based on DNI, GHI, DHI and beam horizontal irradiance measurements, taking the LBL data as reference. Such models are not able to produce as accurate CSR values or circumsolar radiance distributions as RTMs. However, due to their simplicity of use and fast computing, they can be used to easily assess and report CSR at a given location under study depending on the local meteorological conditions.

In this work, a new model to estimate the CSR is presented. This model is developed based on a reference database of modelled CSNI values using libRadtran RTM and AERONET data for six locations scattered around the globe. The libRadtran RTM is used to independently compute both the sun-disk DNI and CSNI. Then, since CSNI measurements are scarce and are not available at the locations under study, the validation of the modelled values is done by comparing ground-based measurements of DNI taken by field pyrheliometers against the modelled DNI, with and without the CSNI component. A sensitivity analysis of the latter, considering the solar zenith angle, number of moments of the aerosol phase function and mesh size when characterizing the circumsolar region, is also performed.

The paper is organised as follows: Section 4.2 presents the general concepts and assumptions when modelling DNI and its circumsolar component. Section 4.3 describes the experimental datasets used. Section 4.4 reports the DNI and CSNI modelling. In Section 4.5, a sensitive study is presented and discussed. Section 4.6 details the DNI and CSNI simulation results. Section 4.7 describes the developed CSR model and Section 4.8 presents results and discussion. Finally, conclusions are drawn in Section 4.9.

4.2 Direct normal and circumsolar irradiance definition

According to ISO-9488 standard [38], DNI (B_n) is defined as the radiant flux received on a plane perpendicular to the axis of a small solid angle centred on the sun disk. Due to the ambiguous definition of this small solid angle and the use of different instruments with distinct aperture angles to measure B_n, several definitions can be found in the literature. This issue led several experts in this field to produce a study on the B_n definition [3]. A consensual definition has been proposed for B_n as well as the terminology that should be used in the field of solar resource assessment, namely DNI and CSNI. The guidelines of the World Meteorological Organization (WMO) include a recommendation on the aperture angle of pyrheliometers. In this way, similar instruments can be used around the world and, for that reason, the same definition of B_n is applied. This leads to a more reliable comparison between the solar resource of different locations. The ISO definition of B_n is given by:

$$B_n(\alpha_l) = \int_0^{2\pi} \int_0^{\alpha_l} P(\xi, \varphi_n) L(\xi, \varphi_n) \cos(\xi) \sin(\xi) d\xi d\varphi_n, \tag{4.1}$$

where α_l is the limit angle of the pyrheliometer, $P(\xi, \varphi_n)$ is the penumbra function of the instrument, also known as acceptance function, $L(\xi, \varphi_n)$ is the sky radiance, ξ is the angular distance from the centre of the sun, also known as scattering angle, and φ_n is the azimuth angle measured in the plane perpendicular to the axis of the solid angle aligned with the centre of the sun disk. The scattering angle is given by [39]:

$$\xi = \cos^{-1}(\cos(\theta_S)\cos(\theta) + \sin(\theta_S)\sin(\theta)\cos(\varphi - \varphi_S)), \tag{4.2}$$

where θ_S and φ_S stand for the solar zenith and azimuth angles, respectively, and θ and φ are the zenith and azimuth angles of a given point in the sky (sky element), respectively. In the literature, it is common to consider the radiance in the vicinity of the sun as radially symmetrical under clear-sky conditions [7, 3, 40]. This assumption is reasonable for solar zenith angles lower than $\approx 85°$ and allows a simplification of Eq. 4.1 into:

$$B_n(\alpha_l) \approx 2\pi \int_0^{\alpha_l} P(\xi) L(\xi) \cos(\xi) \sin(\xi) d\xi. \tag{4.3}$$

A more detailed analysis of this assumption is addressed in Subsection 4.5.1. Each model of pyrheliometer has its own geometrical characteristics, and thus a specific penumbra function. The penumbra function accounts for the response of the pyrheliometer according to the scattering angle due to the effect of the opening window edge on the radiation intensity attenuation. In this work, the geometric penumbra function proposed by Major [41] is used, defined as a function of the slope and limit angles of the pyrheliometer, α_s and α_l, respectively. Considering the referred radial symmetry, the penumbra function is defined by:

$$P(\xi) = \frac{1}{2\pi} \int_0^{2\pi} P(\xi, \varphi_n) d\varphi_n. \tag{4.4}$$

For scattering angles between 0° and α_s, the penumbra function is equal to 1, whereas for scattering angles greater than α_l the penumbra function is equal to 0. Between α_s and α_l, the penumbra function decreases monotonically from 1 to 0 as given by the Major [41] formulas. The azimuthally averaged sky radiance is given by:

$$L(\xi) = \frac{1}{2\pi} \int_0^{2\pi} L(\xi, \varphi_n) d\varphi_n, \tag{4.5}$$

while the averaged CSNI as measured by a pyrheliometer with a limit angle α_l (CS_n^{exp}) is given by:

$$CS_n^{exp}(\delta_S, \alpha_l) \approx 2\pi \int_{\delta_S}^{\alpha_l} P(\xi) L(\xi) \cos(\xi) \sin(\xi) d\xi, \tag{4.6}$$

where $\delta_S \approx 0.2664°$ is the mean angular distance between the centre of the sun and its edge as observed on the surface of the earth (angular radius of the sun) [12]. The sun disk radius varies slightly during the year due to the elliptic orbit of the Earth around the Sun, however the associated error is less than 1.7% if the mean value of δ_S is used [3]. Then, the DNI as measured by a pyrheliometer (B_n^{exp}) is given by:

$$B_n^{exp}(\alpha_s, \alpha_l) = CS_n^{exp}(\delta_S, \alpha_l) + B_n^{sun}(\delta_S), \tag{4.7}$$

in which $B_n(\delta_S)$ is obtained by integrating Eq. 4.3 between 0° and δ_S. A useful parameter used in solar resource assessment and CSP modelling is the circumsolar ratio (CSR), which is defined as:

$$CSR(\alpha_s, \alpha_l) = \frac{CS_n^{exp}(\delta_S, \alpha_l)}{B_n^{exp}(\alpha_s, \alpha_l)}. \tag{4.8}$$

4.3 Experimental data

In this work, aerosol and precipitable water data are needed for the DNI and CSNI simulations, and ground-based measurements of solar irradiance are needed for validation. Aerosol data were obtained from AERONET (AErosol RObotic NETwork), which consists on a ground-based remote sensing aerosol network established by NASA and PHOTONS (PHOtométrie pour le Traitement Opérationnel de Normalisation Satellitaire) [15], and the following products were selected: aerosol optical depth (AOD), aerosol single-scattering albedo (SSA), aerosol phase function (PHFN) and surface albedo (SA) for various wavelengths (440, 675, 870 and 1020 nm), and precipitable water vapour (PWV) content. AERONET V3 Level 1.5 data are automatically filtered to eliminate cloud effects [42] and were used here instead of Level 2.0 in order to have a larger data set, aiming at a better characterization of the locations being assessed. The AERONET data server (https://aeronet.gsfc.nasa.gov) provides a tool to download coincident measurements of several variables at the referred wavelengths except for the case of PWV data, which were linearly interpolated to match exactly

the time stamp of the aerosol parameters listed above, as will be explained in Section 4.4.

Ground-based measurements were obtained from the Baseline Surface Radiation Network (BSRN) [43] and the Institute of Earth Sciences (IES) stations. The BSRN is a project of the Global Energy and Water Cycle Experiment (GEWEX) under the umbrella of the World Climate Research Programme (WCRP). The main objective of this network is to detect changes in the radiation field at the Earth's surface that may be related with climate change. The IES is a Portuguese research centre dedicated to the study of the Earth's system. It includes the Observatory of Atmospheric Sciences installed at the University of Évora, which conducts BSRN-like solar radiation measurements and atmospheric characterization observations, including an AERONET site. Solar radiation measurements in the Évora station of the IES are taken in similar way as in the BSRN stations: two pyranometers (Kipp & Zonen CM6B) and one pyrheliometer (Kipp & Zonen CHP1) are mounted on a sun tracker system (Kipp & Zonen Solys2), including a shading ball assembly for the pyranometer that measures the diffuse component. The sensors are properly maintained and calibrated, and their outputs are sampled every second. The mean, maximum, minimum and standard deviation values of DNI, DHI and GHI are recorded every minute through a programmable data logger. This station is particularly useful to this study since the AERONET and solar radiation stations are at the same location and altitude, only a few meters apart. BSRN and IES data were filtered to ensure data quality using the physically possible and extremely rare limits [44] for DNI, GHI and DHI. The AERONET and BSRN records were matched by rounding the AERONET records to the next minute. Although minor discrepancies may occur, both network records should be representative of the same atmospheric conditions at any given time.

An analysis of other sites with both AERONET and BSRN stations is also carried out, and the locations presented in Table 4.1 are selected because aerosol and solar radiation measurements are available at a short distance and at similar altitudes, and therefore are considered as representative of the same meteorological conditions. The aim here is to study how different meteorological conditions around the globe affect both DNI and CSNI, regarding solar resource assessment and the installation of CSP systems. Detailed information on the stations used in this study can also be found in Table 4.1. For conciseness, each station is identified by its 3-letter BSRN code in what follows. For model development and performance assessment purposes (Sections 4.7 and 4.8), data in each dataset are randomly divided into a training dataset and a validation dataset. The training dataset is composed of approximately two thirds of the total records while the validation dataset is composed of the remaining one third.

Table 4.1: AERONET and BSRN stations used in this study.

Location	BSRN				AERONET				Period
	Code	Lat. (°N)	Long. (°E)	Alt. (m)	Code	Lat. (°N)	Long. (°E)	Alt. (m)	selected
Darwin, AUS	DAR	-12.425	130.831	30	ARM_Darwin	-12.425	130.891	29.9	2012-2014
Évora, PRT	EVR	38.568	-7.912	293	Evora	38.568	-7.912	293	2015-2017
Gobabeb, NAM	GOB	-23.5614	15.042	407	Gobabeb	-23.562	15.041	405	2015-2017
São Martinho da Serra, BRA	SMS	-29.4428	-53.823	489	Sao_Martinho_SONDA	-29.443	-53.823	489	2014-2016
Tamanrasset, DZA	TAM	22.7903	5.529	1385	Tamanrasset_INM	22.790	5.530	1377	2014-2016
Xianghe, CHN	XIA	39.754	116.962	32	Xianghe	39.754	116.962	36	2008-2010

4.4 Direct normal and circumsolar irradiance modelling

The DNI and CSNI simulations were performed using the libRadtran software package [26]. LibRadtran version 1.7 [26] was used despite version 2.0.1 [45] is currently available. The authors are more familiar with version 1.7 and, as stated in Eissa et al. [7], both versions produce the same outputs. LibRadtran is a library of radiative transfer routines, which provides multiple options to set-up and modify an atmosphere with several elements such as gas molecules, clouds and aerosol particles [26]. The main tool of libRadtran is the radiative transfer routine *uvspec*, which allows the user to choose among several solvers of the radiative transfer equation, such as DISORT [46] for the discrete ordinates method or MYSTIC [28] for the Monte Carlo method. In this way, AERONET measurements were used to create an input file to the *uvspec* tool, in order to simulate both DNI and CSNI at the locations and periods of Table 4.1, following a similar methodology to Eissa et al. [7] and Eissa [39]. The first step was to access and process the AERONET data, which is described in the following. The spectral range of simulations used in this work is 200-5000 nm, which covers the spectral range of response of a conventional pyrheliometer (300-4000 nm) [3]. Although the upper limit of response of a standard pyrheliometer is 4000 nm, the wavelength limit of 5000 nm is selected to account for the calibration of the pyrheliometers against windowless absolute cavity radiometers.

The aerosol optical depth (AOD) was retrieved from the AERONET Direct Sun Algorithm while the single-scattering albedo, surface albedo and aerosol phase function were obtained through an inversion method (V3) of the AERONET radiance measurements [42]. The uncertanties associated with these variables are the following: ∼0.01-0.02 for the AOD [42], ∼0.03 for the single-scattering albedo [47], ∼50% for surface albedo [47] and ∼5% for the aerosol phase function [47]. The precipitable water vapour was obtained through the sky irradiance measurements at 940 nm with

an uncertanty of ∼10% [48]. This leads to slightly different timestamps for precipitable water vapour with respect to aerosol data. For this reason, the precipitable water vapour values were linearly interpolated in order to match the aerosol data timestamps. On the other hand, libRadtran requires that the aerosol PHFN be described as a series of Legendre polynomials. Since the AERONET's PHFN data points have irregular angular steps between 0° and 180°, a preliminary spline interpolation was made to obtain a PHFN with a regular angular step of 0.1°, thus providing a finer decomposition. Because aerosol measurements are available at the wavelengths of 440 nm, 675 nm, 870 nm and 1020 nm, the PHFN functions need to be interpolated and extrapolated to define them between 200 and 5000 nm. The interpolation was performed using the Fraunhofer method as presented in Eissa et al. [7], Wilbert et al. [14]. Through this method, the 440 nm and 1020 nm PHFN were used to compute the 200 nm and 5000 nm phase functions, respectively. Finally, the decomposition of the phase functions in Legendre polynomials was performed through the *pmom* tool available with libRadtran [26]. In Section 4.5.3, a more detailed analysis of the number of Legendre polynomials used to decompose the PHFN is presented.

Aerosol optical depth data at 200 and 5000 nm were obtained using aerosol optical data at 440 and 5000 nm, respectively, and Ångström's law [49, 7]. The surface albedo and the single-scattering albedo values at 440 nm and 1020 nm were used to represent the same variables at 200 nm and 5000 nm, respectively. This procedure was adopted for two reasons: (i) because it can be difficult to accurately characterize the spectral surface albedo near the ground-based stations; and (ii) because the type of aerosols available in the several stations is not always the same. Therefore, using a simple model to scale the single-scattering albedo could change its variation along the spectrum.

The input file of the libRadtran simulations was built in the following way: firstly, the auxiliary files were created: (i) the file containing the atmospheric layers (*aerosol_files*), where the wavelength, extinction coefficient, aerosol single-scattering albedo and the moments of Legendre polynomials for the PHFN are specified, and (ii) the file containing the surface albedo data. Next, the libRadtran primary input file is created. A mid-latitude summer atmospheric profile (*afglms*) available in the libRadtran and the solar spectrum reported by Gueymard [50] were used. Latitude, longitude, and altitude were specified according to the location simulated. The command *correlated_k* was used with the option *lowtran* to obtain the spectrally integrated values of irradiance, where the gas absorption parametrisation code is adopted from the SBDART toolbox [51]. The solar zenith and azimuth angles were determined using the BSRN timestamp and latitude and longitude, through the *zenith* tool based on the Blanco-Muriel et al. [52] algorithm. A 1D grid of sky elements with the centre of the sun in one end was created to determine the sky radiance in

the circumsolar region, with 6° of scattering angle in the zenithal direction (constant azimuth) and a mesh interval of 0.1°. The zenith and azimuth angles of these sky elements were determined as a function of the respective scattering angles and solar zenith and azimuth angles thus allowing to obtain the diffuse radiance in the sun disk and circumsolar regions. The number of streams used was 16, which is the default value in libRadtran. All simulations, except for those reported in subsection 4.5.3, were carried out using 2048 Legendre moments to decompose the aerosol phase function.

The sky radiance from the libRadtran output file was used to calculate CSNI (Eq. 4.6) at each station, since not all stations have the same pyrheliometer model installed, which has a direct impact on the penumbra function due to different aperture angles of the instruments. The stations of EVR, GOB and XIA are equipped with a Kipp & Zonnen CHP1 whereas the stations of DAR, SMS and TAM are equipped with an Eppley NIP. These instruments have distinct half-aperture angles. The Kipp & Zonnen CHP1 has an half-aperture angle of 2.5° a slope angle (α_s) of 1.0° and a limit angle (α_l) of 4.0° whereas the Eppley NIP has an half-aperture angle of 2.9°, a slope angle of 1.8° and a limit angle of 4.0° [3]. Both instruments have a reported uncertainty of $\sim$ 2% [7, 53]. The numerical integration of sky radiance (Eq. 4.6) was done through Riemann sums, taking into account the slope and limit angles of the instruments installed at each location. The direct horizontal irradiance from the libRadtran output file was converted into DNI using the zenith angle and it was compared against BSRN ground-based measurements, both without and with the circumsolar contribution, following the methodology presented in Eissa et al. [7] and Eissa [39]. This allows for an indirect validation of the modelled CSNI values, since no measurements of CSNI are available at the locations studied. This procedure is addressed in more detail in Section 4.6.

4.5 Sensitivity analysis

4.5.1 Analysis of the sky radiance distribution in the circumsolar region

In the literature, it is common to present CSNI as the integral of the azimuthally averaged sky radiance, thus assuming both the sun disk and circumsolar region as symmetric. However, for high solar zenith angles (θ) and/or atmospheres with high aerosol concentrations, this assumption may not always hold. In this analysis, a 2D grid of sky elements was created to determine the sky radiance in the circumsolar region, with 6° of scattering angle in the azimuthal direction and 12° in the zenithal direction (half circumsolar region), with a mesh interval of 0.1°. The zenith (θ) and azimuth (φ) angles of these sky elements were determined as a function of the respective scattering angles and solar zenith and azimuth angles. As an example,

the cumulative distribution functions of solar zenith angle, aerosol optical depth at 440 nm and precipitable water vapour at Évora (EVR) are presented in Fig. 4.1, and the CSNI determined along the directions with constant zenith (θ) and azimuth (φ) angles is shown in Fig. 4.2. In the analysis presented in this section, all the CSNI values were calculated for an half-aperture angle of 2.5°, which is the standard half-aperture angle for a pyrheliometer as stated by the WMO [54]. The

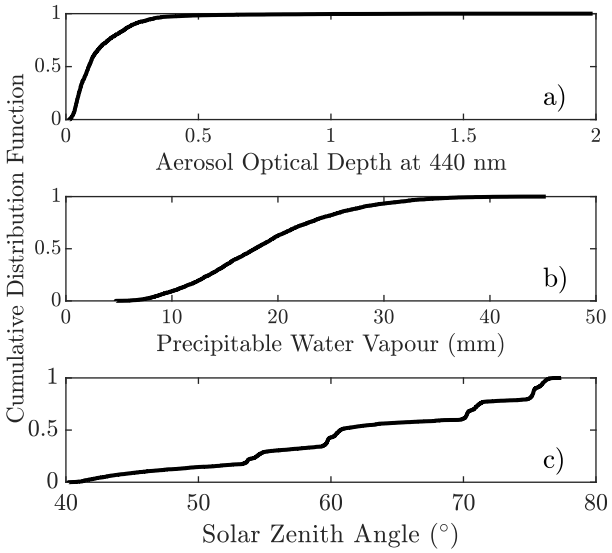

Fig. 4.1: Cumulative distribution functions of: a) aerosol optical depth at 440 nm; b) precipitable water vapour; and c) solar zenith angle for EVR station.

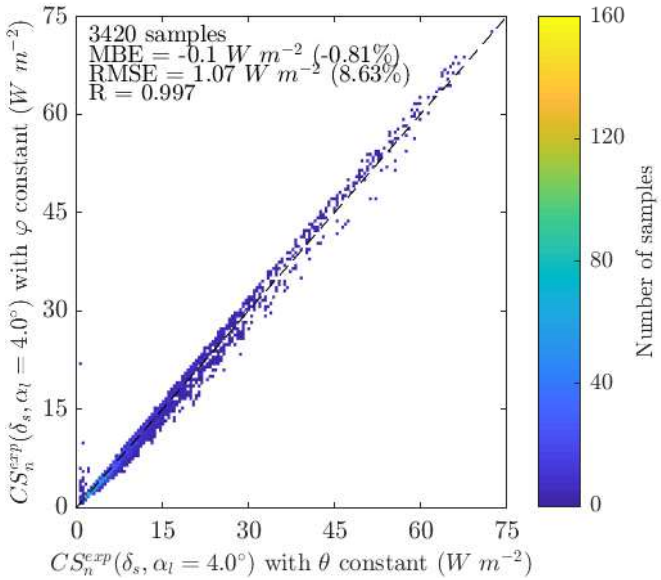

Fig. 4.2: Comparison of circumsolar irradiance obtained through the integration of sky radiance along constant zenith (θ) and azimuth (φ) lines.

results presented in Fig. 4.2 show that CSNI obtained through the integration of

sky radiance along a line of constant φ is close to the CSNI obtained along a line of constant θ, with a mean bias error (MBE) of -0.81%, a root mean square error (RMSE) of 8.63% and a correlation coefficient (R) of 0.997, taking the CSNI obtained along a line of constant φ as reference. Differences are slightly higher with increasing values of CSNI, typically for higher solar zenith angles and/or aerosol concentration in the atmosphere. Nevertheless, since this difference is still small, the azimuthally averaged sky radiance was used in this work to determine CSNI. This simplification also results in lower computation times, since it is sufficient to simulate a smaller portion of the circumsolar region, only along a line of constant azimuth angle.

4.5.2 Variation of circumsolar irradiance with the solar zenith angle

In this subsection, the influence of the solar zenith angle in the determination of DNI and CSNI is studied. Instead of using random values for the input parameters, in this analysis the values for three different points in the cumulative distribution functions (CDF) of the AERONET variables for the EVR station are selected as libRadtran inputs. To do this, the AERONET measurements that were closer to the values that correspond to a CDF of 0.25, 0.50 and 0.75 were found.

AERONET records were selected using the CDF of aerosol single-scattering albedo, aerosol optical depth and surface albedo values for all wavelengths. This procedure consisted in defining an initial small tolerance interval centred on the CDF values. The tolerance interval was then reduced until only one AERONET record remained. In this way, the AERONET records selected to represent the CDF values of 0.25, 0.50 and 0.75 were 10/08/2015 16:55:07, 28/06/2016 18:35:32 and 23/08/2016 07:14:23, respectively. The precipitable water vapour was not used in this selection procedure due to the need of a high tolerance interval to find the representative AERONET records.

Having selected the AERONET measurements to be used in the simulations, only the solar zenith angle was changed between the minimum value for the day of each record and 85°, i.e., the aerosol properties and precipitable water conditions were assumed constant. The value of 85° was chosen considering the known difficulties of models to simulate sky radiance for high solar zenith angles. Fig. 4.3 shows the variation of the sun-disk DNI (B_n^{sun}), the apparent DNI (B_n^{exp}), as well as CSR, as a function of θ. Three cases are presented referring to the selected records that best represent the three points of the CDF values at EVR station.

The circumsolar component for the cases presented in Fig. 4.3 increases as the solar zenith angle also increases. This occurs because of the concomitant increase of the path-length that the sun rays travel in the atmosphere (air mass), leading to a higher dispersion (scattering) of the sun rays, hence higher values of CSNI, and consequently, higher values of CSR.

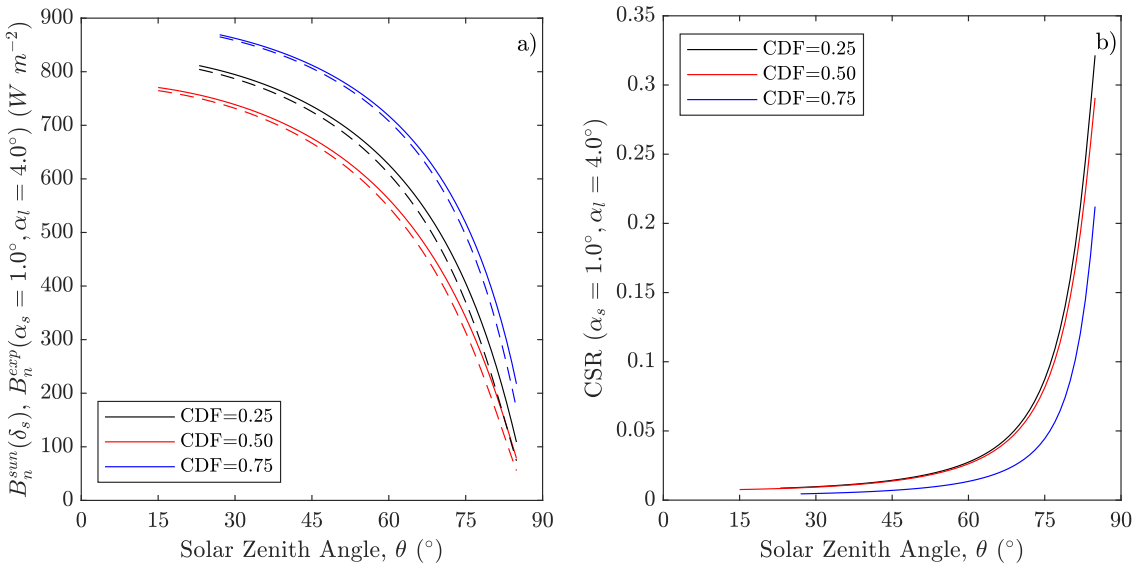

Fig. 4.3: Variation of sun disk DNI ($B_n^{sun}(\delta_S)$, dashed line) and DNI including the CSNI ($B_n^{exp}(\alpha_s, \alpha_l)$, solid line) (a) and CSR (b) with the solar zenith angle (EVR station).

4.5.3 Effect of the number of moments of the aerosol phase function on the circumsolar irradiance modelling

LibRadtran requires that the aerosol phase function be decomposed in a series of Legendre polynomials. Using the *pmom* tool, the aerosol phase function can be decomposed in a user-defined number of polynomials through the *nmom* parameter. In this way, a sensitivity analysis of the number of Legendre polynomials of the PHFN was performed. The number of Legendre polynomials tested was 32, 64, 128, 256, 512, 1024, 2048, 4096 and 8192, for the same representative AERONET records of the CDF values 0.25, 0.50 and 0.75 for the EVR station (Section 4.5.2), as shown in Fig. 4.4.

A lower number of Legendre polynomials results in an underestimation of the CSNI due to the less accurate representation of PHFN. For *nmom* above 256, the CSNI tends to a nearly constant value. Therefore, it is recommended to use a minimum of 256 Legendre polynomials to decompose the PHFN. This number of Legendre polynomials should produce the same outputs as simulations with higher number of polynomials, but saving simulation time and computation resources.

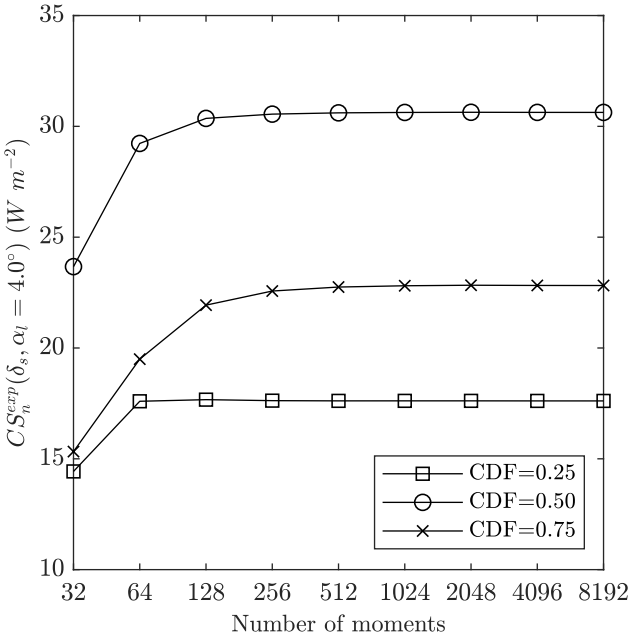

Fig. 4.4: Variation of modelled circumsolar irradiance with the number of Legendre polynomials used in the aerosol phase function decomposition (EVR station).

4.5.4 Grid independence test

The sky radiance is calculated by libRadtran in the sky elements defined by the user. Therefore, the grid of sky elements can be adjusted considering the time required for a simulation to be completed and the desired level of detail in the circumsolar region. Aiming at an accurate characterization of the circumsolar region as well as the fastest possible simulations, several meshes with different scattering angle intervals were tested for the selected records that best characterise the CDF values 0.25, 0.50 and 0.75 (Section 4.5.2). The scattering angle intervals tested were 0.01°, 0.02°, 0.05°, 0.1°, 0.2° and 0.5°. The variation of modelled CSNI values with the scattering angle interval at Évora for the selected records that best characterise the CDF are shown in Fig. 4.5. The modelled CSNI is nearly constant when considering scattering angle intervals up to 0.10° in all cases. On one hand, higher scattering interval values (above 0.20°) lead to a decrease in the accuracy of CSNI modelling, including the numerical integration process of Eq. 4.6, because of the difficulty in defining the sun disk limit with larger mesh intervals. This leads to a less accurate characterization of the circumsolar region and, therefore, to a lower CSNI value, even if efficient interpolation techniques are used. On the other hand, scattering angle intervals lower than 0.10° can be used if a more detailed analysis at the limits of the circumsolar region is required, at the expense of computational resources and simulation time. The scattering angle interval can affect the determination of CSNI to a certain extent, which in turn can affect the fitting and performance assessment

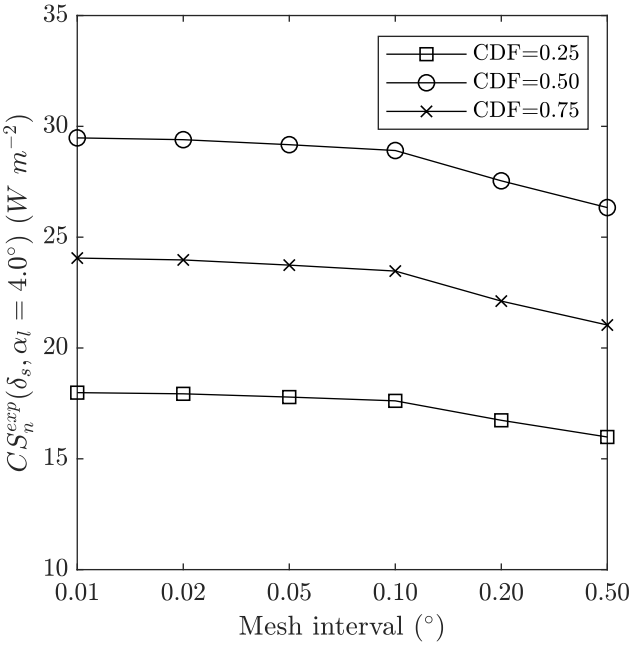

Fig. 4.5: Variation of modelled circumsolar irradiance with the mesh interval (EVR station).

of models, if different scattering angle intervals were used in the model development. Therefore, it is recommended to use a maximum scattering angle mesh interval of 0.10° when simulating CSNI, aiming for accurate model results and faster simulation times.

4.6 Simulation results

4.6.1 Modelled direct normal and circumsolar irradiance validation

The common procedure to evaluate the performance of a model is to directly compare simulated values against high-quality ground-based measurements. However, CSNI measurements are very scarce and are not available at the locations analysed in this study. Therefore, an indirect validation of the CSNI measurements is carried out [7]. In this way, firstly the sun-disk DNI ($B_n^{sun}(\delta_S)$) is compared against measurements from pyrheliometers, which is expected to result in a negative bias because CSNI is not included. Secondly, the apparent DNI ($B_n^{exp}(\alpha_s, \alpha_l)$) is compared to the same measurements, with an expected bias close to zero. An error reduction when adding the CSNI component is taken as an improvement on the simulated data and used here to validate the modelling approach. Statistical indicators such as mean bias error (MBE), root mean square error (RMSE) and correlation coefficient (R) are used to evaluate the accuracy of the simulations. The comparison between sun-disk DNI ($B_n^{sun}(\delta_S)$) and observations is shown in Fig. 4.6, whereas Fig. 4.7 shows the same comparison for the case of the apparent DNI ($B_n^{exp}(\alpha_s, \alpha_l)$).

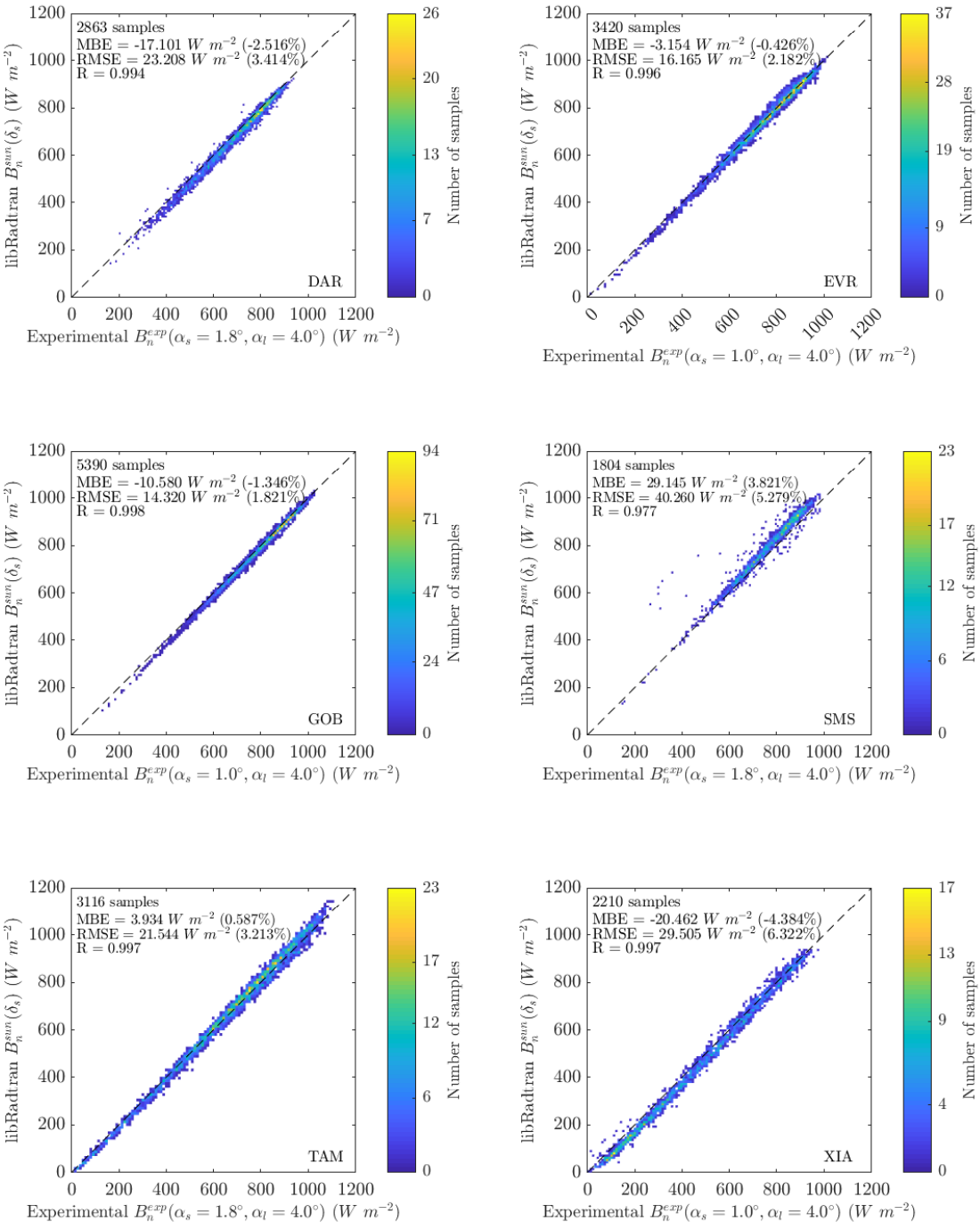

Fig. 4.6: Comparison of sun-disk DNI ($B_n^{sun}(\delta_s)$) to ground-based measurements.

The simulated DNI values show good agreement with the ground-based measurements for all locations simulated in this work. In Fig. 4.6, the simulated values of $B_n^{sun}(\delta_S)$ present a negative bias at DAR, EVR, GOB and XIA, as expected. Only the simulated values for SMS and TAM show a positive bias. This can be explained by small disagreements between the time stamps when the AERONET and BSRN

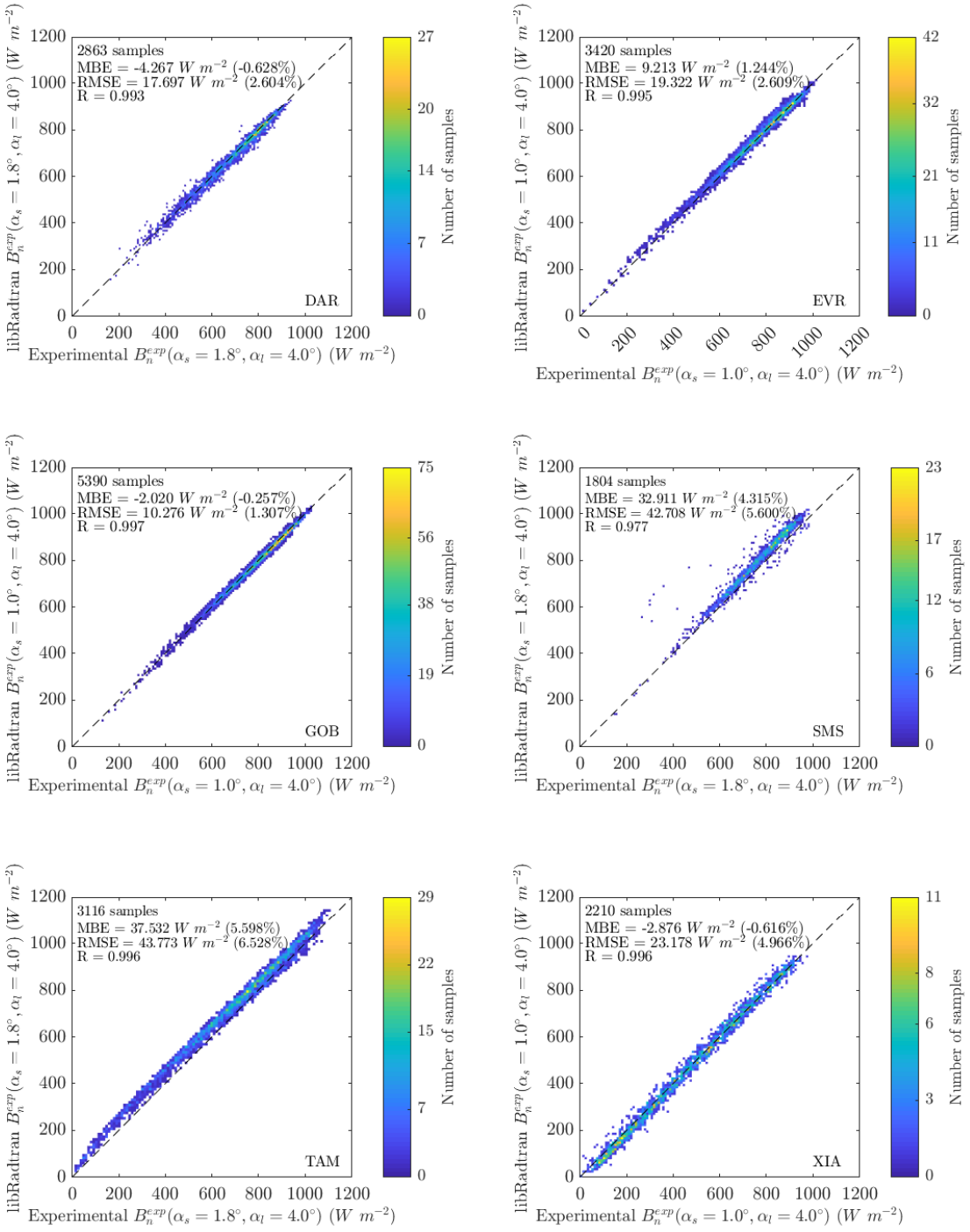

Fig. 4.7: Comparison of apparent DNI ($B_n^{exp}(\alpha_s, \alpha_l)$) to ground-based measurements.

measurements were taken, and both observations and model output uncertainties. Nevertheless, results still agree well with experimental values, with a maximum MBE of -4.38%, a maximum RMSE of 6.32% and a minimum R of 0.977. Adding the $CS_n^{exp}(\alpha_s, \alpha_l)$ to the modelled $B_n^{sun}(\delta_S)$ (Fig. 4.7), the bias between simulated and measured $B_n^{exp}(\alpha_s, \alpha_l)$ is close to zero at all stations, except for the SMS and TAM

stations. The RMSE decreases at DAR, GOB and XIA stations, slightly increases at EVR station and increases at SMS and TAM. Regarding the correlation coefficient, no relevant differences between including or not the $CS_n^{exp}(\alpha_s, \alpha_l)$ are found. The small decrease in performance of the simulations according to MBE and RMSE when adding the $CS_n^{exp}(\alpha_s, \alpha_l)$ for the SMS and TAM stations does not invalidate the modelled values of CSNI, since MBE values around 5% and RMSE values around 6% are in accordance with recent studies from the literature, e.g. [55, 34]. Therefore, the general agreement between $B_n^{exp}(\alpha_s, \alpha_l)$ and ground-based measurements is an indicator of the good quality of the simulated $CS_n^{exp}(\alpha_s, \alpha_l)$ data. For the case of TAM, some malfunctions have been detected by Gueymard [56] on the retrieval of AOD. Although these cases are rare, they can have some impact on the results presented in Fig. 4.6 and Fig. 4.7.

The uncertainties of the pyrheliometer measurements used as reference must be taken into account when analysing the results from Fig. 4.6 and Fig. 4.7. The instruments installed at these locations both have a reported uncertainty of $\sim$ 2%. Following the approach presented in Habte and Sengupta [57], the overall uncertainty with a 95% confidence interval (CI) was determined for both $B_n^{sun}(\delta_S)$ and $B_n^{exp}(\alpha_s, \alpha_l)$, as shown in Fig. 4.8. The overall uncertainty is determined using the uncertainty from the reference data as well as the MBE and RMSE values from the modelled data. This allows for an easy comparison between different data sets, taking into consideration the uncertainties of the reference data.

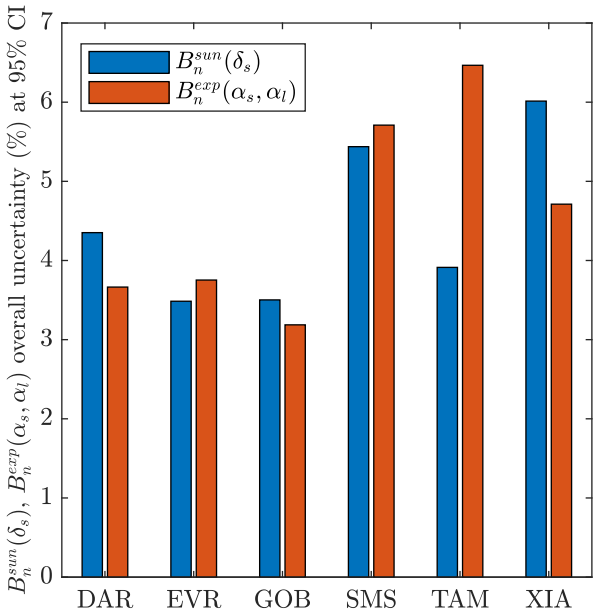

Fig. 4.8: Overall uncertainty of $B_n^{sun}(\delta_S)$ and $B_n^{exp}(\alpha_s, \alpha_l)$ at 95% confidence interval (CI) for all stations, in percentage.

From Fig. 4.8, the overall uncertainty is higher at SMS, TAM and XIA for both

$B_n^{sun}(\delta_S)$ and $B_n^{exp}(\alpha_s, \alpha_l)$. Adding the $CS_n^{exp}(\alpha_s, \alpha_l)$ to $B_n^{sun}(\delta_S)$ results in a decrease of the overall uncertainty at DAR, GOB and XIA and in small increase at EVR and SMS. At TAM, a larger increase on the overall uncertainty is observed. In general, the average overall uncertainty is 4.35% in $B_n^{sun}(\delta_S)$ and 4.44% in $B_n^{exp}(\alpha_s, \alpha_l)$, which approximately doubles the uncertainty in the reference data.

4.6.2 Circumsolar Normal Irradiance and Circumsolar Ratio analysis

Under clear skies, the CSNI is strongly related to the aerosol optical depth and aerosol type [56]. The CSNI relative frequency for the six locations analysed in this study is presented in Fig. 4.9, which allows a comparison of the magnitude of CSNI at the different stations. TAM and XIA have the higher relative frequencies for high values of CSNI, whereas at locations such as GOB and SMS, the relative frequency is higher for low values of CSNI. This implies that the addition of CSNI to the DNI modelled values can have a higher impact on the modelled DNI for locations such as TAM and XIA than in the case of SMS, for instance.

The cumulative distribution functions (CDF) of the CSR for the stations analysed are presented in Fig. 4.10. The SMS and GOB stations have the lowest CSR, with 95% of values under 0.0175 and 0.0423, respectively. On the contrary, TAM and XIA stations present the higher CSR, with 25% of values above 0.0982 and 0.0963, respectively. This information is useful for CSP systems design and operation, alongside more commonly used parameters such as DNI or soiling rate data.

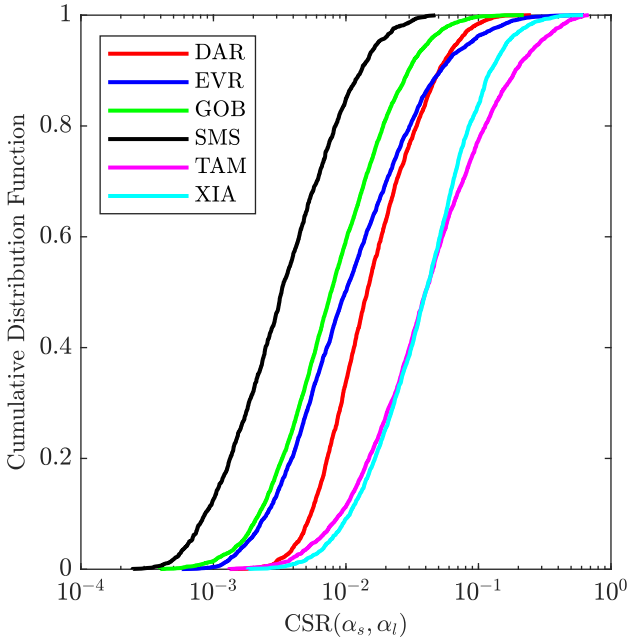

Fig. 4.10: CSR cumulative distribution functions for all stations ($\alpha_s = 1.0$ for EVR, GOB and XIA and $\alpha_s = 1.8$ for DAR, SMS and TAM; $\alpha_l = 4.0$ for all stations).

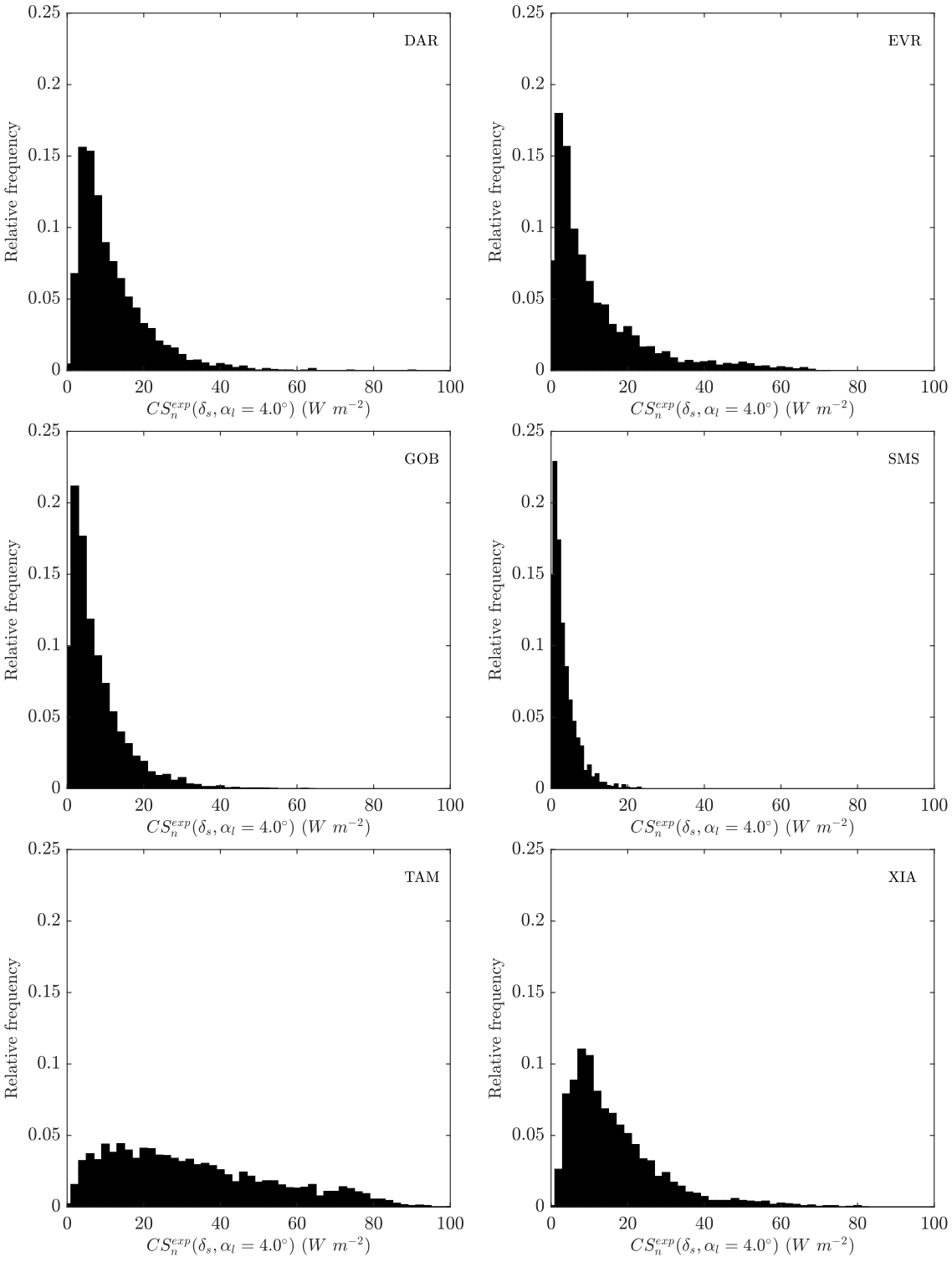

Fig. 4.9: Relative frequency of CSNI.

4.7 Circumsolar irradiance model parametrisation

In this section, a parametrisation is proposed for the determination of CSNI. The objective is to provide a simple model based on widely available solar radiation

measurements such GHI, DHI or DNI, in order to easily estimate CSR and CSNI. To the authors' best knowledge, only Neumann et al. [36], Ivanova [37] and Eissa et al. [7] presented models of this type. A novel model is presented in this work, aiming at a better characterization of the CSNI using the sky clearness index (K_t) - the ratio between GHI at the Earth surface and its counterpart at the top of the atmosphere [58]; the diffuse fraction (K_d) - the ratio between DHI and GHI [59]; and the beam clearness index (K_b) - the ratio between DNI at the Earth surface and DNI at the top of atmosphere [60].

Under clear-sky conditions the circumsolar normal irradiance (CSNI) is directly proportional to the diffuse irradiance, that is, if the diffuse horizontal irradiance (DHI) is higher, then the CSNI is also higher due to augmented scattering of solar radiation in the atmosphere:

$$CSNI \sim DHI. \tag{4.9}$$

Still under clear-sky conditions, the same relationship can be established between the circumsolar ratio (CSR = CSNI/DNI) and K_d:

$$CSR \sim K_d. \tag{4.10}$$

In other words, the ratio between CSNI and the irradiance actually measured by a pyrheliometer (sun-disk DNI plus CSNI) is directly proportional to the ratio between DHI (excluding the circumsolar component) and GHI. However, due to the very different magnitudes of CSNI with respect to sun-disk DNI plus CSNI, and of DHI compared to GHI, it is found that the variation of CSR is better described as a function of K_d if the following relation is used:

$$CSR \sim \frac{K_d}{1 - K_d}, \tag{4.11}$$

which still assures that CSR is higher when K_d is also higher, provided that $0 \leq K_d < 1$, which is always the case under clear-sky conditions. On the other hand, if the measured direct normal irradiance increases with respect to the extraterrestrial irradiance on a plane normal to the sun axis, this is an indication of a lower air mass and/or cleaner atmosphere with lower scattering effect (higher intensity but lower fraction of sky radiance from the solid angle between the sun radius and the limit angle, not considering here the absorption), and thus lower CSR. These relations can be represented as follows:

$$CSR \sim \frac{1}{K_b}; \tag{4.12}$$

$$CSR \sim \frac{1}{K_t}. \tag{4.13}$$

It should be noted that K_b and K_t provide a measure of the total transmissivity of the atmosphere under clear-sky conditions, including the effect of the solar zenith

angle and air mass. Combining the three relations above, the following expression is proposed to model CSR:

$$CSR \sim \frac{K_d}{K_t K_b (1 - K_d)}. \tag{4.14}$$

For a better representation, and due to the different orders of magnitude of the variables involved, the following form is more suitable:

$$CSR(1 - K_d) \sim \frac{K_d}{K_t K_b}, \tag{4.15}$$

and, in order to determine how the group $CSR(1 - K_d)$ depends on the right-hand term of this relation, a transform of Eq. 4.15 is finally proposed:

$$CSR(1 - K_d) = \frac{a}{b + (K_t K_b / K_d)^c}, \tag{4.16}$$

in which a, b and c are fitting coefficients that are determined using the training datasets of the various locations under analysis. Under uniform diffuse sky radiance conditions, CSNI and sun-disk DNI are of the same order of magnitude, and a CSR different from zero can be calculated in that limit (but hardly measured), which depends only on the angular radius of the sun and the limit angle of the pyrheliometer if a uniform diffuse sky radiance is assumed (L in Eq. 4.3, 4.6 and 4.5) and if the penumbra effect is neglected. Also, in that limit, K_d is slightly different from one, with that difference being of the same order of magnitude of the CSR, while the group $K_t K_b / K_d$ tends to zero. This is the reason why the group $CSR(1 - K_d)$ tends to a fixed value at the origin. In the opposite limit of very clear skies (or in the hypothetical limit in which scattering tends to zero), the CSNI and DHI decrease (and in the mentioned hypothetical limit tend to zero) while the group $K_t K_b / K_d$ increases (and tends to infinity in the mentioned limit), which is in accordance with the proposed model.

The model fitting presents low values of mean bias error (MBE), thus indicating a good representation of the training datasets (see Table 4.2). The only exception is the case of XIA, where MBE unexpectedly increases, for reasons still unclear and, therefore, a more detailed analysis on this issue would be required. In Table 4.2, an average value for each coefficient regarding the pyrheliometers installed at each station is also shown. This provides a global model, albeit at a preliminary stage because of the sparse data it is built from. Fig. 4.11 shows data and model adjustment for the case of EVR. The CSR values were obtained from the libRadtran simulations while the clearness indexes K_t and K_b and the diffuse fraction K_d were determined from the experimental values.

The uncertainties associated with the CSR determination are worth noting. For that reason, the relative uncertainty associated to the determination of CSR at EVR is computed and is presented in Fig. 4.12. The uncertainties of the model parameters

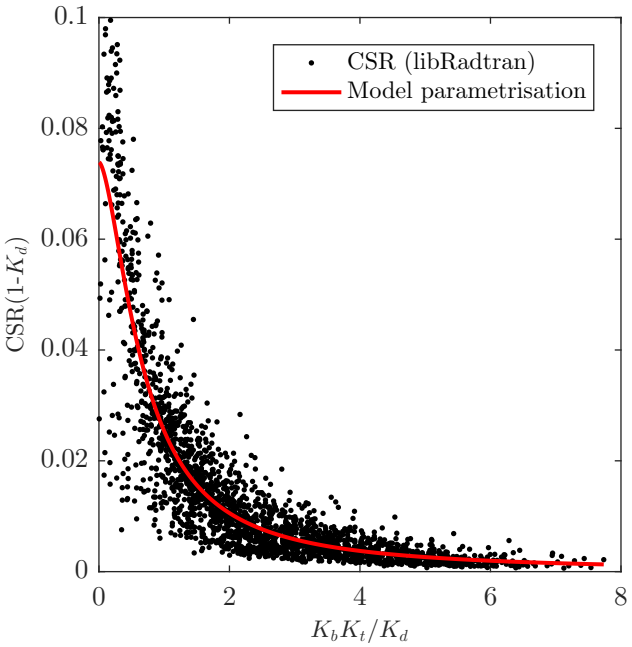

Fig. 4.11: Circumsolar ratio model parametrisation for the EVR station ($\alpha_s = 1.0, \alpha_l = 4.0$).

Table 4.2: Model parameters and respective 95% confidence intervals and mean bias error (MBE) of model fitting for each station and pyrheliometer model.

Station	Parameter			MBE (%)
	a	b	c	
DAR ($\alpha_s = 1.8°, \alpha_l = 4.0°$)	0.0282±0.002	0.5535±0.0795	1.4136±0.1084	-0.5571
EVR ($\alpha_s = 1.0°, \alpha_l = 4.0°$)	0.0386±0.0017	0.5229±0.0401	1.6478±0.0734	-0.6896
GOB ($\alpha_s = 1.0°, \alpha_l = 4.0°$)	0.0478±0.0041	1.3078±0.1713	1.8250±0.0972	-0.0287
SMS ($\alpha_s = 1.8°, \alpha_l = 4.0°$)	0.0376±0.0075	2.3817±0.6336	2.2632±0.2257	-1.3910
TAM ($\alpha_s = 1.8°, \alpha_l = 4.0°$)	0.0876±0.0039	0.8481±0.0529	1.3540±0.0613	0.0092
XIA ($\alpha_s = 1.0°, \alpha_l = 4.0°$)	0.1160±0.0563	4.5406±2.3210	2.4988±0.7156	6.8648
Mean Eppley NIP ($\alpha_s = 1.8°, \alpha_l = 4.0°$)	0.0598	1.4589	1.9587	-
Mean Kipp&Zonen CHP1 ($\alpha_s = 1.8°, \alpha_l = 4.0°$)	0.0453	1.0379	1.6301	-

a, b and c are obtained from their confidence intervals, as presented in Table 4.2. The uncertainties of K_t, K_b and K_d are determined using the uncertainty of the

instruments used to measure GHI, DNI and DHI, respectively, $\sim 2\%$ for DNI [53, 7] and $\sim 5\%$ for GHI and DHI [61]. This results in an average relative uncertainty of approximately 9.5%.

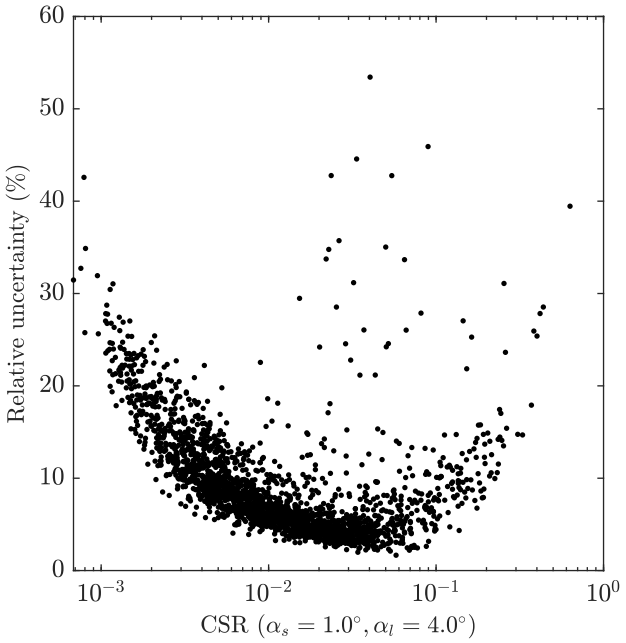

Fig. 4.12: Circumsolar Ratio relative uncertainty at EVR.

4.8 Parametrisation results and discussion

In order to perform a fair comparison against models available in the literature, the model coefficients from Neumann et al. [36] and Eissa et al. [7] were fitted to the same training datasets used in this work. The model from Ivanova [37] is also used in this comparison, however without fitting that model to the data since this is a global model. Thus, the Ivanova [37] model was then compared against the global model presented in this work, determined through the mean values of the site-specific coefficients depending on the pyrheliometer model (i.e., slope and limit angles). Since the number of points is different for each station, this approach is selected instead of determining new coefficients. In this way, each station has the same weight when determining the global model coefficients. The performance of the models is assessed using the validation datasets and the MBE, RMSE, R, fractional bias (FB) and fractional gross error (FGE) statistical indicators. The fractional bias and fractional gross error are defined as:

$$FB = \frac{2}{N}\sum_{i=1}^{N}\frac{I_{e,i} - I_{m,i}}{I_{e,i} + I_{m,i}}; \tag{4.17}$$

$$FGE = \frac{2}{N}\sum_{i=1}^{N}\frac{|I_{e,i} - I_{m,i}|}{|I_{e,i} + I_{m,i}|}, \tag{4.18}$$

respectively, where I_e is the estimated irradiance by the model from Eq. 4.16, I_m is the irradiance determined using libRadtran and N is the total number of observations. Results are presented in Table 4.3, where values in bold represent the best model (site-fitted and global) according to each station/statistical indicator.

Table 4.3: Performance assessment of circumsolar parametrisation models.

Station	Statistical indicator	Adjusted coefficients			Global coefficients	
		Neumann et al. [36]	Eissa et al. [7]	This work	Ivanova [37]	This work
DAR ($\alpha_s = 1.8°, \alpha_l = 4.0°$)	MBE (%)	-5.34	1.19	**-0.88**	93.34	**14.94**
	RMSE (%)	76.08	62.25	**50.58**	132.23	**53.63**
	R	0.69	0.59	**0.74**	0.71	**0.73**
	FB	0.29	0.09	**0.04**	0.62	**0.20**
	FGE	0.70	0.35	**0.28**	0.64	**0.33**
EVR ($\alpha_s = 1.0°, \alpha_l = 4.0°$)	MBE (%)	-26.71	**-0.19**	-1.98	56.18	**-11.52**
	RMSE (%)	158.03	59.17	**43.19**	95.99	**55.17**
	R	0.79	0.81	**0.90**	0.86	**0.86**
	FB	0.49	**0.04**	0.05	0.52	**0.01**
	FGE	1.04	0.37	**0.31**	0.55	**0.33**
GOB ($\alpha_s = 1.0°, \alpha_l = 4.0°$)	MBE (%)	**1.40**	4.77	1.92	105.47	**15.74**
	RMSE (%)	61.21	68.89	**54.82**	147.54	**58.73**
	R	0.73	0.64	**0.79**	0.74	**0.78**
	FB	-0.39	0.14	**0.11**	0.76	**0.20**
	FGE	5.30	0.40	**0.35**	0.77	**0.37**
SMS ($\alpha_s = 1.8°, \alpha_l = 4.0°$)	MBE (%)	6.04	6.37	**-3.70**	238.24	**114.53**
	RMSE (%)	65.40	66.70	**52.34**	319.95	**144.99**
	R	0.68	0.69	**0.81**	0.68	**0.80**
	FB	-0.17	0.10	**-0.04**	1.13	**0.80**
	FGE	1.04	**0.35**	0.35	1.14	**0.81**
TAM ($\alpha_s = 1.8°, \alpha_l = 4.0°$)	MBE (%)	-10.16	5.57	**1.22**	**8.67**	-55.05
	RMSE (%)	73.44	49.52	**29.59**	**49.43**	67.43
	R	0.84	0.68	**0.88**	0.83	**0.88**
	FB	0.39	0.09	**0.01**	**-0.08**	-0.80
	FGE	0.61	0.35	**0.22**	**0.35**	0.80
XIA ($\alpha_s = 1.0°, \alpha_l = 4.0°$)	MBE (%)	**4.12**	8.37	14.26	285.48	**61.80**
	RMSE (%)	**62.72**	69.79	176.28	358.33	**256.63**
	R	**0.49**	0.32	0.02	**0.15**	0.03
	FB	0.21	**0.19**	0.20	1.10	**0.45**
	FGE	**0.45**	0.47	0.52	1.10	**0.61**

From the adjusted coefficients section of Table 4.3, it is clear that the model developed here performs better considering the datasets used. The only exception, again, occurs at XIA, where the model proposed by Neumann et al. [36] outperforms the model presented here. However, closer examination reveals that the decrease of model performance at XIA occurs not only for the proposed model but also for the models of Eissa et al. [7] and Ivanova [37] as well. Generally, even if models have a low bias (some MBE values are under 1% for the model developed in this work), the RMSE values are high due to the difficulty in finding an independent variable that is highly correlated with the CSR data. The second best performer is the model

proposed by Eissa et al. [7]. In their work, they found values of -1.5%, 19.6% and 0.935 for MBE, RMSE and R, respectively, for the TAM station. However, they used a different dataset (AERONET level 2.0 data and different selected periods) and a different libRadtran input file, namely a different PHFN. Regarding the global coefficient section of Table 4.3, the model presented here outperforms the model from Ivanova [37] at every location except TAM. Based on these results, the model developed in this work can be used to estimate CSR, and thus CSNI, at several locations using more common solar radiation data, such as GHI, DHI or DNI.

4.9 Conclusions

In this work, a review and historical perspective of circumsolar irradiance (CSNI) modelling and measurement is presented, alongside a theoretical background on direct normal irradiance (DNI) and CSNI definitions. Furthermore, both sun-disk DNI and CSNI were modelled using AERONET data and the libRadtran RTM. CSNI was validated indirectly by comparing both sun-disk DNI alone and sun-disk DNI plus CSNI against ground-based measurements. The decrease in the error metrics when adding the CSNI predictions to the sun-disk DNI indicates the validity of the modelling approach. This type of validation was performed because there are no CSNI measurements at the locations of interest. MBE, RMSE and R values of around 1%, 2% and 0.99, respectively, were found for DAR, EVR and GOB stations and values around 5% and 6% for MBE and RMSE, respectively, were found for SMS, TAM and XIA stations, when comparing the modelled DNI with CSNI values against ground-based measurements. The slightly higher dispersion between modelled and measured data can be related to the uncertainties associated with the ground-based data and also to the distance between AERONET and BSRN stations. However, a more detailed analysis on this issue would be required.

A fast and simple model has been developed, aiming at the determination of CSNI for a half-aperture angle of 2.5°, using widely available GHI, DHI and DNI measurements. The proposed model performs generally better than other models available in the literature, with lower MBE, RMSE, FB and FGE, and higher correlation coefficient, for most of the datasets used. This model can be used to easily estimate the circumsolar ratio (CSR), and thus CSNI, resorting to widely available solar radiation data. Conversely, it can also be used to estimate the sun-disk DNI measured by a field pirhelyometer.

References

[1] P. Gauché, J. Rudman, M. Mabaso, W. Landman, and T. von Backström. System value and progress of CSP. *Solar Energy*, 152:106–139, 2017.

[2] J. Polo, F.-P. C., and M. Gastón. Analysis on the long-term relationship between DNI and CSP yield production for different technologies. *Solar Energy*, 155: 1121–1129, 2017.

[3] P. Blanc, B. Espinar, N. Geuder, C. Gueymard, R. Meyer, R. Pitz-Paal, B. Reinhardt, D. Renné, M. Sengupta, L. Wald, and S. Wilbert. Direct normal irradiance related definitions and applications: The circumsolar issue. *Solar Energy*, 110: 561–577, 2014.

[4] S. Wilbert, N. Janotte, R. Pitz-Paal, L. van Wely, and N. Geuder. Reduced uncertainties of field pyrheliometers through improved sensor calibration. In *SolarPACES*, 2010.

[5] S. Dugaria, A. Padovan, V. Sabatelli, and D. Del Col. Assessment of estimation methods of DNI resource in solar concentrating systems. *Solar Energy*, 121: 103–115, 2015.

[6] S. Wilbert. *Determination of circumsolar radiation and its effect on concentrating solar power*. Theses, July 2014.

[7] Y. Eissa, P. Blanc, H. Ghedira, A. Oumbe, and L. Wald. A fast and simple model to estimate the contribution of the circumsolar irradiance to measured broadband beam irradiance under cloud-free conditions in desert environment. *Solar Energy*, 163:497–509, 2018.

[8] E. F. M. Abreu, P. Canhoto, and M. J. Costa. Circumsolar irradiance modelling using libradtran and aeronet data. *AIP Conference Proceedings*, 2126(1):190001, 2019.

[9] J. Noring, D. Grether, and A. Hunt. Circumsolar radiation data: The lawrence berkeley laboratory reduced data base. final subcontract report. Technical report, National Renewable Energy Lab., Golden, CO; Lawrence Berkeley Lab., CA, 1991.

[10] D. Buie, A. G. Monger, and C. J. Dey. Sunshape distributions for terrestrial solar simulations. *Solar Energy*, 74:113–122, 2003.

[11] M. Schubnell. Sunshape and its influence on the flux distribution in imaging solar concentrators. *Journal of Solar Energy Engineering*, 114:260–266, 1992.

[12] A. Neumann, A. Witzke, S. A. Jones, and G. Schmitt. Representative Terrestrial Solar Brightness Profiles. *Journal of Solar Energy Engineering*, 124:198–204, 2002.

[13] A. Gambardella and R. Galleano. Characterization of a CCD-camera-based system for measurement of the solar radial energy distribution. *Measurement Science and Technology*, 22:105902 (9pp), 2011.

[14] S. Wilbert, B. Reinhardt, J. DeVore, M. Röger, R. Pitz-Paal, C. Gueymard, and B. R. Measurement of Solar Radiance Profiles With the Sun and Aureole Measurement System. *Journal of Solar Energy Engineering*, 135:041002, 2013.

[15] B. N. Holben, T. F. Ecken, L. Slutsker, D. Tanre, J. P. Buis, A. Setzer, E. Vermote, J. A. Reagan, Y. J. Kaufman, T. Nakajima, F. Lavenu, I. Jankowiak, and A. Smirnov. AERONET – a federated instrument network and data archive for aerosol characterization. *Remote Sensing of Environment*, 66:1–16, 1998.

[16] C. A. Gueymard. Parametrized transmittance model for direct beam and circumsolar spectral irradiance. *Solar Energy*, 71:325–346, 2001.

[17] S. Wilbert, R. Pitz-Paal, and J. Jaus. Comparison of measurement techniques for the determination of circumsolar irradiance. *AIP Conference Proceedings*, 1556:162–167, 2013.

[18] T. H. Jeys and L. L. Vant-Hull. The contribution of the solar aureole to the measurements of pyrheliometers. *Solar Energy*, 18:343–348, 1976.

[19] J. R. Hickey and A. R. Karoli. A variable field of view pyrheliometer. In *Proceedings of the 1977 Annual Meeting of the American Society of the International So1ar Energy Society*, 1977.

[20] G. Major. A method for determining the circumsolar sky function. *Tellus*, 32: 340–347, 1980.

[21] H. Al-Ansary, T. Shafiq, A. Rizvi, and A. El-Leathy. Measurement of Circumsolar Ratio in High Dust Loading Regions Using a Photographic Method. *AIP Conference Proceedings*, 1850:140003, 2017.

[22] S. Wilbert, M. Roger, J. Csambor, M. Breitbach, F. Klinger, B. Nouri, N. Hanrieder, F. Wolfertstetter, D. Schuler, S. Shaswattam, N. Goswami, S. Kumar, A. Ghennioui, R. Affolter, N. Geuder, and B. Krass. Sunshape measurements with conventional rotating shadowband irradiometers. *AIP Conference Proceedings*, 2033:190016, 2018.

[23] E. Thomalla, P. Kopke, H. Muller, and H. Quenzel. Circumsolar radiation calculated for various atmospheric conditions. *Solar Energy*, 30:575–587, 1983.

[24] Y. Eissa, P. Blanc, A. Oumbe, H. Ghedira, and L. Wald. Estimation of the circumsolar ratio in a turbid atmosphere. *Energy Procedia*, 57:1169–1178, 2014.

[25] R. Perez and J. Michalsky. All-weather model for sky luminance distribution - Preliminary configuration and validation. *Solar Energy*, 50:235–245, 1993.

[26] B. Mayer and A. Killing. Technical note: The libRadtran software package for radiative transfer calculations - description and examples of use. *Atmospheric Chemistry and Physics*, 5:1855–1877, 2005.

[27] B. Reinhardt, R. Buras, L. Bugliaro, S. Wilbert, and B. Mayer. Determination of circumsolar radiation from Meteosat Second Generation. *Atmospheric Measurement Techniques*, 7:823–838, 2014.

[28] B. Mayer. Radiative transfer in the cloudy atmosphere. *EPJ Web of Conferences*, 1:75–99, 2009.

[29] Y. Eissa, P. Blanc, L. Wald, and H. Ghedira. Can AERONET data be used to accurately model the monochromatic beam and circumsolar irradiances under cloud-free conditions in desert environment? *Atmospheric Measurement Techniques*, 8:5099–5112, 2015.

[30] I. Cole and R. Gottschalg. Improved Model for Circumsolar Irradiance Calculation as an Extended Light Source and Spectral Implications for High-Concentration Photovoltaic Devices. *IEEE Journal of Photovoltaics*, 6:258–265, 2015.

[31] Z. Sun, J. Li, Y. He, J. Li, A. Liu, and F. Zhang. Determination of direct normal irradiance including circumsolar radiation in climate/NWP models. *Quarterly Journal of the Royal Meteorological Society*, 142:2591–2598, 2016.

[32] P. Haapanala, P. Raisanen, G. M. McFarquhar, J. Tiira, A. Macke, M. Kahnert, J. DeVore, and T. Nousiainen. Disk and circumsolar radiances in the presence of ice clouds. *Atmospheric Chemistry and Physics*, 17:6865–6882, 2017.

[33] R. Perez, P. Ineichen, R. Seals, J. Michalsky, and R. Stewart. Modeling daylight availability and irradiance components from direct and global irradiance. *Solar Energy*, 44:271–289, 1990.

[34] Z. Sun, J. Li, G. Shi, J. Manners, and J. Li. Fast scheme for determination of direct normal irradiance. Part II: Parameterization of circumsolar radiation. *Solar Energy*, 199:256–267, 2020.

[35] B. Zou, H. Yang, Y. Yao, and Y. Jiang. A detailed study on the effects of sunshape and incident angle on the optical performance of parabolic trough solar collectors. *Applied Thermal Engineering*, 126:81–91, 2017.

[36] A. Neumann, B. von der Au, and P. Heller. Measurements of circumsolar radiation at the Plataforma Solar (Spain) and at the DLR (Germany). In *Proceedings of the International Solar Energy Conference, Solar Engineering*, 429–438, Albuquerque, 1998. American Society of Mechanical Engineers.

[37] S. M. Ivanova. Modelling of circumsolar direct irradiance as a function of GHI, DHI and DNI. In *8th International Conference on solar radiation and daylighting Solaris-2017*, 2017.

[38] ISO-9488. Solar Energy: Vocabulary. Standard, International Organization for Standardization, Geneva, CH, Oct. 1999.

[39] Y. Eissa. *Modelling the beam and circumsolar radiation under cloud-free conditions in desert environment*. Theses, Ecole Nationale Supérieure des Mines de Paris, June 2015.

[40] D. Buie and A. G. Monger. The effect of circumsolar radiation on a solar concentrating system. *Solar Energy*, 76:181–185, 2004.

[41] G. Major. Circumsolar correction for pyrheliometers and diffusometers. Technical report, World Meteorological Organization, 1994.

[42] D. M. Giles, A. Sinyuk, M. G. Sorokin, J. S. Schafer, A. Smirnov, I. Slutsker, T. F. Eck, B. N. Holben, J. R. Lewis, J. R. Campbell, E. J. Welton, S. V. Korkin, and A. I. Lyapustin. Advancements in the aerosol robotic network (aeronet) version 3 database – automated near-real-time quality control algorithm with improved cloud screening for sun photometer aerosol optical depth (aod) measurements. *Atmospheric Measurement Techniques*, 12(1):169–209, 2019.

[43] A. Ohmura, E. G. Dutton, B. Forgan, C. Fröhlich, H. Gilgen, H. H., A. Heumo, G. König-Langlo, B. McArthur, G. Müller, R. Philipona, R. Pinker, C. H. Whitlock, K. Dehne, and M. Wild. Baseline Surface Radiation Network (BSRN/WCRP): New Precision Radiometry for Climate Research. *Bulletin of the American Meteorological Society*, 79:1121–1128, 1998.

[44] C. Long and Y. Shi. The QCRad Value Added Product: Surface Radiation Measurement Quality Control Testing, Including Climatology Configurable Limits. 2006.

[45] C. Emde, R. Buras-Schnell, A. Kylling, B. Mayer, J. Gasteiger, U. Hamann, J. Kylling, B. Richter, C. Pause, T. Dowling, and L. Bugliaro. The libRadtran software package for radiative transfer calculations (version 2.0.1). *Geoscientific Model Development*, 9:1647–1672, 2016.

[46] K. Stamnes, S. Tsay, W. Wiscombe, and K. Jayaweera. Numerically stable algorithm for discrete-ordinate-method radiative transfer in multiple scattering and emitting layered media. *Applied Optics*, 27:2502–2509, 1998.

[47] O. Dubovik, A. Smirnov, B. N. Holben, M. D. King, Y. J. Kaufman, T. F. Eck, and I. Slutsker. Accuracy assessments of aerosol optical properties retrieved from Aerosol Robotic Network (AERONET) Sun and sky radiance measurements. *Journal of Geophysical Research: Atmospheres*, 105:9791–9806, 2000.

[48] B. N. Holben, D. Tanré, A. Smirnov, T. F. Eck, I. Slutsker, N. Abuhassan, W. W. Newcomb, J. S. Schafer, B. Chatenet, F. Lavenu, Y. J. Kaufman, J. V. Castle, A. Setzer, B. Markham, D. Clark, R. Frouin, R. Halthore, A. Karneli, N. T. O'Neill, C. Pietras, R. T. Pinker, K. Voss, and G. Zibordi. An emerging ground-based aerosol climatology: Aerosol optical depth from AERONET. *Journal of Geophysical Research: Atmospheres*, 106:12067–12097, 2001.

[49] C. Gueymard and J. Ruiz-Arias. Validation of direct normal irradiance predictions under arid conditions: A review of radiative models and their turbidity-dependent performance. *Renewable and Sustainable Energy Reviews*, 45:379–396, 2015.

[50] C. Gueymard. The sun's total and spectral irradiance for solar energy applications and solar radiation models. *Solar Energy*, 76:423–453, 2004.

[51] P. Ricchiazzi, S. Yang, C. Gautier, and D. Sowle. SBDART: A Research and Teaching Software Tool for Plane-Parallel Radiative Transfer in the Earth's Atmosphere. *Bulletin of the American Meteorological Society*, 79:2101–2114, 1998.

[52] M. Blanco-Muriel, D. C. Alarcón-Padilla, T. López-Moratalla, and M. Lara-Coira. Computing the solar vector. *Solar Energy*, 70:431–441, 2001.

[53] Kipp&Zonen. *CHP1 pyrheliometer instruction manual (version 0811).* 2008.

[54] WMO. *Guide to meteorological instruments and methods of observation.* World Meteorological Organization (WMO), Geneva, Switzerland, 2014.

[55] G. Shi, Z. Sun, J. Li, and Y. He. Fast scheme for determination of direct normal irradiance. Part I: New aerosol parameterization and performance assessment. *Solar Energy*, 199:268–277, 2020.

[56] C. A. Gueymard. *Clear-Sky Radiation Models and Aerosol Effects*, 137–182. Springer International Publishing, 2019.

[57] A. Habte and M. Sengupta. Best Practices to Uncertainty Estimation for the National Solar Radiation Database (NSRDB 1998-2015). In *33rd European Photovoltaic Solar Energy Conference and Exhibition*, 2470–2474, 2017.

[58] B. Liu and R. Jordan. The interrelationship and characteristic distribution of direct, diffuse and total solar radiation. *Solar Energy*, 4:1–19, 1960.

[59] C. Gueymard, J. Bright, D. Lingfors, A. Habte, and M. Sengupta. A posteriori clear-sky identification methods in solar irradiance time series: Review and preliminary validation using sky imagers. *Renewable and Sustainable Energy Reviews*, 109:412–427, 2019.

[60] C. Gueymard and J. Ruiz-Arias. Extensive worldwide validation and climate sensitivity analysis of direct irradiance predictions from 1-min global irradiance. *Solar Energy*, 128:1–30, 2016.

[61] A. Habte, M. Sengupta, A. Andreas, S. Wilcox, and T. Stoffel. Intercomparison of 51 radiometers for determining global horizontal irradiance and direct normal irradiance measurements. *Solar Energy*, 133:372–393, 2016.

Nomenclature

a	model coefficient
B	direct irradiance
b	model coefficient
c	model coefficient
CS	circumsolar irradiance
CNSI	circumsolar normal irradiance
CSR	circumsolar ratio
FB	fractional bias
FGE	fractional gross error
I_e	estimated irradiance by the model
I_m	irradiance determined using libRadtran
K_b	beam clearness index
K_d	diffuse fraction

K_t	sky clearness index
L	sky radiance
MBE	mean bias error
N	total number of observations
P	penumbra function
R	correlation coefficient
RMSE	root mean square error

Greek symbols

α	half-opening angle
δ	angular distance from the centre of the sun
θ	solar zenith angle
ξ	scattering angle
φ	azimuth angle

Subscripts

n	normal
l	limit angle
S	sun
s	slope angle

Superscripts

exp	experimental
sun	sun-disk

Acronyms

AERONET	Aerosol Robotic Network
AOD	aerosol optical depth
BSRN	Baseline Surface Radiation Network
CDF	cumulative distribution function
CI	confidence interval

CPV	concentrating photovoltaics
CNSI	circumsolar normal irradiance
CSP	concentrating solar power
DHI	diffuse horizontal irradiance
DNI	direct normal irradiance
FB	fractional bias
FGE	fractional gross error
GHI	global horizontal irradiance
IES	Institute of Earth Sciences
MBE	mean bias error
NWP	numerical weather prediction
PHFN	aerosol phase function
PWV	precipitable water vapour
R	correlation coefficient
RMSE	root mean square error
RSI	rotating shadowband irradiometer
RTM	radiative transfer model
SA	surface albedo
SSA	single scattering albedo
WMO	World Meteorological Organization

Chapter 5

Prediction of circumsolar irradiance and its impact on CSP systems under clear skies[†]

Abstract

In this work, a model to estimate circumsolar normal irradiance (CSNI) for several half-opening angles under clear skies is developed. This approach uses a lookup table to determine the model parameters and estimate CSNI for half-opening angles between 0.5° and 5°.To develop and validate the proposed model, data from five locations worldwide were used. It was found that the proposed model performs better at the locations under study than the models available in the liteThe impact of CSNI for these different half-opening angles on concentrating solar power (CSP) systems was also studied. It was found that neglecting CSNI could lead to up to a 7% difference between the direct normal irradiance (DNI) measured by a field pyrheliometer and the DNI that is captured by CSP systems. Additionally, a case study for parabolic trough concentrators was performed as a way to estimate the impact of higher circumsolar ratios (CSR) on the decrease of the intercept factor for these systems. It was also concluded that if parabolic trough designers aim to reduce the impact of CSNI variation on the intercept factor, then parabolic troughs with higher rim angles are preferred.

Keywords: Solar Energy; Direct Normal Irradiance; Circumsolar radiation; Concentrating Solar Power systems; Parabolic trough

---

[†]Edgar F.M. Abreu[(1)], Paulo Canhoto[(1,2)], and Maria J. Costa[(1,3,4)]. Prediction of circumsolar irradiance and its impact on CSP systems under clear skies. *Energies* (under review).

[(1)] Institute of Earth Sciences, University of Évora.

[(2)] Mechatronic Engineering Department, School of Sciences and Technology, University of Évora.

[(3)] Physics Department, School of Sciences and Technology, University of Évora.

[(4)] Earth Remote Sensing Laboratory – EaRSLab, University of Évora.

5.1 Introduction

Concentrating Solar Power (CSP) systems highly depends on the intensity of Direct Normal Irradiance (DNI) in their aperture angle [1]. Therefore, it is crucial that designers have access to accurate DNI data to avoid compromising the proper operation and economic viability of such systems. The most reliable way of obtaining accurate DNI data is using a ground-based stations equipped with a pyrheliometer in a sun-tracker system. This instrument needs to track the apparent movement of the sun along its path in the sky to measure the direct beam. However, as this tracking cannot be done with perfect accuracy, these instruments are designed in such a way that they receive radiation not only from the solar disk but also from the surrounding area, known as circumsolar region [2], that is, the aperture half-angle of the instrument is larger than the apparent sun disk radius in order to accommodate the tracking misalignments and errors. On the other hand, this radiosity in the circumsolar region around the sun disk, known as circumsolar irradiance, is not negligible when designing CSP systems, because these systems usually have opening half-angles lower than those of the pyrheliometers, depending on the concentration factor.

The World Meteorological Organization (WMO) recommends that pyrheliometers have an opening half-angle of 2.5º to enable a fair comparison between the DNI measured at different locations around the globe [3]. However, the upper limit of the opening half-angles of common CSP technologies such as parabolic trough, linear Fresnel, dish-Stirling and solar tower are 0.8°, 1.0°, 1.6° and 1.8°, respectively [2, 4], that is, lower than the standard aperture half-angles of pyrheliometers. In other words, CSP systems will not receive the same levels of irradiance as measured by collocated standard pyrheliometers. This difference will increase when the circumsolar radiosity also increases as result of solar radiation scattering in the atmosphere due to higher concentrations of aerosols. The quantification of this difference between the measured DNI and the DNI that is reflected by the mirrors of a given CSP system is one of the principal motivations of this study.

The molecules, aerosols and cirrus clouds scatter the sun rays from the sun disk region to the circumsolar region [5]. When the irradiance from this region of the sky is measured in a surface normal to the sun line it is known as circumsolar normal irradiance (CSNI). In that sense, while experimental values of DNI obtained from pyrheliometer measurements are related only to the total scattering effect and transmittance of the atmosphere, the CSNI is also related to the angular distance from the centre of the sun disk, i.e., the scattering angle [6, 7]. The measurement of CSNI is not straightforward because of the sharp decrease in intensity between the centre of the sun disk and the limit of the field of view of the instrument [2].

However, some attempts to measure CSNI were made and a review on these can be found in Abreu et al. [6].

Regarding CSNI modelling, it is usually carried out using radiative transfer models (RTM) such as libRadtran [8]. However, because RTM models often need high-quality atmospheric data such as aerosol optical depth and precipitable water vapour, some authors have proposed more simple models to predict CSNI. In these models, CSNI is usually estimated as a function of more commonly available solar irradiance data and presented as a circumsolar ratio (CSR), i.e., the ratio between the CSNI and DNI [5, 6, 9, 10]. Such models are defined for a fixed aperture angle except the model from Eissa et al. [5] in which, in addition, the authors presented a way of varying the aperture angle. This takes a similar form of the fixed aperture angle model, but the model coefficients are determined using a sixth-degree polynomial of the aperture angle and allows to estimate CSNI for any defined aperture angle in the range [0.4°, 5.0°]. Although the model of Abreu et al. [6] was initially developed for a fixed aperture angle, the way it was constructed also allows its generalization for any aperture angle with the advantage that it only needs widely available solar irradiance data to predict CSNI, which is one of the main objectives of this study.

Furthermore, information on CSNI is crucial for the design and operation of CSP systems. In CSP plants, the solar irradiance is focused onto an absorber using mirrors [11]. However, due to the difference between the opening half-angles of the pyrheliometers and CSP systems mentioned above, the use of imprecise DNI data (without correctly accounting for the differences of the opening half-angle, that is, without considering CSNI) leads to incorrect assumptions about the solar irradiance that reaches the CSP mirrors. This will increase the uncertainty of the energy generation predictions of CSP systems, which ultimately increases the difficulty of its operation.

The impact of CSNI on CSP systems can be assessed using a variety of tools, namely ray tracing tools, analytical optical performance models and models that use look-up tables or parametrizations of the solar position relative to the CSP mirrors [2]. Ray tracing models describe the solar irradiance as a multitude of solar rays that originate from the sun, reach the concentrator and, finally, the receiver. Examples of ray tracing models can be STRAL [12] and MIRVAL [13], to name a few. Analytical models use analytical equations that can describe the ray's path trough the optical system. Examples of analytical models can be the Bendt-Rabl model [14] and the HFLCAL method [15], to name a few. Lastly, models based on look-up tables use parametrizations or look-up tables to assess the optical performance of a CSP collector according to the solar position. SAM [16] and *greenius* [17, 18] are examples of look-up tables-based models. The approach followed in this study was to use an analytical model to determine how the intercept factor (the ratio of the

irradiance reaching the receiver over the incident irradiance) is affected according to CSR.

In this work, a simple and fast model to derive CSNI is proposed for clear-sky conditions at any desired aperture angle. In other words, the proposed model is able to determine the CSNI that reaches the receiver of any CSP system, such as parabolic troughs, tower systems or dish systems, to name a few. The developed model is also aimed to identify the difference between using ground-based DNI measurements (for the aperture half-angle of the respective pyrheliometer) and DNI modelled data according to the aperture half-angles of typical CSP technologies (with lower aperture angles) at several locations around the globe. This allows to quantify the errors associated with using directly measured DNI data on the simulation of CSP systems. To the authors' best knowledge, the model proposed in this work is the only fast and simple model capable to estimate CSNI at several locations in more than one climate zone, which constitutes another novelty here. Furthermore, the impact of CSNI in CSP systems, specifically in parabolic trough systems, is also studied using the optical performance model from Bendt and Rabl [14].

This paper is organized as follows: Section 5.2 describes the data used; in Section 5.3, the model development and performance assessment are presented; in Section 5.4, prediction of CSNI and its impact on CSP systems, namely in a parabolic trough, is assessed; and in Section 5.5, conclusions are drawn.

5.2 Data

5.2.1 Experimental solar radiation data

In this work, CSNI data corresponding to several half-opening angles and necessary to develop the proposed model were obtained using the libRadtran RTM [8] simulations based on AERONET [19] input data for five locations worldwide. AERONET is a ground-based aerosol network that provides aerosol optical data and microphysical and radiative properties for aerosol research and characterization over more than 25 years. The values retrieved from the AERONET database were the following: aerosol optical depth, aerosol single scattering albedo, aerosol phase function, surface albedo and precipitable water vapour. The AERONET data was retrieved at the wavelengths of 440 nm, 675 nm, 870 nm and 1020 nm. However, the simulations were carried out for the wavelength interval between 200 nm and 5000 nm. This wavelength interval covers not only the spectral response of a conventional pyrheliometer (300-4000 nm) but also the spectral response of windowless absolute cavity radiometers (the 5000 nm upper limit), against which field pyrheliometers are commonly calibrated. To extrapolate the AERONET aerosol data to 200 nm and 5000 nm, Ångström's law was used. For further details on this process, the reader can consult the previous work of Abreu et al. [6]. Ground-based DNI values from BSRN database was also

used in the validation process of the CSNI data for the same locations. BSRN is a network of ground-based radiometric stations with the aim of detecting changes in the radiation field at Earth's surface [20].

The five locations analysed in this work are scattered in the globe and have collocated AERONET and BSRN stations, thus allowing to assume that measurements from both stations at close timestamps. The time difference between AERONET and the radiometric stations data is not higher than 1 minute and therefore it is assumed that, under clear skies, they are representative of the same atmospheric conditions. More information about the locations is presented in Table 5.1.

Table 5.1: Information on the AERONET and radiometric stations and data period used in this work. Legend: Lat. – Latitude, Long. – Longitude, Alt. – Altitude, TR – Tropical, TM – Temperate, AR – Arid.

Location	Code	Lat. (ºN)	Long. (ºE)	Alt. (m)	Climate zone	Period	Data points
Darwin, AUS	DAR	-12.425	130.831	30	TR	2012-14	974
Évora, PRT	EVR	38.568	-7.912	293	TM	2015-17	1163
Gobabeb, NAM	GOB	-23.561	15.042	407	AR	2015-17	1833
S. M. da Serra, BRA	SMS	-29.443	-53.823	489	TM	2014-16	614
Tamanrasset, DZA	TAM	22.790	5.529	1385	AR	2014-16	1060

Regarding data quality control, AERONET data Level 1.5 Version 3 were used here for two main reasons: to use single scattering albedo measurements instead of mean values, and because Version 3 processing algorithm marks a significant improvement in the quality controls of the sun photometer AOD measurements, eliminating the need for manual quality control and cloud screening by an analyst [21, 22]. Concerning solar radiation data, the quality filters from BSRN [20] were used to ensure that extremely rare or physically impossible values were discarded.

The quality control procedure used here ensures that: (i) the simulations to determine DNI and CSNI are as accurate as possible; (ii) the model developed here was created and validated using the most accurate solar irradiance ground-based data available. Moreover, the data used in this work were screened and classified as clear sky by the AERONET algorithm alongside solar radiation data from collocated radiometric stations, in order to ensure that both AERONET and BSRN/Evora data are representative of the same atmospheric conditions.

5.2.2 Modelled DNI and CSNI data

In this work, modelled DNI and CSNI data from the libRadtran RTM are used to develop the proposed CSNI model. The generation of these kind of data is

complex because of: (i) the availability and processing of the required inputs; (ii) the computation time required to simulate extensive datasets such as the one used here. Therefore, the DNI and CSNI data used here were generated and validated in a previous work from the same authors [6]. However, it is worth to mention that the data processing in this work is not the same as in the previously mentioned study [6].

In the previous study mentioned above [6], the libRadtran radiative transfer model was used alongside AERONET to generate DNI and the sky radiance. The latter was then used to generate CSNI data through the integration of sky radiance from the RTM model output in the circumsolar region. The quality of the modelled DNI and CSNI data was then assessed using ground-based DNI data. This validation process was indirect, i.e., the DNI modelled data was compared against the ground-based DNI data, with and without its CSNI counterpart. Since the comparison between modelled and ground-based data was better when the modelled CSNI counterpart was used, it was then concluded that the modelled CSNI data exhibited an acceptable accuracy. Further information of the modelled data, the procedure to generate it and the validation procedure can be found in [6].

5.3 Model development and assessment

5.3.1 Model development

Each pyrheliometer model has its own penumbra function because it has its own geometrical characteristics. This function accounts for the pyrheliometer's response as a function of the scattering angle due to the effect of the opening window edge, which attenuates the intensity of radiation in a transitions range between illuminated and non-illuminated areas [6]. However, assuming a more simple model, the penumbra function can be assumed as a rectangular function [2], i.e., there is no transition range, and an ideal DNI for the opening half-angle α can be defined as follows:

$$B_n^{ideal}(\alpha) = 2\pi \int_0^{\alpha} L(\xi)\sin(\xi)d\xi, \tag{5.1}$$

where L is the sky radiance and ξ is the scattering angle (the angular distance from the centre of the sun). In this way, the direct normal irradiance from the sun disk (B_n^{sun}), can be defined replacing α by the half-angle of the solar disk (δ_S) in the Eq. 5.1. In a similar way, the ideal CSNI, CS_n^{ideal} can be defined as follows:

$$CS_n^{ideal}(\delta_S, \alpha) = 2\pi \int_{\delta_S}^{\alpha} L(\xi)\sin(\xi)d\xi, \tag{5.2}$$

where the constraint $\alpha \geq \delta_S$ is required. In ideal conditions, following a fundamental closure relationship, we can define the ideal DNI as follows:

$$B_n^{ideal}(\alpha) = CS_n^{ideal}(\delta_S, \alpha) + B_n^{sun}. \tag{5.3}$$

The circumsolar ratio (CSR) for this ideal case can also be defined as follows:

$$CSR(\alpha) = \frac{CS_n^{ideal}(\delta_S, \alpha)}{B_n^{ideal}(\alpha)}. \tag{5.4}$$

The model proposed in this work is based on these fundamental relationships regarding the simpler penumbra model of the instruments and, therefore, CSNI and CSR can be determined using only α. To that end, starting from the results of the libRadtran simulation [6], CSNI and CSR were calculated for half-opening angles ranging from 0.5° to 5° with steps of 0.1°, resulting in 46 data points for each record timestamp in each location. Then, the adjustable parameters a, b and c from the CSR model for a given half-opening angle developed by Abreu et al. [6] (described below by Eq. 5.5 and collocated text) were fitted to the data points for each value of α, for all five locations. Finally, the model parameters a, b, and c (46 data points for each parameter) were modelled by fitting a polynomial relation with α according to Eq. 5.6, where $f(\alpha)$ represents the required model parameter. The referred CSR model [6] is given by:

$$CSR(1 - K_d) = \frac{a}{b + (K_t K_b / K_d)}, \tag{5.5}$$

where K_t is the sky clearness index, i.e., the ratio between global horizontal irradiance at the Earth's surface and its counterpart at the top of the atmosphere [23], K_b is the beam clearness index, i.e., the ratio between DNI at the Earth's surface and DNI at the top of atmosphere [24], and K_d is the diffuse fraction, i.e., the ratio between diffuse horizontal and global horizontal irradiance [25]. The general polynomial form to model these parameters as a function of the half-opening angle is in the form:

$$f(\alpha) = C_0 + C_1\alpha + C_2\alpha^2. \tag{5.6}$$

Regarding the polynomial fitting to determine the new model parameters, it was verified that the parameter a can be obtained accurately through a first-degree polynomial while parameters b and c are better adjusted using a second-degree polynomial. The polynomial coefficients to obtain the model parameters are presented in Table 5.2 according to each location as well as their respective coefficients of determination. The locations are grouped according to climatic zone. The model parameters were obtained using a nonlinear least squares method through the Matlab *fit* function. It is worth noting that training and validation datasets comprised of approximately two thirds and one third of the original datasets shown in Table 1, respectively, were created, in order to avoid overfitting.

The polynomial coefficients derived here differ from station to station and from climate zone to climate zone. This can be an indication of the differences in the mean aerosol values and other relevant local meteorological or surface conditions at different stations and climate zones. For example, the atmospheric conditions at

Table 5.2: Polynomial coefficients and respective coefficients of determination of model parameters a, b and c fitting as a function of alpha. Legend: TR – Tropical; TM – Temperate; AR – Arid.

Station	Parameter	Polynomial coefficients			R^2
		C_0	C_1	C_2	
DAR (TR)	a	-0.0094	0.0137	0	0.9978
	b	0.7667	-0.0727	0.0152	0.4325
	c	1.4199	-0.0063	0.0045	0.3446
EVR (TM)	a	-0.0152	0.0206	0	0.9962
	b	0.7403	0.0033	0.0056	0.8524
	c	1.6770	0.0343	-0.0017	0.8817
SMS (TM)	a	-0.0158	0.0213	0	0.9931
	b	2.0406	0.1906	-0.0227	0.3278
	c	2.1955	0.0439	-0.0121	0.2684
GOB (AR)	a	-0.0238	0.0303	0	0.9938
	b	1.2546	0.0286	0.0128	0.9250
	c	1.7457	0.0161	0.0016	0.6406
TAM (AR)	a	-0.0698	0.0740	0	0.9801
	b	1.4890	0.0944	0.0427	0.9919
	c	1.4051	0.0739	0.0024	0.9359

EVR and SMS should be very different even though these two stations belong to the same climate zone. Whilst the EVR station is located at a semi-rural small city, the SMS station is located in a rural area, causing these two sites to have different aerosol profiles. Whilst at SMS the predominant aerosol should be the rural aerosol, at EVR a combination of rural and urban aerosols is shown. This may be the reason why a global model (using all of the data) would not produce acceptable results and, therefore, is not shown here.

5.3.2 Performance assessment

To assess the performance of the proposed procedure based on the model of Abreu et al. [6], including the determination of model parameters through Eq. (6), the CSNI values obtained here and the values from the model of Eissa et al. [5] were compared against the libRadtran CSNI values, for the following values of α: 0.8°, 1.0°, 1.6° and 1.8°. These α values were selected because they represent the upper bound acceptance half-angles of the following CSP technologies: parabolic through, linear Fresnel, dish-Stirling and solar tower, respectively [2, 4]. The performance assessment was carried out using the following statistical indicators: relative mean

bias error (rMBE), relative root mean square error (rRMSE), correlation coefficient (R), fractional bias (FB) and fractional gross error (FGE), defined as follows:

$$\text{rMBE} = \frac{\frac{1}{n}\sum_{i=1}^{n}(pi - oi)}{\overline{o}}, \tag{5.7}$$

$$\text{rRMSE} = \frac{\sqrt{\left[\frac{1}{n}\sum_{i=1}^{n}(pi - o_i)^2}}{\overline{o}} \tag{5.8}$$

$$\text{FB} = \frac{2}{n}\sum_{i=1}^{n}\frac{pi - o_i}{pi + o_i}, \tag{5.9}$$

$$\text{FGE} = \frac{2}{n}\sum_{i=1}^{n}\frac{|pi - o_i|}{|pi + o_i|}, \tag{5.10}$$

$$\text{R} = \frac{\sum_{i=1}^{n}(p_i - \overline{p})(o_i - \overline{o})}{\sqrt{\sum_{i=1}^{n}(p_i - \overline{p})^2 \sum_{i=1}^{n}(o_i - \overline{o})^2}}, \tag{5.11}$$

where p_i is the model prediction, o_i is the corresponding libRadtran simulations, $\overline{p}$ is the average of the model predictions, $\overline{o}$ is the average of the libRadtran simulations and n is the total number of data points.

Since there are no CSNI measured data at the required half-opening angles and locations, the proposed CSNI model was compared against the models from Eissa et al. [5]. In the work of Eissa et al. [5], the authors developed three models: one model for Sollar Village (SV in their work, SOV here), one model for Tamanrasset (TAM) and a third model that resulted in a combination of the data from these two stations. It is worth to mention that these models were derived for a desert environment (i.e., arid climate zone) and its performance is being assessed here at other climate zones. However, to the best knowledge of the authors, there are no other CSNI models available in the literature derived for the remaining climate zones. In this way, the statistical analysis results of the models from Eissa et al. [5] and the model proposed here are presented in Table 5.3 as an example for the half-opening angle of 0.8°. The statistical analysis for the remaining half-opening angles of 1.0°, 1.6° and 1.8° can be found in Appendix A.

This statistical analysis shows that the model proposed in this work generates more accurate results than the other models available in the literature for the datasets used in this study, regardless of the value of half-opening angle, α, for all climate zones (see also Tables in Appendix A).

Looking more closely to the results, the proposed CSNI model performs better at DAR (tropical climate zone) the higher α is, according to all statistical indicators except MBE. The same overall trend is shown for the stations in the temperate climate zone (EVR and SMS stations). Regarding the arid climate zone, all statistical

Table 5.3: Statistical analysis of circumsolar models for a half-opening value of 0.8°. Legend: TR – Tropical; TM – Temperate; AR – Arid.

Station	Statistical indicator	Models			
		Eissa et al. (2018) SOV	Eissa et al. (2018) TAM	Eissa et al. (2018) Combined	This work
DAR (TR)	MBE (%)	-3.6909	-12.7882	-8.8191	**-1.9568**
	RMSE (%)	73.6326	75.1784	74.2138	**65.5111**
	R	0.4558	0.4462	0.4529	**0.6098**
	FB	0.1111	**0.0280**	0.0619	0.0783
	FGE	0.4059	0.3986	0.3984	**0.3373**
EVR (TM)	MBE (%)	-14.5644	-21.9949	-19.0593	**-5.3790**
	RMSE (%)	69.7619	74.1385	71.8608	**51.5307**
	R	0.7372	0.7333	0.7363	**0.8503**
	FB	0.0960	**0.0256**	0.0473	0.0501
	FGE	0.4720	0.4771	0.4700	**0.3787**
SMS (TM)	MBE (%)	54.8555	43.9161	47.2877	**-7.8958**
	RMSE (%)	99.2818	91.2930	93.9774	**62.3977**
	R	0.5886	0.5887	0.5902	**0.7664**
	FB	0.6248	0.5683	0.5809	**-0.0267**
	FGE	0.6940	0.6570	0.6616	**0.4119**
GOB (AR)	MBE (%)	-5.5326	-13.1627	-10.2862	**0.7049**
	RMSE (%)	77.7761	79.8855	78.6863	**66.0703**
	R	0.5857	0.5800	0.5845	**0.7205**
	FB	0.1736	**0.1059**	0.1264	0.1519
	FGE	0.4739	0.4657	0.4637	**0.4149**
TAM (AR)	MBE (%)	-43.2006	-48.8579	-46.3205	**-10.1562**
	RMSE (%)	63.0100	67.4481	65.3594	**37.9758**
	R	0.6365	0.6360	0.6370	**0.7870**
	FB	-0.5482	-0.6302	-0.5975	**-0.0651**
	FGE	0.5774	0.6440	0.6171	**0.2760**

indicators of the present model show better results with the increase of α at GOB. However, the same is not so readily shown at TAM, where the only statistical parameters that increase performance with the increase of α are R and FGE.

The aerosol characteristics and meteorological conditions of the different climate zones have a direct impact on the results presented here. The mean statistical indicators for each climate zone show that the tropical climate zone is where the proposed model performs best according to rMBE and FGE. Regarding the other statistical indicators (RMSE, R and FB), the climate zone in which the proposed model provides best results is the arid climate zone. However, if XIA is taken out of

this analysis due to the reasons mentioned above, then the proposed model would perform best according to R and FB at the other stations located the temperate climate zone.

5.4 Prediction of CSNI and of its impact on the energy capture of CSP systems

5.4.1 Impact on the energy that reaches the aperture of CSP systems

In the work of Abreu et al. [6], modelled DNI values with and without CSNI were validated against ground-based DNI measurements for an aperture half-angle equal of the pyrheliometer. The modelled DNI and CSNI values were there obtained through the integration of sky radiance from libRadtran simulations on the aperture solid angle of the pyrheliometer, with an overall uncertainty of 4,44%. In the present work, those validated DNI data are compared against the modelled DNI obtained in the same way but for typical half-opening values of CSP technologies: 0.8°, 1.0°, 1.6° and 1.8°, for parabolic through, linear Fresnel, dish-Stirling and solar tower, respectively [2, 4]. This comparison was performed using the mean average difference (in percentage) between the DNI corresponding to the half-opening angle of the pyrheliometer installed at each location (DNI(α_{pyr})) and the modelled DNI corresponding to each of the half-opening angles mentioned above (DNI(α)), and is a measure of the error or bias between the energy assessment using the pyrheliometer values and the real value of irradiance that is captured by the CSP systems, as shown in Fig. 5.1. At DAR, SMS and TAM, DNI is measured using a Eppley NIP (α = 2.9°) whilst at EVR and GOB, DNI is measured using a Kipp&Zonnen CHP1 (α = 2.5°).

The average difference between DNI(α_{pyr}) and DNI(α) is higher for lower half-opening angles as expected, and for locations with higher CSR. The locations with higher average difference are TAM and DAR, whilst locations such as GOB and SMS show low average differences between the DNI of the pyrheliometer and the DNI for lower half-opening angles. This is related to the CSR magnitude across different locations, and in turn, with the composition of the atmosphere, in particular with the type and concentration of aerosols. It is worth mentioning that not only the magnitude of the average difference across locations depends on the composition of the atmosphere, but also the slope of lines shown in Fig. 5.1.

Locations with higher aerosol concentration have higher slopes (e.g. TAM) as can be seen in Fig. 5.2, where boxplots for aerosol optical depth (AOD) and single scattering albedo (SSA) at 675 nm are shown. Fig. 5.1 and Fig. 5.2 highlight the need for the consideration of both half-opening aperture angle and CSNI when designing and simulating CSP systems, especially in locations with higher aerosol concentration.

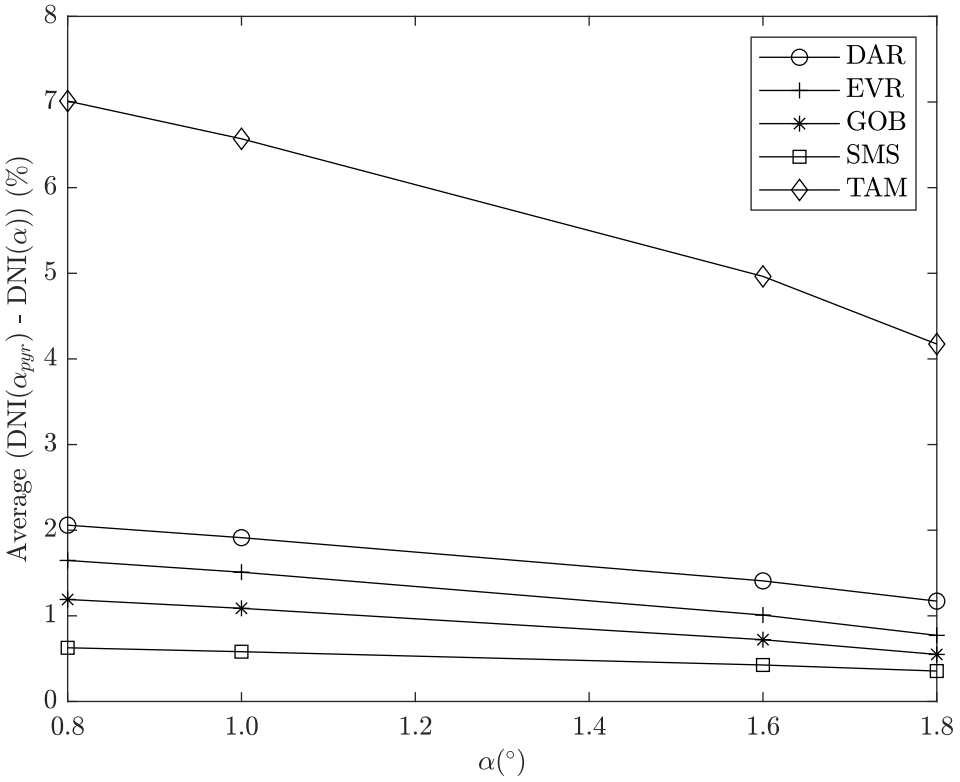

Fig. 5.1: Average difference between DNI(α_{pyr}) and DNI(α).

Differences in the incoming DNI of around 7% and 2% for locations such as TAM and DAR, respectively, can lead to erroneous energy generation estimates, which in turn can jeopardize the economic viability of CSP projects.

5.4.2 Impact on the intercept factor of CSP systems: the case of parabolic trough concentrators

The model from Bendt et al. [14] was used here to quantify in a simple way the impact of CSR in the optical efficiency of a parabolic trough CSP system with cylindrical receiver.

In Bendt et al. [14], an analytical approach is proposed to perform the optical analysis of a solar concentrator instead of using ray tracing software. The former approach is simpler and faster than the later, hence it was used here. By assuming a Gaussian distribution for the sun shape, Bendt et al. [14] were able to determine the intercept factor (the ratio of the irradiance reaching the receiver over the incident irradiance) as a function of the group σC, where σ stands for total optical error and C for concentration ratio.

To achieve this, the model by Bendt et al. [14] determines an effective source that accounts for the shape of the sun, and for all optical errors from the parabolic

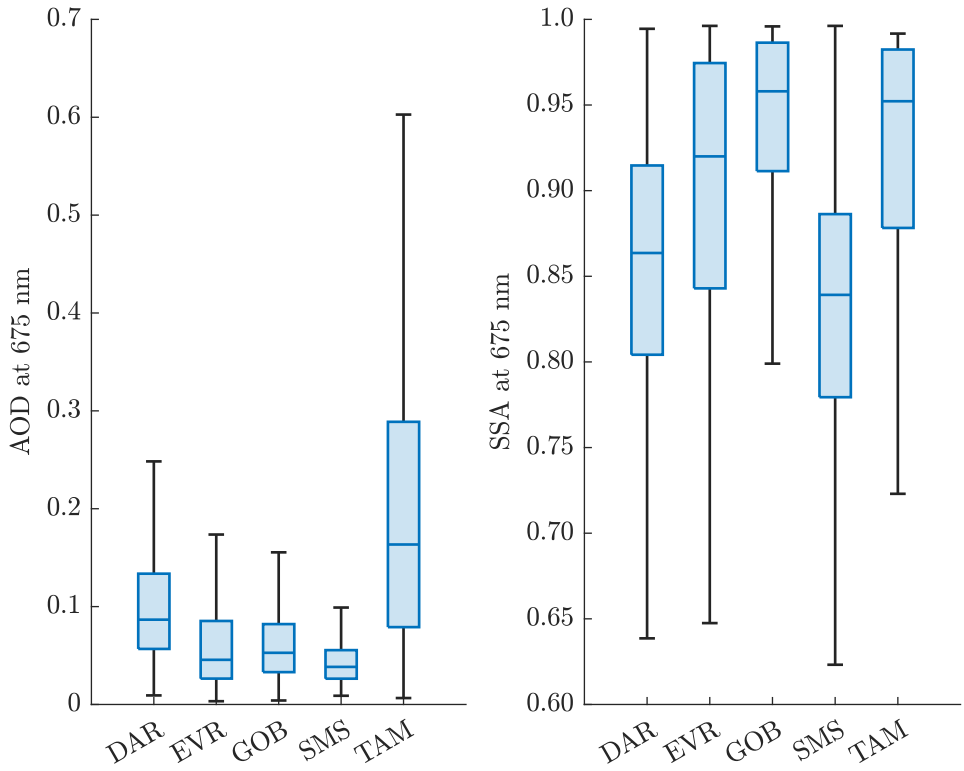

Fig. 5.2: Boxplots for aerosol optical depth (AOD) and single scattering albedo (SSA) for the stations analysed in this work.

trough system. In this way, it is possible to determine the intercept factor.

The total optical error (σ) is defined as the root mean square of angular spread caused by all optical errors of the concentrator (σ_{opt}) and angular width of the sun shape in line focus geometry (σ_{sun}), through the equation:

$$\sigma = \sqrt{\sigma_{opt}^2 + \sigma_{sun}^2}. \tag{5.12}$$

To study the impact of CSNI (or CSR) variation on CSP systems, namely parabolic trough systems, a relationship between σ_{sun} and CSR was established using data from Table 4-1 in Bendt et al. [14]. This table contains data from the 16 standard Lawrence Berkeley Laboratory (LBL) circumsolar irradiance scans [26], namely σ_{sun} and CSR, and its relationship is shown in Figure 5.3. Then, a fit to the data shown in Figure 4-1a of Bendt et al. [14] was performed, enabling the determination of the intercept factor according to CSR using the procedure described below. Firstly, σ_{opt} was fixed at 10 mrad and σ_{sun} varied from 2.5 mrad to 10 mrad. In this way, it was possible to determine the intercept factor for various combinations of concentration factors (C) and rim angles, as shown in Figure 5.4 for a given parabolic trough system. From Figure 5.4, it is clear that higher concentration ratios imply a higher effect of the CSR on the intercept factor of a parabolic trough system, regardless of

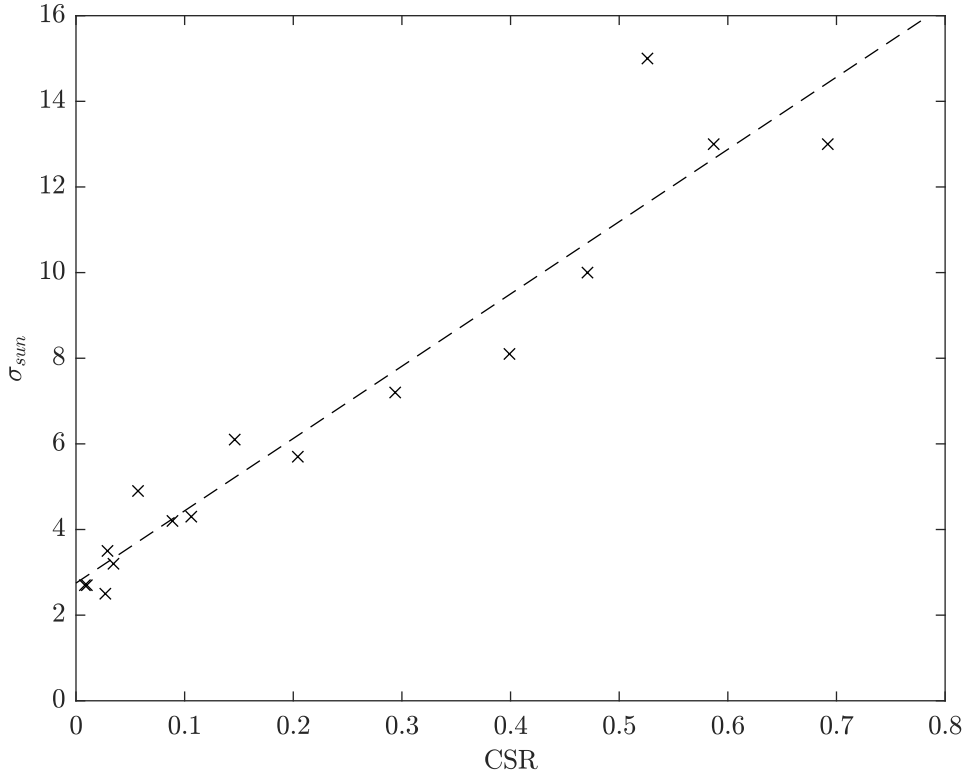

Fig. 5.3: Relationship between CSR and σ_{sun}.

the selected rim angle. Higher CSR values stands for higher dispersion of reflected solar rays from the parabolic through concentrator to the receiver, resulting in a lower intercept factor.

For lower rim angles, the CSR seems to have a larger impact on the intercept factor than for higher rim angles, for the same concentration ratio. This has to do with the aperture angle of the reflector, because lower rim angles correspond to lower acceptance angles of the reflector. Therefore, lower reflector aperture angles result in less irradiance reflected when the circumsolar region is larger (i.e., higher CSR).

Regarding the mitigation of CSR effects on the intercept factor of parabolic trough systems, it appears that using higher rim angles is the best approach based on the results from Figure 5.4. It is expected that the same conclusions could be draw for other CSP systems. For instance, Rabl and Bendt [27] found that the intercept factor of a parabolic dish strongly depended on the rim angle. They also stated that concentrators with a rim angle of 30° are twice more sensitive to CSNI variation than those with a rim angle of 60°. However, those systems are not addressed here for conciseness.

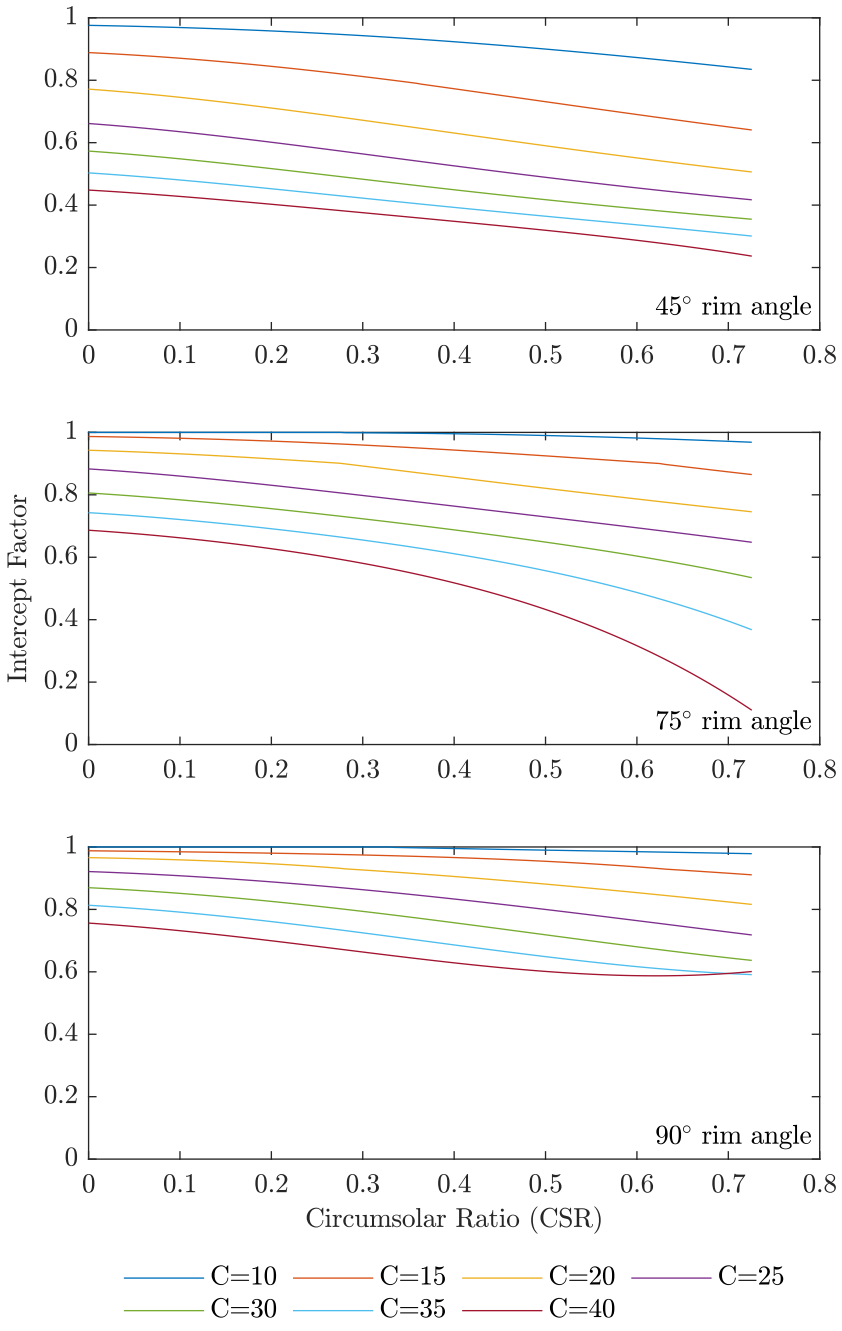

Fig. 5.4: Variation of intercept factor according to CSR for a parabolic trough system with rim angle of 45° (top), 75° (middle) and 90° (bottom).

5.5 Conclusions

In this work, a model to predict circumsolar normal irradiance (CSNI) for several half-opening angles was developed. The model is based on the CSR model developed by Abreu et al. [6] and use a polynomial fitting of the model parameters to estimate CSNI for half-opening angles of interest for CSP systems such as parabolic trough and parabolic disk. It was found that the proposed model performs significantly better at the locations under study here than the other models available in the literature. It was also found that the local aerosol regime and atmospheric conditions have higher impact on model fitting and performance than the overall climate zone of the locations under study.

Regarding the impact of CSNI in CSP systems, it was found that discarding an accurate CSNI estimate could lead to up to a 7% difference between the DNI that is measured by a pyrheliometer and the DNI that is effectively captured by the system. It was also found that these differences are higher for lower half-opening angles, as expected, since the difference between the half-opening angle of the pyrheliometer and the half-opening angle of the CSP system is higher.

The impact of CSNI in the operation of a CSP system, namely with parabolic trough concentrators, was also studied in this work. The authors found that higher CSR values lead to lower intercept factors (the ratio between the irradiance reaching the receiver over the incident irradiance) for these systems. It was also found that if parabolic trough designers aim to reduce the impact of CSNI on the intercept factor, then parabolic troughs with higher rim angles are preferred.

This study also found that further study on the direct impact of the different aerosol and atmospheric characteristics on the development of local or global CSNI models as well as the evaluation of the impact of CSNI in other CSP systems is needed and should be addressed in future work.

5.6 Appendix A

Table 5.4: Statistical analysis of circumsolar models for a half-opening value of 1.0°. Legend: TR – Tropical; TM – Temperate; AR – Arid.

Station	Statistical indicator	Models			
		Eissa et al. (2018) SOV	Eissa et al. (2018) TAM	Eissa et al. (2018) Combined	This work
DAR (TR)	MBE (%)	-8.2830	-16.5275	-12.9445	**-2.2546**
	RMSE (%)	74.3442	76.3812	75.2309	**64.8538**
	R	0.4616	0.4516	0.4585	**0.6277**
	FB	0.0647	**-0.0137**	0.0180	0.0694
	FGE	0.3966	0.3979	0.3946	**0.3282**
EVR (TM)	MBE (%)	-17.4693	-24.2959	-21.6079	**-4.1334**
	RMSE (%)	68.0582	72.5984	70.2776	**48.0732**
	R	0.7515	0.7475	0.7506	**0.8641**
	FB	0.0549	**-0.0116**	0.0084	0.0634
	FGE	0.4575	0.4660	0.4577	**0.3657**
SMS (TM)	MBE (%)	51.2288	41.2298	44.2498	**-7.8774**
	RMSE (%)	94.9101	87.5297	90.0278	**59.3243**
	R	0.5944	0.5952	0.5963	**0.7761**
	FB	0.5935	0.5399	0.5512	**-0.0536**
	FGE	0.6657	0.6321	0.6352	**0.4101**
XIA (TM)	MBE (%)	5.6189	-3.9613	**0.3783**	16.8597
	RMSE (%)	75.4881	75.9470	**75.3239**	167.6824
	R	**0.1380**	0.0843	0.1183	0.0046
	FB	0.1962	**0.1124**	0.1510	0.2039
	FGE	0.5259	0.5243	**0.5226**	0.5388
GOB (AR)	MBE (%)	-9.6566	-16.5366	-13.9658	**0.3956**
	RMSE (%)	76.1568	78.5794	77.2887	**63.2621**
	R	0.5963	0.5905	0.5950	**0.7356**
	FB	0.1261	**0.0626**	0.0812	0.1404
	FGE	0.4574	0.4542	0.4506	**0.4007**
TAM (AR)	MBE (%)	-46.4198	-51.5974	-49.2616	**-11.0781**
	RMSE (%)	64.1861	68.5203	66.4761	**35.9810**
	R	0.6587	0.6591	0.6596	**0.8105**
	FB	-0.6053	-0.6832	-0.6521	**-0.0800**
	FGE	0.6179	0.6882	0.6597	**0.2596**

Table 5.5: Statistical analysis of circumsolar models for a half-opening value of 1.6°. Legend: TR – Tropical; TM – Temperate; AR – Arid.

Station	Statistical indicator	Models			
		Eissa et al. (2018) SOV	Eissa et al. (2018) TAM	Eissa et al. (2018) Combined	This work
DAR (TR)	MBE (%)	-7.3218	-14.4590	-11.3793	**-2.9744**
	RMSE (%)	71.5192	73.2395	72.2564	**61.4056**
	R	0.4884	0.4792	0.4856	**0.6585**
	FB	0.0677	**-0.0004**	0.0262	0.0495
	FGE	0.3861	0.3865	0.3836	**0.3096**
EVR (TM)	MBE (%)	-18.2166	-24.2169	-21.8995	**-6.0038**
	RMSE (%)	69.0040	73.0695	70.9620	**47.4889**
	R	0.7651	0.7615	0.7644	**0.8773**
	FB	0.0501	**-0.0126**	0.0050	0.0379
	FGE	0.4479	0.4538	0.4470	**0.3495**
SMS (TM)	MBE (%)	55.7121	46.3008	48.9693	**-8.7893**
	RMSE (%)	97.6470	90.2461	92.7546	**58.1584**
	R	0.6026	0.6060	0.6058	**0.7872**
	FB	0.6128	0.5599	0.5702	**-0.0604**
	FGE	0.6748	0.6359	0.6409	**0.3856**
XIA (TM)	MBE (%)	14.4717	5.9863	-2.4130	**1.5554**
	RMSE (%)	165.6173	75.3853	75.5905	**75.2117**
	R	-0.0007	**0.1490**	0.1050	0.1325
	FB	0.1795	0.1941	**0.1213**	0.1558
	FGE	0.5254	0.5139	0.5111	**0.5108**
GOB (AR)	MBE (%)	-9.4728	-15.5302	-13.3448	**0.3541**
	RMSE (%)	74.0108	76.0091	74.9340	**60.1126**
	R	0.6099	0.6058	0.6095	**0.7565**
	FB	0.1208	**0.0614**	0.0776	0.1306
	FGE	0.4457	0.4389	0.4367	**0.3819**
TAM (AR)	MBE (%)	-47.7705	-52.1866	-50.1597	**-13.1196**
	RMSE (%)	65.6072	69.3790	67.5585	**36.7252**
	R	0.6736	0.6744	0.6748	**0.8230**
	FB	-0.6253	-0.6952	-0.6679	**-0.1024**
	FGE	0.6334	0.6981	0.6728	**0.2593**

Table 5.6: Statistical analysis of circumsolar models for a half-opening value of 1.8°. Legend: TR – Tropical; TM – Temperate; AR – Arid.

Station	Statistical indicator	Models			
		Eissa et al. (2018) SOV	Eissa et al. (2018) TAM	Eissa et al. (2018) Combined	This work
DAR (TR)	MBE (%)	-11.2779	-17.8084	-15.0134	**-3.1077**
	RMSE (%)	69.4722	71.4864	70.3942	**58.1455**
	R	0.5053	0.4969	0.5029	**0.6813**
	FB	0.0232	-0.0431	**-0.0176**	0.0445
	FGE	0.3809	0.3856	0.3815	**0.3012**
EVR (TM)	MBE (%)	-22.2488	-27.8376	-25.7046	**-6.4557**
	RMSE (%)	70.1129	74.1871	72.1038	**46.6078**
	R	0.7747	0.7717	0.7744	**0.8822**
	FB	0.0009	-0.0634	-0.0456	**0.0261**
	FGE	0.4434	0.4518	0.4445	**0.3420**
SMS (TM)	MBE (%)	50.2532	41.0570	43.6248	**-8.9122**
	RMSE (%)	92.8426	86.0116	88.3135	**56.7631**
	R	0.6065	0.6118	0.6106	**0.7919**
	FB	0.5766	0.5198	0.5312	**-0.0668**
	FGE	0.6454	0.6036	0.6094	**0.3789**
XIA (TM)	MBE (%)	**0.4977**	-7.0951	-3.4456	12.4336
	RMSE (%)	**74.0838**	74.8387	74.2577	162.6876
	R	**0.1570**	0.1161	0.1414	0.0043
	FB	0.1442	**0.0747**	0.1079	0.1622
	FGE	0.5015	0.5038	**0.5010**	0.5180
GOB (AR)	MBE (%)	-13.7353	-19.3993	-17.3911	**0.0122**
	RMSE (%)	74.0969	76.2379	75.1409	**59.0701**
	R	0.6138	0.6110	0.6140	**0.7617**
	FB	0.0719	**0.0109**	0.0273	0.1230
	FGE	0.4310	0.4270	0.4244	**0.3730**
TAM (AR)	MBE (%)	-50.6642	-54.6602	-52.8180	**-13.9390**
	RMSE (%)	68.0443	71.5566	69.8481	**37.1550**
	R	0.6778	0.6787	0.6792	**0.8243**
	FB	-0.6735	-0.7412	-0.7149	**-0.1121**
	FGE	0.6772	0.7426	0.7171	**0.2589**

References

[1] J. Polo, C. Fernández-Peruchena, and M. Gastón. Analysis on the long-term relationship between dni and csp yield production for different technologies. *Solar Energy*, 155:1121–1129, 2017.

[2] P. Blanc, B. Espinar, N. Geuder, C. Gueymard, R. Meyer, R. Pitz-Paal, B. Reinhardt, D. Renné, M. Sengupta, L. Wald, and S. Wilbert. Direct normal irradiance related definitions and applications: The circumsolar issue. *Solar Energy*, 110: 561–577, 2014.

[3] WMO. *Guide to meteorological instruments and methods of observation. Volume I - Measurement of Meteorological Variables.* World Meteorological Organization (WMO), Geneva, Switzerland, 2021.

[4] A. Rabl. Comparison of solar concentrators. *Solar Energy*, 18(2):93–111, 1976.

[5] Y. Eissa, P. Blanc, H. Ghedira, A. Oumbe, and L. Wald. A fast and simple model to estimate the contribution of the circumsolar irradiance to measured broadband beam irradiance under cloud-free conditions in desert environment. *Solar Energy*, 163:497–509, 2018.

[6] E. F. M. Abreu, P. Canhoto, and M. J. Costa. Development of a clear-sky model to determine circumsolar irradiance using widely available solar radiation data. *Solar Energy*, 205:88–101, 2020.

[7] E. F. M. Abreu, P. Canhoto, and M. J. Costa. Circumsolar irradiance modelling using libRadtran and AERONET data. *AIP Conference Proceedings*, 2126(1): 190001, July 2019.

[8] B. Mayer and A. Kylling. Technical note: The libradtran software package for radiative transfer calculations - description and examples of use. *Atmospheric Chemistry and Physics*, 5(7):1855–1877, 2005.

[9] S. M. Ivanova. Modelling of circumsolar direct irradiance as a function of GHI, DHI and DNI. In *8th International Conference on solar radiation and daylighting Solaris-2017*, 2017.

[10] A. Neumann, B. von der Au, and P. Heller. Measurements of circumsolar radiation at the Plataforma Solar (Spain) and at the DLR (Germany). In *Proceedings of the International Solar Energy Conference, Solar Engineering*, 429–438, Albuquerque, 1998. American Society of Mechanical Engineers.

[11] P. Forman, S. Penkert, C. Kämper, T. Stallmann, P. Mark, and J. Schnell. A survey of solar concrete shell collectors for parabolic troughs. *Renewable and Sustainable Energy Reviews*, 134:110331, 2020. ISSN 1364-0321.

[12] B. Belhomme, R. Pitz-Paal, P. Schwarzbözl, and S. Ulmer. A New Fast Ray Tracing Tool for High-Precision Simulation of Heliostat Fields. *Journal of Solar Energy Engineering*, 131(3), June 2009.

[13] P. L. Leary and J. D. Hankins. User's guide for MIRVAL: a computer code for comparing designs of heliostat-receiver optics for central receiver solar power plants. Technical Report SAND-77-8280, Sandia National Lab. (SNL-CA), Livermore, CA (United States), Feb. 1979.

[14] P. Bendt, A. Rabl, H. W. Gaul, and K. A. Reed. Optical analysis and optimization of line focus solar collectors. 9 1979.

[15] P. Schwarzbözl, R. Pitz-Paal, and M. Schmitz. Visual HFLCAL - A Software Tool for Layout and Optimisation of Heliostat Fields. In T. Mancini and R. Pitz-Paal, editors, *Proceedings*, Berlin, Sept. 2009. ISBN 978-3-00-028755-8.

[16] P. Gilman, N. Blair, M. Mehos, C. Christensen, S. Janzou, and C. Cameron. Solar advisor model user guide for version 2.0. 8 2008.

[17] V. Quaschning, W. Ortmanns, R. Kistner, and M. Geyer. Greenius: a new simulation environment for technical and economical analysis of renewable independent power projects. In *International Solar Energy Conference*, volume 16702, 413–417. American Society of Mechanical Engineers, 2001.

[18] J. Dersch, P. Schwarzbözl, and T. Richert. Annual Yield Analysis of Solar Tower Power Plants With GREENIUS. *Journal of Solar Energy Engineering*, 133(3), July 2011.

[19] B. Holben, T. Eck, I. Slutsker, D. Tanré, J. Buis, A. Setzer, E. Vermote, J. Reagan, Y. Kaufman, T. Nakajima, F. Lavenu, I. Jankowiak, and A. Smirnov. Aeronet—a federated instrument network and data archive for aerosol characterization. *Remote Sensing of Environment*, 66(1):1–16, 1998.

[20] A. Driemel, J. Augustine, K. Behrens, S. Colle, C. Cox, E. Cuevas-Agulló, F. M. Denn, T. Duprat, M. Fukuda, H. Grobe, M. Haeffelin, G. Hodges, N. Hyett, O. Ijima, A. Kallis, W. Knap, V. Kustov, C. N. Long, D. Longenecker, A. Lupi, M. Maturilli, M. Mimouni, L. Ntsangwane, H. Ogihara, X. Olano, M. Olefs, M. Omori, L. Passamani, E. B. Pereira, H. Schmithüsen, S. Schumacher, R. Sieger, J. Tamlyn, R. Vogt, L. Vuilleumier, X. Xia, A. Ohmura, and G. König-Langlo.

Baseline surface radiation network (bsrn): structure and data description (1992–2017). *Earth System Science Data*, 10(3):1491–1501, 2018.

[21] D. M. Giles, A. Sinyuk, M. G. Sorokin, J. S. Schafer, A. Smirnov, I. Slutsker, T. F. Eck, B. N. Holben, J. R. Lewis, J. R. Campbell, E. J. Welton, S. V. Korkin, and A. I. Lyapustin. Advancements in the aerosol robotic network (aeronet) version 3 database – automated near-real-time quality control algorithm with improved cloud screening for sun photometer aerosol optical depth (aod) measurements. *Atmospheric Measurement Techniques*, 12(1):169–209, 2019.

[22] A. Sinyuk, B. N. Holben, T. F. Eck, D. M. Giles, I. Slutsker, S. Korkin, J. S. Schafer, A. Smirnov, M. Sorokin, and A. Lyapustin. The aeronet version 3 aerosol retrieval algorithm, associated uncertainties and comparisons to version 2. *Atmospheric Measurement Techniques*, 13(6):3375–3411, 2020.

[23] B. Y. Liu and R. C. Jordan. The interrelationship and characteristic distribution of direct, diffuse and total solar radiation. *Solar Energy*, 4(3):1–19, 1960.

[24] C. A. Gueymard and J. A. Ruiz-Arias. Extensive worldwide validation and climate sensitivity analysis of direct irradiance predictions from 1-min global irradiance. *Solar Energy*, 128:1–30, 2016.

[25] C. A. Gueymard, J. M. Bright, D. Lingfors, A. Habte, and M. Sengupta. A posteriori clear-sky identification methods in solar irradiance time series: Review and preliminary validation using sky imagers. *Renewable and Sustainable Energy Reviews*, 109:412–427, 2019.

[26] J. Noring, D. Grether, and A. Hunt. Circumsolar radiation data: The lawrence berkeley laboratory reduced data base. final subcontract report. Technical report, National Renewable Energy Lab., Golden, CO; Lawrence Berkeley Lab., CA, 1991.

[27] A. Rabl and P. Bendt. Effect of Circumsolar Radiation on Performance of Focusing Collectors. *Journal of Solar Energy Engineering*, 104(3):237–250, 08 1982.

Nomenclature

a	model coefficient
B	direct irradiance
b	model coefficient

C	concentration ratio
c	model coefficient
CS	circumsolar irradiance
CSR	circumsolar ratio
FB	fractional bias
FGE	fractional gross error
K_b	beam clearness index
K_d	diffuse fraction
K_t	sky clearness index
L	sky radiance
MBE	mean bias error
n	total number of data points
o	libRadtran simulations
$\overline{o}$	average of libRadtran simulations
p	model prediction
$\overline{p}$	average of model predictions
R	correlation coefficient
RMSE	root mean square error

Greek symbols

α	half-opening angle
δ	angular distance from the centre of the sun
ξ	scattering angle
σ	optical error

Subscripts

n	normal
i	data point
pyr	pyrheliometer
opt	optical
sun	angular width of the sun shape

Superscripts

$ideal$	under ideal conditions

Acronyms

Alt	altitude
AOD	aerosol optical depth
AR	arid climate zone
CSNI	circumsolar normal irradiance
CSP	concentrating solar power
CSR	circumsolar ratio
DNI	direct normal irradiance
FB	fractional bias
FGE	fractional gross error
Lat	Latitude
Long	Longitude
MBE	mean bias error
R	correlation coefficient
RMSE	root mean square error
RTM	radiative transfer model
SSA	single scattering albedo
TM	temperate climate zone
TR	tropical climate zone
WMO	World Meteorological Organization

Chapter 6

Conclusions

In this thesis, the modelling and measurement of direct and circumsolar normal irradiance (DNI and CSNI, respectively) was addressed as well as their impact on the energy generation of CSP systems.

Regarding the modelling of DNI, a new simple and fast model was developed based on minute resolution data and climate zone classification. After an extensive review of the literature and statistical analysis, it was found that the developed model outperformed the other 121 analysed models at the temperate and tropical climate zones, and ranked high at the remaining arid and high albedo climate zones. The developed model is one of the few present in the literature that can be used to estimate diffuse horizontal irradiance (DHI), and consequently DNI, using only global horizontal irradiance (GHI) data and that can be customized according to the climate zone under study. Furthermore, this model can also be used to perform quality control of long-term data series as well as gap-filling.

Other options to model DNI were also studied in this thesis, namely the use of parametrization and radiative transfer models, because this is, presumably, the most accurate way of gathering information on DNI. Furthermore, as these more complex models require several (and often complex) input variables, three data sources were also studied in combination with three models. To that end, the models under analysis were the libRadtran radiative transfer model (RTM) [1, 2], and the SMARTS [3, 4] and REST2 [5] parametrization models. Concerning the data sources, AERONET [6], MERRA-2 [7, 8, 9] and CAMS [10, 11, 12, 13] were the selected databases. Experimental measurements of direct normal, diffuse horizontal and global horizontal irradiance from the radiometric station of ICT at Évora were used as reference for the assessment of the model/data source combos. It was found that at Évora, clear-sky DNI can be simulated with similar accuracy using any of the tested models, combined with either one of three input datasets. In more detail, it was found that the model/data source combos that provide the best performance in predicting DNI are libRadtran/MERRA-2 according to some statistical indicators, and SMARTS/AERONET according to other statistical indicators. Interestingly, it

was also found that the more complex model (libRadtran) and the "reference" dataset (AERONET) did not always produce the best DNI estimates. Tentative explanation for this findings can be (i) imperfect clear-sky screening, (ii) measurement uncertainty in the AERONET data and subsequent error propagation to the irradiance estimates, and (iii) experimental errors associated to the measured DNI (despite the high level of station's maintenance and data quality control).

Regarding the modelling of CSNI, the libRadtran RTM was used together with AERONET data to estimate the sky radiance and, from that, the CSNI through numerical integration in the typical field of view of a pyrheliometer. Alongside the CSNI modelling, the sun-disk DNI was also estimated which enabled the indirect validation of the CSNI data. This was done by comparing the sun-disk and sun-disk + circumsolar irradiance against the experimental (measured) DNI. Since adding the circumsolar irradiance to the sun disk irradiance resulted in an improvement of the modelled data accuracy taking the experimental values as reference, it was therefore concluded that the modelled CSNI values were reliable. This resulted in the creation of a CSNI database that served to train and validate a newly proposed CSNI model that only requires as input widely available solar radiation data such as GHI, DHI and DNI. The proposed CSNI model performs generally better than other models available in the literature according to statistical analysis presented in Section 4.8. It is worth to mention that this fast and simple model to determine CSNI opened new possibilities, including: (i) estimate the sun-disk DNI from pyrheliometer measurements; and (ii) determine the DNI for any aperture angle with a given imposed circumsolar irradiance profile. However, instead of this second possibility, and due to the simplicity of the proposed model and since a database of sky radiance was already created, the option was to generalize the proposed model for any aperture angle aiming to make it readily usable for CSP design and operation tasks. This also has the advantage of implicitly modelling the circumsolar irradiance profile as a function of the mentioned widely available solar irradiance measurements.

The original CSNI model mentioned above was developed to estimate CSNI to a half-aperture angle of 2.5°, the recommended half-aperture angle of pyrheliometers by the WMO [14]. However, this half-aperture angle is larger than the half-aperture angle of the common concentrating solar power (CSP) systems. Therefore, a generalized CSNI model capable of estimating CSNI for different half-aperture angles (based on the CSNI model described above) was also developed. It was found that this proposed general CSNI model performs significantly better at the locations under study than the other models available in the literature. Furthermore, it was also confirmed that the local aerosol regime and atmospheric conditions impact the model fitting and performance more than the climate zone of the locations under study.

Regarding the impact of CSNI in CSP systems, it was found that discarding an

accurate CSNI estimate could lead to a difference up to a 7% between the DNI that is measured by a pyrheliometer and the DNI that is effectively captured by the system. It was also found that these differences are higher for lower half-opening angles, as expected, since the difference between the half-opening angle of the pyrheliometer and the half-opening angle of the CSP system is higher. To assess the impact of CSNI in CSP systems, a case study using parabolic trough concentrators was analysed. It was found that higher CSR values lead to lower intercept factors (the ratio between the irradiance reaching the receiver and the incident irradiance in the concentrator aperture). Furthermore, it was also found that if the impact of CSNI variation on the intercept factor is to be reduced, then parabolic troughs with higher rim angles are preferred.

The measurement of DNI, DHI and GHI was conducted concurrently with the work presented in this thesis. The radiometric station of ICT at Évora was maintained regularly, namely cleaning the pyrheliometer's window and pyranometers' glass domes, checking the sun tracker and instruments alignment and performing periodic calibrations of the sensors, as the example shown in Appendix A. Regarding the measurement of CSNI, the first steps to modify a conventional pyrheliometer in order to change its half-opening angle and, consequently, gather information on CSNI, were taken. More information about this on-going experiment can be found in Appendix B.

Regarding future work, there are several research lines that can be explored following this thesis, namely: (i) studying the error propagation from the atmospheric data inputs to modelled irradiance, taking into consideration model architecture and local conditions; (ii) studying the impact of different aerosol and atmospheric conditions in the development of local and global CSNI models; (iii) evaluating the impact of CSNI in other CSP systems such as parabolic dishes, solar towers, linear Fresnel with and without secondary optics and beam-down central tower systems; (iv) generating CSNI datasets for more locations, aiming to better characterize this part of the solar radiation and to have more data to develop more accurate models; and (v) constructing affordable and easy to operate systems capable of accurately measuring CSNI.

References

[1] C. Emde, R. Buras-Schnell, A. Kylling, B. Mayer, J. Gasteiger, U. Hamann, J. Kylling, B. Richter, C. Pause, T. Dowling, and L. Bugliaro. The libradtran software package for radiative transfer calculations (version 2.0.1). *Geoscientific Model Development*, 9(5):1647–1672, 5 2016.

[2] B. Mayer and A. Kylling. Technical note: The libradtran software package for

radiative transfer calculations – description and examples of use. *Atmos. Chem. Phys.*, 23, 2005.

[3] C. A. Gueymard. The smarts spectral irradiance model after 25 years: New developments and validation of reference spectra. *Solar Energy*, 187:233–253, 7 2019.

[4] C. A. Gueymard. Parameterized transmittance model for direct beam and circumsolar spectral irradiance. *Solar Energy*, 71(5):325–346, 11 2001.

[5] C. A. Gueymard. Rest2: High-performance solar radiation model for cloudless-sky irradiance, illuminance, and photosynthetically active radiation – validation with a benchmark dataset. *Solar Energy*, 82(3):272–285, 3 2008.

[6] B. Holben, T. Eck, I. Slutsker, D. Tanré, J. Buis, A. Setzer, E. Vermote, J. Reagan, Y. Kaufman, T. Nakajima, F. Lavenu, I. Jankowiak, and A. Smirnov. Aeronet—a federated instrument network and data archive for aerosol characterization. *Remote Sensing of Environment*, 66(1):1–16, 10 1998.

[7] V. Buchard, C. A. Randles, A. M. da Silva, A. Darmenov, P. R. Colarco, R. Govindaraju, R. Ferrare, J. Hair, A. J. Beyersdorf, L. D. Ziemba, and H. Yu. The merra-2 aerosol reanalysis, 1980 onward. part ii: Evaluation and case studies. *Journal of Climate*, 30(17):6851–6872, 9 2017.

[8] R. Gelaro, W. McCarty, M. J. Suárez, R. Todling, A. Molod, L. Takacs, C. A. Randles, A. Darmenov, M. G. Bosilovich, R. Reichle, K. Wargan, L. Coy, R. Cullather, C. Draper, S. Akella, V. Buchard, A. Conaty, A. M. da Silva, W. Gu, G.-K. Kim, R. Koster, R. Lucchesi, D. Merkova, J. E. Nielsen, G. Partyka, S. Pawson, W. Putman, M. Rienecker, S. D. Schubert, M. Sienkiewicz, and B. Zhao. The modern-era retrospective analysis for research and applications, version 2 (merra-2). *Journal of Climate*, 30(14):5419–5454, 7 2017.

[9] A. Molod, L. Takacs, M. Suarez, and J. Bacmeister. Development of the geos-5 atmospheric general circulation model: evolution from merra to merra2. *Geoscientific Model Development*, 8(5):1339–1356, 5 2015.

[10] A. Benedetti, J.-J. Morcrette, O. Boucher, A. Dethof, R. J. Engelen, M. Fisher, H. Flentje, N. Huneeus, L. Jones, J. W. Kaiser, S. Kinne, A. Mangold, M. Razinger, A. J. Simmons, and M. Suttie. Aerosol analysis and forecast in the european centre for medium-range weather forecasts integrated forecast system: 2. data assimilation. *Journal of Geophysical Research*, 114(D13):D13205, 7 2009.

[11] J. Flemming, V. Huijnen, J. Arteta, P. Bechtold, A. Beljaars, A.-M. Blechschmidt, M. Diamantakis, R. J. Engelen, A. Gaudel, A. Inness, L. Jones, B. Josse, E. Katragkou, V. Marecal, V.-H. Peuch, A. Richter, M. G. Schultz, O. Stein, and A. Tsikerdekis. Tropospheric chemistry in the integrated forecasting system of ecmwf. *Geoscientific Model Development*, 8(4):975–1003, 4 2015.

[12] A. Inness, M. Ades, A. Agustí-Panareda, J. Barré, A. Benedictow, A.-M. Blechschmidt, J. J. Dominguez, R. Engelen, H. Eskes, J. Flemming, V. Huijnen, L. Jones, Z. Kipling, S. Massart, M. Parrington, V.-H. Peuch, M. Razinger, S. Remy, M. Schulz, and M. Suttie. The cams reanalysis of atmospheric composition. *Atmospheric Chemistry and Physics*, 19(6):3515–3556, 3 2019.

[13] J.-J. Morcrette, O. Boucher, L. Jones, D. Salmond, P. Bechtold, A. Beljaars, A. Benedetti, A. Bonet, J. W. Kaiser, M. Razinger, M. Schulz, S. Serrar, A. J. Simmons, M. Sofiev, M. Suttie, A. M. Tompkins, and A. Untch. Aerosol analysis and forecast in the european centre for medium-range weather forecasts integrated forecast system: Forward modeling. *Journal of Geophysical Research*, 114(D6):D06206, 2009.

[14] W. M. O. (WMO). Guide to Instruments and Methods of Observation. Volume I - Measurement of Meteorological Variables. Technical Report WMO-No. 8, Geneva, 2021.

Appendix A

Example of a calibration protocol according to ISO 9059:1990

UNIVERSIDADE DE ÉVORA

ICT Instituto de Ciências da Terra Institute of Earth Sciences

Calibration Protocol

Calibration site latitude:	38.567773˚	**Linke turbidity range:**	2.45 to 3.90
Calibration site longitude:	-7.911419˚	**Temperature range:**	12.7˚C to 31.1˚C
Calibration site altitude:	290 m	**Wind speed range:**	0 m/s to 4.8 m/s
Pyrheliometer model	Kipp&Zonen CHP1	**Calibration period:**	24/10/2017 to 31/10/2017
Serial number:	131241	**Valid readings:**	3919 readings distributed over 183 series
Reference pyrheliometer:	K&Z CHP1 (140129)	**Sensitivity:**	7.70 µV/(W/m^2)
Solar azimuth range:	-0.22˚ to 66.35˚	**Std of Fj related to F:**	0.044 W/m^2
Solar elevation range:	8˚ to 39.19˚	**Root mean square deviation of DNI:**	0.854 W/m^2
DNI range:	302.8 W/m^2 to 961.2 W/m^2	**Bias of DNI:**	-0.021 W/m^2

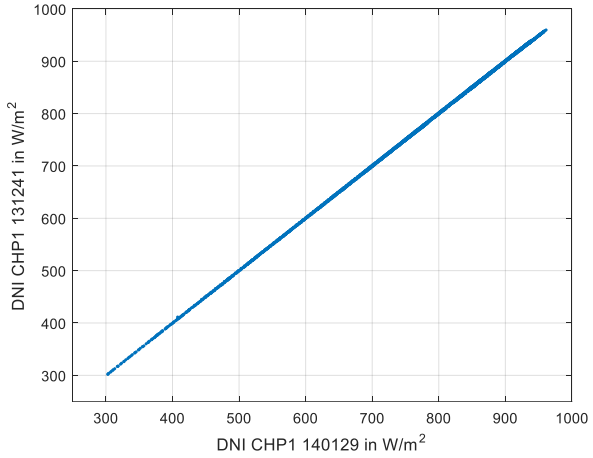

Figure 1 - DNI with identified sensibility versus DNI reading reference.

Évora, 06/11/2017

Appendix B

Modification of a pyrheliometer to measure CSNI

In this section, the first steps to modify the field-of-view of a conventional pyrheliometer through the variation of its collimator length and opening diameter in order to gather information on CSNI are described.

The modified pyrheliometer is composed by a revolver with four possible combinations of tube lengths and diameters and a stepper motor, which automatically enable varying the field-of-view of the pyrheliometer.

Firstly, a 3D software was used to draw a 3D model of all components in order to study the best fit of the revolver, stepper motor and motor support enclosure in the pyrheliometer body and its connection to the sun tracker axis, considering all the constraints to this system to function properly. Such 3D model is shown in Fig. B.1.

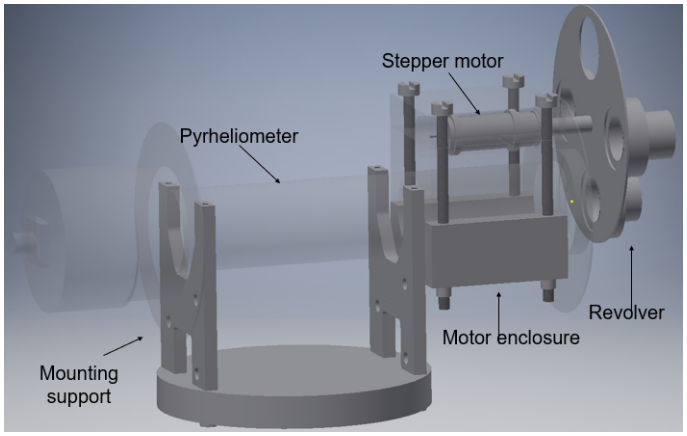

Fig. B.1: 3D model of the system's components.

Secondly, the revolver was printed using a 3D printer and the stepper motor shaft and enclosure were built at the workshops of ICT and Physics Department of the University of Évora. In a first approach, the system was then controlled using an Arduino board. Later, it is intended to test controlling the stepper motor with the same datalogger of the radiometric station in order to synchronize the different measurements. The pyrheliometer with the motor and revolver attached is shown in Fig. B.2.

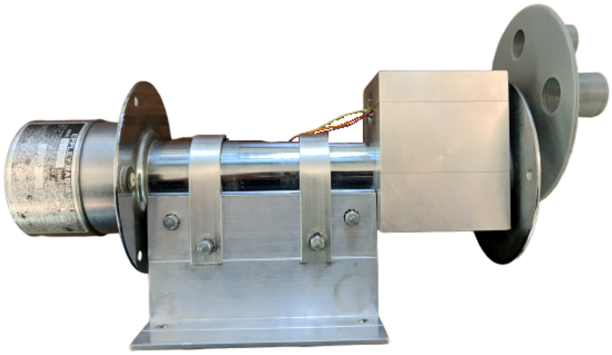

Fig. B.2: Field pyrheliometer (Eppley NIP) with motor and revolver attached.

Thirdly, an indoor test and calibration procedure of the modified pyrheliometer is to be performed using a collimated illuminator and a reference pyrheliometer. The indoor calibration experimental setup is shown in Fig. B.3. Lastly, the system is to be installed in a suntracker and information on CSNI will be gathered.

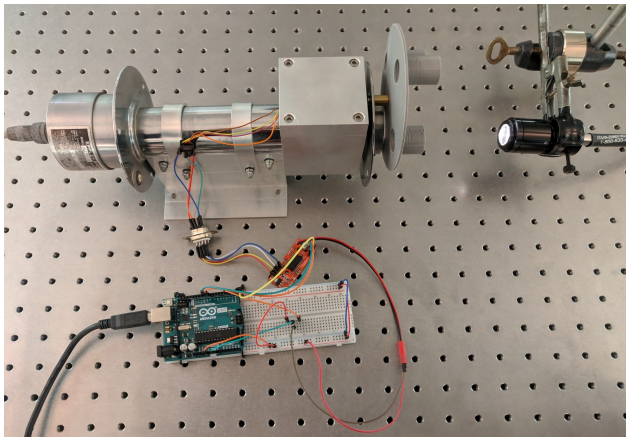

Fig. B.3: Indoor calibration experimental setup.

UNIVERSIDADE DE ÉVORA
INSTITUTO DE INVESTIGAÇÃO
E FORMAÇÃO AVANÇADA

Contactos:

Universidade de Évora

Instituto de Investigação e Formação Avançada - IIFA

Palácio do Vimioso | Largo Marquês de Marialva, Apart. 94

7002-554 Évora | Portugal

Tel: (+351) 266 706 581